

Ultrasonic Health Monitoring of Thermoplastic Composite Aircraft Primary Structures

Ochôa, Pedro

DOI

[10.4233/uuid:23197e0d-8c67-4fe6-a359-be95cc843fcc](https://doi.org/10.4233/uuid:23197e0d-8c67-4fe6-a359-be95cc843fcc)

Publication date

2019

Document Version

Final published version

Citation (APA)

Ochôa, P. (2019). *Ultrasonic Health Monitoring of Thermoplastic Composite Aircraft Primary Structures*. [Dissertation (TU Delft), Delft University of Technology]. <https://doi.org/10.4233/uuid:23197e0d-8c67-4fe6-a359-be95cc843fcc>

Important note

To cite this publication, please use the final published version (if applicable).
Please check the document version above.

Copyright

Other than for strictly personal use, it is not permitted to download, forward or distribute the text or part of it, without the consent of the author(s) and/or copyright holder(s), unless the work is under an open content license such as Creative Commons.

Takedown policy

Please contact us and provide details if you believe this document breaches copyrights.
We will remove access to the work immediately and investigate your claim.



Pedro Ochôa

Ultrasonic Health Monitoring of Thermoplastic Composite Aircraft Primary Structures



Pedro Ochôa

Propositions

accompanying the dissertation

ULTRASONIC HEALTH MONITORING OF THERMOPLASTIC COMPOSITE AIRCRAFT PRIMARY STRUCTURES

by

Pedro André Viegas Ochôa de Carvalho

1. It is not feasible to separate the guided wave modes in ultrasonic signals acquired from composite structures with realistic geometric complexity.
2. The certification of guided wave based SHM systems for aerospace applications will hardly be achieved through experimental methods only.
3. Successful guided wave measurements during flight are not a utopia.
4. There is no such thing as teamwork in Academia.
5. The beginning of the integration of a foreigner in another culture is primarily dependent on the successful recognition of the non-verbal communication patterns among people of the receiving society.
6. Business models based on profiting from the illness of others are aberrations in the so-called modern societies.
7. Competition does not lead to excellence.
8. The development of agriculture as an economic activity is the historical root cause of all man-made mass destruction in the world.
9. The incorporation of thermodynamics in labour law can bring more justice to the (re)distribution of wealth in society.
10. Revolution starts in bed, takes roots at the table, and is put into effect on the street.

These propositions are regarded as opposable and defensible, and have been approved as such by the promoters Prof. dr. ir. R. Benedictus and Dr. R.M. Groves.

Stellingen

behorende bij het proefschrift

ULTRASONIC HEALTH MONITORING OF THERMOPLASTIC COMPOSITE AIRCRAFT PRIMARY STRUCTURES

door

Pedro André Viegas Ochôa de Carvalho

1. Het is niet mogelijk om de geleide-golfmodi te scheiden in ultrasone signalen die uit composietstructuren met realistische geometrische complexiteit worden verkregen.
2. De certificering van op geleide golven gebaseerde SHM-systemen voor lucht- en ruimtevaarttoepassingen zal nauwelijks alleen door experimentele methoden worden bereikt.
3. Succesvolle geleide-golfmetingen tijdens de vlucht zijn geen utopie.
4. Er bestaat niet zoiets als teamwerk in academia.
5. Het begin van de integratie van een buitenlander in een andere cultuur is in de eerste plaats afhankelijk van de succesvolle herkenning van de non-verbale communicatiepatronen tussen mensen in het gastland.
6. Bedrijfsmodellen gebaseerd op het profiteren van de ziekte van anderen zijn afwijkingen in de zogenaamde moderne samenlevingen.
7. Competitie leidt niet tot excellentie.
8. De ontwikkeling van landbouw als economische activiteit is de historische oorzaak van alle door de mens veroorzaakte verwoesting in de wereld.
9. Het inbrengen van thermodynamica in het arbeidsrecht kan meer recht doen aan de (her)verdeling van welvaart in de samenleving.
10. Revolutie begint in bed, schiet wortel aan tafel en wordt op straat toegepast.

Deze stellingen worden opponeerbaar en verdedigbaar geacht en zijn als zodanig goedgekeurd door de promotoren Prof. dr. ir. R. Benedictus en Dr. R.M. Groves.

ULTRASONIC HEALTH MONITORING OF
THERMOPLASTIC COMPOSITE AIRCRAFT PRIMARY
STRUCTURES

ULTRASONIC HEALTH MONITORING OF
THERMOPLASTIC COMPOSITE AIRCRAFT PRIMARY
STRUCTURES

Dissertation

for the purpose of obtaining the degree of doctor
at Delft University of Technology,
by the authority of the Rector Magnificus Prof. dr. ir. T.H.J.J. van der Hagen,
chair of the Board of Doctorates,
to be defended publicly on
Thursday, 17th October 2019 at 10:00 hours

by

Pedro André VIEGAS OCHÔA DE CARVALHO

Master of Science in Aerospace Engineering,
Instituto Superior Técnico, Portugal
born in Lisbon, Portugal

This dissertation has been approved by the promotor.

Composition of the doctoral committee:

Rector Magnificus	Chairman
Prof. dr. ir. R. Benedictus	Technische Universiteit Delft, promotor
Dr. R.M. Groves	Technische Universiteit Delft, promotor
Dr. I.F. Villegas	Technische Universiteit Delft, copromotor

Independent members:

Prof. dr. F. Scarano	Technische Universiteit Delft
Prof. dr. V. Giurgiutiu	University of South Carolina, United States of America
Prof. dr. H. Dong	Norges teknisk-naturvitenskapelige universitet, Norway
Prof. dr. K. Van Den Abeele	Katholieke Universiteit Leuven, Belgium
Prof. dr. ir. M. Mulder	Technische Universiteit Delft, reserve member



Keywords:

Ultrasonic guided wave, Structural health monitoring, Thermoplastic composites, Aircraft structures, System reliability

Printed by:

Ipskamp Printing (www.ipskampprinting.nl)

Front and back covers:

Network of piezoceramic transducers for ultrasonic guided wave based monitoring of a critical area of a stiffened panel from a torsion box of a component-scale horizontal stabiliser.

Copyright © 2019 by P.A. Viegas Ochôa de Carvalho

All rights reserved. No part of this publication may be reproduced, stored in a retrieval system or transmitted in any form or by any means, electronic, mechanical, photocopying, recording or otherwise, without the prior written permission of the author.

This research was part of the Thermoplastic Affordable Primary Aircraft Structure 2 (TAPAS 2) project, supported by the Netherlands Enterprise Agency of the Ministry of Economic Affairs.

ISBN 978-94-028-1730-0

An electronic version of this dissertation is available at
<http://repository.tudelft.nl/>.

*Aos meus pais, Pedro e Graça.
À minha irmã, Inês.
Aos meus avós, Francisco e Júlia, e Fernando e Emília.
To Jildou.*

Summary

Composites are used in more than half of the primary structures of the most modern large civil aircraft, yet there is a limited capability for predicting damage progression in these materials. This makes it impossible to correctly determine inspection intervals, and has put maintenance costs and airworthiness under pressure. Consequently, a real need for a new maintenance philosophy has arisen. One philosophy in which structural condition can be assessed in an almost real-time basis in order to know when and where repairs must be made. For this philosophy to be transformed into condition based maintenance (CBM) programmes, it is crucial to develop structural health monitoring (SHM) systems capable of performing damage diagnostic and remaining useful life prognostic.

At the same time, the urge to reduce production costs has led to consistent developments in thermoplastic composite (TpC) technology. In particular, new possibilities have been unlocked for automated assembly processes based on welding. This context constitutes a unique opportunity for integrating research on SHM into the advances of TpC technology, in order to contribute to a combined reduction of production and maintenance costs, and thus to the development of a truly cost-effective composite airframe.

Over the last three decades, ultrasonic guided waves (GWs) have been recognised as having a great potential for detailed quantitative diagnostic of damage in composite structures. However, there are still no certified GW based SHM (GW-SHM) applications for civil aircraft. The reason for that is a limited understanding about the interaction between measurement variability factors associated with real operational environments, damage types, materials and geometric complexity. Therefore, the aim of the research presented in this thesis was to accelerate the bridging of those knowledge gaps and thereby to improve the reliability of GW-SHM for composite aircraft.

The research presented in this thesis progresses from structural element to component-scale structure. At element scale the focus was on understanding complex aspects of GW propagation in TpC structural details. The effects of manufacturing-related variations on GW transmission across TpC ultrasonically welded joints were studied. A two-step investigation was undertaken, initially only with pristine joints produced with different welding conditions, and then also with joints manufactured with defects introduced in a controlled way. Time-domain and frequency-domain analysis of the pattern of reverberations from the joint overlap and their interference with the directly transmitted wave packets enabled the differentiation between two defective scenarios, unwelded areas and adherend fibre bundle distortion.

The development of reliable GW-SHM capabilities implies systematisation and standardisation of practices, but also realistic outputs to make those practices feasible. Therefore, before progressing to higher scales of structural size and complexity, the research was focused on developing a systematic methodology for designing a GW-SHM system. The methodology is not limited to a single damage scenario, does not resort to unrealistic GW mode selection, and is applicable to a generic real-scale (1:1) composite aircraft primary structure. The proposed design methodology was validated on a stiffened panel of a component-scale horizontal stabiliser torsion box, entirely made of carbon-fibre

reinforced TpC. The structure was subjected to multiple low-energy impacts in order to induce barely visible impact damage (BVID) of different severities and in different critical locations.

At real scale it is crucial to understand the effects of real operational-environmental variability factors on GW signals of the structure. Hence, GW measurements were performed on the aforementioned component-scale torsion box panel, subjected to high-amplitude low-frequency vibration (HA-LFV). The visible effect of HA-LFV on ultrasonic GW propagation was the presence of coherent noise in the filtered signals. This coherent noise was interpreted as the result of superposition of multiple dispersive wave groups produced by mode conversion at the moment of reflection on the corrugated panel surface. It was also observed that the coherent noise amplitude depends on the amplitude of the LFV, and on the ratio between the LFV frequency and the ultrasonic excitation frequency. These relationships can potentially be explored for the development of a HA-LFV compensation mechanism for enabling in-service GW based damage diagnostic.

In conclusion, this thesis has put forward three possible paths for improving the reliability of GW-SHM systems for composite aircraft. First, to the early detection of manufacturing defects by investigating the relationship between GW propagation and assembly process parameters at structural element scale. Second, to reduce the uncertainty in the damage diagnostic by increasing the systematisation of the GW-SHM system design. Third, to increase the robustness of damage diagnostic capabilities by studying the effects of real operational-environmental variability factors on GW propagation at real scale.

Samenvatting

Composieten worden toegepast in meer dan de helft van de primaire structuur van de modernste grote commerciële straalvliegtuigen. Echter, is er nog steeds een beperkte mogelijkheid om de progressie van schade in deze materialen te voorspellen. Dit maakt het onmogelijk om inspectie-intervallen correct te bepalen en komen onderhoudskosten en luchtwaardigheid onder druk te staan. Hierdoor is er een reële behoefte ontstaan voor een nieuwe onderhoudsfilosofie. Een filosofie waarin de structurele conditie bijna real-time kan worden beoordeeld om te weten waar en wanneer reparaties moeten worden uitgevoerd. Om deze filosofie te transformeren in toestandsafhankelijk onderhoudsprogramma's (*condition based maintenance*, CBM), is het cruciaal om structurele gezondheidsmonitoringssystemen (*structural health monitoring*, SHM) te ontwikkelen die in staat zijn om schade te diagnosticeren en een prognose te kunnen stellen van de resterende gebruiksduur.

Tegelijkertijd heeft de drang om productiekosten te verlagen geleid tot gestage ontwikkelingen in de thermoplastische composiet (TpC) technologie. In het bijzonder zijn er nieuwe mogelijkheden ontwikkeld voor geautomatiseerde assemblageprocessen door middel van lassen. Deze context biedt een unieke kans om onderzoek naar SHM te integreren in de vooruitgang van de TpC-technologie om bij te dragen aan een gecombineerde reductie van productie- en onderhoudskosten en daarmee ook aan de ontwikkeling van een echt kosteneffectief samengesteld composieten casco.

Gedurende de laatste drie decennia is erkend dat ultrasone geleide golven (*ultrasonic guided waves*, GW's) een grote potentie hebben voor een gedetailleerde kwantitatieve diagnose van schade in composietstructuren. Er zijn echter nog steeds geen gecertificeerde, op GW gebaseerde, SHM(GW-SHM)-toepassingen voor civiele vliegtuigen. Dit komt door het beperkte inzicht in de interactie tussen meetvariabiliteitsfactoren die verband houden met reële operationele omgevingen, schadetypes, materialen en geometrische complexiteit. Daarom was het doel van het onderzoek gepresenteerd in dit proefschrift, om de overbrugging van die kennishiaten te versnellen en daarmee het verbeteren van de betrouwbaarheid van GW-SHM voor composieten vliegtuigen.

Het onderzoek in dit proefschrift gaat van element naar component schaal. Op elementschaal lag de focus op het begrijpen van de complexe aspecten van de GW-voortbeweging in structurele TpC-details. De effecten van aan de fabricage gerelateerde variaties op GW-transmissie in ultrasoon gelaste verbindingen van TpC werden bestudeerd. Het onderzoek werd uitgevoerd in twee stappen. Aanvankelijk werden alleen ongerepte verbindingen geproduceerd met verschillende lasomstandigheden. Vervolgens werden ook verbindingen vervaardigd met defecten die op gecontroleerde wijze zijn aangebracht. Tijd domein- en frequentiedomeinanalyse van het galmpatroon van de overlappende verbindingen en hun interferentie met de direct uitgezonden golfpakketten maken het mogelijk om onderscheid te maken tussen twee defect scenario's: niet-gelaste gebieden en vervorming van vezelbundels.

De ontwikkeling van betrouwbare GW-SHM-mogelijkheden impliceert systematisering en standaardisatie van werkwijzen, maar ook realistische resultaten om die praktijken haalbaar te maken. Daarom was het onderzoek vooral gericht op het ontwikkelen van een systematische methodologie voor het ontwerpen van een GW-SHM-

systeem voordat het doorgaat naar hogere schalen van structurele omvang en complexiteit. De methodologie is niet beperkt tot een enkelvoudig schadescenario, maakt geen gebruik van onrealistische GW-modusselectie en is van toepassing op een generieke grootschalige (1:1) primaire structuur van een composieten vliegtuig. De voorgestelde ontwerpmethodologie werd gevalideerd op een verstijfd paneel van een torsiedoos van een component schaal horizontale stabilisator gemaakt van met koolstofvezel versterkt TpC. De structuur werd onderworpen aan meerdere lage energie-inslagen om nauwelijks zichtbare inslagshade (*barely visible impact damage*, BVID) met verschillende gradaties en op verschillende kritieke locaties te veroorzaken.

Op ware grootte schaal is het van cruciaal belang om de effecten van operationele en omgevingsvariabiliteitsfactoren op de GW-signalen van de structuur te begrijpen. Vandaar dat GW-metingen werden uitgevoerd op de bovengenoemde torsiedoospaneel, dat onderworpen was aan hoge amplitude laagfrequente trillingen (*high-amplitude low-frequency vibration*, HA-LFV). Het zichtbare effect van HA-LFV op ultrasone GW-voortbeweging was de aanwezigheid van coherente ruis in de gefilterde signalen. Deze coherente ruis werd geïnterpreteerd als het resultaat van superpositie van meerdere dispersieve golfgroepen geproduceerd door modusomzetting op het moment van reflectie op het gegolfde paneeloppervlak. Er werd ook waargenomen dat de coherente ruisamplitude afhangt van de amplitude van de LFV en van de verhouding tussen de LFV-frequentie en de ultrasone excitatiefrequentie. Deze relaties kunnen mogelijk worden verkend voor de ontwikkeling van een HA-LFV-compensatiemechanisme om in-service diagnostische schadeanalyse mogelijk te maken op basis van GW.

Concluderend heeft dit proefschrift drie mogelijke paden voorgesteld voor het verbeteren van de betrouwbaarheid van GW-SHM-systemen voor composieten vliegtuigen. Ten eerste om methoden te ontwikkelen voor het vroegtijdig opsporen van fabricagefouten door de relatie tussen GW-voortbeweging en assemblageprocesparameters op structurele elementenschaal te onderzoeken. Ten tweede om de onzekerheid in de schadediagnostiek te verminderen door de systematisering van het GW-SHM-systeemontwerp te vergroten. Ten derde, om de robuustheid van schade diagnostische capaciteiten te vergroten door de effecten van reële operationele omgevingsvariabiliteitsfactoren op GW-voortbeweging op ware grootte schaal te bestuderen.

*“As a child, be well-behaved;
As a young man, be the master of yourself;
As an adult, be just;
As an elder, be wise;
As a dying man, be without sorrow.”*

Louis, R. De Delphes à l’Oxus, inscriptions grecques nouvelles de la Bactriane. In:
Comptes-rendus des séances de l’Académie des Inscriptions et Belles-Lettres, 112^e année,
N.3, 1968, pp. 416-457

Contents

Summary.....	vii
Samenvatting.....	ix
Nomenclature	xvii
List of figures.....	xxv
List of tables.....	xxix
1 Introduction.....	1
1.1. Opportunities for structural health monitoring (SHM) of composite aircraft	2
1.2. The challenges of SHM system certification	3
1.3. Research goal and scope.....	4
1.4. Thesis outline.....	4
References	5
2 Literature review.....	7
2.1. Thermoplastic composites (TpCs) for primary aircraft structures	8
2.2. Ultrasonic welding of TpCs.....	8
2.2.1. Internal structure of static ultrasonic welds	9
2.2.2. Manufacturing defects in static ultrasonic welds	10
2.3. Damage in composite structures.....	10
2.4. Fundamentals of ultrasonic guided wave (GW) propagation	12
2.4.1. Wave guiding mechanism.....	12
2.4.2. GWs in plates.....	14
2.4.3. GWs in structures.....	16
2.4.4. GWs in composite materials	20
2.4.5. GW transducers.....	20
2.4.6. Temperature and loading effects.....	22
2.5. Modelling GWs in structures.....	24
2.6. GW signal processing.....	27
2.6.1. Mathematical definitions	27
2.6.2. Signal filtering	29
2.6.3. Temperature effect compensation.....	30
2.6.4. Damage indicators	31
2.7. SHM of fixed wing aircraft	35
2.7.1. System functions.....	35
2.7.2. System capabilities and requirements	36
2.8. SHM reliability quantification	37
2.9. Knowledge gaps	38
References	39

3	Methodology.....	51
3.1.	Research process	52
3.2.	Experiments.....	54
3.2.1.	Element scale.....	54
3.2.2.	Component scale	55
3.2.3.	Extra tests	57
3.3.	Models.....	57
3.4.	Signal processing	57
3.5.	Revisiting the thesis chapter order	59
	References	59
4	GWs in TpC ultrasonic welds: Effect of welding travel	61
4.1.	Introduction	62
4.2.	Test specimen manufacturing.....	62
4.3.	GW testing	63
4.3.1.	Model of dispersive properties	63
4.3.2.	Definition of the GW excitation	65
4.3.3.	Test setup.....	66
4.4.	Results and discussion.....	67
4.4.1.	Response observation	67
4.4.2.	Signal onset	69
4.4.3.	Transmission coefficient.....	71
4.4.4.	Correlation coefficient.....	78
4.4.5.	Non-destructive inspections	81
4.5.	Conclusions	84
	References	84
5	GWs in TpC ultrasonic welds: Diagnostic of manufacturing defects.....	87
5.1.	Introduction	88
5.2.	Test specimen manufacturing.....	88
5.3.	Experiments.....	90
5.3.1.	Ultrasonic GW testing	90
5.3.2.	Complementary testing and evaluation	92
5.4.	Results and discussion.....	92
5.4.1.	Selection of the reference state	92
5.4.2.	Evaluation of process consistency	93
5.4.3.	Ultrasonic GW detection	96
5.5.	Conclusions	104
5.6.	Notes on the SHM system design.....	105
	References	106
6	SHM system design	107
6.1.	Introduction	108
6.2.	Theoretical basis.....	108
6.2.1.	Total sensor output	108
6.2.2.	Electro-mechanical response of PZT transducer	109
6.2.3.	Energy transfer from the PZT transducer to the structure	110
6.2.4.	Measurement equipment capabilities	110
6.2.5.	PZT transducer thickness effects	111

6.3.	Design methodology	111
6.3.1.	Previous approaches	111
6.3.2.	Proposed design methodology	112
6.4.	Design implementation.....	114
6.4.1.	PZT material selection	114
6.4.2.	Study of the critical areas.....	114
6.4.3.	Final transducer network configuration	122
6.4.4.	Design checks	124
6.5.	Design methodology validation	124
	References	124
7	Reliability analysis.....	127
7.1.	Introduction	128
7.2.	Reliability analysis protocol	128
7.2.1.	Variability factors	129
7.2.2.	Generation of stochastic database	130
7.2.3.	Definition of the detection threshold	131
7.2.4.	Estimation of the probability-of-detection.....	131
7.2.5.	Estimation of the relative operating characteristics and levels	136
7.3.	Development of the modelling approaches	138
7.3.1.	Simulation of ultrasonic GW excitation.....	139
7.3.2.	Simulation of composite material	143
7.4.	Component-scale model	145
7.5.	Results and discussion	148
7.5.1.	Perfect actuator bonding	149
7.5.2.	Degraded actuator bonding	160
7.5.3.	Brief considerations about causality	162
7.6.	Conclusions	162
	References	163
8	Component-scale testing	167
8.1.	Introduction	168
8.2.	Test campaign.....	168
8.2.1.	Test specimen	168
8.2.2.	Test setup.....	169
8.2.3.	Test procedure.....	172
8.3.	Validation of the SHM system design methodology	175
8.3.1.	Visual inspection results	175
8.3.2.	NDT results.....	176
8.3.3.	GW-SHM results	178
8.4.	Effects of audible structural vibration on GW propagation.....	183
8.4.1.	Working hypothesis	184
8.4.2.	High-amplitude low-frequency vibration (HA-LFV) effects	184
8.4.3.	Audible sound wave (SW) effects	197
8.4.4.	Diagnostic capabilities under HA-LFV or SW	198
8.5.	Conclusions	200
	References	202

9	Conclusions and recommendations	205
9.1.	Main conclusions and contributions.....	206
9.1.1.	GWs in ultrasonically welded TpC structures	206
9.1.2.	Systematization of GW-SHM system design	207
9.1.3.	Reliability analysis of GW-SHM systems	208
9.1.4.	Effects of HA-LFV on GW signals	208
9.1.5.	Considerations about signal processing.....	209
9.1.6.	SHM as a catalyst for composite aircraft design optimisation.....	209
9.2.	Recommendations	209
9.2.1.	Damage progression diagnostic in TpC structures	209
9.2.2.	Guided wave transducers.....	210
9.2.3.	Towards three level diagnostic	210
9.2.4.	New damage indicator.....	210
9.2.5.	Improvement of the SHM environment model.....	211
9.2.6.	Effects of HA-LFV on GW propagation	212
9.2.7.	Flying research	212
	References	212
A	Supplementary data.....	215
	Acknowledgments.....	233
	Curriculum Vitae.....	235
	List of publications	237

Nomenclature

Latin symbols

$[c^E]$	Elastic stiffness matrix under constant electric field	N/m ²
$[d]$	Piezoelectric strain coefficient (or charge constant) matrix	m/V
$[e]$	Piezoelectric stress coefficient matrix	N/Vm
$[g]$	Piezoelectric voltage constant matrix	Vm/N
$[s^D]$	Elastic compliance matrix under constant electric displacement	m ² /N
$[s^E]$	Elastic compliance matrix under constant electric field	m ² /N
$\{D\}$	Electric displacement vector	C/m ²
$\{\tilde{D}\}$	Electric displacement temperature coefficient vector	C/°C.m ²
$\{E\}$	Electric field vector	V/m
$\{\tilde{E}\}$	Pyroelectric voltage coefficient vector	V/°Cm
$\{S\}$	Strain vector	
$\{T\}$	Stress vector	Pa
a	Damage size	mm
\hat{a}	Damage indicator response for damage size a	
A_1	First argument of Equation (7.35)	
A_2	First argument of Equation (7.37)	
A_3	First argument of equation (7.39)	
a_{90}	Damage size detected 90% of the times	mm
$a_{90 95}$	Damage size detected 90% of the times, with a confidence of 95%	mm
AH_i	Anti-symmetric shear-horizontal mode of order $i = 0, 1, 2, \dots$	
ai	Anti-symmetric Lamb mode of order $i = 0, 1, 2, \dots$ in an adherend	
Ai	Anti-symmetric Lamb mode of order $i = 0, 1, 2, \dots$ in plate or joint overlap	
a_{ij}	i^{th} ($i = 1, 2, \dots$) repeated measure of the j^{th} ($j = 1, 2, \dots$) damage size	mm
\hat{a}_{ij}	i^{th} ($i = 1, 2, \dots$) repeated measure of the damage indicator for j^{th} damage size	
a_p	Damage size estimated to be detected with a probability of p	mm
A_{PZT}	Transducer surface area	mm ²
AR	Amplitude ratio	
avg	Mean	
a_w	Wavelet scale	
Ax	Signal amplitude	V
b_0, b_1	Linear model parameters	
\hat{b}_0, \hat{b}_1	Linear model parameter estimates	
b_{0i}	Random effect of the i^{th} ($i = 1, 2, \dots$) repeated measure	
B_1	Second argument of Equation (7.35)	
B_2	Second argument of Equation (7.37)	
b_w	Wavelet time dilation	
C	Electrical capacitance	F
C_1	Third argument of equation (7.35)	
C_2	Third argument of equation (7.37)	
CC	Correlation coefficient	

CEP	Correct event prediction rate	
c_g	Group velocity	m/s
C_{Iw}	Confidence interval width	mm
c_L	Longitudinal bulk wave velocity	m/s
c_p	Phase velocity	m/s
$c_{p,pzt}$	Bulk pressure wave speed in the piezoceramic material	m/s
cr	Number of correct rejections	
CR	Correct rejection rate	
c_S	Shear bulk wave velocity	m/s
CWT	Continuous wavelet transform	
C_Ψ	Coefficient for admissibility condition of a wavelet function	
D	Transducer disc diameter	mm
D_1	Fourth argument of Equation (7.35)	
D_3	Second argument of Equation (7.39)	
de	Number of detections	
\overline{de}	Number of non-detections	
De	Detection	
\overline{De}	Non-detection	
DI	Damage indicator	
E	Young's modulus	GPa
$E(\dots)$	Expected value	
$E_{[state]}$	Signal energy for a specific structure state (state = <i>dmg</i> , state = <i>ref</i> , or other)	V ² s
E_{DI}	Error of the damage indicator	
$env(t)$	Signal envelope	V
E_r	Energy ratio	
ER	Energy ratio	
E_s	Signal energy	V ² s
ev	Number of events	
\overline{ev}	Number of non-events	
Ev	Event	
\overline{Ev}	Non-event	
EWC	Entropy of the wavelet coefficients	
f	Frequency	kHz
\tilde{f}	Body force vector	N
$f(\dots)$	Function of	
f_a	Frequency corresponding to wavelet scale a	Hz
fal	Number of false alarms	
f_c	Centre frequency	kHz
f_{ch}, F_{ch}	Characteristic frequency	kHz
FEP	False event prediction rate	
FFT	Fast Fourier transform	
FFT_{norm}	Normalised FFT spectrum	
F_{GW}	Ultrasonic guided wave frequency	kHz
F_{LFV}	Frequency of the low-frequency vibration	Hz
f_{low}	Frequency bandwidth lower limit	kHz
FND	False negative detection rate	
FPD	False positive detection rate	
FT	Fourier transform	

f_{up}	Frequency bandwidth upper limit	kHz
g	Dimensionless ratio of frequency response functions	
G	Shear modulus	GPa
$g(\dots)$	Function of	
$G(\omega)$	Frequency response function	
h	Number of hits	
HT	Hilbert transform	
I	Electrical current	A
$\mathbf{I}(\theta)$	Fisher information matrix	
J_n	Bessel function of the first kind of order $n = 0, 1, 2, \dots$	
k	Signal sample point number	
k_{bw}	Frequency bandwidth parameter	
k_p	Planar electromechanical coupling coefficient of a piezoceramic material	
k_{pzt}	Dynamic stiffness of the piezoceramic transducer	N/m
k_{str}	Dynamic stiffness of the structure	N/m
L	Likelihood	
m	Number of damage size observations	
ME	Missed event rate	
ms	Number of misses	
m_{thr}	Multiple of the detection threshold base value	
n	Number of repeated measures	
$N(\dots)$	Normal distribution	
N, N_{pts}	Number of sample points in a signal	
N_{as}	Number of actuator-sensor pairs	
N_{cyc}	Number of cycles in the excitation pulse	
n_{lam}	Number of laminas in a plate	
no	Total number of observations in a contingency table	
N_{sp}	Number of test specimens in a batch	
p	Probability	
P	Signal power	V ²
p_{rad}	Proportion of in-plane radial motion for the numerical response	
PTC	Power transmission coefficient	
Q	Quantity	
$\mathbf{Q}(\theta)$	Likelihood variation rate matrix	
$R(\dots)$	Cross-correlation between signals	
$R(0)$	Cross-correlation between two signals at zero lag	
r_a	Actuator radius	mm
RMS	Root mean square	
$RMSD$	Root mean square deviation	
s_{dmg}	Normalised damaged state signal	
SH_i	Symmetric shear-horizontal mode of order $i = 0, 1, 2, \dots$	
si	Symmetric Lamb mode of order $i = 0, 1, 2, \dots$ in an adherend	
Si	Symmetric Lamb mode of order $i = 0, 1, 2, \dots$ in plate or joint overlap	
s_{ref}	Normalised reference state signal	
std	Standard deviation	
$std\%$	Percent standard deviation	
t	Time	s
$t_{10\%}$	10%-duration time	s
th	Thickness	mm

\bar{t}_h	Mean thickness	mm
thr	Detection threshold	
thr_o	Base value of the detection threshold	
TND	True negative detection	
TOF	Time of flight	s
TPD	True positive detection rate	
tr	Welding travel	mm
\mathbf{u}	Column vector equal to $[1 \ z_p]^T$	
\vec{u}	Displacement vector	m
U_1	Numerical in-plane displacement along the x -direction	m
u_z	Numerical out-of-plane displacement	m
V	Voltage	V
V_3	Numerical out-of-plane velocity	m/s
V_o	Piezoceramic sensor output voltage	V
V_{rad}	Numerical radial velocity	m/s
V_{tot}	Total simulated ultrasonic guided wave response	V
w	Weight for weighted average	
w_a	Wavelet coefficient at scale a	
W_{ISA}	Static-voltage-induced strain energy generated by a piezoelectric actuator	J
W_{str}	Energy generated by piezoelectric actuator transmitted to the host structure	J
x	Time-domain signal	
x, y, z	Spatial coordinates	m
x_a	Analytic signal	V
x_n	n^{th} point of a discrete signal	V
Y	Electrical admittance of the piezoceramic transducer	S
Z	Electrical impedance of the piezoceramic transducer	Ω
z_p	p^{th} quantile of the standard cumulative normal distribution	

Greek symbols

$[\beta^T]$	Inverse permittivity coefficient matrix	m/F
$[\epsilon^T]$	Electric permittivity matrix	F/m
$\{\alpha^E\}$	Thermal expansion coefficient vector	
α	Statistical uncertainty level	
α_{mode}	Shear coefficient dependent on Lamb wave mode shapes	
β	Ratio of structure dynamic stiffness to piezoceramic dynamic stiffness	
γ	Ratio of angular frequency to piezoceramic bulk pressure wave speed	
Γ	Two-dimensional parameter for piezoceramic transducer shear-lag model	
$\gamma_{xy}(0)$	Coherence between two signals at zero lag	
Δ	Variation	
ϵ	Linear model random error	
ϵ_0	Electric permittivity of free-space	F/m
ϵ_{ij}	Random error of the linear model associated with the i^{th} ($i = 1, 2, \dots$) repeated measure of the j^{th} ($j = 1, 2, \dots$) encountered damage size	
ϵ_{ISA}	Static voltage-induced strain on piezoceramic transducer	
ζ	Parameter used in Equation (7.10) for the confidence region definition for hit/miss analysis	

θ	Probability-of-detection model parameter	
Θ	Temperature	°C
$\hat{\theta}$	Maximum likelihood estimate	
$\hat{\theta}^2$	Total variance estimate	
λ	Wavelength	mm
λ_L	First Lamé parameter	GPa
μ	Probability-of-detection model parameter	
$\hat{\mu}$	Probability-of-detection model parameter estimate	
μ_{dyn}	Dynamic viscosity	Pa.s
μ_L	Second Lamé parameter	GPa
$\nu_{[body]}$	Poisson's ratio for a contraction in the most relevant direction of a body (body = a or other subscripts, or no subscript)	
ν_{ij}	Poisson's ratio for a contraction in direction j due to an extension in direction I ($i = 1, 2; j = 2, 3$)	
ξ	Wavenumber	m ⁻¹
ρ	Material density	kg/m ³
σ	Probability-of-detection model parameter	
$\hat{\sigma}$	Probability-of-detection model parameter estimate	
Σ_{pod}	Covariance matrix of the probability-of-detection model	
Σ_{reg}	Covariance matrix of the linear regression	
τ	Shear stress	Pa
τ^2	Variance of linear regression random errors	
τ_{lag}	Time lag	s
Φ	Matrix of the first partial derivatives of the probability-of-detection model parameters with respect to the linear regression model parameters	
φ	Signal phase	rad
Φ	Standard cumulative normal distribution	
χ^2_2	Chi-squared distribution with two degrees of freedom	
ϕ	Instantaneous phase of time-domain signal	rad
ψ	Two-dimensional stiffness coefficient between structure and piezoceramic transducer	
Ψ	Mother wavelet function	
ω	Angular frequency	rad/s
ω^2	Variance of repeated measure random effects	

Subscripts

a	Actuator
$actuator$	Actuator signal
AD	Adherend
ch	Characteristic
DI	Damage indicator
dmg	Damage state
eq	Equivalent
inc	Incident
Lef	Left adherend

<i>max</i>	Maximum
<i>num</i>	Numeric
<i>over</i>	Overlap
<i>p</i>	Transducer pair or propagation path
<i>pzt, PZT</i>	Pb[Zr_xTi_{1-x}]O₃ (lead zirconate titanate chemical formula); refers to transducer made of that material
<i>r</i>	Relative
<i>ref</i>	Reference state
<i>Right</i>	Right adherend
<i>sensor</i>	Sensor signal
<i>stoch</i>	Stochastic
<i>trans</i>	Transmitted
<i>x</i>	Signal <i>x</i>
<i>xx</i>	Signal <i>x</i> with respect to itself
<i>xy</i>	Signal <i>x</i> with respect to signal <i>y</i>
<i>y</i>	Signal <i>y</i>
<i>yy</i>	Signal <i>y</i> with respect to itself

Superscripts

<i>A</i>	Anti-symmetric mode
<i>dmg</i>	Damage state
<i>ref</i>	Reference state
<i>S</i>	Symmetric mode
<i>*</i>	Complex conjugate

Abbreviations

a, A	Anti-symmetric
AE	Acoustic emission
Amp	Amplitude
AR	Amplitude ratio
A-SHM	Automated structural health monitoring
A-scan	Ultrasonic amplitude point view
B-scan	Ultrasonic amplitude cross-sectional view
BSS	Baseline signal stretch
BVID	Barely visible impact damage
BWG	Background wave groups
CBM	Condition based maintenance
CC	Correlation coefficient
CEP	Correct event prediction rate
CF	Carbon fibre
CR	Correct rejection rate
C-scan	Ultrasonic amplitude planar view
CWT	Continuous wavelet transform
D	Damage

DI	Damage indicator
ED	Energy-director
EFIT	Elastodynamic finite integration technique
EM	Electro-mechanical
ER	Energy ratio
EWC	Entropy of the wavelet coefficients
FE	Finite-element
FEP	False event prediction rate
FFT	Fast Fourier transform
FND	False negative detection rate
FPD	False positive detection rate
FT	Fourier transform
GLM	Generalised linear model
GW	Guided wave
GW-SHM	Guided wave based structural health monitoring
HA-LFV	High-amplitude, low-frequency vibration
HT	Hilbert transform
iFFT	Inverse fast Fourier transform
IL	Impact location
L	Longitudinal
LFV	Low-frequency vibration
LISA	Local interaction simulation approach
Mag	Magnitude
MAPOD	Model-assisted probability of detection
maxV	Maximum voltage
ME	Missed event rate
ND	Not damaged
NDT	Non-destructive testing
NPSD	Normalised power spectral density
OBS	Optimal baseline selection
PEEK	Polyether ether ketone
PEKK	Polyetherketoneketone
POD	Probability-of-detection
PPS	Polyphenylene sulphide
PTC	Power transmission coefficient
PZT	$\text{Pb}[\text{Zr}_x\text{Ti}_{1-x}]\text{O}_3$ (chemical formula for lead zirconate titanate)
RMSD	Root mean square deviation
ROC	Relative operating characteristics
ROL	Relative operating level
s, S	Symmetric
SAFE	Semi-analytical finite-element
SBR	Signal-to-background ratio
SFE	Spectral finite-element
SH	Shear-horizontal
SHM	Structural health monitoring
SLSS	Single-lap shear strength
S-SHM	Scheduled structural health monitoring
ST	State
SV	Shear-vertical

SW	Sound waves
TND	True negative detection rate
TOF	Time-of-flight
TpC	Thermoplastic composite
TPD	True positive detection rate
UAV	Unmanned aerial vehicle
UW	Ultrasonic welding

List of figures

Figure 2.1	Cross-sectional micrograph of weld.	9
Figure 2.2	Typical structure of barely-visible impact damage.	11
Figure 2.3	Bulk wave particle motions in infinite elastic solid media.	12
Figure 2.4	Classification of guided wave in finite solid media.	13
Figure 2.5	Ray-tracing representation of the generation of Lamb waves.	14
Figure 2.6	Phase velocity curves for Lamb modes in an AL6082 plate.	15
Figure 2.7	GW signals acquired from two consecutive positions.	16
Figure 2.8	Feature guiding process in a single-lap joint.	17
Figure 2.9	GW mode shapes in the adherend and in the overlap.	18
Figure 3.1	Building block used for the research framework.	52
Figure 3.2	Articulation of the research activities.	54
Figure 3.3	Single-lap joint produced by ultrasonic welding and tested.	55
Figure 3.4	Ultrasonic welding setup.	55
Figure 3.5	Horizontal stabilizer torsion box stiffened panel.	56
Figure 3.6	Definition of the stringer delamination (or disbond) area.	57
Figure 4.1	Ultrasonic welding curves used for process parameter selection.	63
Figure 4.2	Overlap cross-section diagram.	64
Figure 4.3	Dispersion curves for the single CF/PPS adherends.	65
Figure 4.4	Phase velocity dispersion curves for the different systems.	65
Figure 4.5	Diagram of the test specimen, with transducer positions.	66
Figure 4.6	Setup used for the GW tests.	67
Figure 4.7	GW responses at T40 position for 200 kHz and 250 kHz.	68
Figure 4.8	Diagram of single reverberation after incident s0 mode.	69
Figure 4.9	Onset time for the s0 mode for a) 200 kHz, and b) 250 kHz.	69
Figure 4.10	Detail showing the coupling of the sensors to the specimens.	71
Figure 4.11	Numerical results for signal onset.	71
Figure 4.12	Variation of PTC with welding travel for 200 and 250 kHz.	72
Figure 4.13	Normalised displacement mode shapes of Lamb modes.	73
Figure 4.14	Normalised displacement mode shapes of Lamb modes.	74
Figure 4.15	Normalised displacement mode shapes of Lamb modes.	77
Figure 4.16	Variation of CC if the signals with welding travel.	78
Figure 4.17	Normalised power spectral density at 200 kHz and 250 kHz.	80
Figure 4.18	Variation of the correlation coefficient of the NPSD curves.	80
Figure 4.19	A- and B-scans from 5 MHz phased-array inspections.	82
Figure 4.20	Variation of the magnitude of the weld interface reflection.	83

Figure 5.1	A) Diagram with mould, neat PPS layers and composite stack.	88
Figure 5.2	Power and travel curves as function of energy for initial weld.	89
Figure 5.3	Different phases of the UW process with triangular EDs.	90
Figure 5.4	Setup used for GW testing.	90
Figure 5.5	Single-lap joint with piezo-ceramic transducer discs.	91
Figure 5.6	Simulated group velocity curves.	91
Figure 5.7	Single-lap shear strength as a function of welding time.	92
Figure 5.8	Fracture surfaces of the a) bottom and b) top adherends.	93
Figure 5.9	Fracture surfaces of the a) bottom and b) top adherends.	93
Figure 5.10	Ultrasonic A- and B-scans of the weld of specimen B01-04.	94
Figure 5.11	Fracture surfaces of the a) bottom and b) top adherends.	95
Figure 5.12	Ultrasonic A- and B-scans of the weld of specimen B02-03.	95
Figure 5.13	Ultrasonic A- and B-scans of the weld of specimen B03-04.	96
Figure 5.14	Signal energy for each batch at all excitation frequencies.	96
Figure 5.15	a) Variation of adherend thickness per batch.	97
Figure 5.16	Overlap thickness for each batch.	97
Figure 5.17	Characteristic frequency shift for the three batches.	98
Figure 5.18	Guided wave mode shapes with non-null in-plane component.	99
Figure 5.19	Time-of-flight for the three batches at all excitation frequencies.	100
Figure 5.20	Force-displacement curves from the single-lap shear tests.	101
Figure 5.21	Ultrasonic GW signals from a) batch 2 and b) batch 3.	102
Figure 5.22	Average normalized cumulative energy curves.	102
Figure 5.23	Complement of the CC between the full time-domain signals.	103
Figure 5.24	Complement of the CC between batch 2 and the other batches.	103
Figure 6.1	Dispersion curves for the skin of areas 1-2.	115
Figure 6.2	Dispersion curves for the skin of area 3.	115
Figure 6.3	Sensor output function and electro-mechanical admittance.	118
Figure 6.4	Electrical current (computed according to Ohm's law $I = V / Z$).	120
Figure 6.5	Normalized energy transferred by the PZT actuator.	121
Figure 6.6	Transducer network on a) critical area 1 and b) critical area 2.	123
Figure 6.7	Transducer network on critical area 3.	124
Figure 7.1	Flowchart of the reliability analysis protocol.	128
Figure 7.2	Setup of the extra GW tests performed on the aluminium plate.	139
Figure 7.3	Convergence study results.	141
Figure 7.4	Comparison of the numerical and experimental signals.	142
Figure 7.5	Comparison of the numerical and experimental signals.	142
Figure 7.6	Comparison of the numerical and experimental signals.	144
Figure 7.7	Comparison of the numerical and experimental signals.	145
Figure 7.8	View A: Complete model with the panel, stringers and ribs.	146

Figure 7.9	Positions of the PZT transducers on the model.	146
Figure 7.10	Portions of the actuator area corresponding to a) 100% bonding.	148
Figure 7.11	Simulated ultrasonic wavefield (<i>z-displacement</i>) after excitation.	148
Figure 7.12	DI databases obtained with error 1 and error 2.	149
Figure 7.13	POD curves and 95% confidence bounds obtained at 112 kHz.	150
Figure 7.14	POD curves obtained at 112 kHz.	151
Figure 7.15	POD for critical damage size as function of repeated measures.	152
Figure 7.16	Semi-width of the 95% confidence bounds.	152
Figure 7.17	POD curves and 95% confidence bounds for $thr = 3thr_0$.	153
Figure 7.18	POD curves and 95% confidence bounds at 112 kHz, \hat{a} vs a .	155
Figure 7.19	POD curves and 95% confidence bounds at 198 kHz, \hat{a} vs a .	156
Figure 7.20	a) TPD and FPD rates for 112 kHz as functions of the threshold.	156
Figure 7.21	a) CEP and ME rates as functions of critical damage of interest.	159
Figure 7.22	DI databases obtained for 112 kHz.	160
Figure 7.23	POD curves and 95% confidence bounds at 112 kHz.	161
Figure 8.1	Horizontal stabilizer torsion box stiffened panel.	169
Figure 8.2	Portable impact gun positioned on the outer side of the skin.	169
Figure 8.3	Guided wave measurement setup.	170
Figure 8.4	Transducer network on a) critical area 1 and b) critical area 2.	170
Figure 8.5	Transducer network on critical area 3.	171
Figure 8.6	Electro-mechanical susceptance measurement setup.	171
Figure 8.7	Connection of the mechanical shaker to the torsion box panel.	172
Figure 8.8	Frequency spectrum of the applied HA-LFV.	173
Figure 8.9	General views of the torsion box panel.	174
Figure 8.10	Barely-visible damages after first impact on area 3.	176
Figure 8.11	Ultrasonic C-scans of stringer run-outs.	177
Figure 8.12	Ultrasonic C-scans of stringer at area 3.	178
Figure 8.13	Weighted-average DI values for each state.	179
Figure 8.14	RMSD _f for sparse transducer network at 123 kHz.	182
Figure 8.15	Evolution of the transducer network degradation during the test.	183
Figure 8.16	Signals from actuator-sensor pair 6-9 (Area 2) at 123 kHz.	185
Figure 8.17	Average filtered signal.	186
Figure 8.18	Evolution of the signal-to-background ratio (SBR).	186
Figure 8.19	Signals from actuator-sensor pair 6-9 (Area 2) at 213 kHz.	187
Figure 8.20	Signals from actuator-sensor 6-9 (Area 2) at 335 kHz.	187
Figure 8.21	Signal-to-background ratio (SBR) without and with HA-LFV.	188
Figure 8.22	Group velocity dispersion curves for the skin of areas 1-2.	189
Figure 8.23	Raw signals from actuator-sensor pair 6-9 (Area 2).	189
Figure 8.24	Variation of $t_{10\%}$ and f_{ch} due to differences in GW scattering.	190

Figure 8.25	Variation of $t_{10\%}$ and f_{ch} due to the HA-LFV.	191
Figure 8.26	Normalised FFT spectra of the signals.	191
Figure 8.27	Normalised FFT spectra of the signals.	192
Figure 8.28	Definition of the geometry of the model of the plate.	192
Figure 8.29	Free vibration mode shapes.	193
Figure 8.30	Numerical time-domain signals for runs 1 to 5.	194
Figure 8.31	Group velocity dispersion curves for the aluminium plate.	195
Figure 8.32	Numerical time-domain signals for runs 6 to 10.	196
Figure 8.33	Variation of signal-to-background ratio (SBR).	196
Figure 8.34	Variation of $t_{10\%}$ and f_{ch} in the numerical signals.	197
Figure 8.35	Signals from actuator-sensor pair 2-4 (area 1) at 123 kHz.	198
Figure 8.36	SBR for all actuator-sensor pairs of area 1, after 50 J impact.	198
Figure 8.37	Frequency-domain CC-based DI for all tested HA-LFV cases.	199
Figure 8.38	Frequency-domain CC-based DI for all tested audible SW cases.	199

List of tables

Table 3.1	Mechanical properties of the CF/PPS material used.	54
Table 3.2	Mechanical properties of the CF/PEKK composite material used.	56
Table 3.3	Approximate composite ply stacking sequence for the skin.	57
Table 4.1	Measured dimensions of adherends and energy directors.	64
Table 4.2	Measured overlap dimensions and weld line thicknesses.	64
Table 4.3	Phase analysis of the S0 and A1 carrier modes at 250 kHz.	75
Table 4.4	Phase analysis of the S0 and A1 carrier modes at 350 kHz.	77
Table 5.1	Welding process control parameters for the three batches.	90
Table 6.1	Piezoelectric charge and voltage constants in the 31-direction.	114
Table 6.2	Inversely calculated centre frequency.	116
Table 6.3	Frequencies of the relevant local maxima of the sensor output.	118
Table 6.4	Frequencies of the relevant local maxima of the sensor output.	121
Table 6.5	PZT transducer numbers and their configuration.	123
Table 6.6	Approximate spatial coordinates of the PZT transducers.	123
Table 7.1	Main variability factors for an ultrasonic GW-SHM system.	129
Table 7.2	Summary of the parametric values used.	130
Table 7.3	General contingency table of possible binary outcomes.	137
Table 7.4	Properties of the APC 850 piezoelectric ceramic material.	140
Table 7.5	Properties of the CF/PPS woven composite material [29].	143
Table 7.6	Layup sequences used for all composite parts.	147
Table 7.7	Approximate wavelength of the S0 and A0 Lamb modes.	154
Table 8.1	Impact locations along the stringers.	174
Table 8.2	Real energy of the impacts and skin indentation depth.	175
Table 8.3	Variation of energy ratio between damage states D3 and D3+D3.	180
Table 8.4	Variation of energy ratio between damage states D3 and D3+D3.	180
Table 8.5	Weighting factors for all propagation paths within area 3.	181
Table 8.6	Weighting factors for all propagation paths within area 3.	181
Table 8.7	Runs of the FE parametric study.	193

1

Introduction

What we do in life, echoes in eternity.

(Gladiator)

There is a need for structural health monitoring in civil aviation as an enabler of condition based maintenance, which is a crucial implementation step for optimizing maintenance resource allocation and allowing the modern composite aircraft to operate as safely and efficiently as their metal counterparts. As developments in thermoplastic composites technology for affordable aircraft primary structures speed up, renewed opportunities become available for research in structural health monitoring, with both fields benefitting from each other as the level of multi-purpose technology integration increases. Ultrasonic guided waves play an important role in that research. Due to their inherent capability of detailed interaction with intra-material features and long-range propagation on component scale, they enable quantitative diagnostic of damage in composite structures.

This research aims at bringing the reliability of ultrasonic guided wave based structural health monitoring systems closer to certification level. To do so, the focus is placed on understanding interactions between environmental-operational factors, monitoring system, structure and guided wave propagation.

1.1. Opportunities for structural health monitoring (SHM) of composite aircraft

Maintenance is perhaps the key for the success of civil aviation as one of the safest means of transportation in the world. Airlines make sure each aircraft in the fleet follows a rigorous programme of inspections to find structure and system degradation, if existing, and repairs or replacements are executed, if necessary [1]. In this way it is possible to keep structural and system integrity in line with airworthiness regulations.

The schedule and detail level of the periodic inspections must take into account the typical aircraft mission (expected number and type of flight cycles) and the expected flight demand for the fleet. Thus it is crucial to be able to predict degradation to an acceptable level of accuracy. From a structural point of view, it should be possible to estimate the number of flight cycles until damage reaches a size which can compromise the load bearing capabilities. Damage growth predictions are usually made by resorting to fracture mechanics, which is well established for metallic materials [1,2]. As a result, civil aviation statistics show an impressively low number of accidents caused by structural failures [3].

With the pressure for reducing costs in aviation, namely in fuel consumption, new high-performance composite materials were developed [4] and eventually applied in more than half of the structure of the fourth generation commercial jet aircraft, such as the Boeing B787 and the Airbus A350. However, the appearance and progression of damage in composites is dramatically different from metals, and the current models are not yet capable of making predictions with acceptable accuracy [5]. This poses a serious challenge to airlines when it comes to plan the periodic inspections of composite aircraft. And it could also raise some safety issues, as there is uncertainty about the degradation of the composite structure. Therefore, there is a real need for an alternative maintenance philosophy in which structural condition is assessed in an almost real-time basis in order to know when and where repairs must be made. This is the so-called condition based maintenance (CBM) [6] approach.

For CBM programmes to be implemented structural behaviour data must be acquired by monitoring systems formed by transducer networks permanently installed on the structure. These structural health monitoring (SHM) [6] systems then use the collected data to perform damage diagnostic and subsequently issue a prognostic of the remaining useful life of the component or part, which then constitutes the basis for the advice to manage the maintenance programme. In other words, before CBM practices can be adopted, research on SHM of composite structures must be conducted in order to understand how reliable SHM systems can be developed.

As airlines become aware of new maintenance challenges, aircraft manufacturers have been increasingly interested in developing more cost-effective solutions for composite aircraft primary structures. This stimulates research on new composite materials and structures along with the necessary manufacturing and assembly technologies [7]. In particular, thermoplastic composites (TpCs) are regarded as promising alternatives to thermoset composites. The fact that parts can be welded together overcomes typical issues of mechanical fastening of composites, such as stress concentrations and delaminations due to hole-drilling, and of adhesive bonding, such as the needed surface preparation and curing cycle, and it is one of the main factors contributing to the cost effectiveness of thermoplastic composite materials. There are three main techniques for welding of continuous fibre reinforced TpCs, resistance, induction and ultrasonic welding. From an industrial point of view, the latter shows high potential for automation, due to its short

processing times [8], which creates a strong research interest. This context proves to be extremely important for the aircraft industry, because of the new opportunities it creates. Performing SHM research on new TpC aircraft structures, in an effort to expand the knowledge about damage diagnostic in composites and increase the integration of SHM functionalities into the composite structures, enables the acquisition of knowledge which will be crucial for providing the future 5th generation of commercial aircraft with CBM-ready design.

1.2. The challenges of SHM system certification

The selection of a physical phenomenon to interrogate a structure depends on the function the SHM system is designed to perform. When it comes to identifying and quantifying damage in composite structures typically used in aircraft, research has shown that active interrogation of ultrasonic guided waves (GWs) has a high potential [9,10]. The mechanism that induces ultrasonic propagation in thin-walled structures in the form of GWs enables sensitive interaction with incipient within-thickness damage features such as barely-visible impact damage (BVID) and delaminations, while covering relatively large areas at the aircraft component scale (i.e. up to a 2 m). Moreover, the transducers employed for exciting GWs in the structure are typically made from lead zirconate titanate (PZT) materials, which can be produced in shapes and sizes that are unobtrusive for the structure, can remain permanently installed, and can combine the functions of actuation and sensing. Therefore, PZT transducer technology for GW based SHM (GW-SHM) is well aligned with the requirements for implementing SHM on fixed wing aircraft [6].

Despite the encouraging results of research on GW-SHM of composite structures obtained in the last three decades and the potential maintenance cost reduction for airlines, there are still no certified in-service applications on commercial aircraft. The reason for that is related to the very limited number of GW-SHM systems tested on composite structures with real material and geometric complexity until today [11]. As a result, many projects have not been able to deliver the capabilities for unambiguous damage diagnostic, and several knowledge gaps still remain. That is the case, for example, of studies in simple flat plates [12-14], sometimes with artificial damages (e.g. Teflon tape inserts mimicking real delaminations or BVID), which are then used to develop GW signal processing and damage-related feature extraction algorithms that are tuned for those simplistic scenarios. It is also true for other cases [15-17] where GW signal processing algorithms are developed using only numerically generated signals which are based on unrealistic GW excitation (e.g. point-force application, pure GW mode-shape activation) and do not include the combined effects of environmental-operational factors (e.g. structural vibrations, temperature). In other cases [18,19] no attention is paid to the way the excitation signal and the transducer geometry are selected, and how these parameters influence the damage diagnostic capabilities.

So, in short, there has been a lack of investigations targeting component-scale and full-scale structures in order to address issues related to GW propagation in complex and large geometries in different scenarios and under the effect of multiple environmental-operational factors, as well as problems related to the SHM system hardware, its functioning and installation. However, conducting SHM research at this complexity scale is met with a serious challenge. Contrary to non-destructive testing (NDT), SHM transducers must be permanently bonded to the structure, which makes test campaigns time-consuming and costly, because a large number of components have to be

manufactured, instrumented and tested in order to cover all the possible scenarios in a statistically relevant way [20]. Consequently, projects are often simplified or made incomplete for feasibility reasons.

1.3. Research goal and scope

It is time to accelerate the progress of SHM research to certification level by “*testing the SHM system’s robustness in representative environments*” [11]. Therefore, the ultimate goal of this research is to improve the reliability of GW-SHM for composite aircraft. To that end, the boundary of application was pushed further to real-scale (1:1) structural component, without neglecting the complex aspects of the physics of GW propagation in the process of GW-SHM system design and validation.

Therefore, this thesis encompasses the certification challenges identified in Section 1.2, placed under the framework of integration of SHM technology with new design and manufacturing processes for TpC aircraft structures. The following broad research topics are covered:

- a) GWs in TpC ultrasonic welds;
- b) GW-SHM system design and performance;
- c) Effect of operational factors on GW propagation;
- d) SHM reliability analysis.

In this thesis, research was conducted at the element and component structural complexity scales of the building-block approach in order to progressively tackle different SHM reliability challenges. Common to both scales were the guidelines adopted for the consistent and systematic development of signal processing and feature extraction algorithms and SHM system design.

1.4. Thesis outline

This thesis is organised in eight chapters. After the Introduction (Chapter 1), Chapter 2 reviews the state-of-the-art of the research on TpCs for aircraft primary structures, and on GW-SHM for fixed wing aircraft, thereby providing the background necessary to understand the conducted studies. Having identified the knowledge gaps in the literature review, Chapter 2 ends with the definition of the questions formulated to address those gaps. In Chapter 3 the methodology to search for an answer to the research questions is defined. Chapters 4 and 5 address the questions about GW propagation in TpC ultrasonic welds. Chapter 6 creates a bridge between element-scale and full-scale by presenting the development of a novel multi-parameter methodology for designing a GW-SHM system in a systematic way. In Chapter 7 component-scale structural complexity is reached by describing developments for model-assisted reliability analysis of a GW-SHM system in a defective transducer scenario. Chapter 8 describes the studies enabled by the test campaign conducted on a real-size TpC composite aircraft primary structure. Those include the study of the effects of structural vibrations on GW propagation and consequent damage diagnostic performance, and the validation of the SHM system design methodology devised in Chapter 6. Finally, Chapter 9 presents the conclusions of this thesis and gives recommendations for future research on GW-SHM of composite structures.

References

1. Megson THG. *Aircraft Structures for Engineering Students*. 4th ed. Oxford: UK: Butterworth-Heinemann; 2007.
2. Schijve J. *Fatigue of Structures and Materials*. Springer, 2nd edition, 2009.
3. Statistical summary of commercial jet airplane accidents – Worldwide operations 1959-2016. Seattle: Boeing, July 2017.
4. Kassapoglou C. *Design and Analysis of Composite Structures: With Application to Aerospace Structures*. Wiley, 2nd edition, 2013.
5. Kassapoglou C. Fatigue life prediction of composite structures under constant amplitude loading. *J Compos Mater* 2007; 41(22): 2737-2754.
6. ARP6461:2013-09. Guidelines for implementation of structural health monitoring on fixed wing aircraft; 2013.
7. Red C. The outlook for thermoplastics in aerospace composites, 2014-2023. *High-Performance Composites* Sep 2014; 22(5): 54-63.
8. Villegas IF. In situ monitoring of ultrasonic welding of thermoplastic composites through power and displacement data. *J Thermoplast Compos* 2015; 28(1): 66-85.
9. Su Z, Ye L, Lu Y. Guided Lamb waves for identification of damage in composite structures: A review. *J Sound Vib* 2006; 295: 753-780.
10. Mitra M, Gopalakrishnan S. Guided wave based structural health monitoring: A review. *Smart Mater Struct* 2016; 25(053001): 1-27.
11. Wenk L, Bockenheimer C. Structural health monitoring: a real-time on board ‘stethoscope’ for condition-based maintenance. *Airbus Technical Magazine - Flight Airworthiness Support Technology*. August, 2014: p. 22.
12. Ramadas C, Balasubramaniam K, Joshi M, Krishnamurthy CV. Interaction of guided Lamb waves with n asymmetrically located delamination in a laminated composite plate. *Smart Mater Struct* 2010; 19(065009): 1-11.
13. Castings M, Singh D, Viot P. Sizing of impact damage in composite materials using ultrasonic guided waves. *NDT&E Int* 2012; 46: 22-31.
14. Dziendzikowski M, Kurnyta A, Dragan K, Klysz S, Leski A. In situ barely visible impact damage detection and localization for composite structures using surface mounted and embedded PZT transducers: A comparative study. *Mech Syst Signal Pr* 2016; 78: 91-106.
15. Ng CT, Veidt M. Scattering of the fundamental anti-symmetric Lamb wave at delaminations in composite laminates. *J Acoust Soc Am* 2011; 129(3) 1288-1296.
16. Ng CT, Veidt M, Rose, LRF, Wang CH. Analytical and finite element prediction of Lamb wave scattering at delaminations in quasi-isotropic composite laminates. *J Sound Vib* 2012; 331: 4870-4883.

17. Murat BIS, Khalili P, Fromme P. Impact damage detection in composite panels using guided ultrasonic waves. *AIP Conf Proc* 2014; 1581: 286-293.
18. Lu Y, Ye L, Wang D, Zhong Z. Time-domain analyses and correlations of Lamb wave signals for damage detection in a composite panel of multiple stiffeners. *J Compos Mater* 2009; 43(26): 3211-3230.
19. Sherafat MH, Guitel R, Quaegebeur N, Lessard L, Hubert P, Masson P. Guided wave scattering behaviour in composite bonded assemblies. *Compos Struct* 2016; 136: 696-705.
20. Forsyth DS. Structural health monitoring and probability of detection estimation. *AIP Conf Proc* 2016; 1706(20004): 1-6.

2

Literature review

This chapter provides an overview of the knowledge that constitutes the backbone of this research. It starts with the structures that are intended to be monitored, by looking at the developments in TpC technology as a means to increase the cost-effectiveness of aircraft primary structures. The focus is placed on the mechanical properties and internal structure of TpC joints produced by ultrasonic welding, which is a process with potential for automation and, thus, for large series manufacturing. Down at the material scale, this chapter goes into the fundamentals of ultrasonic GW propagation and interaction with different structural features. The chapter also provides a detailed review of the algorithms that have been developed in GW research for signal processing and feature extraction. Then the chapter goes on to put SHM, and its associated functions and capabilities, into perspective within the context of CBM. Finally, the chapter addresses the problem of SHM system reliability quantification, which is a crucial step to progress SHM to real applications.

In order to complete the definition of the line of research for this project, the chapter ends with the identified knowledge gaps and the questions that were formulated to guide the research in the process of acquiring the missing knowledge.

2.1. Thermoplastic composites (TpCs) for primary aircraft structures

TpCs are promising alternatives to thermoset composites in the aerospace industry in the pursuit of more cost-effective manufacturing [1]. TpC parts can be welded together by melting the polymeric material at their interfaces and consolidating the joint under pressure, without risking degradation of material properties [2]. It overcomes the typical issues of mechanical fastening of composites, such as stress concentrations and delaminations due to hole drilling, and of adhesive bonding, such as the needed surface preparation and curing cycle, and it is one of the main factors contributing to the cost-effectiveness of composite materials [3].

There are three main techniques that are considered suitable for welding of continuous fibre reinforced TpCs: resistance, induction and ultrasonic welding (UW) [4]. In resistance welding heat is generated by the Joule effect in a very thin resistive mesh placed at the welding interface. Induction welding makes use of thermal energy generated through resistive heating and/or hysteresis losses which are activated in electrically-conductive and magnetic materials by an alternating electromagnetic field. UW relies on the conversion of the kinetic energy of high-frequency mechanical vibrations to thermal energy at the weld interface through surface and intermolecular friction.

Comparing the three aforementioned welding techniques, UW stands out as the one allowing the highest static mechanical properties, the lowest through-thickness porosity in the consolidated joints, and the shortest processing times [4]. This last characteristic, in particular, makes UW of TpCs an interesting technique for automation [5] and has motivated extensive research, as discussed in Section 2.2. That research has increased knowledge about the melting, flow and strength development mechanisms at the weld interface, enabling important advances for the application of this joining method to an industrial scale.

2.2. Ultrasonic welding of TpCs

In order to predominantly generate heat at the weld interface, thin pieces of thermoplastic polymer known as ‘energy-directors’ (EDs) can be placed between the parts to be welded. Once melted, the flow of the EDs promotes intimate contact and subsequently molecular interdiffusion across the overlap [4]. When welding two TpC parts together by UW, the aim is to allow the almost complete outflow of the molten ED without damaging the adjacent laminate layers [5]. This way it is possible to ensure a minimum weld line thickness which maximizes molecular interdiffusion and thereby bonding. Research has shown that it is possible to consistently maximise the static shear strength of single-lap joints by controlling sonotrode displacement such that the static UW process is stopped at the maximum power plateau/point [5,6]. Building upon this knowledge and on previous research [7,8], Villegas et al. [9,10] studied the UW of TpC with different ED geometries, namely loose flat film and integrated ridges with triangular cross-section, in order to understand the comparative processing advantages of both geometries. In an effort to upscale the UW capabilities, Zhao et al. [11] demonstrated that it is possible to apply sonotrode displacement controlled UW sequentially in order to produce multi-spot welded joints with consistent quality.

Despite these achievements, there are still limitations when it comes to assembling real structures, such as fuselage frames and curved panels, which require large joints.

Current research on continuous UW [12] shows that the use of a thin woven mesh ED improved the uniformity and strength of the joints in comparison to a thin flat ED. These are encouraging results for addressing the challenge of welding long areas at high-speeds. However, to proceed to complex geometries it is still necessary to develop a way to control the continuous UW process in an equivalently consistent fashion as for static UW. For that, further research has to be conducted to understand the material transformations occurring at the weld interface and to correlate them to the continuous UW process variables. Looking ahead in time, the potential future application of UW for assembling TpC structures at an industrial scale must face the challenge of automation to enable high production rates. It will first require the acquisition of knowledge about the control of boundary conditions during the UW process for consistent final weld quality, and the development of UW tooling that can be adapted to robots and to perform UW in narrow spaces [13].

Given the relevance of static UW for this thesis (as explained in Chapter 3), it is deemed important to describe the characteristics of the internal structure of ultrasonic welds. Attention is also paid to the possible welding defects, which, although small, may affect the load bearing capability of welded joints when fatigued.

2.2.1. Internal structure of static ultrasonic welds

At the UW process stage which consistently allows the maximisation of the static shear strength of single-lap joints, the ED has almost completely flowed out of the overlap and the matrix in the immediately adjacent layers of the adherents have melted [5]. As a result the weld line thickness is close to zero with respect to the total joint thickness ($\sim 10^{-2}$ mm), as shown in Figure 2.1.

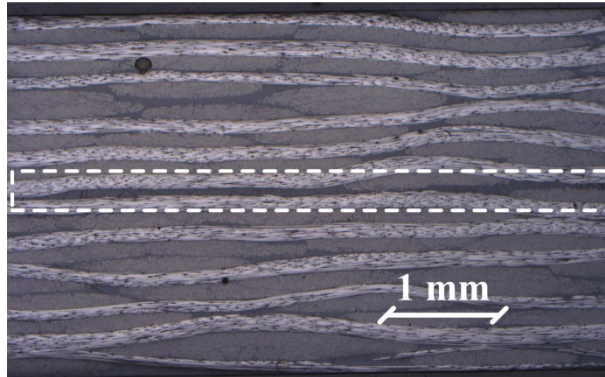


Figure 2.1. Cross-sectional micrograph of weld produced for maximum single-lap shear stress. The region of the weld line is highlighted by the dashed line.

The layers of laminate adjacent to the weld line, where the matrix partially fuses during the heating process, define a region which is called the heat affected zone. Its size is determined by the applied force and vibration amplitude, and it is usually within the first two layers of laminate [6]. This transformation occurs due to heat transferred from the weld interface to the substrates and also due to heat generated within the laminates themselves. In the consolidation step, the temperature of the weld usually decreases at a

fast rate (common values for polyether ether ketone composites are below ± 600 °C/min [14]). This parameter determines the final crystallographic structure of the polymeric material. Under these typically fast cooling rates crystallization is reduced, and an amorphous structure is formed. Changes in crystallinity affect the stiffness of the polymeric material, with lower crystallinity levels resulting in lower stiffness values [15,16]. Therefore, after cooling down, besides the existence of residual stresses across the weld, the matrix properties in the heat affected zone are different than in the rest of the composite.

2.2.2. Manufacturing defects in static ultrasonic welds

When the weld interface properties of a consolidated static ultrasonic weld does not match those that are typically obtained for maximum static single-lap shear strength (SLSS), it can be said that there is a manufacturing defect. That mismatch can be characterised by two main types of defects, which can be identified by correlating the fracture surfaces after single-lap shear testing and the UW process parameter curves [5,6,10]. If the sonotrode displacement (from here onwards called welding travel) is lower than the value at the maximum power point, the welds are incomplete, with welded and unwelded areas (visible from semi-crystalline remnants on the fracture surface), and only partial outflow of the ED. If the travel is taken to a point at which the power curve has passed beyond the peak, the ED is completely squeezed out from the welding interface, with melt and flow of the matrix beyond the first layer of the adherends, which leads to adherend fibre bundle distortion.

2.3. Damage in composite structures

The inability of a structure to perform its primary function constitutes a structural failure [17]. This is usually the result of progression of either initial defects that arise during material processing or component fabrication, or of damage that is directly induced during in-service operation.

For general composites structures, in the category of initial defects, there are those at the material processing level which include fibre and filament faults, over-aging, moisture absorption, material variability, just to name a few [17]. Normally their dimensions are at the microscopic scale or below. At the component fabrication level, defects include for example contamination, fibre-matrix debonds, ply overlaps or gaps, fibre kinks and misalignments, voids/porosity, warping, and, in the cases of mechanically fastened joints, fastener hole drilling defects such as drill burn and exit delaminations [17].

In-service damage can have multiple causes. One is material property degradation by hostile environments, in which radiation, temperature and chemical composition play a role [17]. Another one is fatigue, in which cyclic loading promotes the progression of initial manufacturing defects into damage, according to multiple simultaneous damage mechanisms which depend on the internal architecture of the composite material [18]. Matrix cracks tend to grow and eventually reach fibre-matrix interfaces, leading to fibre-matrix debonding. These debonding cracks act as stress raisers and, as they reach the ply interfaces, they magnify the interlaminar stress, leading to delaminations. In the worst case, delaminations cause overstressing of the intact plies and consequent failure of the component.

The mechanical action of external objects onto the structure, such as inappropriate repair, debris impact, tool drop impact, or ground vehicle impact, can also cause in-service damage. Among other examples of damage like material crushing, surface scratches and hole wear, low-energy impact damage is of particular concern for composite aircraft structures [19]. Although it is usually barely visible, low-energy impact damage typically has a complex structure of interconnected matrix cracks, fibre-matrix debonding, fibre breakage and delaminations beneath the slight surface indentation [20,21], as depicted in Figure 2.2.

Moreover, because it might not directly affect structural performance, there is no indication justifying a non-destructive inspection, which means that BVID can remain undetected even in periodic maintenance inspections. The widespread occurrence of low-energy impacts over the aircraft structure [19] increases the probability of having sudden strength reduction, especially because contrary to metals, the fatigue damage accumulation in composites can be considerably faster due to their high brittleness [23].

As a remedy to this situation, aircraft design has adopted a conservative approach, making structures thicker and hence heavier. From an SHM point of view, the interest lies in detecting not the initial manufacturing defects, as they will be present in the pristine out-of-production-line structure, but the progression of damage in its early states or from an in-service damaging event, while the performance of the structure is still unaffected. The accomplishment of such goal will enable composite aircraft design to become less conservative and therefore more lightweight.

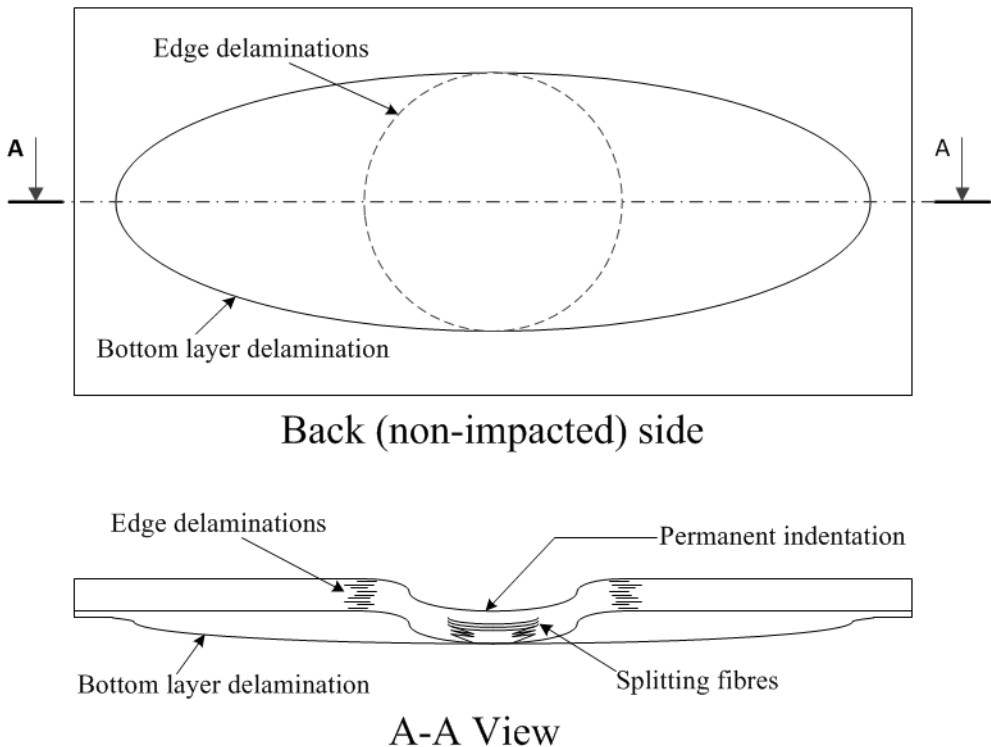


Figure 2.2. Typical structure of barely-visible impact damage (based on [22]).

2.4. Fundamentals of ultrasonic guided wave (GW) propagation

As briefly introduced in Chapter 1, GW interrogation is a very promising technique for quantitative SHM of composite structures, because of its capabilities of large surface interrogation and high sensitivity to different defects. The basic idea behind GW-SHM is to measure differences between two ultrasonic signals corresponding to two different states of the structure. Those differences depend on multiple interactions between the GWs and the structure during propagation from the actuator to the sensor. Therefore, it is important to understand the physics governing GW propagation.

2.4.1. Wave guiding mechanism

In an infinite isotropic, elastic solid media a mechanical disturbance can be propagated by inducing uncoupled particle motion in three directions, defining three bulk wave polarization vectors as depicted in Figure 2.3. The longitudinal (L) and the shear vertical (SV) modes occur in the same xz -plane (commonly called the sagittal plane), with the L mode polarized in the direction of propagation and the SV in the perpendicular direction. The shear horizontal (SH) mode has the polarization vector in the xy -plane, perpendicular to both the direction of wave propagation and the sagittal plane.

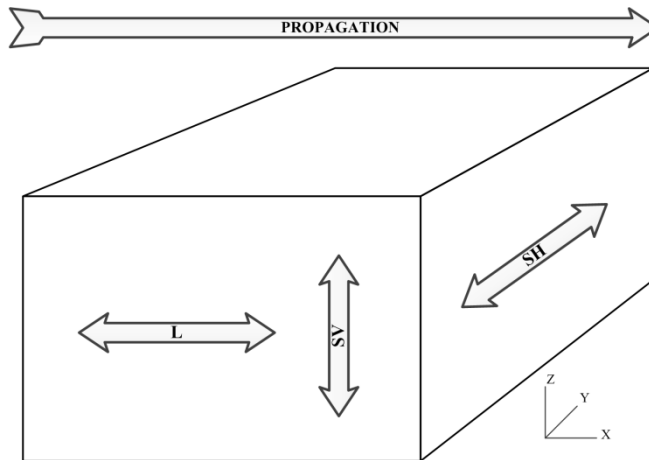


Figure 2.3. Bulk wave particle motions in infinite elastic solid media: Longitudinal (L), Shear-vertical (SV) and Shear-horizontal (SH).

In the case of high frequency ultrasound (typically above 2 MHz [24]) in a vast solid medium, the fundamental particle motions in an infinite space can be considered for describing bulk wave propagation. However, when that mathematical abstraction is no longer valid, and the boundaries (surfaces) of finite solids must be taken into account, the relation between the z -dimension, Dim , and the wavelength, λ , determines the type of wave that can occur. As shown in the classification presented in Figure 2.4, and considering a solid medium in vacuum or air, if Dim is much larger than the wavelength, λ , the waves

behave as if they were propagating in a semi-infinite medium, thus being constrained by only one free surface. When the fundamental modes reach the upper surface, pure shear vertical motion is no longer possible due to the coupling between vertical and horizontal displacements at the bending surface [25], and thus the SV mode is transformed into a flexural mode. At that moment, all the modes are reflected and remain inside the solid. The polarization of the longitudinal and flexural modes in the same plane allows conversion between the two modes to take place at the moment of reflection [24], inducing strongly coupled particle motions in the x and z directions which travel together at a common velocity in a new wave. Because $Dim \gg \lambda$, the flexural portion of the wave is only felt within a limited region close to the surface, the amplitude of the total resulting wave decays as depth increases and approaches zero at approximately one wavelength from the upper surface. Therefore these waves behave as surfaces waves, and are called Rayleigh waves [26]. SH modes in semi-infinite media have similar characteristics to SH bulk waves. Consequently they do not experience mode conversion and they are uncoupled from Rayleigh waves. The process of confinement that has just been described is called wave guiding, and any medium where it is allowed to occur is called a waveguide. Rayleigh waves are the simplest case of GWs.

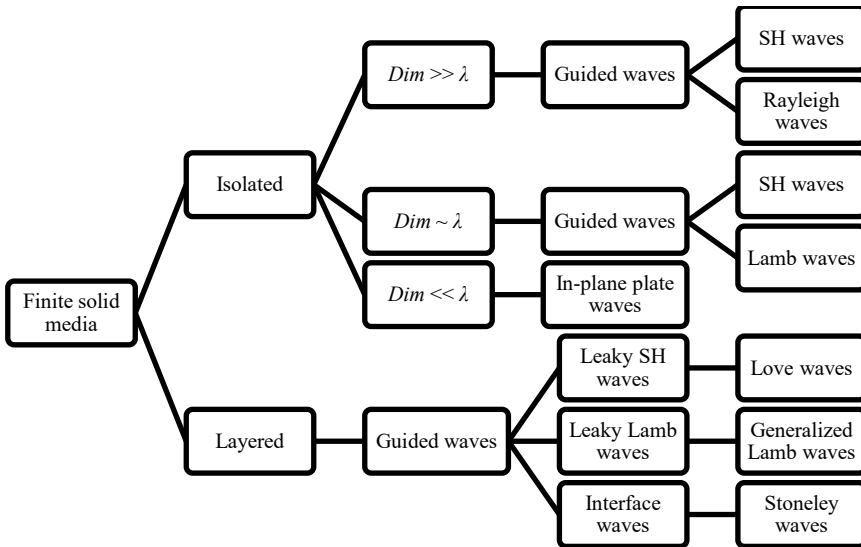


Figure 2.4. Classification of guided wave in finite solid media.

When Dim is of the same order of magnitude as λ , the wavefront sees a finite medium bounded by two surfaces, and waves are reflected from both of them. The same confinement process described for a semi-infinite medium takes place for each surface. In this case, however, the existence of two boundaries imposes the transformation of both SV and L particle motions into two mixed-motion modes with coupled vertical and horizontal displacements. The SV motion is transformed into a quasi-flexural motion, and the L motion is transformed into quasi-longitudinal motion. Because the distance between the boundaries is of the order of magnitude of the wavelength, the reflected waves superimpose and interact with each other. Interference between modes occurs and new types of GWs are generated, as illustrated in Figure 2.5. The superposition of different SH

modes originates SH plate waves (horizontally polarized). The superposition of quasi-longitudinal and quasi-flexural modes (equivalent to superimposing two opposing Rayleigh waves) generates Lamb waves (vertically polarized). Following the principle of transverse resonance [24], the new GWs propagate in the x direction and correspond to a pattern of standing waves in the z direction, whose resonance modes depend on frequency.

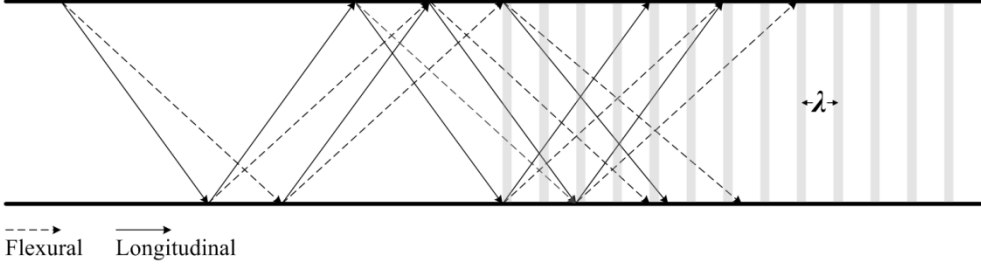


Figure 2.5. Ray-tracing representation of the generation of Lamb waves in a plate cross-section (adapted from [27]).

2.4.2. GWs in plates

Plate GWs (SH and Lamb waves) are described by

$$\mu^n \nabla^2 \vec{u}^n + (\lambda_L^n + \mu_L^n) \vec{\nabla} (\vec{\nabla} \cdot \vec{u}^n) + \rho^n \vec{f}^n = \rho^n \frac{\partial^2 \vec{u}^n}{\partial t^2} \quad (2.1)$$

where μ_L and λ_L are the Lamé constants, ρ is the density, \vec{u} is the displacement vector, \vec{f} is the body force vector, and n is the number of layers in the plate [28]. In the far-field, these waves can be considered as three-dimensional plane waves that are z -invariant, i.e. their wavefronts are parallel to the z -axis and the wave disturbances are invariant along the z coordinate [25]. Therefore the displacement potentials method based on Helmholtz decomposition can be used to solve Equation (2.1) for an isotropic elastic medium. The resulting displacement fields of SH and Lamb waves can be symmetric or anti-symmetric with respect to the plate mid-plane, thereby defining symmetric (S) or anti-symmetric (A) modes, respectively. The order of the mode is related to the number of nodes in its mode-shape across the thickness. To designate the symmetric and anti-symmetric Lamb modes or order i , the adopted notation is simply S_i and A_i , respectively. To designate the symmetric and anti-symmetric SH modes, the adopted notation is SH_i and AH_i .

Multiple modes of different orders can occur at the same time, their number being frequency dependent. Below a certain frequency, called the first cut-off frequency, only a limited amount of modes exist. In the case of Lamb waves, propagation is then restricted to the two fundamental (zero-order) S_0 and A_0 modes, whereas for SH waves only the SH_0 mode occurs. In that range, the S_0 and A_0 Lamb modes are particularly interesting, because they interact differently with damage. The symmetric displacement field is quasi-longitudinal and is sensitive to defects anywhere in the thickness (except delaminations [29]), whereas the anti-symmetric displacement field is quasi-flexural and more sensitive to surface cracks [25,29,30].

The solutions of the wave equation can be used to plot the phase velocity of plate GWs as a function of frequency, as presented in Figure 2.6.

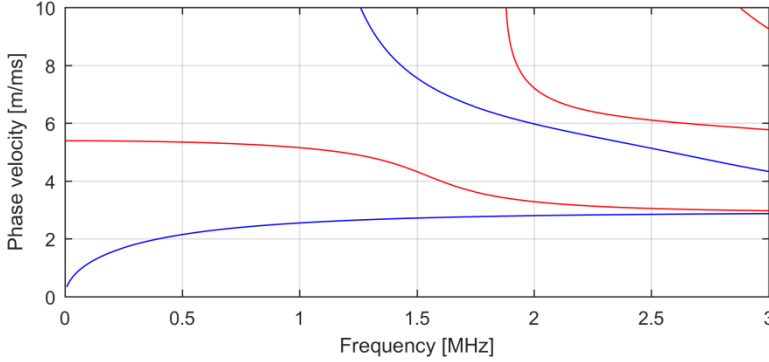


Figure 2.6. Phase velocity curves for Lamb modes in an AL6082 plate of 1.5 mm thickness: in blue the A modes, in red the S modes (computed with DISPERSE v2.0.20a).

The phase velocity curves clearly illustrate the multi-modal nature of GWs. Firstly, for small frequency values only the S0 and A0 Lamb modes occur. As the frequency increases, the number of Lamb wave modes that can simultaneously exist also increases. Secondly, it is clear that the phase velocity varies with frequency. Lamb waves are thus said to possess a dispersive nature. These observations can be extended to SH waves, since they are also dispersive. However, the SH0 mode has a null eigenvalue [25], and therefore has a constant phase velocity equal to the bulk shear wave velocity.

To better understand dispersion it is necessary to go into a more detailed explanation of the phenomenon. As explained before, GW modes are by nature the result of the superposition of multiple wave components, each with its own slightly different phase due to the multiple reflections at the plate surfaces. As a result, these multiple components are alternately in and out of phase promoting constructive and destructive interference. This generates a beat pattern which is characterized by the presence of wave packets along the time axis of the signal. An isolated wave packet in a GW signal corresponds to an individual GW mode and it propagates with a group velocity, c_g :

$$c_g = \frac{c_p}{1 - \frac{f}{c_p} \frac{\partial c_p}{\partial f}} \quad (2.2)$$

which is a function of phase velocity, c_p , and frequency, f . As the initial waveform propagates, the phase differences induced by the guiding mechanism reflections increase, and so does the length of the waveform. If simultaneous GW modes have similar group velocities, or if one of them is strongly dispersive, then the corresponding wave packets can overlap in the acquired time response preventing the distinction of the different modes, as in Figure 2.7: in a) it is possible to identify the first and second wave packets separately (with peaks around 54 μ s and 76 μ s), while in b) that is no longer possible.

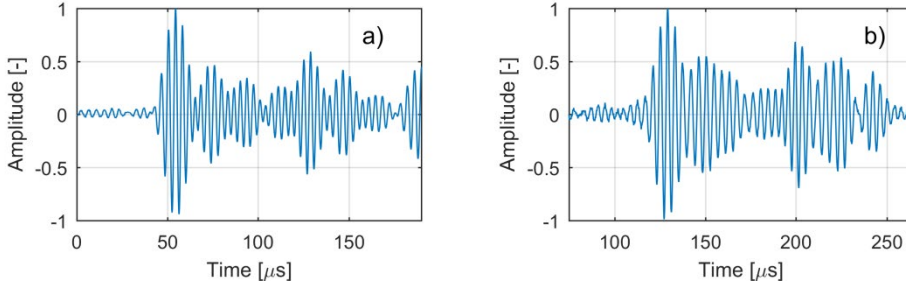


Figure 2.7. GW signals acquired from two consecutive positions. The sensor corresponding to a) was positioned 400 mm before the the sensor corresponding to b) in the propagation direction. In a) it is possible to identify the first and second wave packets separately, while in b) all the wave groups are overlapped.

2.4.3. GWs in structures

In real structures, waveguides are not isolated. Instead, they are in contact with other solid media by means of joints, but also having some free surface sections. When velocity and stress vector continuities are imposed as boundary conditions of the GW equation for a solid-solid interface, a new characteristic equation is obtained. By solving this new equation, two solutions can be obtained, one real and one imaginary [24].

The real solution corresponds to a wave which propagates in the sagittal plane along the interface. This is called a Stoneley wave (see Figure 2.4), and it is approximately non-dispersive and unattenuated in lossless media, i.e., the decay length is much larger than the wavelength of the wave. The existence of these waves is limited to a solution space where the densities and Lamé constants, λ_L and μ_L , of the two media approximately satisfy the following condition [31]:

$$\frac{\rho_1}{\rho_2} = \frac{\lambda_{L,1}}{\lambda_{L,2}} = \frac{\mu_{L,1}}{\mu_{L,2}} \quad (2.3)$$

As the density ratio increases, the ratio of the vertical displacement amplitude to the horizontal one increases. However, as ρ_1 approaches ρ_2 , the horizontal component shrinks, eventually tending to zero. In Stoneley wave existence conditions, the corresponding wave velocity will be between the Rayleigh wave velocity and the shear wave velocities of the two contacting media.

The imaginary solution corresponds to an attenuated mode which radiates energy into the adjacent layer, called a leaky GW. In the case of leaky sagittal modes they are called generalized Lamb waves, whereas in the case of leaky SH modes they are called Love waves (see Figure 2.4). The radiation of acoustic energy can be explained by a process of phase matching between the guided wave and the leaky condition in the adjacent medium. Due to local resonance at the contact surface, the two media are acoustically coupled and the GW is allowed to leak [24]. Consequently, for a guided mode to radiate, its phase velocity must be greater than or equal to the phase velocity of the equivalent guided mode in the adjacent layer. The leaky GW loses energy and attenuates as it continues to propagate, with the attenuation per wavelength given by the ratio of the acoustic impedances of the material layers.

2.4.3.1. GWs in lap joints

A special case of leaky GWs can occur in regions where structural components are joined together. A plate guided mode in the overlap of a joint propagates with a higher frequency-thickness product than in the adjacent panel. If the higher thickness-frequency product corresponds to a lower phase velocity, then the mode does not radiate an equivalent wave to the next adjacent plate and remains confined to the thicker region, as shown in Figure 2.8.

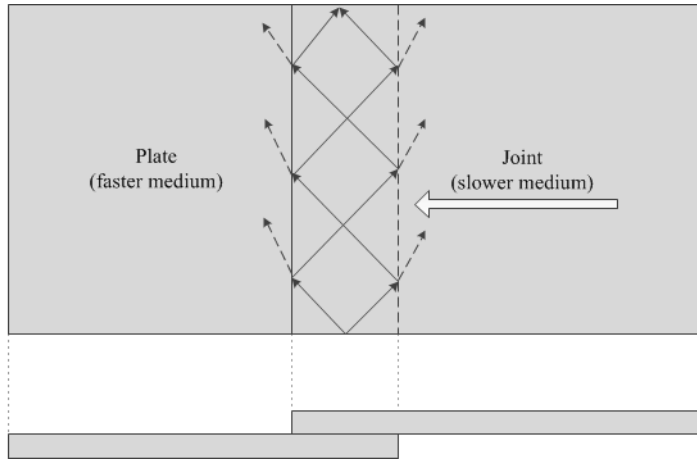


Figure 2.8. Feature guiding process in a single-lap joint.

This is called a feature guided mode [32-34]. However, the new guided mode can simultaneously be a leaky mode if its phase velocity along the feature is higher than that of another (different) mode in the adjacent panel. These feature GWs can be used for SHM of more complex structural areas because the concentration of their acoustic energy along the joint allows them to travel relatively long distances.

The transmission of GWs across a lap joint does not depend only on a matching condition for the phase velocity of the possible GW modes, but also on their mode-shapes. When reaching the thickness discontinuity of the joint, part of the GW energy in the adherend is transmitted to the overlap by a process of particle motion coupling. Only a limited number of overlap particle motions combinations can be induced, because only a limited number of GW modes can exist at a certain frequency. A mode in the adherend can activate its equivalent mode in the overlap (i.e. the mode in the overlap with the same type of particle motion), but also a mode of a different type and order. When the latter takes place, the transformation is called mode conversion [35].

However, it is not always guaranteed that all overlap modes can be activated. For an overlap mode to be generated its mode-shape must have some compatibility with the mode-shape of the impinging adherend mode, which implies that the mode-shape of the adherend mode must at least partially match the lower half of the mode-shape of the overlap mode (see Figure 2.9). In mathematical terms the match between mode-shapes is measured by the degree of orthogonality between them [36]. When the overlap modes reach the right-hand side adherend, adherend modes are activated according to the

aforementioned mechanism, thereby completing carrying of ultrasonic energy across the joint. From here onwards, adherend (of single-plate) GW modes are designated by lower case letters (e.g. a_0 and s_0), while joint-overlap (or carrier) GW modes are designated by uppercase letters (e.g. A_0 and S_0).

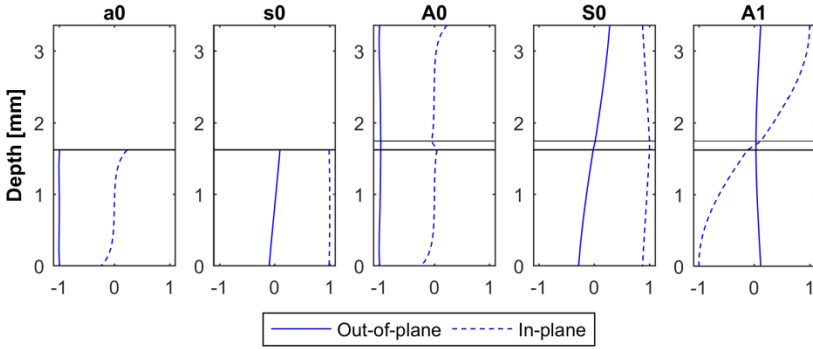


Figure 2.9. GW mode shapes in the adherend (a_0 and s_0) and in the overlap (A_0 , S_0 , A_1). While the a_0 and s_0 are compatible with the A_0 and S_0 , respectively, the s_0 and the A_1 are only partially compatible (through the out-of-plane component).

Lowe et al. [37] went deeper into the physics of transmission across lap joints by investigating the mechanism that governs mode conversion at the edges of the overlap. By using finite element analysis and the two-dimensional fast Fourier transform (FFT), they proved that if there are multiple carrier modes, the strength of transmission of the adherend s_0 Lamb mode is determined by their interference when mode conversion occurs at the exiting edge of the overlap. That interference can be constructive or destructive, depending on the relative phases of the carrier modes. The longer the bond and the higher the wavenumber of the carrier modes (which is a function of bond thickness), the larger the phase change during propagation through the overlap. This makes interference more constructive, and therefore strengthens the transmission.

Wave transmission across a solid-solid interface occurs simultaneously with reflection. The particle motion reorganization process for a reflection is governed by the same logic described above. In the case of a lap joint, there is a first reflection at the overlap edge where the wave enters, with adherend modes reflecting and converting into each other. The GWs transmitted into the overlap eventually reach the exiting edge, where ultrasonic transmission and reflection with overlap mode conversion occur. Backward-travelling modes undergo another reflection at the entering edge with new mode conversion, and finally leave the overlap after mode converting to one of the adherend modes. This sequence of events is called a reverberation [35,37]. The carrier modes keep on reverberating, with decreasing amounts of energy crossing the overlap each time, until the remaining energy is practically null.

It is then clear that changes in the internal structure of a joint can lead to the (dis)appearance of GW modes across the overlap. Therefore, even if identification of pure GW mode might not be feasible, knowing how and which modes are transformed allows the correlation of whole-signal changes to damage, thereby enabling its diagnostic.

2.4.3.2. GW interaction with defective lap joints

Most of the research about this topic has been focused on the interaction of Lamb waves with adhesively bonded metallic joints. Rokhlin [35] used theoretical and experimental analysis to show that the sensitivity of Lamb modes to the bond properties depends on the sensitivity of their carrier modes to the same properties. In turn, this sensitivity is determined by the mode-shapes in the overlap, which also vary with joint shape. Rokhlin pointed out that if bond monitoring is to be performed, then the excitation Lamb mode should be selected such that it is allowed to convert (to some extent) to the necessary carrier modes. Lanza di Scalea et al. [38] adopted a fully experimental approach based on air-coupled piezoelectric transducers to study the strength of transmission of the a_0 Lamb mode across adhesively bonded aluminium-epoxy-aluminium joints. Not only were they able to confirm the aforementioned carrier mode principles by measuring intermediate (adherend-overlap) transmission coefficients, they were also able to distinguish different bond conditions by measuring overall (adherend-overlap-adherend) transmission coefficients. Suitable frequencies for bond monitoring were assessed, with different frequencies between 0.3 and 1.2 MHz being sensitive to different bond states.

In the research of Matt et al. [39] the problem of GW-SHM of fully composite joints was finally addressed by studying the transmission of the s_0 mode across adhesive bonds. The test case was a carbon-epoxy wing skin-to-spar configuration containing areas of different bond condition, namely properly-cured, poorly-cured and disbanded. The specimens were instrumented with permanently attached inter-digital transducers which were used to acquire overall energy transmission coefficients. Changes in ultrasonic strength of transmission allowed three different bond states to be discriminated, although the most sensitive frequency range (100-300 kHz) was considerably lower than the one found in [38] (580-670 kHz) for adhesively bonded metallic joints.

Other studies have focused particularly on finding reliable ways of correlating changes in GW propagation with realistic defects in joints. Singher et al. [40] and Singher [41] investigated the interaction of ultrasonic GW with adhesively bonded single-lap metallic joints produced with different surface treatments. Each surface treatment resulted in a different bond strength. So, to understand the effect of different surface treatment on GW propagation they used an analytical spring-mass model to describe the forces between the two adherends. As they explain, “*in a quasi-static approach, the shear mechanical behaviour of the interface adhesive-adherend is represented by a density of springs with stiffness constant k* ” [41]. The situation of $k \rightarrow 0$ corresponds to free surfaces, while $k \rightarrow \infty$ consists of a perfect bond. And they add, “*we thus attribute the parameter k , the strength of the bond*”. From the analytical model results, they observed a monotonic reduction of group velocity of the first symmetric GW mode with decreasing spring-stiffness constant, which is equivalent to a monotonic reduction of group velocity with decreasing bond strength. This trend was then observed experimentally, thereby confirming the validity of the model. When working in the frequency domain, Singher [41] observed that the ultrasonic GW signal transmitted across the joint always had a negative shift of the characteristic frequency with respect to the ultrasonic excitation signal. They attribute “*the fading of the high frequencies due to adhesive absorption*” [41]. Furthermore, they also saw that this negative shift increased with decreasing bond strength. Therefore, they concluded that both group velocity and characteristic frequency shift can be used for quantifying adhesive bond strength. Kundu et al. [42] focused specifically on the detection of kissing bonds (i.e. tight physical contact between adherends without any mechanical bond). They showed that while most of the ultrasonic GW modes are insensitive to these

manufacturing defects, the higher-order mode A1 is sensitive due to its non-null shear stress distributions at the bond interface within a certain range of phase velocities.

2.4.4. GWs in composite materials

2

GW propagation in composite materials is far more complex than in homogeneous isotropic media. Their anisotropic layered structure makes stiffness higher in the direction with highest fibre concentration. Thus, the maximum phase velocity occurs when the wave propagates parallel to that direction and the minimum occurs when the wave propagates perpendicular to it [43,44]. As a result, ultrasonic energy is steered and focused. In unidirectional laminates, for example, the directions of the group and phase velocity vectors coincide only when parallel or perpendicular to the fibre orientation, whereas for intermediate angles the group and phase velocity vectors are not aligned [45].

Because the fibre direction changes across the thickness of the laminate, particle motion along one direction can induce motion in the perpendicular one. Consequently, all GW modes are coupled, some of them with very similar group velocities, as in the case of the S0 mode and the SH0 mode. This makes it almost impossible to identify the different GW modes, and to correlate their changes to interactions with different damage types [45].

Adding to the aforementioned complexities, the large number of interfaces within composite materials induces stronger attenuation (i.e. faster decay with propagation distance) and dispersion than in isotropic materials, especially for the A0 mode, making the wave pattern more difficult to analyse.

Nevertheless, Lamb wave group velocity has been shown to be sensitive to small variations of composite material properties mimicking material degradation from manufacturing and in-service defects [46]. Additionally, when predominantly exciting the S0 and A0 modes, it was possible to see some selective sensitivity to fibre and matrix dominated properties, respectively, in different frequency ranges. On the other hand, the S0 mode seems to be insensitive to delaminations, as pointed out by Wilcox et al. [29]. By studying the cross-sectional wave stress field for several stacking sequences Percival and Birt [47] observed that shear stress falls to zero at some ply interfaces in some of the investigated cases. They suggested that delaminations at those interfaces might not be detected because the S0 stress field remains unaffected.

In short, although the fundamental principles are still applicable, GW propagation in structures made of anisotropic materials cannot be simply described by the classical closed-form solutions for isotropic materials [25,24], especially when up-scaling from plate to assembly level. It must rely on the use of accurate numerical models, as addressed in Section 2.5.

2.4.5. GW transducers

Among other requirements, the selected transducers for SHM of aircraft structures should have no adverse effect on the structure, minimal disturbance of the monitored area (unobtrusive), small dimensions, low weight, low power consumption, and should be permanently installed on the structure. [48]. Currently, the only transducer technology that meets these requirements and is capable of effectively accomplishing GW based diagnostic is based on PZT transducers [25, 49]. Piezoelectric materials can be produced in shapes and sizes which are unobtrusive for the structure, whether as simple thin circular and rectangular wafers [25], or in the inter-digital format of comb-shape electrodes on a thin

piezoelectric substrate [50-52]. Moreover, they are easy to instrument and install, they can remain permanently bonded, and can combine the functions of actuation and sensing. Although most transducers employ piezo-ceramic material, research in piezo-composite materials [53-57] has achieved very promising results not only regarding the actual actuation/sensing capabilities, but also regarding the potential for further integration of GW-SHM systems in new TpC structures.

As mentioned above, PZT transducers can combine the functions of actuation and sensing because they can transform electric energy into mechanical energy, and vice-versa. For the purpose of GW actuation, mechanical strain is generated by an applied electric field according to the converse piezoelectric effect [58]:

$$\{S\} = [s^E]\{T\} - [d]\{E\} - \{\alpha^E\}\Theta \quad (2.4)$$

$$\{D\} = [d]\{T\} + [\varepsilon^T]\{E\} + \{\tilde{D}\}\Theta \quad (2.5)$$

where $\{S\}$ and $\{T\}$ are the strain and stress vectors, respectively, $\{E\}$ and $\{D\}$ are the electric field and electric displacement vectors, and Θ is the temperature; $[s^E]$ is the compliance coefficient matrix and $[\varepsilon^T]$ is the electric permittivity; $[d]$ is the piezoelectric strain coefficient matrix, which quantifies the strain induced per unit of electric field; $\{\alpha^E\}$ is the thermal expansion coefficient vector and $\{\tilde{D}\}$ is the electric displacement temperature coefficient vector. Equation (2.4) allows the prediction of the strain generated at a given stress, and hence it can be called the “actuation equation”. This equation can be re-written in order to express the generated stress as a function of the applied electric field:

$$\{T\} = [c^E]\{S\} - [e]\{E\} - [c^E]\{\alpha^E\}\Theta \quad (2.6)$$

where $[c^E]$ is the elastic stiffness matrix and $[e]$ is the piezoelectric stress coefficient matrix. This formulation will be useful later in Chapter 7.

Equivalently, the direct piezoelectric effect can be employed to convert mechanical strain into an electric field [58]:

$$\{S\} = [s^D]\{T\} - [g]\{D\} - \{\alpha^D\}\Theta \quad (2.7)$$

$$\{E\} = -[g]\{T\} + [\beta^T]\{D\} + \{\tilde{E}\}\Theta \quad (2.8)$$

Where $[g]$ is the piezoelectric voltage coefficient which quantifies the electric field induced per unit stress; $[\beta^T]$ is the inverse permittivity coefficient and $\{\tilde{E}\}$ is the pyroelectric voltage coefficient. Equation (2.8) allows the prediction of the electric field induced by the deformation of the piezoelectric material, and hence it can be called the “sensing equation”. The superscripts D and E indicate that the quantities are measured at zero electric displacement and at zero electric field, respectively.

Piezoceramics are polycrystalline materials which do not typically display macroscopic piezoelectric properties due to their randomly polarized microscopic structure [58]. During fabrication, a strong electric field can be applied at high temperatures (i.e. poling) to enable the desired macroscopic piezoelectric properties. For example, when poling is applied along the thickness and an electric field is created between the bottom

and the top surfaces, the PZT wafer undergoes a thickness-wise expansion and a lateral contraction.

The performance of PZTs as ultrasonic GW transducers for damage diagnostics depends on several key parameters that must be selected before installing the SHM system, namely piezoelectric properties, geometry, excitation frequency content, and the network configuration (i.e. the relative position of the transducers within the area to be monitored). Usually the excitation centre frequency is selected by assuming the ideal scenario of pure guided mode excitation [59-61] or time-domain discrimination between guided modes [62,63], after which a theoretically optimal dimension for the PZT transducer can be found from the wavelength tuning effect [64-66]. Another criterion for choosing the excitation centre frequency is to match the minimum resolvable distance by a certain pure guided mode with the minimum size of the damage to be detected [50].

GW interrogation is performed either by capturing the ultrasonic echoes produced at the damage-material interface (pulse-echo configuration), or by acquiring the signal transmitted through the damage site (pitch-catch configuration), or a combination of both. Usually several actuator-sensor pairs are deployed as a transducer network, potentially allowing localization algorithms to be implemented. Thus, when it comes to transducer placement, it is common to either use a high density network around a confined region (less than half metre) within the larger critical area [67-69], or to mathematically optimize the configuration for the detection of specific damage scenarios/sizes [70]. For a preliminary level of optimization, the necessary parametric studies can be conducted efficiently by solving the two-dimensional analytical wave equations with externally incorporated damage-wave interaction coefficients for simplified geometries and materials [71,72]. As it will be explained in Section 2.9, it is not feasible to rely on pure GW mode analysis for PZT transducer network design.

2.4.6. Temperature and loading effects

The difference in selected signal features between the current response and the baseline is the key principle behind the identification of structural state changes, thereby enabling SHM of complex structures. However, in real operational scenarios, varying environmental conditions induce signal fluctuations which may compromise the diagnostic accuracy. From all environmental factors, temperature and loading are among those that change constantly and quickly during normal aircraft operation, whether in flight or on the ground.

One effect of thermal variation on GW propagation originates from changes in material elastic properties. In the case of composite materials, the effect is predominantly felt in the matrix Young's and shear moduli [73-76]. As a result, response amplitude and propagation velocities are affected [28]. Since the shifts in phase and group velocities are different, besides variations in time-of-flight (TOF) of modes there is also an instantaneous phase change. As reported by Kijjanka et al. [77], an increase in temperature results in larger TOFs (i.e. decreased group velocity), and decreased amplitude and instantaneous phase. Another thermal effect is expansion/contraction of the solid medium, modifying the propagation distance. This also causes deviation in TOF of incident and reflected waves [28].

Additionally, the properties of the transducers are also affected. The critical point is the Curie temperature (usually in the vicinity of 300 °C for commonly used piezoceramics) above which the piezoelectric properties are lost. If the temperature remains below that

point, PZT transducers remain functional, even in cryogenic environments [78]. However, the induced variation in piezoelectric and material properties, as well as in dimensions has a measurable effect on the resonance and anti-resonance behaviour, which can interfere with the GW actuation and sensing capabilities. Furthermore, the bonding between the piezoceramic and host structure also degrades, which may be more detrimental for transducer performance than the effect on the piezoelectric properties itself.

When static stress is applied on a structure, strains are generated along preferential directions. That imposes uneven (i.e. anisotropic) changes in propagation distance (by Poisson's effect), mass density, and elastic properties, which in turn induce shifts in the dispersion curves of the material to other frequency-thickness points thereby forcing phase and groups velocities to change accordingly. Gandhi et al. [79] applied the theory of acoustoelasticity to the Lamb wave case in order to understand the influence of stress and wavenumber-stress angle in different modes at different frequencies. From their theoretical and experimental results they observed a linear dependence of phase velocity change with applied stress and with wavenumber-stress angle at a single frequency. Especially below 2.5 MHz.mm, when a tensile stress is applied along the propagation direction, the change in s_0 mode phase velocity is negative, while for the a_0 mode it is positive. In that frequency regime the particle motion responsible for the s_0 mode is mostly longitudinal. Since the particles are longitudinally further away from each other than in the unstressed state, it is more difficult for them to propagate their motion than in the unstressed state. On the other hand, in this frequency regime the a_0 mode is mainly flexural. Due to Poisson's effect, the applied stress brings the particles closer to each other along the out-of-plane direction, thereby promoting a faster propagation of flexural motion. For an ultrasonic excitation beyond 2.5 MHz.mm, *"the changes in phase velocity reduce and flatten"* [79].

The exact solution of the GW equation for the combined effect of temperature and load is obtained by including thermo-acousto-elastic behaviour. That is what Dodson [80] did when he studied the sensitivity of phase and group velocities to thermal variations and applied static stress. He observed not only that both effects are functions of GW frequency, but also that at specific frequencies some guided modes are insensitive to variations. Moreover, he identified certain angles between the wave vector and the loading direction for which there are frequency ranges where the sensitivity of Lamb modes to applied loads is reduced. Finally, he concluded that the influence of thermal variation on the sensitivity of Lamb waves to applied stress is most noticeable at very low frequency.

Static loading, however, does not correspond to the normal conditions in which GW-SHM systems are designed to operate, since data must be acquired during aircraft service, namely in pre-flight checks or in flight. During these phases the structure is subjected to external dynamic mechanical perturbations which change its normal planar shape. In typical pre-flight preparations, the wings of an aircraft are exposed to wind gusts. During taxiing, most of the primary structure of an aircraft undergoes severe vibration. In flight, the primary structure of an aircraft is constantly subjected to vibration. All these cases constitute occurrences of high-amplitude (1 to 30 mm), low-frequency (relative to ultrasound) vibration (HA-LFV). Additionally, in pre-flight there are always audible sound waves (SW) coming from operating machinery (inside and outside the aircraft), and in flight most of the structure is exposed to high intensity SW produced by the engines.

To this date there is no known published research about the physical effects of structural vibrations on GW propagation. Still, Banerjee and Kundu [81] studied GW propagation in plates with permanent periodic shape. They developed an analytical model in order to study symmetric and anti-symmetric Lamb modes in two-dimensional sinusoidally corrugated plates. The permanent plate corrugation can be taken as an

approximate representation of the instantaneous effect of vibration on the structure. Contrary to the wave guiding mechanism in flat plates, in which the reflected wavenumber vector always has a forward component (following Snell's law), in corrugated plates that does not always happen. In these cases, there is a resonance between the guided modes which may propagate either in opposite directions, or in the same direction. They concluded that at some frequencies, resonance between symmetric or anti-symmetric modes of different orders *"can occur when the difference between or summation of wavenumbers of the two modes is a multiple"* [81] of the plate corrugation wavenumber. At these resonances mode conversion can occur, which in turn may lead to conditions where either the wave cannot propagate, called stop bands, or multiple modes can coexist with the same phase velocity, called cross-over points.

In a more applied approach, Radzienski et al. [82] published results of the combined use of vibration and GW testing for improved health assessment of composite panels. A sandwich panel was instrumented with a single thin piezoceramic disc which sent excitation signals formed by a continuous 2058 Hz wave periodically alternated with ultrasonic 30kHz windowed tone-bursts. A scanning laser vibrometer was used in order to measure the time-domain mechanical response at the centre and at one corner of the panel. At the first location they were able to detect a typical GW signal modulated by a sinusoid of longer period, while at the second location they observed a long-period sinusoid with high-frequency perturbations. In the frequency domain, both responses showed a clear separation between the 2058 Hz and the 30 kHz components. Nevertheless, it is important to note that the 2058 Hz vibration and the 30 kHz GW excitations had comparable amplitude. Additionally, when the lower frequency sine was periodically interrupted by the higher-frequency one, a synchronization pulse was sent to the acquisition unit in order to trigger the recording. These two facts prevented the overshadowing of the GW signals by the total mechanical response at the centre of the panel.

It goes without saying that the combined effect of thermal variation and loading becomes even more important in the case of composite materials, where the strong directional dependency is enhanced.

2.5. Modelling GWs in structures

Ultrasonic GWs are phenomena that take place at the microscale, both in time and space, making it difficult to study the physical parameters that govern their interactions with the structure solely through experiments. Additionally, the transducers in an SHM system must be permanently bonded/installed onto the structure, which implies that a large number of structural components would have to be produced, instrumented and tested if a fully experimental study of an SHM system in the different relevant damage scenarios and environmental-operational conditions was to be conducted. A way to work around these challenges is to employ numerical models for ultrasonic GW simulations.

By far the most widespread approach for computing wave propagation, the finite element (FE) method has shown very promising developments over the years. In 1992 Alleyne and Cawley [83] investigated the sensitivity of individual Lamb modes to particular types of notches in a metallic plate modelled in two dimensions (2D), finding excellent agreement with experimental results. Later on, Alleyne et al. [84] analysed the reflection of axially symmetric cylindrical GWs from circumferential notches in metallic pipes, arriving at equivalently satisfying results. In 2005, Diligent and Lowe [85] researched the reflection of the S0 Lamb mode from a flat-bottom circular hole in an

isotropic plate, arriving at important observations about interference between reflection from the leading and trailing edges of the hole. In a series of systematic studies, Rajagopal and Lowe [86-88] and Ratsessepp et al. [89] used the FE method to perform detailed investigations about the angular influence of part- and through-thickness cracks on the scattering of the SH0 mode in isotropic plates, in an effort to explore the non-dispersive characteristics of this mode for damage detection.

Going up in structural and material complexity, Dalton [90] analysed GW propagation through simplified metallic fuselage joints (e.g. adhesively bonded joints) using two-dimensional dynamic FE modelling. Cerniglia et al. [91] applied FE analysis with an explicit integration rule to simulate GW propagation in a three-layer aluminium/epoxy plate with wedge-transducers attached to the surface, obtaining a good match with experimental data. Using a two-dimensional FE model, Ricci et al. [92] studied GW interrogation of a composite stiffened panel with an impact-induced delamination underneath the flange, supporting their results by experimental data. In the same line of research, Murat et al. [93] investigated the interaction of the A0 Lamb mode with BVID in a thin composite plate. Relying on full three-dimensional FE simulations, the damage produced by a low-energy impact was modelled as a single delamination (with adjacent nodes separated by a very small distance, according to the “zero-volume” approach [94]) surrounded by a layer of elements whose material stiffness values were reduced by 75% (in order to mimic the fibre breakage and matrix cracking [95,96]). In the end a reasonably good agreement was found between numerical and experimental results, with the differences being mainly due to the definition of BVID in the model which did not represent the actual internal damage. In 2017, De Luca et al. [97] demonstrated the capabilities of the FE method for combining impact and wave propagation models into a single simulation, thereby obtaining more accurate predictions of GW interaction with BVID than with the approach of mimicking damage by reducing elastic material properties.

The quantification of SHM system reliability can also be assisted by the use of numerical simulations, as shown by Memmolo et al. [98] who experimentally validated a FE model of GW propagation in a composite plate, which was employed to generate damage indicator (DI) data for different scenarios of BVID. The numerical DI values were then disturbed by adding Gaussian noise in order to mimic experimental uncertainty. In this way it was possible to create multiple pseudo-stochastic data points for each damage level, thereby enabling hit/miss counting and subsequent probability-of-detection (POD) curve estimation.

However, accurate FE simulations of GW propagation come with a price. Due the small ultrasonic GW wavelengths, correct spatial representation of the waves requires a large number of elements. Moreover, because the time that the fastest wave component takes to travel across an element must be respected to allow the equations to converge and be solved, the time increment must be very low (according to the Courant-Friedrichs-Lewy condition [99]). As a result, FE models are computationally demanding, often requiring long running times, even when explicit integration is employed. In an effort to overcome such difficulties, different alternative methods have been developed for solving problems of ultrasonic GW propagation.

Some authors have developed hybrid formulations in order to reduce the size of the models without compromising the accuracy of the results. For example, Liu et al. [100] combined FE discretization with boundary integral representation in order to study Rayleigh-Lamb scattering at surface and in-depth cracks, and Predoi et al. [101] employed

FE steady state analysis and modal projection to research the influence of viscoelasticity on the multi-modal scattered field at a notch.

Wave-based methods have been developed as a way of improving the efficiency of numerical calculations, and the most common among them is the spectral finite element (SFE) method [102], also called the semi-analytical finite element (SAFE) method. The principle is to use frequency-dependent interpolation functions instead of high-order polynomials as in the FE method, allowing the order of the problem size to be considerably reduced. The system is solved in the frequency domain. The frequency response function is obtained for a unit impulse, which allows the response to different loadings to be obtained in a single analysis, and the output is transformed to the time domain using the inverse fast Fourier transform (iFFT).

This method was used by Fan [34] to investigate GW propagation in structures with irregular cross-section. Deng and Yang [103] applied Hamilton's principle (instead of Helmholtz's displacement potentials) to formulate the GW equations and solved a SAFE model of a composite adhesively bonded joint with different bonding conditions, including disbond state. Wieslaw and Maciej [104] used the SFE method to simulate crack detection and localization in composite plates by exciting guided waves at the centre of the model. In an interesting approach, Kim and Lee [105] adopted Timoshenko beam theory and Mindlin-Herrmann rod theory to derive the equations of motion for the quasi-flexural and quasi-longitudinal guided modes, respectively, and developed a two-dimensional SFE model of a symmetric composite beams. After validating their method, the authors investigated the effects of a delamination in the propagation of GWs. Focusing on the same problem as Kim and Lee, Khalili et al. [106] relied on the user-defined element option of ABAQUS to successfully implement a SFE model based on wavelet interpolation functions. In a hybrid approach, Song et al. [107] combined the SAFE and boundary element methods to perform numerical calculations of GW scattering in a plate overlap. The solution was obtained by modelling the overlap region with the boundary element formulation, and connecting it to two semi-infinite plates described by finite elements.

In an important study for SHM reliability quantification purposes, Janapati et al. [108] investigated in detail the sensitivity of damage detection to specific intra-measurement variability sources. They took small aluminium coupons with through-thickness cracks at a central hole, and bonded an actuator-sensor PZT pair on to each of them. A parametric study was conducted with the SFE method for seven different damage scenarios by varying the PZT material properties, structure material properties and adhesive properties, adhesive thickness, and sensor location. By comparing the numerical and experimental results they were able to establish quantitative correlations between isolated sources of variability and their actual observed effect on the DI, thereby partially characterizing the factors that influence the performance of the transducer network.

Nevertheless, the SFE method also has limitations. Although it is particularly suitable for solving GW propagation in waveguides of constant arbitrary cross-section, allowing three-dimensional problems to be reduced to 2D, it is not capable of modelling geometric discontinuities. *"Therefore, in order to numerically study the interactions of the guided mode with different types of defects, it is necessary to apply 3D time-step FE simulation"*, as justified by Fan and Lowe [33]. New numerical methods capable of incorporating the efficiency of lower-order methods and the versatility of the FE method have started to be developed. Some researchers have turned their attention to the local interaction simulation approach (LISA) to analyse GW propagation in three-dimensional composite plates [109] and to simulate the operation of ultrasonic transducers [110]. This method is based on

replacing the second-order derivatives in the elastodynamic equations by recursive (or iterative) relations based on finite differences. To handle heterogeneous structures LISA relies on sharp interface models to match stresses and displacements at the cross-points at the intersection of cells. Another method with equivalent capabilities is the elastodynamic finite integration technique (EFIT) [111,112]. By relying on the integral form of Newton-Cauchy's and Hook's equations, and on the staggered grid concept it can achieve as adequate GW simulations as other commercial FE tools, such as ABAQUS, ANSYS and COMSOL [113].

2.6. GW signal processing

Signal processing is the constituent of an GW-SHM system that is responsible for generating information from raw data, and, as such, it is the key enabler of damage diagnostic. The algorithms for signal processing encompass the operations of filtering, environmental-operation factor compensation and damage metric computation. Before describing the most common approaches for these operations, the necessary mathematical definitions are introduced.

2.6.1. Mathematical definitions

Starting with the time-domain, let $x(t)$ be a time-domain GW signal defined between the initial and final recorded instants. The energy, Es , of the signal is defined by the time integral [114,115]:

$$Es = \int_{-\infty}^{+\infty} |x(t)|^2 dt \quad (2.9)$$

The Hilbert transform (HT) of the signal is defined as:

$$HT(t) = \frac{1}{\pi} \int_{-\infty}^{+\infty} \frac{x(\tau_{lag})}{t - \tau_{lag}} d\tau_{lag} \quad (2.10)$$

Because the Hilbert transform applies a phase shift of $\pi/2$ to the signal, it is possible to define a complex variable called the analytic signal, $x_a(t)$, with the real part equal to the original signal and the imaginary part equal to the Hilbert transformed signal [28]:

$$x_a(t) = x(t) + iHT(t) = env(t) \cdot e^{i\phi(t)} \quad (2.11)$$

where $env(t)$ is the absolute value of $x_a(t)$ and corresponds to the envelope of the original signal:

$$env(t) = |x_a(t)| = \sqrt{x^2(t) + HT^2(t)} \quad (2.12)$$

and $\phi(t)$ is the instantaneous phase.

The instantaneous angular frequency, $\omega(t)$, can then be calculated as:

$$\omega(t) = \frac{d\phi(t)}{dt} \quad (2.13)$$

from which the instantaneous frequency, $f(t)$, is obtained just by multiplying by $1/2\pi$.

The GW signal can also be represented in the frequency-domain by applying the Fourier transform (FT):

$$FT(\omega) = \int_{-\infty}^{+\infty} x(t) \cdot e^{-2\pi i \omega t} dt \quad (2.14)$$

For processing of a discrete signal, x_n , the discrete form of the FT is implemented using numerical mathematical algorithms to reduce the necessary number of computations, resulting in the so-called fast Fourier transform (FFT):

$$FFT(k) = \sum_{n=1}^N x_n e^{-\frac{2\pi i}{N} kn} \quad (2.15)$$

where $k = 1, 2, \dots, N$, and N is the number of sampling points in the signal.

The signal energy can also be obtained by integrating the spectrum in the frequency domain:

$$Es = \frac{1}{2\pi} \int_{-\infty}^{+\infty} |FT(\omega)|^2 d\omega \quad (2.16)$$

Another useful representation of the signal can be obtained by computing the continuous wavelet transform (CWT) [116]:

$$CWT(a_w, b_w) = \frac{1}{\sqrt{a_w}} \int_{-\infty}^{+\infty} x(t) \cdot \Psi^* \left(\frac{t - b_w}{a_w} \right) dt \quad (2.17)$$

where Ψ is a function called the mother wavelet; multiple values of scale a_w and time b_w are used to impose different dilations and a translations to Ψ ; and the superscript $*$ indicates complex conjugate.

Applying the CWT is similar to applying the FT to multiple consecutive narrow time windows of the signal. However, in this case, the definition of the window is based on an orthogonal, amplitude modulated wavelet function, and not on a pure sinusoid. While b_w corresponds to a time-shift, a_w induces either a compression of a dilation of the wavelet. The higher the scale a_w , the more spread out is the wavelet, and vice-versa. So, the scale is inversely proportional to frequency: $f_a = f_c/a_w$, where f_a and f_c are the frequency corresponding to scale a_w and the centre frequency of the wavelet, respectively. In this sense, it is correct to say that CWT is a time-frequency-domain representation of the signal. Because there are many different types of wavelets, it is possible to obtain different results of the transform of the same original signal.

The time-domain signal $x(t)$ can be reconstructed through the inverse continuous wavelet transform:

$$x(t) = \frac{1}{C_\Psi} \int_{b_w \geq 0} \int_{a_w \geq 0}^{+\infty} CWT(a_w, b_w) \frac{1}{\sqrt{a_w}} \Psi\left(\frac{t-b_w}{a_w}\right) \frac{1}{a_w^2} da_w db_w \quad (2.18)$$

where C_Ψ stems from the admissibility condition that the wavelet function Ψ must satisfy [116]:

$$0 < C_\Psi = \int_{-\infty}^{+\infty} \frac{|\Psi(t)|^2}{t} dt < \infty \quad (2.19)$$

2.6.2. Signal filtering

Although ultrasonic GW measurements are typically conducted at frequencies above 20 kHz, acquired signals are still affected by noise. Considering only the SHM system hardware, the noise sources can be internal or external. Intrinsic noise can be generated in the electronics of the data acquisition equipment due to mechanisms associated with thermal motion charge-carriers in conductive material and with the passage of electric current [117]. External noise in the form of interfering signals can come from electromagnetic or electrostatic sources. For the first case, noise can be induced by voltage transients or electrical currents (usually occurring in nearby cabling), by operating computers (typically at frequencies of several gigahertz) and by power supplies (which work at frequencies of hundreds of kilohertz). For the second case, noise can be induced by electric charges generated by the friction of the materials inside vibrating cables (almost unavoidable in aerospace vehicles), or by voltage generated in circuit-board materials which exhibit some piezoelectricity and thus are sensitive to vibrations. On top of that, there might also be structural loads inducing low-frequency fluctuations. Hence, in short, ultrasonic GW signals have to be filtered before any information is derived from them.

Digital oscilloscopes have basic filtering capabilities incorporated, usually based on averaging algorithms [118]. Each point of the signal is filtered by computing the average of its N neighbouring points, with the weights attributed to the neighbouring points allowed to vary between 0 and 1. In well-controlled laboratory conditions, with limited environmental changes, these basic filters are often enough to significantly reduce random noise. However, in more realistic measurement conditions, which can include structural vibrations and temperature changes, the dominant noise and fluctuations are hardly random. As a result, moving-average filtering is not enough, because it becomes necessary to isolate the frequency band of the GW signal of interest by applying a band-pass or a high-pass filter.

One option is a Butterworth filter [93]. Although this type of digital filter is known to allow a maximally flat pass-band (i.e. without ripples or oscillations), and a total roll-off to zero magnitude, the stop-band tends to be relatively soft. The stop-band slope can be increased by increasing filter order at the expense of promoting overshoots or ringing in the step-response. Two alternatives are the Chebyshev and Elliptic (also known as Cauer) filters, which have faster roll-off than Butterworth filters, but are never flat in the pass-band [119]. A compromise solution between the Butterworth and the Chebyshev types is

the Legendre-Papoulis filter, which combines a flat magnitude in the pass-band and a roll-off rate between that of the other two filter types [120].

In any case, due to the existence of a stop-band and a roll-off rate, a signal filtered with one of the aforementioned digital filters still contains frequencies outside the band of interest. To overcome this problem, it is possible to compute the CWT of the signal and use only the coefficients at the frequency band of interest to reconstruct the time-domain signal through the inverse CWT. This constitutes CWT filtering, and it is a well-established, effective approach for GW-SHM [28,121-125].

2.6.3. Temperature effect compensation

As explained in Section 2.4.6, temperature variations affect ultrasonic GWs directly and indirectly, with temperature-induced changes having the same order of magnitude as damage-induced ones, which can thus lead to an erroneous damage diagnostic if not compensated for. This problem has received (and continues to receive) the attention of researchers, with two classes of compensation techniques being developed: data-based and physics-based.

The most widespread data-based temperature compensation techniques are the optimal baseline selection (OBS) and the baseline signal stretch (BSS). The OBS approaches require baseline signals to be recorded at a range of discrete temperatures with a relatively small spacing between them. The most suitable baseline for the damage diagnostic is then selected as the one that has the best time-trace match with the current signal [126]. For evaluating the time-trace similarity different possible criteria can be implemented. The BSS techniques attempt to compensate the temperature effects on the monitored GW signal by stretching, compressing or distorting the baseline signal until it best matches the monitored signal [127]. Depending on the scale of the necessary correction, the match can be evaluated according to different criteria. BSS is considerably less data-intensive than OBS, because multiple signal transformations can be iteratively applied until the best match is obtained. It might of course be the case that those transformations do not entirely mimic the real effect of temperature change. A combination of OBS and BSS can be implemented [126,128] as a solution that keeps the advantages of both approaches. On one hand, with the OBS part it is possible to capture the true effect of temperature variation within the desired range in the set of baseline signals. On the other hand, the BSS part allows the number of necessary baselines to be reduced because fine compensation can be applied through signal transformations.

Similarly to OBS, Moix-Bonet et al. [129] have recently used Gaussian mixture models of two signal features, for damaged and undamaged states acquired between -40 °C and 85 °C, and computed the corresponding Mahalanobis squared distance. When the damage-induced changes in the signal were orthogonal to those induced by temperature variation, they could distinguish them and produce a diagnostic. Nevertheless, this approach also requires large amounts of data to be acquired for the creation of a reference state across the desired temperature range.

Fendzi et al. [130] proposed a data-driven technique that requires less data collection than normal OBS, in which thermally induced GW signal amplitude and phase shifts were directly correlated to temperature. The amplitude and phase shifts were extracted from a limited set of signals (including the baseline) at the desired temperature range and were used to build a regression model, which could then be employed for the GW signal compensation at any arbitrary temperature within the desired range.

By following the same logic, it is possible to implement an even simpler compensation mechanism by assuming that the main effect of temperature variation on GW signals can be translated into a phase change. By adding the difference in instantaneous phase between the baseline and the current signal to the analytic form of the current signal (computed with Equation (2.11)), the thermal influence on the GW signal is partially removed [128,131]

Physics-based approaches resort to simulations of the SHM environment, in which explicit temperature dependency of the material properties of the structure, transducer and transducer adhesive have to be modelled, in order to predict the effect of temperature on ultrasonic GW signals [132]. Although physics-based approaches can reveal very detailed interactions, it is not always possible to establish the required material models in an accurate way.

2.6.4. Damage indicators

From a signal processing point of view, “damage” is a structural state that is different from the “pristine” state which is defined as the benchmark, reference or baseline. Thus, damage diagnostic entails a comparison which must be quantified. That is made possible by extracting signal features and computing a damage indicator (DI). The signal feature can be extracted in the time-domain or the frequency-domain, and it is also possible to fuse different metrics to increase the robustness of the diagnostic. In the following sub-sections a collection of the most used DIs is provided, although it is not meant to be exhaustive.

2.6.4.1. Time-domain

An interesting feature to explore for correlation with stiffness and damping changes in the structure is the so-called 10%-duration time, $t_{10\%}$ [133]. This is the time it takes for the signal amplitude to decay from its maximum to 10% of its value. If the structural stiffness decreases, this time interval is expected to increase. So, one possible way of quantifying the variation of $t_{10\%}$ between the reference (subscript *ref*) and the damage states (subscript *dmg*) is:

$$DI = \frac{|t_{10\%,ref} - t_{10\%,dmg}|}{t_{10\%,ref}} \quad (2.20)$$

Because wave velocity is related to material properties, the same ratio can also be defined for the TOF (time-of-flight) of the first GW signal arrival in order to extract an indication of stiffness degradation.

One way of quantifying wave attenuation and scattering due to the presence of damage is through the difference of absolute maximum amplitude between the reference signal, x_{ref} , and the damaged signal, x_{dmg} , normalised by that of the reference signal [28]:

$$DI = \frac{|\max(x_{ref}) - \max(x_{dmg})|}{|\max(x_{ref})|} \quad (2.21)$$

Another way is to quantify the spread of energy around the damage through the variation of signal energy, normalized by that of the reference [28], with signal energy defined by Equation (2.9):

$$DI = \frac{|E_{ref} - E_{dmg}|}{E_{ref}} \quad (2.22)$$

A common approach to perform a quantitative comparison between baseline and damaged signals is to compute their correlation coefficient (CC) [25,28,134], which provides a dimensionless measure of their linear dependence. If the signals are directly and negatively correlated $CC = -1$; if the signals are directly and positively correlated $CC = +1$; if the signals are not correlated $CC = 0$. Hence, the complement of the absolute value of CC can be used to obtain a metric which increases when the difference between reference and damaged signals increases:

$$DI = 1 - |CC| = 1 - \left| \frac{1}{N-1} \sum_{i=1}^N \left(\frac{x_{ref,i} - avg_{ref}}{std_{ref}} \right) \left(\frac{x_{dmg,i} - avg_{dmg}}{std_{dmg}} \right) \right| \quad (2.23)$$

where N is the number of sample point in the signals, and avg and std are the mean and standard deviation of the signals, respectively.

The root mean square deviation (RMSD) is another way to quantify the match between two signals, and is also widely used as a DI [25]:

$$RMSD = \sqrt{\frac{\sum_{i=1}^N (x_{dmg,i} - x_{ref,i})^2}{\sum_{i=1}^N x_{ref,i}^2}} \quad (2.24)$$

Cross-correlation between two signals at zero lag, $R(0)$, can also be used to define the coherence between two signals at zero lag, $\gamma_{xy}(0)$, of which the complement can be taken to define a DI [135]:

$$DI = 1 - \gamma_{xy}(0) = \frac{R_{xy}(0)}{\sqrt{R_{xx}(0)R_{yy}(0)}} \quad (2.25)$$

where R_{xy} denotes the cross-correlation between the baseline and the damaged signal, R_{xx} the auto-correlation of the baseline, and R_{yy} the auto-correlation of the damaged signal. The cross-correlation between two arbitrary signals at τ_{lag} lag can be calculated by [131]:

$$R_{xy}(\tau_{lag}) = \frac{\int_0^{+\infty} [x(t) - avg_x] [y(t + \tau_{lag}) - avg_y] dt}{std_x std_y} \quad (2.26)$$

By applying a normalisation to the signals, it is possible to define a DI which seems to be resistance to non-damage occurrences [108]:

$$DI = \sum_{i=1}^N (s_{ref,i} - s_{dmg,i})^2 \quad (2.27)$$

where s_{dmg} is defined by:

$$s_{dmg} = \frac{x_{dmg}}{\sqrt{\sum_{i=1}^N x_{dmg,i}^2}} \quad (2.28)$$

and s_{ref} is equal to:

$$s_{ref} = \frac{x_{ref} \cdot \sum_{i=1}^N (x_{ref,i} \cdot s_{dmg,i})}{\sum_{i=1}^N x_{ref,i}^2} \quad (2.29)$$

2.6.4.2. Frequency-domain

Working in the frequency domain can in some cases allow more detailed signal analysis, because it is possible to observe the spectrum components that change. Thus, the normalized spectrum difference between the baseline and damage can be used as DI [28]:

$$DI = \frac{\sum_{i=1}^N |FFT_i^{ref} - FFT_i^{dmg}|}{\sum_{i=1}^N |FFT_i^{ref}|} \quad (2.30)$$

where FFT denotes the fast Fourier transform coefficients computed according to Equation (2.15), and N is the number of points in the spectrum.

An important signal property is the characteristic frequency, which can be calculated as the average of all f_i frequencies in the FFT signal, weighted by the corresponding FFT coefficients [41]:

$$f_{ch} = \frac{\sum_{i=1}^N FFT_i \cdot f_i}{\sum_{i=1}^N FFT_i} \quad (2.31)$$

The change in f_{ch} can then be useful in defining a DI:

$$DI = \frac{|f_{ch,ref} - f_{ch,dmg}|}{f_{ch,ref}} \quad (2.32)$$

The amplitude of frequency response of a structure monitored by a certain actuator-sensor pair:

$$G(\omega) = \frac{FFT_{sensor}(\omega)}{FFT_{actuator}(\omega)} \quad (2.33)$$

can also be used to define the metric:

$$g = \frac{\log(|G^{ref}|)}{\log(|G^{dmg}|)} - 1 \quad (2.34)$$

which in turn can be plugged into the definition a DI as a figure of merit [136]:

$$DI = \frac{1}{2} \times \frac{\sum_{i=1}^N w_i g_i^2}{\sum_{i=1}^N w_i} \quad (2.35)$$

where N is the number of points in the frequency spectra w_i are weighting factors the depend on the measuring equipment and on the statistics of the data.

2.6.4.3. Information fusion

In some cases, it may be advantageous to combine or fuse metrics to form a new DI which enables a more clear diagnostic. This was used in the example of simply taking the product of the amplitude difference ratio (Equation (2.20)) and the propagation interval difference ratio (Equation (2.21)) [28]. Another interesting option is to combine the correlation coefficient, the amplitude difference ratio and the energy difference ratio as follows [125]:

$$DI = \frac{\sqrt{CC^2 + AR^2 + ER^2}}{\sqrt{3}} \quad (2.36)$$

with the definition of the CC given in Equation (2.23), the amplitude ratio (AR) taken from Equation (2.21), and the energy ratio (ER) from Equation (2.22).

The fusion of DI information can also aim at increasing the robustness of the diagnostic against temperature variation. For an SHM system equipped with a transducer network of N_{as} actuator-sensor pairs, the following formula can be used to distinguish between local (damage) and global (temperature) changes [128]:

$$DI = DI_{\max} - \frac{\sum_{p=1}^{N_{as}-1} DI_p}{N_{as} - 1} \quad (2.37)$$

where DI_p is the DI for each transducer pair and DI_{max} is maximum DI. A global change will affect all the transducer pairs, resulting in a high average of the $N_{as}-1$ lowest DIs, and thus in a low final DI. On the contrary, a local change will only induce DI variation in some transducer pair, resulting in a low average of the $N_{as}-1$ lowest DIs, and a high final DI.

The approach of generating a new DI by linear combination [134,137] is well aligned with the utilization of multi-path transducer networks for monitoring a critical area as whole. According to the multi-path unit-cell concept [138,139], the DI converges to its “real” value as the number of relevant wave propagation paths increases. Thus, if the number of propagation paths is increased in a meaningful way for the areas to be monitored, while preventing the network from becoming overly dense, then it is not necessary to solve an actual mathematical optimization problem for defining the transducer placement. So, for a monitored area, the DI can be calculated as the weighted-average of all N_{as} paths in the area:

$$DI = \sum_{p=1}^{N_{as}} w_p DI_p \quad (2.38)$$

where the weighting factors w_p are computed such that they are representative of the relevance of the transducer pair for the overall diagnostic:

$$w_p = \frac{DI_p}{\sum_{p=1}^{N_{as}} DI_p} \quad (2.39)$$

The application of this concept makes the DI independent of propagation path orientation with respect to the structural elements in the monitored area, thereby generating a DI value which corresponds to a measure of the total change in the scatter field.

2.7. SHM of fixed wing aircraft

2.7.1. System functions

Every SHM system uses data (inputs) acquired from permanently mounted sensors to perform two main functions, operational and damage monitoring. Operational monitoring includes fatigue, environmental and exceedance monitoring. These three actions gather information about the external actions onto the structure (e.g. strains, loads, temperature variations) and provide information on the actual structural usage (which might differ from the design spectra). The latter can be used to identify possible critical spots in the structure. Having identified the regions prone to fracture, another more local sensor network can be activated in order to monitor damage in accordance to residual strength analysis or other failure criteria. In this way it is possible to “*reduce the rate of false negative and false positive indications*” [48]. As the data is processed, a quantitative diagnostic is produced, and an advisory indication is issued (outputs).

Within SHM, there can be scheduled and automated applications, S-SHM and A-SHM, respectively [48]. The former is part of the scheduled maintenance tasks and consists of interacting with the SHM system while the aircraft is fully stationary in the

hangar. It enables data acquisition from components that are difficult to access and that would have to be disassembled for detailed manual inspection. Thus S-SHM can be an auxiliary in scheduled inspections by trained personnel, thereby reducing maintenance costs, human-based errors and improving safety.

The latter corresponds to collecting and processing data multiple times while the aircraft is in operation, including in pre-flight phase and during flight. In this way it is possible to obtain an almost real-time evolution of structural condition, and to provide with timely advice about where and when maintenance actions are necessary, thereby maximizing aircraft availability and improving safety even further. Hence, A-SHM is the key enabler of CBM, as introduced in Chapter 1. Therefore, from here onwards the term SHM refers to A-SHM, as defined in the ARP6461 [48].

2.7.2. System capabilities and requirements

Before developing the architecture of an SHM system it is necessary to define the capabilities that it should possess in order to deliver the intended functions.

In general, an event can be characterized by performing the following four actions [48,102]:

- a) Detection of the occurrence of an event
- b) Identification of the location of the event
- c) Determination of the magnitude of the event
- d) Estimation of the influence of the event on the structure

By observing the above list it is possible to adopt a more specific classification for operational and damage monitoring functions. From a) to c) all the capabilities consist of acquiring actual characteristics of the current state, while the last one is about estimating an effect on structural performance. Therefore, it is possible to regroup the SHM functions into diagnostic (a to c) and prognostic (d).

For the diagnosis and prognosis outputs to be considered reliable, the system is bound by requirements that establish the acceptable limits of performance. These are protocols that aim to ensure the intended SHM functions are successfully delivered during the useful life of the system and according to prescribed aircraft safety levels. In particular for airborne equipment, the following families of requirements can be formed (more detailed specifications on each of the requirements can be found in [48]):

- | | |
|------------------------------|---------------------------------------|
| • Functional requirements | • Structural requirements |
| • Operational requirements | • Installation requirements |
| • Performance requirements | • Maintainability requirements |
| • Physical requirements | • Interface requirements |
| • Environmental requirements | • Safety and reliability requirements |

The level of constraint imposed by the aforementioned requirements will vary depending on the intended SHM application. In other words, the system will be required to produce enough information to prove it is capable of meeting the functions for which it was designed. Once the system has shown to meet the necessary requirements, it must be validated and certified in order to ensure it is in line with the continued airworthiness regulations. Only then can it be considered ready for operational usage.

2.8. SHM reliability quantification

Certification of an SHM system requires the determination of the probability of detecting a certain type of damage with a critical value, the probability of not detecting that same critical damage, and the probability of false detection, in different environments and during the expected useful life of the system. In a nutshell, it is necessary to answer the question *How reliable is the system?*

Contrary to NDT techniques [140], no standard methods have been established for empirically quantifying the reliability of an SHM system, mostly because the transducers must be permanently mounted on the structure. That apparently simple constraint imposes monetary obstacles related to the prohibitive cost of large test campaigns that would be required to produce, instrument and test a large number of real-scale (1:1) components in all the necessary scenarios to validate the performance of a single SHM system. Technical obstacles also arise from the fact that it is hard to mimic real operational and environmental scenarios in the laboratory.

This situation has led research on reliability characterisation of ultrasonic SHM systems to consider small planar coupons, either metallic or composite, in order to prevent test campaigns from becoming unfeasible, while adapting and extending the reliability assessment methods traditionally employed in NDT. Cobb et al. [141,142] developed a regression-based measurement model to estimate the POD of fatigue cracks in small rectangular aluminium coupons inspected with shear wave transducers. However, their methodology required an extensive experimental database of DI values correlated with the observed crack length, which took “*several years*” [141] to be compiled. In an effort to overcome this challenge, protocols have been established for model-assisted probability of detection (MAPOD) determination [143-147]. They enable numerical parametric studies for evaluating the different monitoring scenarios, in which properties of the material, structure, transducers, environment, etc. can be varied according to the associated distributions. Knowledge of these physical factors and their distributions should be previously acquired either through a limited number of experiments, or through properly validated physics-based models. Hence, MAPOD allows large amounts of DI points to be generated for statistical analysis, while reducing the size and cost of experimental campaigns.

An important contribution to the implementation of MAPOD protocols was given by Janapati et al. [108] who conducted a detailed investigation on the sensitivity of damage detection to specific intra-measurement variability sources. To induce variability in the different GW-SHM system parameters, they had PZT actuator-sensor pairs bonded onto small aluminium coupons by six different technicians. The coupons were damaged by through-thickness cracks at a central hole, and GW signals were acquired at 250 kHz. A parametric study was then conducted with the SFE method for seven different damage scenarios by varying the PZT material properties, structure material properties and adhesive properties, adhesive thickness, and sensor location. By comparing the numerical and experimental results they were able to establish quantitative correlations between isolated sources of variability and their actual observed effect on the DI, thereby partially characterizing the factors that influence the performance of the transducer network.

Also a difference with respect to NDT techniques is the fact that SHM data consists of repeated measurements made with the same transducers, in the same location on the same structure. This means that data points are not independent observations. The statistical

methods should incorporate this property to allow a valid determination of the POD curves. In the case of a MAPOD determination, the sum-of-uniforms method can be used to introduce correlation between numerical data points, thereby mimicking data dependency [148]. In the case of experimental monitoring data, linear mixed-effects models are possible solutions [149] to account for data dependency in the regression describing the DI as a function of damage size.

2.9. Knowledge gaps

The guidance necessary to accomplish the research goal described in Section 1.3 can be summarised in the following main research question:

What are possible steps for increasing the reliability of GW monitoring of thermoplastic composite aircraft structures with real geometric and material complexity, without losing sight of the physics governing GW interactions with critical structural details?

When reviewing the latest advancements on ultrasonic welding of TpCs (Section 2.2) it became clear that the joints produced by that technique have a unique structure, with properties that are considerably different from adhesive bonds and are still not fully understood. Not only the bonding nature is different (unlike adhesion, fusion bonding relies on molecular interdiffusion), with unclear influence on the continuity of strain-stress across the overlap and on the possible manufacturing defects, but also the range of bond thicknesses is ten times smaller than in the case of adhesively bonded joints. Consequently, the interactions experienced by GWs in TpC ultrasonically welded joints fall outside the domain of understanding obtained from previous research (Section 2.4.3). This led to the following sub-question:

Q1) How does the internal structure of the ultrasonic weld influence the propagation of ultrasonic guided waves through a thermoplastic composite joint?

Reliability implies systematisation and standardisation of practices, but also realistic outputs to make those practices feasible. This should be the underlying principle when transferring the knowledge about GW propagation acquired at element-scale to full-scale. However, as discussed in Section 2.4.5, when it comes to a crucial step such as designing an SHM system, the commonly used approach relies on a single GW mode analysis. Since that is only possible in very specific and simplistic cases, the accomplishment of a diagnostic tends to be ensured by the use of a highly dense transducer network around a confined region (less than half metre) within the larger critical area. In a real SHM application for composite aircraft structures, in which GW propagation is direction-dependent, and where there are various three-dimensional geometric complexities and environmental/operational factors acting together, it is not realistic to rely on pure GW mode analysis. Furthermore, the requirements for minimization of hardware usage, system power consumption, and the influence of the transducer network on structural behaviour make it infeasible to deploy dense transducer networks. Above all, the common SHM system design approaches are unrealistic if GW-SHM systems are to reach certification level for commercial aviation, as they do not encompass the full complexity of the coupled physics underlying GW transduction, nor do they take multiple damage scenarios into

account. In short, the lack of a systematic procedure for selecting/designing the transducer network and excitation signal is a major gap preventing the progress towards certification of GW based SHM systems. Therefore:

Q2) How can the multiple parameters controlling the coupled physics of GW transducing be systematically integrated in the design of an SHM system for a real-scale composite aircraft primary structure?

Once an SHM system is designed, it is crucial to evaluate its performance in different scenarios in order to arrive at a quantitative reliability characterisation. As explained in Section 2.8, research is active in improving model-assisted protocols for incorporating knowledge of the physical variability factors into validated numerical models capable of simulating the SHM system response, thus enabling the determination of POD curves. Although there are already plenty of case-studies available, key factors such as full geometric complexity, material anisotropy, and transducer network degradation have still not been simultaneously taken into account. Hence, an essential research sub-question is:

Q3) What is the reliability of a GW-SHM system in diagnosing BVID in a real-scale composite stiffened panel in the scenario of a defective transducer?

Finally, if GW-SHM systems are to reach the certification phase, they must be able to reliably perform damage diagnostic with data acquired in real environmental-operational conditions, namely temperature changes and high-amplitude LFV (low-frequency vibration). To that end, mechanisms must be put in place to compensate for the effect of those variations on GW signals, which in turn requires an understanding of the physics behind those effects. Temperature effects have been the subject of multiple studies, and some compensation mechanisms have already been able to achieve promising results (Section 2.4.6). However, to this date there is no known published research about the LFV-GW interaction. Therefore, it is imperative to ask:

Q4) How do high-amplitude low-frequency structural vibrations affect ultrasonic GW propagation?

These research questions will be addressed in the order presented above in Chapters 4 to 8. By answering them, this thesis aims to bring GW-SHM of composite aircraft one step closer to certification level. In turn this is expected to contribute to the integration of GW-SHM technology with the new TpC structures, thereby opening the doors for the implementation of CBM practices in civil aviation.

References

1. Red C. The outlook for thermoplastics in aerospace composites, 2014-2023. *High-Performance Composites* Sep 2014; 22(5): 54-63.
2. Yousefpour A, Hojjati M, Immarigeon JP. Fusion bonding/welding of thermoplastic composites. *J Thermoplast Compos Mater* 2004; 17: 303-341.
3. Ageorges C, Ye L, Hou M. Advances in fusion bonding techniques for joining thermoplastic matrix composites: a review. *Composites Part A* 2001; 32: 839-857.

4. Villegas IF, Moser L, Yousefpour A, Mitschang P, Bersee HEN. Process and performance evaluation of ultrasonic, induction and resistance welding of advanced thermoplastic composites. *J Thermoplast Compos* 2012; 26(8): 1007-1024.
5. Villegas IF. In situ monitoring of ultrasonic welding of thermoplastic composites through power and displacement data. *J Thermoplast Compos* 2015; 28(1): 66-85.
6. Villegas IF. Strength development versus process data in ultrasonic welding of thermoplastic composites with flat energy directors and its application to the definition of optimum processing parameters. *Composites Part A* 2014; 65: 27-37.
7. Tateshi N, North TH, Woodhams RT. Ultrasonic welding using tie-layer materials. Part I: Analysis of process operation. *Polym Eng Sci* 1992; 32: 600-611.
8. Yan J, Wang X, Li R, Xu H, Yang S. The effects of energy director shape on temperature field during ultrasonic welding of thermoplastic composites. *Key Eng Mater* 2007; 353-358: 2007-2010.
9. Villegas IF, Valle Grande B, Bersee HEN, Benedictus R. A comparative evaluation between flat and traditional energy directors for ultrasonic welding of CF/PPS thermoplastic composites. *Compos Interface* 2015; 22(8): 717-729.
10. Villegas IF, Palardy G. Ultrasonic welding of CF/PPS composites with integrated triangular energy directors: melting, flow and weld strength development. *Compos Interface* 2017; 24(5): 515-528.
11. Zhao T, Broek C, Palardy G, Villegas IF, Benedictus R. Towards robust sequential ultrasonic spot welding of thermoplastic composites: Welding process control strategy for consistent weld quality. *Composites Part A* 2018; 109: 355-367.
12. Jongbloed B, Teuwen J, Palardy G, Villegas IF, Benedictus R. Improved weld uniformity in continuous ultrasonic welding of thermoplastic composites. Paper presented at: 18th ECCM; June 24-28, 2018; Athens, Greece.
13. Köhler F, Jongbloed B, Filipe T, Herrmann A, Villegas IF, Benedictus R. A roadmap for developing an industrial continuous welding process for thermoplastic composites. Paper presented at: 4th ITHEC; October 30-31, 2018; Bremen, Germany.
14. Patricia PP, Bersee HEN, Beukers, A. Residual stresses in thermoplastic composites – A study of the literature – Part I: Formation of residual stresses. *Compos Part A Appl S* 2006; 37: 1847-1857.
15. Talbott MF, Springer GS, Berglund LA. The effects of crystallinity on the mechanical properties of PEEK polymer and graphite fiber reinforced PEEK. *J Compos Mater* 1987; 21:1056-1081.
16. Koutras N, Amirdine J, Boyard N, Villegas IF, Benedictus R. Characterisation of crystallinity at the interface of ultrasonically welded carbon fibre PPS joints. *Compos Part A Appl S* 2019; 125(105574): 1-11.
17. Heslehurst RB. *Defects and Damage in Composite Materials and Structures*. Boca Raton, USA: CRC Press; 2014.
18. Talreja R. Fatigue of composite materials: damage mechanisms and fatigue-life diagrams. *Proc Roy Soc Lon Ser-A* 1981; 378(1775): 461-475.

19. Faivre V, Morteau E. Damage tolerant composite fuselage sizing – Characterisation of accidental damage threat. *Flight Airworthiness Support Technology* 48; August, 2011: 10-16.
20. Richardson MOW, Wisheart MJ. Review of low-velocity impact of composite materials. *Composites Part A* 1996; 27A: 1123-1131.
21. Agrawal S, Singh KK, Sarkar PK. Impact damage on fibre-reinforced polymer matrix composite – A review. *J Compos Mater* 2014; 48(3): 317-332.
22. Aktaş M, Atas C, İçten BM, Karakuzu R. An experimental investigation of the impact response of composite laminates. *Compos Struct* 2009; 87: 307-313.
23. Meyers MA, Chawla KK. *Mechanical Behaviour of Materials*. New York, USA: Cambridge University Press; 2009.
24. Cheeke JDN. *Fundamentals and Applications of Ultrasonic Waves*. Florida, USA: CRC Press; 2002.
25. Giurgiutiu V. *Structural Health Monitoring With Piezoelectric Wafer Active Sensors*. 2nd ed. Academic Press – Elsevier; 2014.
26. Rayleigh L. On Waves Propagated along the Plane Surface of an Elastic Solid. *Proc Lond Math Soc* 1885; s1-17(1): 4-11.
27. Matt HM. *Structural Diagnosis of CFRP Composite Aircraft Components by Ultrasonic Guided Waves and Built-in Piezoelectric Transducers*. San Diego, USA: University of California; 2006.
28. Su Z, Ye L. *Identification of Damage Using Lamb Waves: From Fundamentals to Applications*. In: Pfeiffer F, Wriggers P, eds. *Lecture Notes in Applied and Computational Mechanics* 48. Springer; 2009.
29. Wilcox PD, Lowe MJS, Cawley P. Mode and Transducer Selection for Long Range Lamb Wave Inspection. *J Intel Mat Sys Str* 2001; 12: 553-565.
30. Su Z, Ye L, Lu Y. Guided Lamb waves for identification of damage in composite structures: A review. *J Sound Vib* 2006; 295: 753-780.
31. Hsieh TM, Hirshman KA, Lindgren EA, Rosen M. *Characterization of elastic properties of interfaces in composite materials*. USA: Department of the Navy, Office of Naval Research; 1990. *Final Report*.
32. Sargent JP. Corrosion detection in welds and heat-affected zones using ultrasonic Lamb waves. *Insight* 2006; 48(3): 160-167.
33. Fan Z, Lowe MJS. Interaction of welded-guided waves with defects. *NDT&E Int* 2012; 47: 124-133.
34. Fan Z. *Applications of Guided Wave Propagation on Waveguides With Irregular Cross-Section*. London, UK: Imperial College London; 2010.
35. Rokhlin SI. Lamb wave interaction with lap-shear adhesive joints: theory and experiment. *J Acoust Soc Am* 1991; 89(6): 2758-2765.
36. Ditri JJ. Some results on the scattering of guided elastic SH waves from material and geometric waveguide discontinuities. *J Acoust Soc Am* 1996; 100(5): 3078-3087.

37. Lowe MJS, Challis RE, Chan CW. The transmission of Lamb waves across adhesively bonded lap joint. *J Acoust Soc Am* 2000; 107(3): 1333-1345.
38. Lanza di Scalea F, Rizzo P, Marzani A. Propagation of ultrasonic guided waves in lap-shear adhesive joints: case of incident a0 Lamb wave. *J Acoust Soc Am* 2004; 115(1): 146-156.
39. Matt H, Bartoli I, Lanza di Scalea F. Ultrasonic guided wave monitoring of composite wing skin-to-spar bonded joints in aerospace structures. *J Acoust Soc Am* 2005; 118: 2240-2252.
40. Singher L, Segal Y, Segal E. Considerations in bond strength evaluation by ultrasonic guided waves. *J Acoust Soc Am* 1994; 96(4): 2497-2505.
41. Singher L. Bond strength measurement by ultrasonic guided waves. *Ultrasonics* 1997; 35: 305-315.
42. Kundu T, Maji A, Ghosh T, Maslov K. Detection of kissing bonds by Lamb waves. *Ultrasonics* 1998; 35: 573-580.
43. Thomson WT. Transmission of Elastic Waves through a Stratified Solid Medium. *J Appl Phys* 1950; 21(89): 89-93.
44. Giurgiutiu V, Santoni-Bottai G. Structural health monitoring of composite structures with piezoelectric-wafer active sensors. *AIAA J* 2011; 49(3): 565-581.
45. Putkis O, Dalton RP, Croxford AJ. The anisotropic propagation of ultrasonic guided waves in composite materials and implications for practical applications. *Ultrasonics* 2016; 65: 390-399.
46. Pant S, Laliberte J, Martinez M, Rocha B, Ancrum D. Effects of composite lamina properties on fundamental Lamb wave mode dispersion characteristics. *Compos Struct* 2015; 124: 236-252.
47. Percival WJ, Birt EA. A study of Lamb wave propagation in carbon-fibre composites. *Insight* 1997; 39(10): 728-735.
48. ARP6461:2013-09. Guidelines for implementation of structural health monitoring on fixed wing aircraft; 2013.
49. Croxford AJ, Wilcox PD, Drinkwater W, Konstantinidis G. Strategies for guided-wave structural health monitoring. *Proc R Soc A* 2007; 463: 2961-2981.
50. Wilcox PD. *Lamb Wave Inspection of Large Structures Using Permanently Attached Transducers*. London, UK: Imperial College London; 1998.
51. Manka M, Rosiek M, Martowicz A, Uhl T. Interdigital transducers for Lamb-wave based SHM systems: design and sensitivity analysis. *Mechanics and Control* 2011; 30(2): 79-84.
52. Manka M, Rosiek M, Martowicz A, Stepinski T, Uhl T. Tunable interdigital transducer for Lamb waves. Paper presented at: 7th EWSHM; July 8-11, 2014; Nantes, France.
53. Marin-Franch P, Martin T, Tunnicliffe DL, Das-Gupta DK. PTCa/PEKK piezo-composites for acoustic emission detection. *Sensor Actuat A-Phys* 2002; 99: 236-243.

54. Van Den Ende DA, Van Kempen SE, Wu X, Groen WA, Randall CA, Van Der Zwaag S. Dielectrophoretically structured piezoelectric composites with high aspect ratio piezoelectric particles inclusions. *J Appl Phys* 2012; 111(124107): 1-13.
55. Khanbarch H, Van Der Zwaag S, Groen WA. Effect of dielectrophoretic structuring on piezoelectric and pyroelectric properties of lead titanate-epoxy composites. *Smart Mater Struct* 2014; 23(105030): 1-11.
56. Hufenbach WA, Modler N, Winkler A, Ilg J, Rupitsch SJ. Fibre-reinforced composite structures based on thermoplastic matrices with embedded piezoceramic modules. *Smart Mater Struct* 2014; 23(025011): 1-10.
57. Heber T, Gude M, Hufenbach W. Production process adapted design of thermoplastic-compatible piezoceramic modules. *Composites Part A* 2014; 59: 70-77.
58. Giurgiutiu V. Electroactive and magnetoactive materials. In: Giurgiutiu V. *Structural Health Monitoring With Piezoelectric Wafer Active Sensors*. 2nd ed. Academic Press – Elsevier; 2014.
59. Su Z, Ye L. Selective generation of Lamb wave modes and their propagation characteristics in defective composite laminates. *Proc Instn Mech Engrs* 2004; 218: 95-110.
60. Ramadas C, Balasubramaniam K, Joshi M, Krishnamurthy CV. Interaction of guided Lamb waves with an asymmetrically located delamination in a laminated composite plate. *Smart Mater Struct* 2010; 19: 1-11.
61. Sherfat MH, Guitel R, Quaegebeur N, Lessard L, Hubert P, Masson P. Guided wave scattering behavior in composite bonded assemblies. *Compos Struct* 2016; 136: 696-705.
62. Ng CT, Veidt M. Scattering of the fundamental anti-symmetric Lamb wave at delaminations in composite laminates. *J Acoust Soc Am* 2011; 129(3): 1288-1296.
63. Memmolo V, Monaco E, Boffa ND, Maio L, Ricci F. Guided wave propagation and scattering for structural health monitoring of stiffened composites. *Compos Struct* 2018; 184: 568-580.
64. Raghavan A, Cesnik CES. Modeling of piezoelectric-based Lamb-wave generation and sensing for structural health monitoring. *Proc SPIE* 2004; 5391: 419-430.
65. Giurgiutiu V. Tuned Lamb wave excitation and detection with piezoelectric wafer active sensors for structural health monitoring. *J Intell Mater Syst Struct* 2005; 16: 291-305.
66. Sohn H, Lee SJ. Lamb wave tuning curve calibration for surface-bonded piezoelectric transducers. *Smart Mater Struct* 2010; 19(015007): 1-12.
67. Zhao X, Gao H, Zhang G, Ayhan B, Yan F, Kwan C, Rose JL. Active health monitoring of an aircraft wing with embedded piezoelectric sensor/actuator network: I. Defect detection, localization and growth monitoring. *Smart Mater Struct* 2007; 16: 1208-1217.
68. Moix-Bonet M, Wierach P, Loendersloot R, Bach M. *Damage Assessment in Composite Structures Based on Acousto-Ultrasonics – Evaluation of Performance*. In:

Wölcken P, Papadopoulos M, eds. *Smart Intelligent Aircraft Structures (SARISTU)*. Switzerland: Springer; 2016: 617-629.

69. Wandowski T, Malinowski PH, Ostachowicz WM. Circular sensing networks for guided waves based structural health monitoring. *Mech Syst Sig Process* 2016; 66-67: 248-267.
70. Salmanpour MS, Khodaei ZS, Aliabadi MH. Transducer placement optimisation scheme for a delay and sum damage detection algorithm. *Struct Contol Health Monit* 2017; 24(e1898): 2-20.
71. Shen Y, Giurgiutiu V. WaveFormRevealer: An analytical framework and predictive tool for the simulation of multi-modal guided wave propagation and interaction with damage. *Struct Health Monit* 2014; 13(5): 491-511.
72. Shen Y, Giurgiutiu V. Combined analytical FEM approach for efficient simulation of Lamb wave damage detection. *Ultrasonics* 2016; 69: 116-128.
73. Vargalui A. *Temperature effects on an acoustic emission based structural health monitoring system – Applied to composite materials*. Delft, The Netherlands: Delft University of Technology; 2015.
74. Tsai SW. *Composites Design*. 4th ed. Dayton, USA: Think Composites; 1988.
75. Meyer DR, Bersee HEN, Beukers A. Temperature effect on reinforced thermoplastic composite properties for primary aircraft structure applications. Paper presented at: 49th AIAA/ASME/ASCE/AHS/ASC Structures, Structural Dynamics, and Materials Conference; April 7-10, 2008; Schaumburg, IL, USA.
76. Bai Y, Keller T, Vallée T. Modeling of stiffness of FRP composites under elevated and high temperatures. *Compos Sci Technol* 2008; 68: 3099-3106.
77. Kijanka P, Radecki R, Packo P, Staszewski WJ, Uhl T. GPU-based local interaction simulation approach for simplified temperature effect modeling in Lamb wave propagation used for damage detection. *Smart Mater Struct* 2013; 22(035014): 1-16.
78. Giurgiutiu V, Postolache C, Tudose M. Radiation, temperature, and vacuum effects on piezoelectric wafer active sensors. *Smart Mater Struct* 2016; 25(035024): 1-25.
79. Gandhi N, Michaels JE, Lee SJ. Acoustoelastic Lamb wave propagation in biaxially stressed plates. *J Acoust Soc Am* 2012; 132(3): 1284-1293.
80. Dodson JC. *Guided Wave Structural Health Monitoring With Environmental considerations*. Blacksburg, USA: Virginia Polytechnic Institute and State University; 2012.
81. Banerjee S, Kundu T. Symmetric and anti-symmetric Rayleigh-Lamb modes in sinusoidally corrugated waveguides: An analytical approach. *Int J Solids Struct* 2006; 43(21): 6551-6567.
82. Radzienski M, Cao M, Wei X, Kudela P, Ostachowicz W. Combined vibration and guided wave-based approach for composite panels health assessment. *Proc SPIE* 2017; 10170(101702D): 1-8.
83. Alleyne DN, Cawley P. The interaction of Lamb waves with defects. *IEEE T Ultrason, Ferr* 1992; 39(3): 381-397.

84. Alleyne DN, Lowe MJS, Cawley P. The reflection of guided waves from circumferential notches in pipes. *J Appl Mech* 1998; 65: 635-641.
85. Diligent O, Lowe MJS. Reflection of the s_0 Lamb mode from a flat bottom circular hole. *J Acoust Soc Am* 2005; 118(5): 2869-2879.
86. Rajagopal P, Lowe MJS. Short range scattering of the fundamental shear horizontal guided wave mode normally incident at a through thickness crack in an isotropic plate. *J Acoust Soc Am* 2007; 122(3): 1527-1538.
87. Rajagopal P, Lowe MJS. Scattering of the fundamental shear horizontal guided wave by a part-thickness in an isotropic plate. *J Acoust Soc Am* 2008; 124 (5): 2895-2904.
88. Rajagopal P, Lowe MJS. Angular influence on the scattering of fundamental shear horizontal guided waves by a through-thickness crack in an isotropic plate. *J Acoust Soc Am* 2008; 124 (4): 2021-2030.
89. Ratassepp M, Lowe MJS, Cawley P, Klauson A. Scattering of the fundamental shear horizontal mode in a plate when incident at a through crack aligned in the propagation direction of the mode. *J Acoust Soc Am* 2008; 124(5): 2873-2882.
90. Dalton RP. *The Propagation of Lamb Waves Through Metallic Aircraft Fuselage Structure*. London, UK: Imperial College London; 2000.
91. Cerniglia D, Pantano A, Montinaro N. 3D simulations and experiments of guided wave propagation in adhesively bonded multi-layered structures. *NDT&E Int* 2010; 43: 527-535.
92. Ricci F, Mal AK, Monaco E, Maio L, Boffa ND, Di Palma M, Lecce L. Guided waves in layered plate with delaminations. Paper presented at: 7th EWSHM; July 8-11, 2014; Nantes, France.
93. Murat BIS, Khalili P, Fromme P. Impact damage detection in composite panels using guided ultrasonic waves. *AIP Conf Proc* 2014; 1581: 286-293.
94. Guo N, Cawley P. The interaction of Lamb waves with delaminations in composite laminates. *J Acoust Soc Am* 1993; 94(4): 2240-2246.
95. Castings M, Singh D, Viot P. Sizing of impact damages in composite materials using ultrasonic guided waves. *NDT&E Int* 2012; 46: 22-31.
96. Singh D, El Guerjouma R, Bentahar M. Interaction of fundamental Lamb modes with a point impact damaged zone in composite plates. Paper presented at: *Acoustics 2012 Nantes Conference*; April 23-27, 2012; Nantes, France.
97. De Luca A, Caputo F, Khodaei ZS, Aliabadi MH. Damage characterization of composite plates under low velocity impact using ultrasonic guided waves. *Composites Part B* 2018; 138: 168-180.
98. Memmolo V, Ricci F, Maio L, Boffa ND, Monaco E. Model assisted probability of detection for a guided waves based SHM technique. *Proc SPIE* 2016; 9805(980504): 1-12.
99. Courant R, Friedrichs K, Lewy H. On the partial difference equations of mathematical physics. *IBM J Res Dev* 1967; 11(2): 215-234.

100. Liu W, Datta SK, Shah AH. Transient scattering of Rayleigh-Lamb waves by surface-breaking and buried cracks in a plate. *Rev Prog Quant NDE* 1992; 11: 73-80.
101. Predoi MV, Castings M, Moreau L. Influence of material viscoelasticity on the scattering of guided waves by defects. *J Acoust Soc Am* 2008; 124(5): 2883-2894.
102. Gopalakrishnan S, Ruzzene M, Hanagud S. *Computational Techniques for Structural Health Monitoring*. London, UK : Springer; 2011.
103. Deng Q, Yang Z. Propagation of guided waves in bonded composite structures with tapered adhesive layer. *Appl Math Model* 2011; 35: 5369-5381.
104. Wieslaw O, Maciej R. Structural health monitoring by means of elastic wave propagation. *J Phys Conf Ser* 2012; 382(012003): 1-8.
105. Kim S, Lee U. Effects of delamination on guided waves in symmetric laminated composite beam. *Math Probl Eng* 2014; 956043: 1-12.
106. Khalili A, Samarutunga D, Jha R, Lacy TE, Gopalakrishnanrth S. Wavelet spectral finite element based user-defined element in ABAQUS for modelling delamination in composite beams. Paper presented at: *23rd AIAA/AHS Adaptive Structure Conference*; January 5-9 , 2015; Kissimmee, Florida, USA.
107. Song W, Rose JL, Galán JM, Abascal R. Ultrasonic guided wave scattering in a plate overlap. *IEEE T Ultrason, Ferr* 2005; 52(5): 892-903.
108. Janapati V, Kopsaftopulos F, Li F, Lee SJ, Chang FK. Damage detection sensitivity characterization of acousto-ultrasound-based SHM techniques. *Struct Health Monit* 2016; 15(2): 143-161.
109. Nadella KS, Cesnik CES. Local interaction simulation approach for modeling wave propagation in composite structures. *CEAS Aeronaut J* 2013; 4: 35-48.
110. Hashemiyan Z, Packo P, Kochanski W, Staszewski WJ, Uhl T, Verma P. Local interaction simulation approach vs. finite element modeling for fault detection in medical ultrasonic transducer. *Key Eng Mat* 2014; 588: 157-165.
111. Ambrozinski L, Packo P, Stepinski T, Uhl T. Ultrasonic guided waves based method for SHM – Simulations and experimental test. Paper presented at: *5th WCSCM* July 12-14, 2010; Tokyo, Japan.
112. Chinta PK, Kleinert W. Elastic wave modeling in complex geometries using elastodynamic finite integration technique. Paper presented at: *11th ECNDT*; October 6-10, 2014; Prague, Czech Republic.
113. Leckey CAC, Wheeler KR, Hafiychuk VN, Hafiychuk H, Timuçin DA. Simulation of guided-wave ultrasound propagation in composite laminates: Benchmark comparisons of numerical codes and experiment. *Ultrasonics* 2018; 84: 187-200.
114. Smith SW. *Digital Signal Processing: A Practical Guide for Engineers and Scientists*. Newness – Elsevier Science, 2nd edition, USA, 2003.
115. *Time Frequency Signal Analysis and Processing: A Comprehensive Reference*. Boualem Boashash (Ed.), Elsevier Ltd., 2003.

- 116.Staszewski WJ, Pierce SG, Worden K, Philip WR, Tomlinson GR, Culshaw B. Wavelet signal processing for enhanced Lamb-wave defect detection in composite plates using optical fiber detection. *Opt Eng* 1997; 36(7): 1877-1888.
- 117.Vasilescu G. *Electronic Noise and Interfering Signals – Principles and Applications*. Germany: Springer; 2005.
- 118.Smith SW. *Digital Signal Processing: A Practical Guide for Engineers and Scientists*. USA: Newnes – Elsevier; 2003.
- 119.Bianchi G, Sorrentino R. *Electronic Filter Simulation and Design*. USA: McGraw-Hill; 2007.
- 120.Chrysomallis MT, Sahalos JN. Filter synthesis using products of Legendre polynomials. *Electr Eng* 1999; 81: 419-424.
- 121.Li F, Meng G, Kageyama K, Su Z, Ye L. Optimal mother wavelet selection for Lamb wave analyses. *J Intel Mat Syst Str* 2009; 20: 1147-1161.
- 122.Niethammer M, Jacobs LJ. Time-frequency representations of Lamb waves. *J Acoust Soc Am* 2011; 105(5): 1841-1847.
- 123.Liu Z, Sun K, Song G, He C, Wu B. Damage localization in aluminium plate with compact rectangular phased piezoelectric transducer array. *Mech Syst Signal Pr* 2016; 70-71: 625-636.
- 124.Rébillat M, Hmad O, Kadri F, Mechbal N. Peaks over threshold-based detector design for structural health monitoring: Application to aerospace structures. *Struct Health Monit* 2018; 17(1): 91-107.
- 125.Pant S, Martinez M, Yanishevsky M, Backman D. Damage detection methodology for structural health monitoring (SHM) application based on multi-frequency anti-symmetric guided waves. Paper presented at: 9th EWSHM; July 10-13, 2018; Manchester, UK.
- 126.Croxford AJ, Moll J, Wilcox PD, Michaels JE. Efficient temperature compensation strategies for guided wave structural health monitoring. *Ultrasonics* 2010; 50: 517-528.
- 127.Lu Y, Michaels, JE. A methodology for structural health monitoring with diffuse ultrasonic waves in the presence of temperature variations. *Ultrasonics* 2005; 43: 717-731.
- 128.Dworakowski Z, Ambrozinski L, Stepinski T. Multi-stage temperature compensation method for Lamb wave measurements. *J Sound Vib* 2016; 382: 328-339.
- 129.Moix-Bonet M, Eckstein B, Wierach P. Temperature compensation for damage detection in composite structures using guided waves. Paper presented at: 9th EWSHM; July 10-13, 2018; Manchester, UK.
- 130.Fendzi C, Rébillat M, Mechbal N, Guskov M, Coffignal G. A data-driven temperature compensation approach for structural health monitoring using Lamb waves. *Struct Health Monit* 2016; 15(5): 525-540.
- 131.Ambrozinski L, Magda P, Dragan K, Stepinski T, Uhl T. Temperature compensation based on Hilbert transform and instantaneous phase for Lamb waves-based SHM

systems of aircraft structures. Paper presented at: 9th IWSHM; September 10-12, 2013; Palo Alto, USA.

132. Roy S, Lonkar K, Janapati V, Chang FK. A novel physics-based temperature compensation model for structural health monitoring using ultrasonic guided waves. *Struct Health Monit* 2014; 13(3): 321-342.
133. Farrar CR, Worden K. *Structural Health Monitoring: A Machine Learning Perspective*. UK: John Wiley & Sons, 2013.
134. Guskov M, Rébillat M, Mechbal N, Balmes E. A characterization framework for simulation-based LWSHM algorithms. Paper presented at: 9th EWSHM, July 10-13, 2018; Manchester, UK.
135. Michaels JE. Detection of structural damage from the local temporal coherence of diffuse ultrasonic signals. *IEEE T Ultrason, Ferr* 2005; 52(10): 1769-1782.
136. Choi K, Keilers Jr CH, Chang FK. Impact damage detection in composite structures using distributed piezoceramics. Paper presented at: 35th AIAA/ASME/ASCE/AHS/ASC Structures, Structural Dynamics, and Materials Conference; April 18-20, 1994; South Carolina, USA.
137. Dziendzikowski M, Kurnyta A, Dragan K, Klysz S, Leski A. In situ barely visible impact damage detection and localization for composite structures using surface mounted and embedded PZT transducers: A comparative study. *Mech Syst Signal Pr* 2016; 78: 91-106.
138. Janapati V, Yadav SK, Kumar A, Ikegami R, Habtour E. Fatigue crack quantification approach based on multi-path unit-cell concept in sensor network. Paper presented at: 8th EWSHM; July 5-8, 2016; Bilbao, Spain.
139. Yadav SK, Chung H, Kopsaftopoulos F, Chang FK. Damage quantification of active sensing acousto-ultrasound-based SHM based on a multi-path unit-cell approach. Paper presented at: 11th IWSHM; September 12-14, 2017; Palo Alto, CA, USA.
140. MIL-HDBK-1823A. Nondestructive Evaluation System Reliability; Department of Defence USA; April 2009.
141. Cobb AC, Michaels JE, Michaels TE. Ultrasonic structural health monitoring: a probability of detection case study. *AIP Conf Proc* 2009; 1096: 1800-1807.
142. Cobb AC, Fisher J, Michaels JE. Model-assisted probability of detection for ultrasonic structural health monitoring. Paper presented at: 4th European-American Workshop on Reliability of NDE; June 24-16, 2009; Berlin, Germany.
143. Thompson RB. A unified approach to the model-assisted determination of probability of detection. *AIP Conf Proc* 2008; 975: 1685-1692.
144. Aldrin JC, Medina EA, Lindgren EA, Buynak C, Steffes G, Derriso M. Model-assisted probabilistic reliability assessment for structural health monitoring systems. *AIP Conf Proc* 2010; 1211: 1965-1972.
145. Aldrin JC, Medina EA, Lindgren EA, Buynak CF, Knopp JS. Protocol for reliability assessment of structural health monitoring systems incorporating model-assisted

- probability of detection (MAPOD) approach. Paper presented at: 8th *IWSHM*; September 13-15, 2011; Palo Alto, CA, USA.
146. Aldrin JC, Medina EA, Lindgren EA, Buynak CF, Knopp JS. Case studies for model-assisted probabilistic reliability assessment for structural health monitoring systems. *AIP Conf Proc* 2011; 1335: 1589-1596.
147. Aldrin JC, Medina EA, Santiago J, Lindgren EA, Buynak CF, Knopp JS. Demonstration study for reliability assessment of SHM systems incorporating model-assisted probability of detection approach. *AIP Conf Proc* 2012; 1430: 1543-1550.
148. Shook BD, Millwater HR, Enright MP, Hudak Jr SJ, Francis WL. Simulation of recurring automated inspection on probability-of-fracture estimates. *Struct Health Monit* 2008; 7(4): 293-307.
149. Kabban CMS, Greenwell BM, DeSimio MP, Derriso MM. The probability of detection for structural health monitoring systems: Repeated measures data. *Struct Health Monit* 2015; 14(3): 252-264.

3

Methodology

The underlying principle of the work in this thesis is that the improvement in reliability of GW-SHM systems for composite aircraft implies, on the one hand, gaining knowledge about GW interactions at different levels of structural complexity, and, on the other hand, developing systematic approaches for the deployment of the monitoring capabilities. This chapter explains the framework devised to incorporate the aforementioned principle and to address the research questions. The methods employed in the research process are also described. The methodological details that are specific to the different studies are described in the corresponding chapters.

3.1. Research process

For convenience, the research questions formulated at the end of the previous chapter are repeated below:

- Q1) How does the internal structure of the ultrasonic weld influence the propagation of ultrasonic guided waves through a thermoplastic composite joint?
- Q2) How can the multiple parameters controlling the coupled physics of GW transducing be systematically integrated in the design of SHM system for a real-scale composite aircraft primary structure?
- Q3) What is the reliability of a GW-SHM system in diagnosing BVID in a real-scale composite stiffened panel in the scenario of a defective transducer?
- Q4) How does high-amplitude low-frequency structural vibrations affect ultrasonic GW propagation?

The building block approach (shown in Figure 3.1) was adopted to guide the research process in order to ensure that developments at each complexity level are based on conclusions from the one below. This enabled the SHM system to be developed in a consistent and robust way, without losing track of the physics of the problem while being aware of the feasibility challenges for each complexity level.

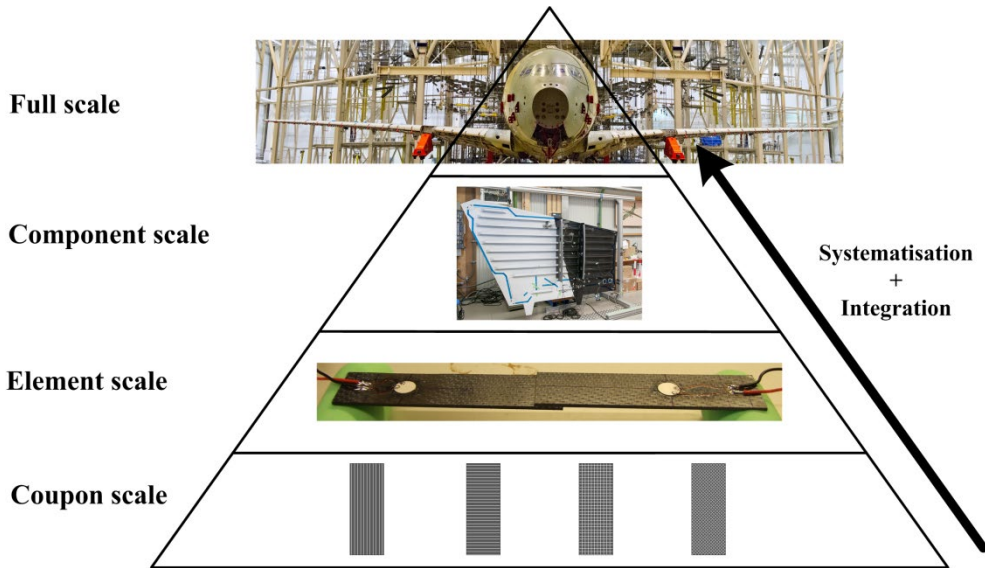


Figure 3.1 Building block used for the research framework.

The studies conducted to address research question Q1) involved testing ultrasonic welds, which are considered as structural *elements*. Although they had coupon size, they consisted of parts joined together and thus had a scale of structural complexity above that of material *coupon* testing.

The research focused on *element* scale was limited in addressing the complexity of the ultrasonic GW scatter field encountered in real structures. So, although it is possible to

“get away” without actually designing the monitoring system for the GW tests on small *element*-scale joints, the diagnostic at real scale (1:1) is strongly influenced by the transducer parameters and network configuration, mainly because propagation distances are much larger and the complexity of the scatter field is much higher. Therefore, to go up in complexity, systematisation and integration were necessary. To that end, question Q2) was addressed by focusing on the development of a novel methodology for designing the GW-SHM system.

With the findings from question Q2), an SHM system was designed for a *component*-level structure. That structure was a 1:1 (*real* scale) demonstrator of a stiffened panel of a torsion box, with *real* dimensions and complexity. It is important to highlight that throughout this thesis the “*component*-scale panel” is often referred to as the “*real*-scale panel” in order to emphasise that, although the term *full*-scale could not be used because the boundary conditions did not represent the complete assembly of the structure, the dimensions and geometric complexity were exactly the same as those found at full scale.

The validation of the novel GW-SHM system design methodology was then conducted on the *component*-scale structure in two phases. Firstly, a reliability analysis of the SHM system was performed (research question Q3)) by resorting to a model-assisted approach, for which an approximate numerical model of a critical part of the structure was built. Secondly, by demonstrating the capabilities of the SHM system for detecting BVID of different severities and in different critical locations.

For the second validation phase, it was important to make the connection with the findings at *element* scale. The research at *element* scale was important for understanding the effect of weld line thickness variations and the effect of manufacturing defects on the transmission of GWs across ultrasonically welded TpC joints. Since the fusion bonding in both ultrasonically welded joints and co-consolidated joints works through the mechanism of molecular interdiffusion, the physical principles behind the diagnostic approach developed at *element* scale were therefore transferred to *component* scale for detecting BVID in the co-consolidated joints of the stiffened panel of the horizontal stabiliser torsion box.

The study to answer question Q4) was conducted on the aforementioned *component*-scale torsion box panel, which was in this case subjected to realistic LFV. The modelling approach developed for the model-assisted reliability analysis was also employed to further understand the relationship between GW and LFV parameters.

In the pursuit of systematization across all structural complexity scales, the algorithms for processing the signals obtained from experiments and models were always the same (see Figure 3.2). It is important to highlight that the research was not focused on developing new signal processing algorithms, but on making a new, more robust application of existing ones.

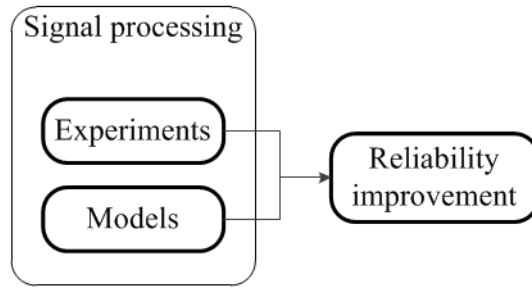


Figure 3.2. Articulation of the research activities across all structural complexity levels.

3

3.2. Experiments

3.2.1. Element scale

Thermoplastic composite plates were manufactured from Cetex® five harness satin weave carbon fibre (CF) fabric reinforced polyphenylene sulphide (PPS) semipreg material, supplied by Ten Cate Advanced Composites [1]. The mechanical properties are summarised in Table 3.1. Six layers were stacked according to the $[0^\circ/90^\circ]_{3s}$ sequence, where 0° and 90° correspond to the warp and weft directions, respectively. The stack was subjected to 320°C and 10 bar for 15 min.

Table 3.1. Mechanical properties of the CF/PPS material used for the element scale specimens [1,2].

E_{11} [GPa]	E_{22} [GPa]	E_{33} [GPa]	G_{12} [GPa]	G_{13} [GPa]	G_{23} [GPa]	ν_{12}	ν_{13}	ν_{23}	ρ [kg/m ³]
56.5	56.4	10.5	4.3	3.1	3.1	0.08	0.41	0.41	1600

After manufacturing, the plates were water-jet cut into adherends with nominal dimensions of $101.6\text{ mm} \times 25.4\text{ mm} \times 1.62\text{ mm}$ (longest dimension parallel to the 0° direction of the laminate), as shown in Figure 3.3. A clamping tool (see Figure 3.4) was used to ensure the overlap had a nominal length of 12.7 mm (according to standard ASTM D1002 [3]), while preventing undesirable movement of the samples during the ultrasonic welding process.

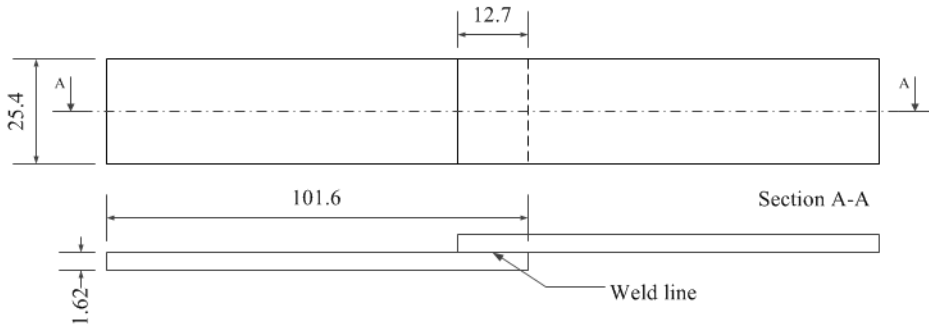


Figure 3.3. Single-lap joint produced by ultrasonic welding and tested with ultrasonic GWs (dimensions in mm).

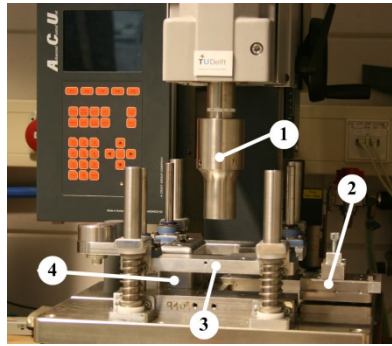


Figure 3.4. Ultrasonic welding setup: 1) sonotrode, 2) top clamp, 3) upwards-sliding frame for top clamp, 4) bottom clamp.

To gain the understanding of GW interaction with TpC ultrasonic welds necessary to provide a complete answer to research question Q1), two studies were conducted, one with only pristine joints, and one with defective joints, which required different ED types for the welding. The PZT transducers for GW testing were bonded onto the upper surface of the adherends, with the actuator and sensor on opposite sides of the joint (pitch-catch configuration). Details about the GW test setup and EDs employed for each of the studies can be found in Chapters 4 and 5.

3.2.2. Component scale

A component-scale horizontal stabilizer torsion box panel entirely made of carbon fibre (CF) reinforced polyetherketoneketone (PEKK) was made available by Fokker Aerostructures BV for the SHM tasks of the Thermoplastic Affordable Primary Aircraft Structure 2 (TAPAS 2) project. The CF/PEKK composite material properties are listed in Table 3.2. The structure had real-scale (1:1) dimensions and complexity, and consisted of a co-consolidated stiffened skin with multiple I-stringers in butt-joint configuration, and two riveted ribs, as depicted in Figure 3.5. The panel had a maximum length and width of about 2.9 and 1.7 m, respectively, with skin thickness varying between 1.8 and 8.1 mm, and rib thickness between 3 and 3.5 mm.

Table 3.2. Mechanical properties of the CF/PEKK composite material used for the horizontal stabilizer torsion box panel, as provided by Fokker Aerostructures BV.

E_{11} [GPa]	E_{22} [GPa]	E_{33} [GPa]	G_{12} [GPa]	G_{13} [GPa]	G_{23} [GPa]	ν_{12}	ν_{13}	ν_{23}	ρ [kg/m ³]
141	10.4	10.4	5.46	5.46	3.32	0.30	0.30	0.45	1560

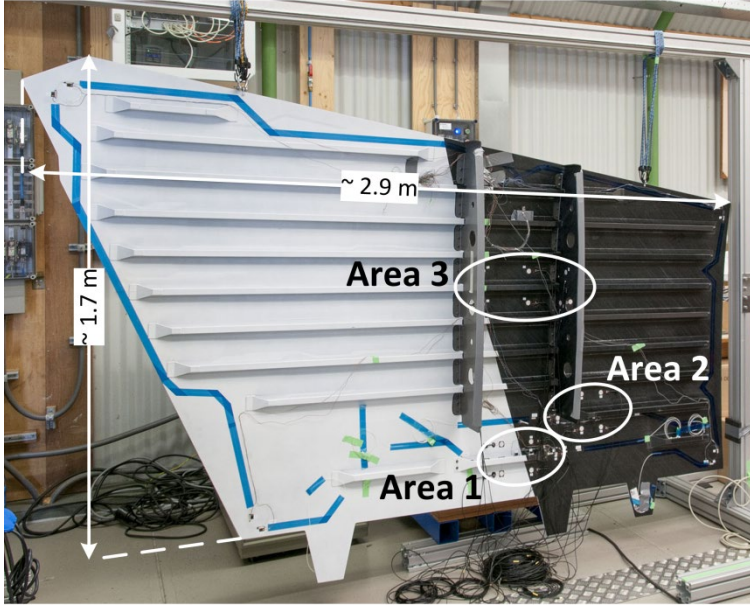


Figure 3.5. Horizontal stabilizer torsion box stiffened panel, with the three critical areas highlighted.

According to the manufacturer, the torsion box panel had to be able to withstand a low-energy impact at the outer side of the stringer-skin joint without showing a delamination (or disbond) area (see Figure 3.6) larger than 100 mm² and without showing visible cracks on the surface of the joint fillet radius. Given that the I-stringer thickness was 3 mm, Fokker Aerostructures BV defined the critical disbond length (i.e. disbond before reaching the maximum allowable area of 100 mm²) to be equal to 20 mm. For this reason the three critical areas highlighted in Figure 3.5 were selected for the monitoring studies. The ply stacking sequence for the composite skin of the critical areas was symmetric and quasi-isotropic, as in the approximate version of the layup presented in Table 3.3.

The proposed methodology for designing the GW-SHM system in a systematic way (research question Q2)) was validated during a component-scale test campaign by evaluating the performance in diagnosing realistic BVID. The effects of LFV on GW propagation (research question Q4)) were studied during that same test campaign. The instrumentation and setup used for the GW tests performed on the torsion box panel are described in detail in Chapter 8.

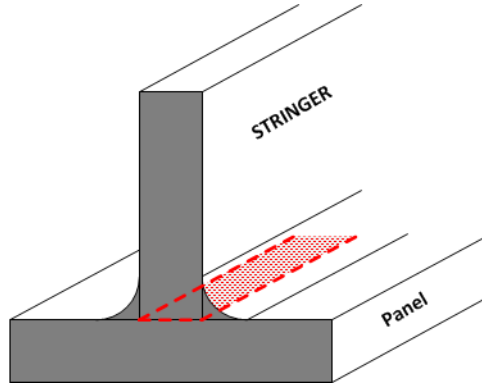


Figure 3.6. Definition of the stringer delamination (or disbond) area (delimited by dashed line).

Table 3.3. Approximate composite ply stacking sequence for the skin of each critical area.

Area	Ply thickness [mm]	Ply fibre orientation [°]
1 and 2	[0.53/0.53/0.80/0.65] _s	[135/45/0/90] _s
3	[0.28/0.28/0.55/0.41] _s	

3.2.3. Extra tests

Extra GW tests were conducted at multiple frequencies on a flat plate made of aluminium 6082 alloy, with nominal dimensions of 1500 mm × 900 mm × 1.5 mm. The acquired data was used for validating part of the numerical models (see Section 3.3) and for testing multiple signal processing algorithms (see Section 3.4).

3.3. Models

An approximate three-dimensional FE model of critical area 3 of the torsion box was constructed in order to allow a reliability analysis of the designed SHM system, and hence address research question Q3). The damage scenario considered was that of BVID at the stringer-skin joint. The determination of the POD curve was based on varying some parameters directly related to the transducer network, together with the damage size, and by adding random intra-measurement variability to the DI points generated from the numerical signals. The implementation of the statistical methods is explained in Chapter 7.

Also as explained in detail in Chapter 7, the model was developed in an incremental way. First, the approach for simulating the ultrasonic excitation was validated by comparison with GW signals acquired on a flat aluminium plate (see Section 3.2.3). Then, the GW signals collected during the studies on TpC ultrasonic welds were used to validate the simulation approach for the composite laminate.

3.4. Signal processing

The SHM framework briefly presented in Section 2.7 should not be seen as a means to replace detailed NDT inspections. By looking at the SHM system requirements, one

reaches the conclusion that for SHM systems to achieve the same level of detail in damage characterisation as NDT techniques, would require a tremendously large number of transducers (i.e. a very *dense* transducer networks). This would entail high power consumption, considerable additional weight on the aircraft, and huge amounts of data which would have to be either stored or transmitted by telemetry. Instead the implementation of SHM should aim at optimising the maintenance programme by deploying a *sparse* transducer network capable of providing with reliable quantitative indication about the condition of areas of the aircraft primary structure that are critical for the load bearing capabilities, especially those with difficult access. When the DI reached a certain threshold, an advice would be issued to direct NDT inspections in a more efficient way. This approach is sometimes denominated as *hot-spot* monitoring.

Research on GW-SHM (see Sections 2.4 to 2.6) has shown it is very difficult to acquire a full and exact description of damage (type, size, location) with *sparse* transducer networks. This is even more true in the case of composite structures, where the direction-dependence and the coupling of the GW modes makes it practically (almost) impossible to separate the different GW modes in the acquired signal [4]. Adding this to the fact that coupled GW modes and reflections end up overlapping, one can conclude that it is pointless to try to observe changes in individual modes and correlate them to the presence of specific damage types. The focus should be on generating *accurate-enough* quantitative measures of damage that indicate its presence within the monitored area and show a monotonic evolution with damage severity.

It is necessary to adopt a realistic and feasible protocol for GW based damage diagnostic. For this purpose, the signal processing approaches employed in this thesis are said to be *minimalist* or *high-level*. They are *minimalist* because they do not resort to sophisticated signal processing that is able to extract information only in very simplistic structural scenarios (e.g. flat plate). In other words, they keep the algorithm complexity level at a minimum, so that the diagnostic capabilities are deployable in the largest possible diversity of cases, and the SHM system reliability is increased. The intended reliability increase is expected to be achieved at the expense of some spatial resolution in damage localisation, as damage is detected and quantified at the *high-level* of the critical area. But it is still possible to keep precision below the metre and to obtain a diagnostic map of all the monitored areas in the aircraft. In short, this thesis considers only the detection of the existence and the quantification of the severity of damage.

The signal processing in this research was based on existing algorithms, as described in Section 2.6. The DIs were based on the formulas provided in Section 2.6.4. Bandpass filtering based on the CWT was applied only to make sure that the diagnostic signals were not contaminated with frequencies outside the ultrasonic excitation spectrum. In order to establish a criterion for the selection of the wavelet function, a study was conducted on GW signals acquired from experiments on an aluminium plate (see Section 3.2.3) and on TpC ultrasonically welded joints (see Section 3.2.1). For all the signals, the normalized Shannon entropy of the wavelet coefficients (EWC) at scale a was computed as [5]:

$$EWC(a_w) = \sum_{i=1}^N \left(\frac{w_{a,i}^2}{A} \right) \cdot \ln \left(\frac{w_{a,i}^2}{A} \right) \quad (3.1)$$

with $A = \sum_{a=1}^{\max a_w} \sum_{i=1}^N w_{a,i}^2$, and where $w_{a,i}$ denotes the wavelet coefficient of the i^{th} signal point at scale a_w , $\max a_w$ is the maximum scale, and N is the length of the signal.

The value of EWC gives a measure of the degree or disorder of the wavelet decomposition process. According to Li et [5], the higher the concentration of the process energy, the lower the entropy. Thus, the wavelet that allows the lowest EWC valley should be the optimal one. While trying all the different types of wavelet functions allowed by the *cwt* function of MATLAB 2016b with varying wavelet centre frequency (recall the relationship $f_a = f_c/a_w$ between the scale a_w , the frequency corresponding to scale a_w , f_a , and the wavelet centre frequency f_c), it was observed that the value of the EWC valley always decreased with increasing wavelet centre frequency. This meant that minimisation of the EWC valley could not be the only selection criterion.

Furthermore, it was also noticed that there was a deviation between the frequency at which the EWC valley occurred and the main frequency of the signal, and that this deviation was different for different wavelet functions and for different wavelet centre frequencies. Such a deviation means the CWT energy is concentrated at a frequency which is not exactly the same as the main signal frequency. As a result, the wavelet with the lowest EWC valley does not necessarily allow for the best time resolution. Therefore, the criterion for selecting the optimal wavelet was changed such that the EWC valley had a low value, and the deviation between the EWC valley frequency and the main signal frequency was minimum.

The improved selection criterion was then applied to all the experimental signals, and it was observed that the smallest EWC valley frequency deviation was always for the Morlet wavelet with centre frequency equal to the Nyquist frequency. Thus, this was the wavelet function that was selected for CWT filtering in this research

3.5. Revisiting the thesis chapter order

Since the building block approach plays an important role in guiding the research process of this thesis, it was decided to organise the chapters so that they follow the progression of structural complexity scales. Chapters 4 and 5 focus on GW propagation in element scale TpC ultrasonic welds. The bridge to real-scale (1:1) structures is made in Chapter 6, where a novel methodology is proposed for designing a GW-SHM system in a systematic way. The reliability of the SHM system designed for the component-scale torsion box panel is then analysed in Chapter 7. Finally, the component-scale test campaign is presented in Chapter 8, covering the validation of the SHM system design methodology and addressing the effects of high-amplitude low-frequency structural vibrations on GW propagation.

References

1. TenCate Cetex TC1100 PPS Resin System, TenCate Advanced Composites, Product Datasheet Revised 05/2014.
2. Daggumati S, De Baere I, Van Paepegem W, Degrieck J, Xu J, Lomov SV, Verpoest I. Local damage in a 5-harness satin weave composite under static tension: part II - Meso-FE modelling. *Compos Sci Technol* 2010; 70: 1934-1941.
3. ASTM D1002-10, Standard Test Method for Apparent Shear Strength of Single-Lap-Joint Adhesively Bonded Metal Specimens by Tension Loading (Metal-to-Metal), 2010.

4. Putkis O, Dalton RP, Croxford AJ. The anisotropic propagation of ultrasonic guided waves in composite materials and implications for practical applications. *Ultrasonics* 2016; 65: 390-399.
5. Li F, Meng G, Kageyama K, Su Z, Ye L. Optimal mother wavelet selection for Lamb wave analyses. *J Intel Mat Sys Str* 2009; 20: 1147-1161.

4

GWs in TpC ultrasonic welds: Effect of welding travel

This chapter presents an experimental study about the influence of welding travel (i.e. the vertical displacement of the sonotrode) on the transmission of GWs across ultrasonically welded TpC joints in single-lap configuration. The main aim was to start to understand how GWs interact with the pristine internal structure of ultrasonic welds, so that benign, manufacturing-related structural features can be distinguished from damaging ones in signal interpretation.

A fully experimental approach based on surface-mounted PZT transducers was adopted to test specimens produced with three different welding conditions, at two excitation frequencies. The power transmission coefficient and the correlation coefficient were investigated for their ability to perform quantitative identification of small variations of weld line thickness and molecular interdiffusion at the weld interface. The GW test results were compared with ultrasonic phased-array inspections to provide extra insight on the internal structure of TpC ultrasonic welds.

4.1. Introduction

As discussed in Section 2.9, it is not yet understood how the internal structure of the ultrasonic weld influences the propagation of ultrasonic GWs through a TpC joint (research question Q1)). Villegas [2] showed that different welding travel values directly result in different weld line thicknesses. However, when welds produced with different travels are tested for lap shear strength, different features are also observed on the fracture surface. This seems to indicate that travel also affects the effectiveness of molecular interdiffusion between the resin-rich weld line and the adherends, which is attributed to different reputation times (i.e. time available for the thermal motion of the entangled polymeric molecules).

If UW is to be used for joining TpC components in aircraft primary structures, intrinsic variability resulting from the manufacturing/assembly process could potentially come from different final overlap thickness. Therefore, it was decided to address research question Q1) incrementally, by starting with a study of the transmission of GWs across pristine overlaps produced with different UW travel.

4

4.2. Test specimen manufacturing

Three groups of five TpC joints were produced with distinct welding travel values. By simply varying the welding travel, and assuming there was no difference in heating and cooling rates, the clearest resulting change would be the amount of ED that was squeezed out of the overlap, and hence the weld line thickness. Additionally, some differences in molecular interdiffusion at the welding interface were expected, as mentioned in Section 4.1.

The material, stacking sequence and consolidation procedure of the TpC plates used for the adherends were described in Section 3.2.1. The selection of the welding process parameters for each specimen batch was based on research conducted by Villegas [2,3] and Villegas et al. [4], which has been introduced in Section 2.2. It was decided to adopt the welding condition that would lead to the maximum lap shear strength as the reference case (which would later be used to acquire the baseline response). Two other conditions were chosen such that they would cover the welding stage during which the ED is molten and starts to flow. The first one is around the beginning of the travel and power increase, and the second one is between the first and the reference points.

Based on experience acquired by Villegas [2,3], the nominal thickness of the flat PPS ED was chosen to be 0.25 mm, and a force and vibration amplitude of 500 N and 86.2 μm were used, respectively. Within these specifications, a first weld was produced with a travel equal to the ED thickness, in order to obtain the full travel-power curves (extracted from the UW machine) which are depicted in Figure 4.1. With the region of maximum power ending at around 440 ms (point of maximum lap shear strength), and the beginning of the travel increase before 300 ms, the three welding travels to be investigated were defined to be at 0.12, 0.08 and 0.02 mm (batches 1, 2 and 3, respectively, in Figure 4.1). Keeping the same force and vibration amplitude regimes, and using the 0.25 mm thick ED, three batches of five welded joints were manufactured with the three different travel values.

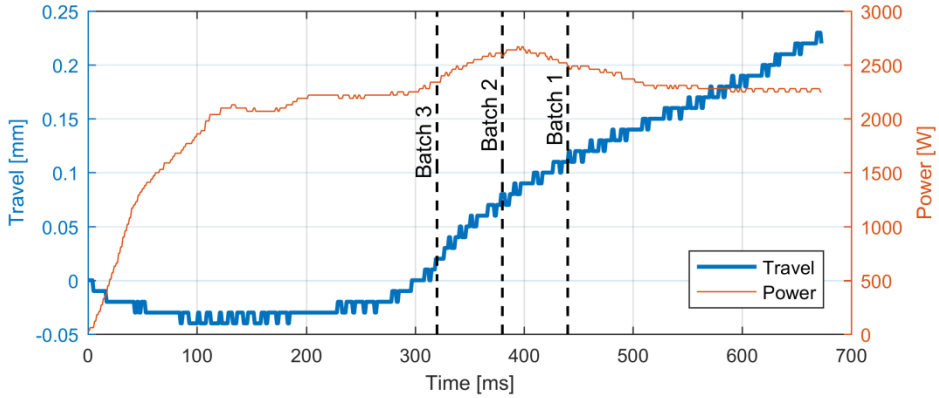


Figure 4.1. Ultrasonic welding curves used for process parameter selection.

It is important to note that in the UW procedure used for this research the adherends have to be tightly clamped inside a metal fixture, which is not compatible with having the piezoelectric transducers installed on the adherend surface. This imposes strong limitations in the definition of the baseline, because the same specimen cannot be welded with one travel value, Lamb wave tested, and then welded with another larger travel value. Therefore, it was not possible to have a “pure” baseline. However, since it has been proven possible to use UW to produce TpC joints in a controlled and repeatable way [2-4], it was considered appropriate to have three batches of five joints, with those belonging to the group of 0.12 mm welding travel functioning as the reference state.

4.3. GW testing

4.3.1. Model of dispersive properties

The selection of the excitation regime for the GW interrogation required first an analysis of the dispersive properties of the different material systems under research. To this end, the phase and group velocity curves were traced using the DISPERSE v2.0.20a software (Imperial College, London), in which the propagation domain had to be simulated. The woven CF/PPS adherends were modelled as an infinite 1.62 mm thick fully anisotropic plate in vacuum, with the elastic moduli, Poisson’s ratios and density as defined by Daggumati et al. [5] (see Table 3.1). The joints (i.e. overlaps) were modelled as infinite layered constructions composed of two 1.62 mm thick CF/PPS plates (with the same properties as before), and one fully connected layer in between representing the weld line, as represented in Figure 4.2.

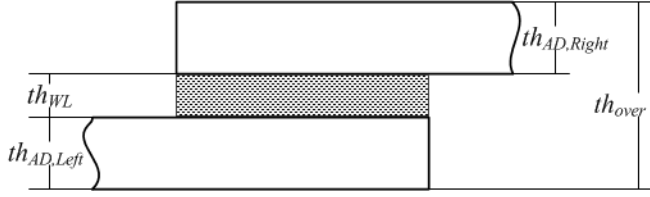


Figure 4.2. Overlap cross-section diagram, with a graphical definition of the variables in Equation (4.1).

It is important to note that the programme did not allow molecular interdiffusion between the weld line and the adherends to be taken into account. As mentioned before, all the weld line properties were considered to be unaffected by the travel variation except for its thickness. So, the weld line for each welding condition was modelled as a layer of isotropic material with the elastic properties of the PPS neat resin [6] and the thickness, th_{WL} , calculated according to:

$$th_{WL} = \overline{th}_{over} - \overline{th}_{AD,Left} - \overline{th}_{AD,Right} \quad (4.1)$$

where $\overline{th}_{AD,Left}$ and $\overline{th}_{AD,Right}$ denote the mean measured thickness of the left-hand-side and right-hand-side adherends, respectively, and \overline{th}_{over} is the mean measured thickness of the overlaps, (listed in Table 4.1 and Table 4.2).

Table 4.1. Measured dimensions of adherends and energy directors.

	Adherend thickness, th_{AD} [mm]		ED thickness [mm]
	Left	Right	
Avg.	1.62	1.63	0.23
StD.	0.02	0.01	0.01

Table 4.2. Measured overlap dimensions and weld line thicknesses used in the model.

Travel, tr [mm]	Overlap thickness, th_{over} [mm]		Calculated weld-line thickness, th_{WL} [mm]
	Avg.	StD.	
0.12	3.28	0.01	0.03
0.08	3.32	0.01	0.07
0.02	3.37	0.01	0.12

The obtained dispersion curves of the adherends are as shown in Figure 4.3. The phase velocity curves of the different joint overlaps are compared in Figure 4.4.

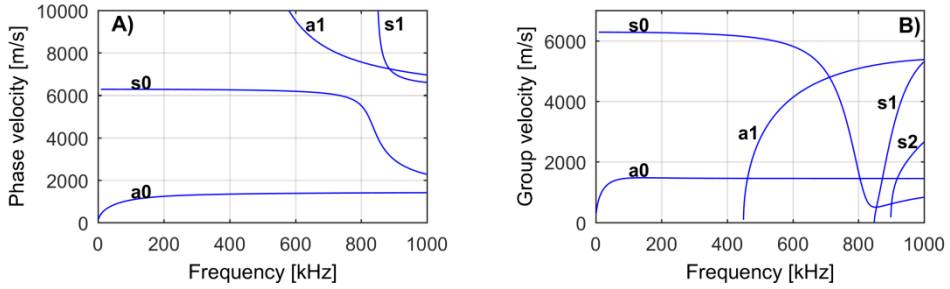


Figure 4.3. Dispersion curves for the single CF/PPS adherends: A) phase velocity; B) group velocity. The visualisation of the cut-off of the a1 mode is more accurately represented in b), because the y limit of 10000 m/s in a) is too low to show the a1 phase velocity tending to infinity.

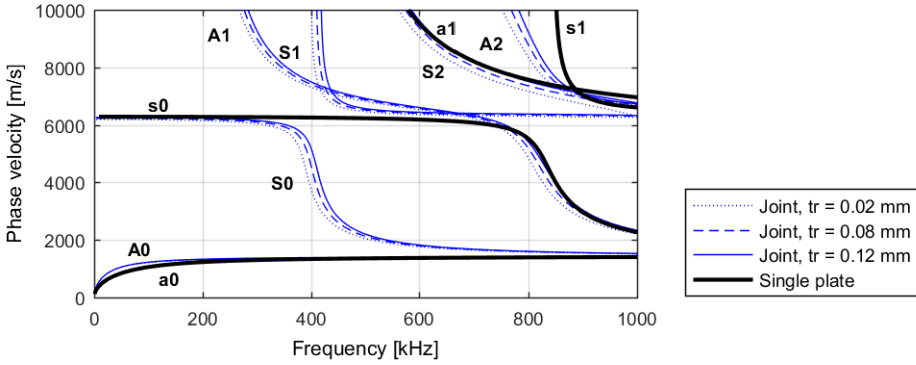


Figure 4.4. Phase velocity dispersion curves for the different systems (adherend modes indicated in small letters, overlap modes indicated in capital letters).

4.3.2. Definition of the GW excitation

In the specific scope of this study, it was important to try to establish correlations between the excited modes, their interaction with the structural discontinuities and how the GW modes were transmitted across the single-lap joint. Thus, the choice of the GW excitation frequency followed similar criteria to those adopted by Lowe et al. [7] in order to minimize the number of test variables and thereby enhance signal interpretation. Firstly, the signal should be as simple as possible, which means the frequency range should only allow the minimum number of guided modes to be excited. Secondly, the signal shape should be as independent from the propagation distance as possible, in order to isolate the variables related to the transformation taking place at the joint. Therefore, the modes should be as non-dispersive as possible. Additionally, the excited wavelengths should be small enough to prevent the waves from being in the standing regime. Taking this into account, the first candidate frequencies can be selected. From Figure 4.3a) and Figure 4.3b) it is possible to observe that below 450 kHz (1st cut-off) only the zero-order modes can be excited in the simple adherends and that their dispersion is low (as seen from their low slope at that frequency). One could then select a range of candidate excitation frequencies, between 200 and 450 kHz.

To ensure that the main excitation was below the 1st cut-off in both the adherend and the joint cross-section, a frequency of 200 kHz was selected. However, higher-order carrier modes can play an important role in the transmission of energy across the joint [7,8]. Therefore, it was decided to use a second excitation frequency of 250 kHz to allow the A1 carrier-mode to occur in the overlap. While this value remains below the first cut-off in the adherend, it is slightly above the 1st cut-off in the overlap, as shown in Figure 4.4. The excitation signals used were sinusoidal tone-bursts with five cycles and Hanning amplitude-modulation. These choices allowed a compromise between narrow frequency band and duration, i.e., a compromise between the number of parasitic frequencies and the level of overlapping of the zero-order modes.

At the time of this study, the only suitable, available piezo-ceramic transducer were wafers which were 0.4 mm thick, 8 mm wide and 16 mm long, made from APC 850 material, supplied by APC International Ltd. Because the longer the main vibration dimension, the stronger the piezoelectric response of the transducer, it was decided to use the length as the dimension parallel to the wave propagation direction.

4

4.3.3. Test setup

The test configuration selected for this study is illustrated by the diagram of Figure 4.5, in which the single-lap joint introduced in Section 3.2.1 is shown together with the actuation and sensing positions.

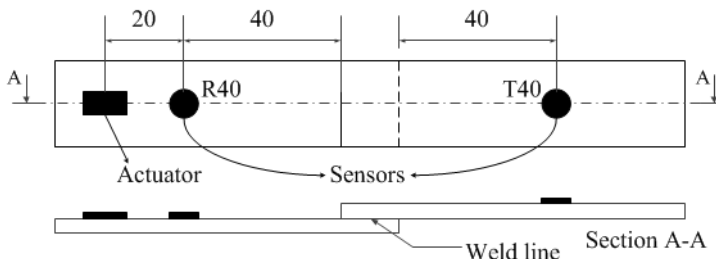


Figure 4.5. Diagram of the test specimen, with transducer positions (dimensions in mm). The waves reflected from the overlap were acquired at position R40, the wave transmitted across the overlap were acquired at position T40.

GW tests were conducted according to the set-up shown in Figure 4.6. An Agilent 33500B arbitrary waveform generator was used to create five-cycle sinusoidal tone-bursts modulated by a Hanning amplitude window with a maximum value of 8 V. These signals were transmitted to the specimens at 200 and 250 kHz by APC 850 piezo-ceramic 16 mm × 8 mm × 0.4 mm wafers glued to one of the adherends with cyanoacrylate, 60 mm away from the overlap (see Figure 4.5). The ultrasonic responses (available in [9]) were captured by two Mistras WSc general purpose wideband sensors placed 40 mm before and after the overlap. The main propagation direction was considered to be parallel to the length of the specimens, and therefore along the warp direction of the composite fabric (see Subsection 3.2.1). The sensors were coupled to the specimens by Sonotech shear gel and small mechanical clamps, and directly connected to a PicoScope 6402A digital oscilloscope which was operated by a computer.

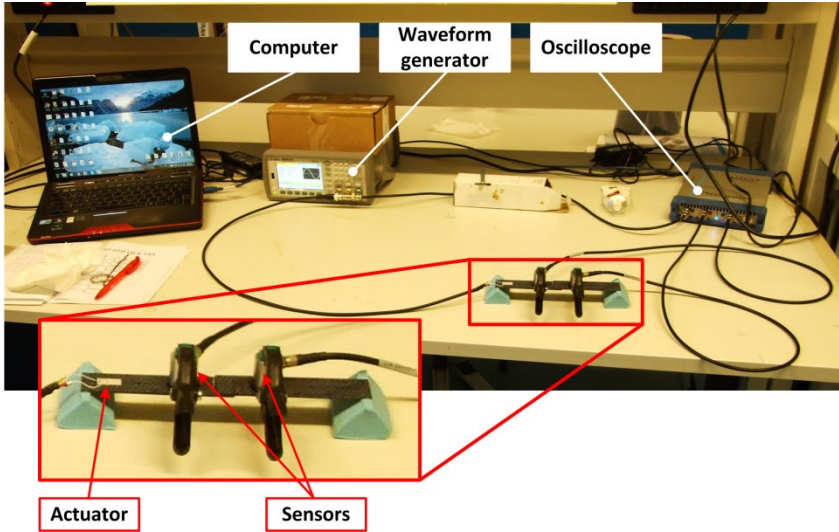


Figure 4.6. Setup used for the GW tests.

4.4. Results and discussion

4.4.1. Response observation

By observing responses acquired 40 mm after the overlap at 200 and 250 kHz, such as those depicted in Figure 4.7A and Figure 4.7B respectively, it is not possible to say that there was only one excited mode (s_0 or a_0). The existence of multiple overlapping edge reflections, together with joint reverberations, prevents the unambiguous evaluation of any other wave packets besides the first direct one when using pure time-domain signal processing. Thus, both the a_0 and s_0 modes are considered to be present. In order to cope with the impossibility of performing pure mode analysis, this study relies on full response characteristics to understand the influence of welding travel on the transmission of GWs across TpC ultrasonically welded joints.

In general, it must be assumed that each adherend mode can convert to any of the carrier modes. However, in reality, a mode is not “*excited if its field distribution is orthogonal to the excitation field.*” [7] Thus, as explained in Section 2.4.3.1, a certain carrier mode will be excited only if its mode shape in the lower layer of the overlap is similar to the mode shape in the adherend (before the overlap). Following this logic, the Lamb modes arriving at the sensor on the other side of the joint are determined by the match between the mode shapes of the excited carrier modes in the upper layer of the overlap and the mode shapes of Lamb modes in the adherend.

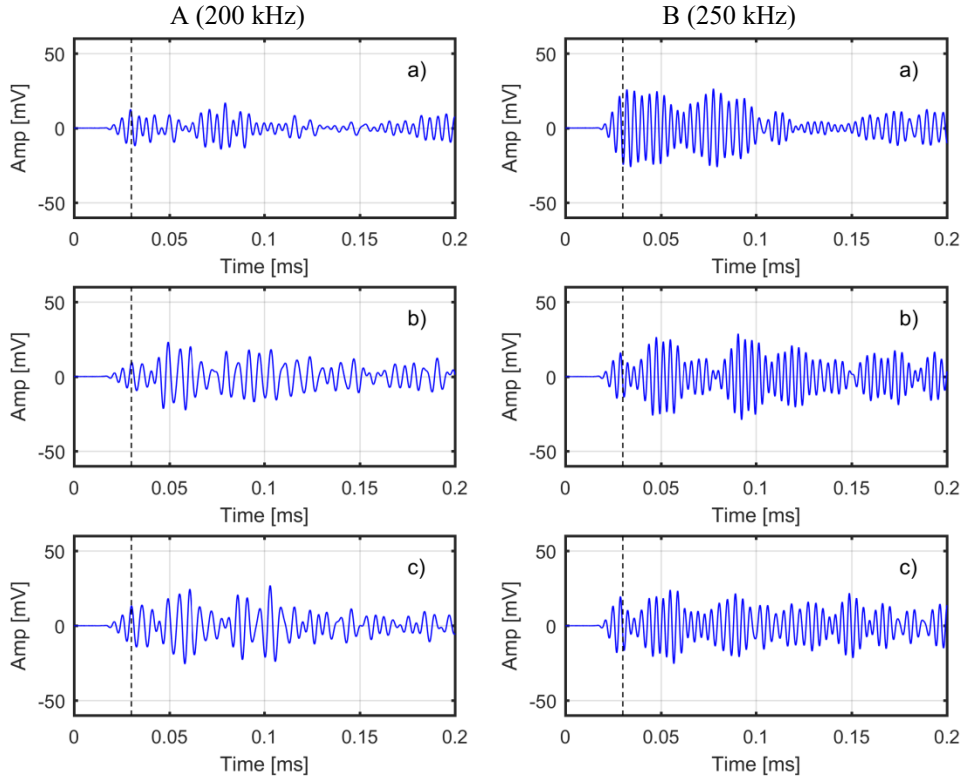


Figure 4.7. GW responses at T40 position for 200 kHz (column A) and 250 kHz (column B) excitation, from a specimen produced with welding travel of a) 0.12 mm, b) 0.08 mm, and c) 0.02 mm. The vertical dashed line indicates the approximate arrival time of the s0-S0-A0-S0-s0 reverberation.

At 200 kHz, the possible carrier modes are A0 and S0, while at 250 kHz the A1 can also exist. Since both the a0 and s0 modes are excited, also both the A0 and S0 carrier modes will appear in the overlap, after mode conversion at the edge of the joint. By mode shape similarity, the a0 mainly converts to A0, and the s0 mainly converts to S0. The A1 carrier mode might play some role in the transmission of the s0 energy across the joint at 250 kHz, since their out-of-plane displacement distributions are both approximately null.

Besides the direct transmission, part of the energy transmitted into the overlap reverberates, according to the mechanism explained in Section 2.4.3.1. So, for the incident s0 mode, S0 is generated, then converted to A0 which is again converted to S0, which then converts to s0 when being transmitted outside the overlap. This sequence of events is depicted in Figure 4.8. The estimated arrival time of this first reverberation (s0-S0-A0-S0-s0) at both 200 and 250 kHz is around 0.03 ms for all the three welding travels, with minor differences between them, as indicated by the dashed line in the plots of Figure 4.7. This reverberation group overlaps with the trailing edge of the first arriving s0 group and edge reflections.

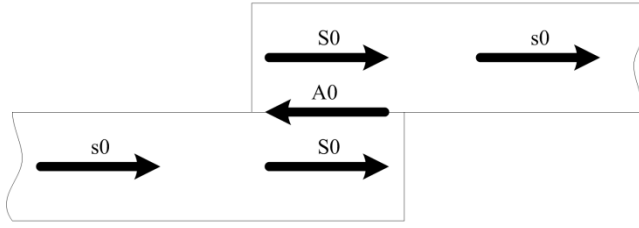


Figure 4.8. Diagram of single reverberation after incident s_0 mode.

4.4.2. Signal onset

As explained in Section 4.4.1, the onset of the signal at the T40 sensor corresponds to the arrival of the directly transmitted s_0 mode. According to theory, for the same welding travel (i.e. same joint type), the s_0 arrival time follows the evolution of phase velocity with frequency in an inverse way. Thus, for each weld condition, the arrival time is expected to increase when the frequency is raised from 200 to 250 kHz, with the differences lying between 1×10^{-5} and 2×10^{-5} ms (barely noticeable).

Also according to theory (see Figure 4.4), for the same frequency, the lower the welding travel, the thicker the overlap (assuming weld line thickness is the only varying parameter when travel is changed), and hence the lower the phase velocity, which implies a later arrival time. The decrease in phase velocity with increasing weld line thickness means the average stiffness of the overlap cross-section is in fact decreasing.

The experimental results for the onset time (depicted in Figure 4.9) were obtained with the threshold method [10,11], not directly applied to the signal but to the normalized signal envelope. The threshold level was set to 0.46% of the normalised envelope amplitude so that all onsets would be correctly captured. The computed values show some deviations from theory, especially at 200 kHz. Although the average s_0 arrival times are higher for 250 kHz than for 200 kHz for all three welding conditions (thereby following the theoretical trend), the experimental values are on average 0.70 and 0.23 μ s lower than the theoretical values for 200 and 250 kHz, respectively. Taking the theoretical results as the “true values”, then the average relative error was around 3.9% and 1.3% for 200 and 250 kHz, respectively.

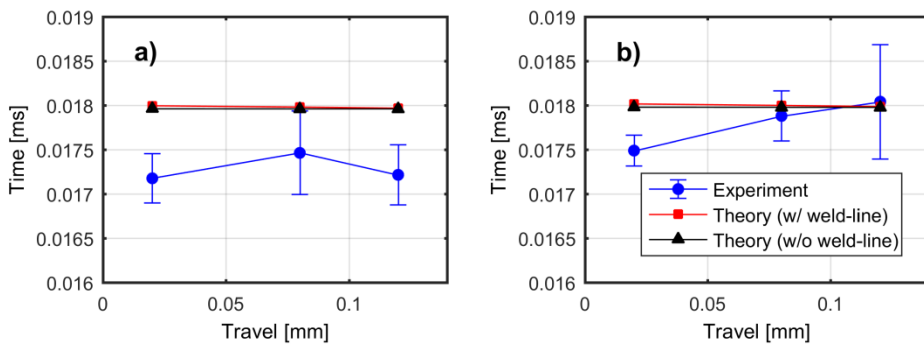


Figure 4.9. Onset time for the s_0 mode for a) 200 kHz, and b) 250 kHz.

One possible explanation for the differences between theoretical and experimental results could be that the adopted model overestimates the arrival time of the directly transmitted s0 mode. This would indicate that the actual average stiffness along the entire propagation path was higher than in the model. The fully anisotropic properties adopted to model the CF/PPS composite material have been proven to accurately describe the laminate used in this research [5], and are in total agreement with the values provided in the CF/PPS material datasheet [6]. However, because there is still no accurate characterisation of ultrasonic weld interfaces, the weld line was considered as an isotropic layer of neat PPS polymer, with properties taken from the datasheet of the material used in this study [6]. When a rigid connection between two solid layers is chosen, DISPERSE assumes the interface is defined by a clear boundary across which there is stress continuity. This means the modelled interface between the composite layer and the weld line resembles that of a “perfect” adhesively bonded joint, where the two materials are completely “glued” together. However, ultrasonic welding works through fusion bonding which promotes molecular interdiffusion between the materials (actual material mixing), thereby joining them together [3]. Therefore, one could argue that the differences between theoretical and experimental arrival times were due to inaccurate modelling of the properties of the weld interface, which in the present case seems to be stiffer than the modelled one. If the weld line is assumed to be normal material of the CF/PPS laminate, and the overlap is modelled as being entirely made of TpC material with a total thickness equal to the value obtained with the corresponding welding condition (as listed in Table 4.2), then it could be possible to evaluate the effect of considering a stiffer overlap. Comparing the arrival times predicted for these equivalent overlaps with the previously presented theoretical values (also plotted in Figure 4.9 as the case “without weld-line”), there is only a small difference between them which is not enough to justify the experimental results.

Another explanation could be in the clamps used to prevent the sliding movement of the sensors on the surface of the specimens, as shown in Figure 4.10. By applying pressure on both surfaces, the stiffness of the regions around the sensors might have been slightly increased, thereby allowing for a local increase of wave velocity and consequently a decrease in onset time. To test this hypothesis, Abaqus/Explicit (Dassault Systèmes Simulia Corp.) was used to build an FE model of the single-lap joint specimens, where the sensor clamp effect was also simulated. This model constitutes one of the incremental steps in the development of the model of one of the critical areas of the component-scale torsion box panel, as explained in Section 3.3. For a detailed description of the model, the reader is referred to Section 7.3.2.

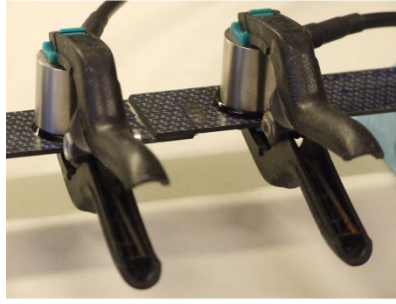


Figure 4.10. Detail showing the coupling of the sensors to the surface of the specimens.

Simulations were performed for the three cases of welding travel and the two excitation frequencies. For each of these travel-frequency pairs, the clamped and unclamped (or free) scenarios were taken into account. The onset times of the signal from sensing position T40 (see Figure 4.5) were extracted with the same threshold method as previously described, and are plotted in Figure 4.11a) and Figure 4.11b), for 200 and 250 kHz, respectively. The graphs show that the numerical signal onset times in the clamped scenario are lower than those in the free scenario, for both frequencies. Moreover, the values are in the same range as those in Figure 4.9. Therefore, the numerical results seem to confirm the hypothesis that the sensor clamps were responsible for the experimental signal onset times being lower than the theoretical ones.

In any case, even though it was not possible to draw any conclusions about the material properties of the ultrasonic welds, it seems valid to state that the arrival time of the direct transmission s0-S0-s0 can potentially be used to detect changes in the stiffness of the weld when compared to the pristine state.

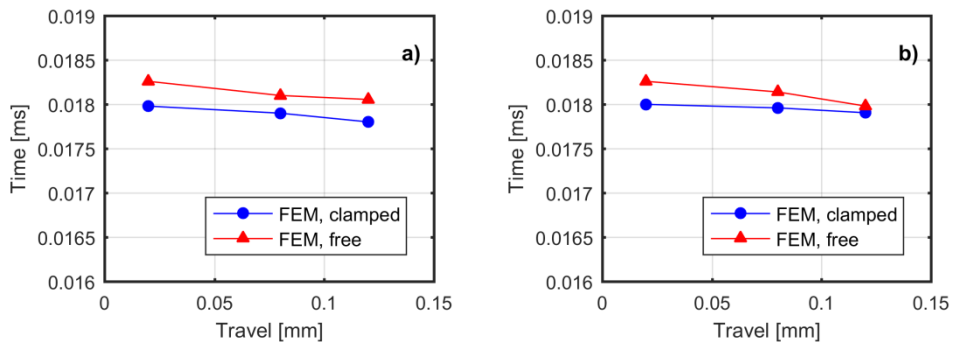


Figure 4.11. Numerical results for signal onset with and without clamped sensor for a) 200 kHz, and for b) 250 kHz.

4.4.3. Transmission coefficient

The methods of analysis used in this research did not allow the evaluation of the transmission of each mode individually across the lap joint. However, it was possible to evaluate the efficiency of transmission of the total incident energy, i.e. the transmission of

the a0 and s0 Lamb modes together. The power transmission coefficient (PTC) was computed for each specimen at each frequency according to:

$$PTC = 10 \log_{10} (P_{trans} / P_{inc}) \quad (4.2)$$

where the incident power, P_{inc} , for each condition, at each frequency, was taken as the average of the powers, P_i , of the signal acquired at the position R40 from all N_{sp} specimens in each batch:

$$P_{inc} = \sum_{i=1}^{N_{sp}} P_i / N_{sp} \quad (4.3)$$

and the transmitted power, P_{trans} , (as well as the individual power values P_i) for each specimen was equal to the squared root means square (RMS) level of the signal x (which had N_{pts} sample points):

$$P = (1/N_{pts}) \sum_{j=1}^{N_{pts}} x_j^2 = RMS^2(x) \quad (4.4)$$

The PTC results obtained at 200 and 250 kHz are plotted in Figure 4.12.

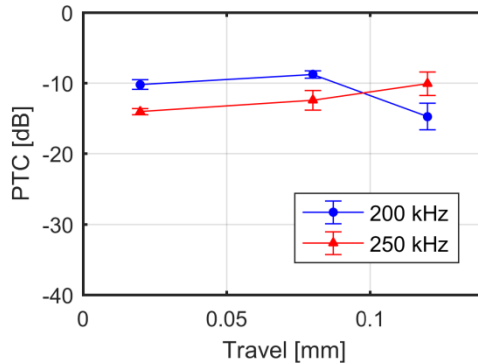


Figure 4.12. Variation of PTC with welding travel for 200 and 250 kHz.

For both frequencies, the values obtained were between -10 and -15 dB, which corresponds to 10% and 3% of the incident signal power, respectively. These low values are within the expected range, based on the considerations by Lowe et al. [7] about the influence of bond length and bond thickness on the Lamb wave transmission across adhesively bonded lap joints (see Section 2.4.3.1). Since there are only tenuous variations of weld line thickness and intermolecular diffusion at the weld interface from 0.12 mm to 0.02 mm welding travel, the variation of PTC with that parameter is also small, and with no apparent common trend. At 200 kHz, the PTC remains almost constant (around -10 dB) from 0.02 to 0.08 mm travel, and decreases to approximately -15 dB for 0.12 mm travel. At 250 kHz, the coefficient is around -14 dB for 0.02 mm travel, and goes up 2 dB per each travel change, ending at around -10 dB for 0.12 mm travel. However, bearing in mind

that this analysis includes both Lamb modes (a_0 and s_0) and neglecting (for now) the reverberations of the carrier modes, it may be possible to establish a reason for the observed evolutions. For that it is necessary to consider the displacement mode shapes of the Lamb modes in the adherend (the two leftmost columns) and carrier modes in the overlap (the two and three rightmost columns), at 200 and 250 kHz, depicted in Figure 4.13 and Figure 4.14, respectively.

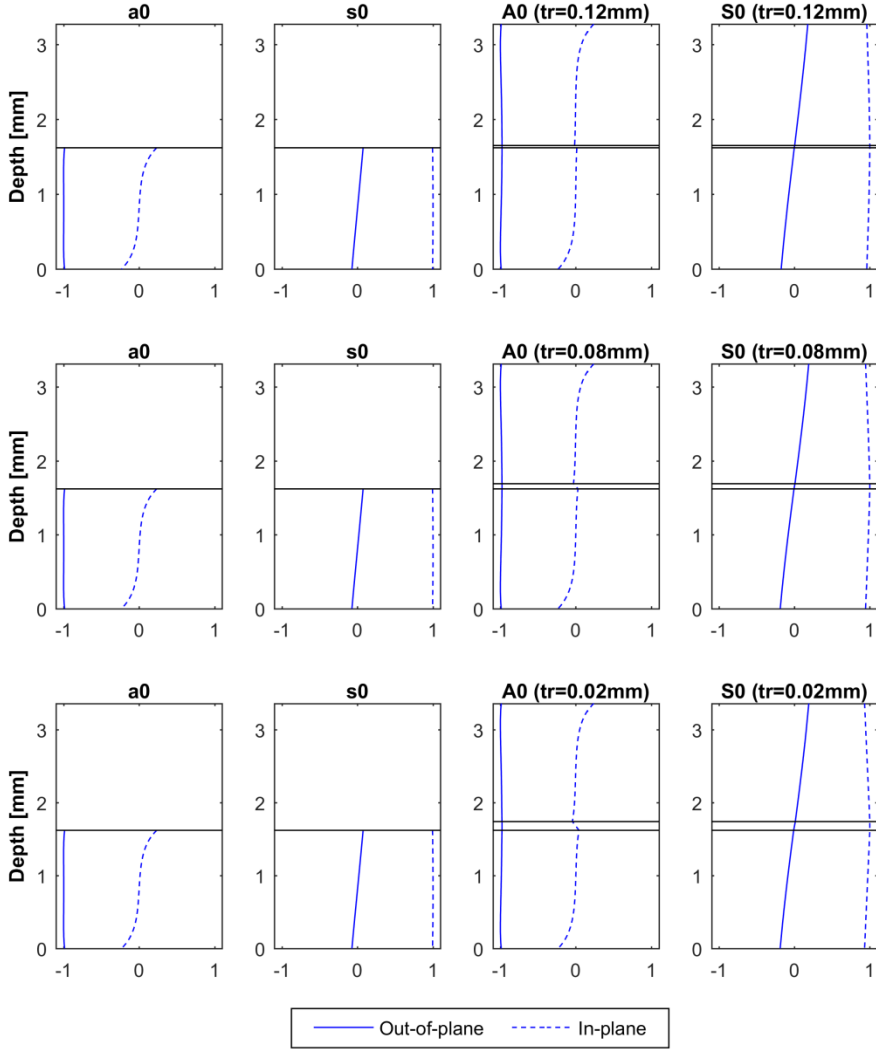


Figure 4.13. Normalised displacement mode shapes of the a_0 and s_0 Lamb modes in the adherend and the A_0 and S_0 modes in the overlap at 200 kHz, for the three welding travel values.

At 200 kHz (see Figure 4.13), the a_0 and s_0 Lamb modes in the adherend can only convert to the A_0 and S_0 carrier modes in the overlap region. The conversion of the s_0 to the S_0 mode is expected to have approximately the same efficiency for the three travel

values, as the match of the displacement mode shapes is almost unchanged. So, the energy of the transmitted s_0 is expected to remain approximately constant for the tested travel values. The same cannot be said for the a_0 - A_0 conversion. As welding travel increases (i.e. weld line thickness decreases), the curvature of the in-plane displacement distribution in the vicinity of the weld line decreases, worsening the match between the A_0 mode-shape in the lower overlap layer and the incident a_0 mode shape in the adherend, thereby decreasing the efficiency of the a_0 mode transmission and, in turn, the energy of that mode across the joint. This could explain the reduction of the power transmission coefficient for 0.12 mm travel.

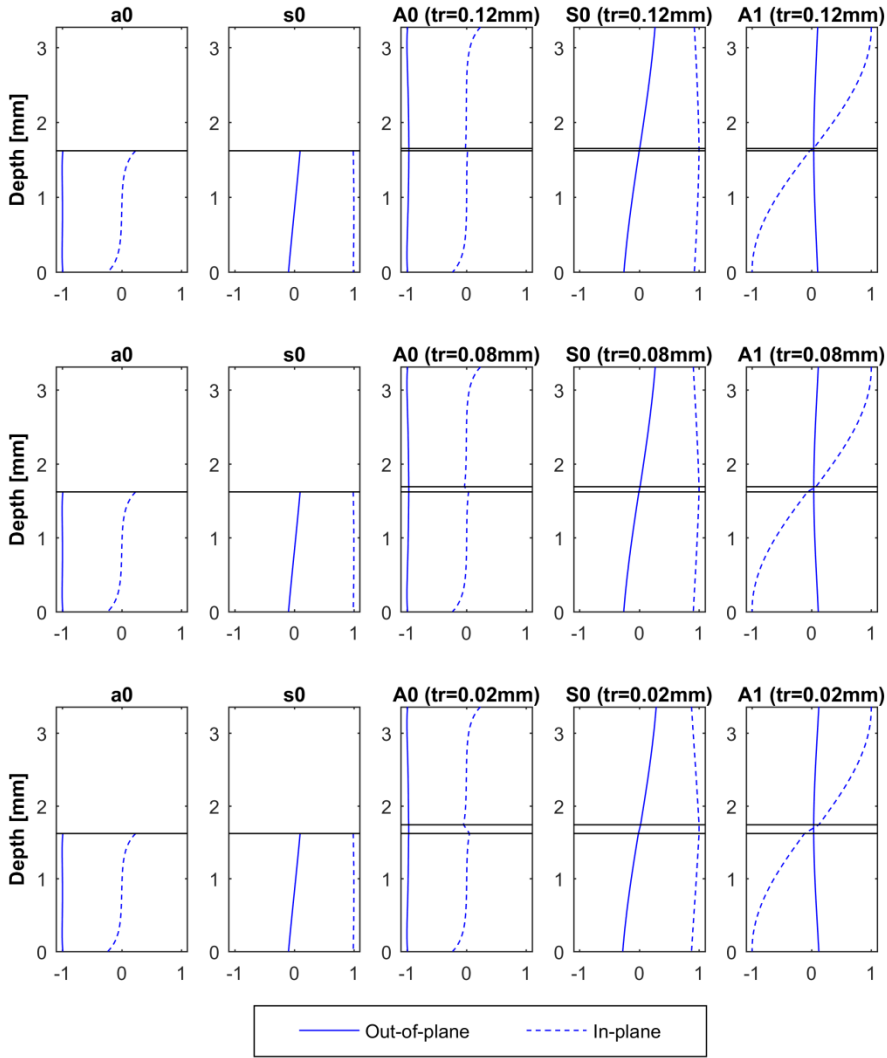


Figure 4.14. Normalised displacement mode shapes of the a_0 and s_0 Lamb modes in the adherend and the A_0 , S_0 , and A_1 modes in the overlap at 250 kHz, for the three welding travel values.

At 250 kHz (see Figure 4.14), the same evolution for the a0-A0 conversion is still observed. However, more factors come into play in the transmission of the s0 mode. Since the out-of-plane displacement distribution of the A1 mode in the lower overlap layer is relatively close to that of the s0 mode in the adherend, that overlap mode might also play a role in transmitting the energy across the joint. The velocities of the S0 and A1 modes are quite different, but the modes still interfere at the end of the overlap, when the second mode conversion back to s0 takes place. That interference can be more destructive or constructive, depending of the relative phase of each carrier mode after travelling the distance equal to the overlap length. According to Lowe et al. [7], two tendencies play a role in determining the nature of the interference. On one hand, the larger the propagation distance, the higher the phase change and the more constructive is the interference at the end of the overlap. On the other hand, the higher the wave number of the carrier mode (dependent on the overlap thickness), the higher the phase change, and the more constructive is the interference.

In this case, where the overlap length is not a varying parameter, the small (and not so different) overlap thicknesses of the three welding travel batches do not promote enough phase change to favour constructive interference (when compared to the phase changes obtained by Lowe et al. [7]), as summarised in Table 4.3, thereby reducing the efficiency of the s0 mode transmission and the energy of that mode across the joint. Furthermore, as welding travel decreases (i.e. weld line thickness increases), the change in in-plane displacement distribution of the S0 is noticeable (more curvature), thereby worsening the match with the adherend s0 mode shape. These two occurrences together could explain why the power transmission coefficient for 0.02 mm was lower than at 200 kHz.

Table 4.3. Phase analysis of the S0 and A1 carrier modes at 250 kHz (the variations of the phase change, $\Delta\phi$, are the differences to the previous welding conditions).

Travel [mm]	250 kHz					
	0.12		0.08		0.02	
Mode	S0	A1	S0	A1	S0	A1
Total $\Delta\phi$ [rad]	3.22	1.49	3.24	1.62	3.26	1.75
Variation $\Delta\phi$ [rad]	0.02	0.13	0.03	0.13		
Variation $\Delta\phi$ [%]	0.64	8.67	0.82	8.34		

As travel goes up, the match between the s0 and the S0 mode shapes improves, and the efficiency of conversion from s0 to S0 and back increases, therefore increasing PTC to -10 dB. It is worth noticing that, due to the balance between the two (contrary) evolutions for the a0-A0 and s0-S0 conversions, the rate at which the PTC increases at 250 kHz for the whole range of travel values (27 dB/mm from 0.02 to 0.08 mm, and 59 dB/mm from 0.08 to 0.12 mm) is lower than the rate at which it decreases at 200 kHz from 0.08 to 0.12 mm (149 dB/mm).

Although transmission phenomena are frequency dependent, the obtained overall PTC seems to be relatively insensitive to differences in welding travel at the tested frequencies. Hence, it was decided to further elaborate on the evolution of this relationship with frequency. For that, it is first important to pay attention to the bandwidth of the excitation signal. The excitation tone-burst does not have only one frequency component, but a finite frequency band. Most of the energy is transmitted at the centre frequency (which can also

be called as nominal excitation frequency), although there is always some energy which is transmitted though modes excited at all the other side frequencies. The bandwidth is determined by the type of amplitude modulation and the number of cycles of the tone-burst [12]. If one would want to study GW transmission at the maximum possible frequency without generating any higher order mode in the adherends, then the bandwidth upper limit should not go beyond the first cut-off frequency, which is approximately 449 kHz for the TpC laminate used in this study (see Figure 4.3). In the case of a 350 kHz five-cycle sinusoidal tone-burst with amplitude modulation by a Hanning window, the bandwidth would be [154; 546] kHz. Clearly, this signal would excite the a_1 mode, therefore the number of cycles should be increased to ten so that the bandwidth would become [252; 448] kHz. If the excitation were to be generated at a higher centre frequency, then an even higher number of cycles would have to be used, which would make the signal more complex and difficult to interpret. Therefore, taking into account these constraints, 350 kHz can be considered as the maximum advisable excitation frequency for the type of material system used in this study. The displacement mode shapes at that frequency, plotted in Figure 4.15, can then be used to make some estimates.

The a_0 and s_0 distributions in the adherend (the two leftmost columns) show little variation when compared to 200 and 250 kHz (Figure 4.13 and Figure 4.14, respectively). Also the A_0 distribution in the overlap region remains almost the same, with the out-of-plane displacement mode shape showing slightly more curvature than at 250 kHz. So, the efficiency of a_0 - A_0 conversion, and in turn the a_0 transmission across the overlap, would probably show the same trend with welding travel as previously described, although with lower transmitted power than at 250 kHz.

The same double s_0 transmission mechanism explained for 250 kHz would also be present at 350 kHz, although in this case, the match of the s_0 and S_0 mode shapes would be worse due to a higher curvature of the S_0 in-plane displacement distribution and a larger deviation from zero of the S_0 out-of-plane displacement distribution. The larger mode shape dissimilarity between s_0 and S_0 modes together with the destructive interference of the S_0 and A_1 modes at the end of the overlap (i.e. when mode converting to s_0) would probably result in a PTC value for 0.02 mm travel lower than at 250 kHz. Then, since the s_0 - S_0 mode shape matching slightly improves with increasing welding travel (due to a small reduction of curvature of the distributions), and since little variation of phase change with welding travel would be expected (as summarised in Table 4.4), the efficiency of s_0 - S_0 conversion would increase with welding travel at a low rate. Therefore, it seems valid to state that the PTC at 350 kHz would have the same evolution with welding travel, although with some offset to slightly lower values. In the presence of damage in (or around) the joint, the PTC would be expected to go down to -30 dB or even lower [13].

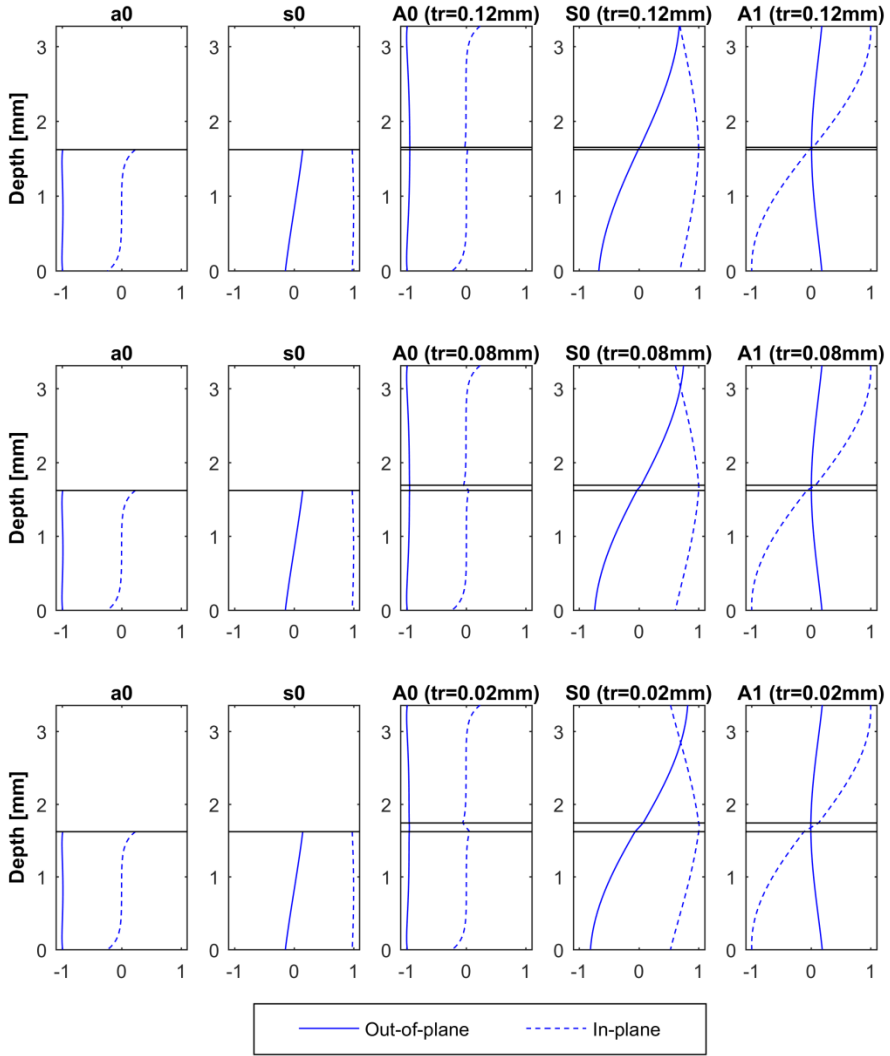


Figure 4.15. Normalised displacement mode shapes of the a_0 and s_0 Lamb modes in the adherend and the A_0 , S_0 and A_1 modes in the overlap at 350 kHz, for the three welding travel values.

Table 4.4. Phase analysis of the S_0 and A_1 carrier modes at 350 kHz (the variations of phase change, $\Delta\phi$, are the differences to the previous welding conditions).

Travel [mm]	350 kHz					
	0.12		0.08		0.02	
Mode	S_0	A_1	S_0	A_1	S_0	A_1
Total $\Delta\phi$ [rad]	4.64	3.46	4.71	3.52	4.81	3.58
Variation $\Delta\phi$ [rad]	0.07	0.06	0.11	0.07		
Variation $\Delta\phi$ [%]	1.41	1.72	2.24	1.93		

4.4.4. Correlation coefficient

In an effort to make the analysis more conclusive, the correlation coefficient (CC) was employed, as defined in Equation (2.23) in Section 2.6.4.1 but without taking the complement. It was decided to correlate the signals from specimens of each condition with a time-domain baseline signal representing the 0.12 mm travel condition. This time-domain baseline was defined as the average signal computed with the five signals extracted from the specimens of 0.12 mm travel batch. The results for 200 and 250 kHz are plotted in Figure 4.16.

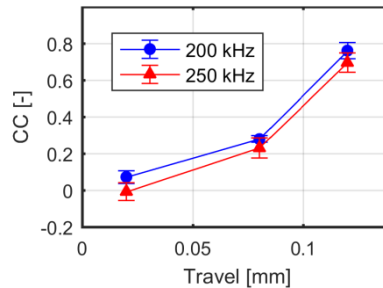


Figure 4.16. Variation of CC if the signals with welding travel at 200 and 250 kHz.

Following from the CC formula, the larger the deviation from unity, the worse the match of the signal with the baseline. Keeping this in mind, at 200 kHz it is possible to observe a 72% difference for 0.08 mm travel and 93% for 0.02 mm travel, while at 250 kHz differences of 77% and 100% are observed for 0.08 and 0.02 mm travel, respectively. This trend shown for both frequencies indicates that CC is a much more sensitive parameter to welding travel variations (i.e. combined changes of weld line thickness and molecular interdiffusion at the weld interface) than PTC. The existence of small PTC variations and large CC variations for the same welding travel values indicates that, at the tested frequencies, the differences between batches of signals are not only due to amplitude (i.e. energy content) changes, but also, and mainly, due to shape changes, as it can be understood from simple visual comparison of the responses in Figure 4.7A and Figure 4.7B.

From specimen to specimen there is unavoidable experimental variability due to small differences in transducer coupling and alignment, sample dimensions and fibre alignment. The coupling influences the captured signal amplitude, while the alignment and geometry influence the incident and reflected fields, and thereby the scatter pattern. Thanks to the adopted baseline definition, it is possible to approximately assess the influence of this inherent experimental variability by looking at the CC for the 0.12 mm travel, which corresponds to a difference of 24% and 31% for 200 and 250 kHz, respectively. Besides being partially incorporated into the baseline definition by the averaging process, these factors are always present for all specimens of the three welding conditions, and therefore they are not responsible for the large deviations in CC. In fact, even if the standard deviation of the data points is taken into account, the variation in CC is still considerably more pronounced than in the case of the PTC parameter.

What differs on a material scale from one welding travel batch to the other is the weld line thickness and the effectiveness of molecular interdiffusion at the weld interface (as mentioned in Section 4.1). The previously observed trends for the influence of weld line thickness on the direct transmission of the modes also apply to the transmission of the reverberated signals. The reverberation wave packets have always lower amplitude than the main signal, so the result of changes in their transmission efficiency becomes much more clear in the interference pattern caused by their superposition with the directly transmitted wave packets. Thus, at 200 kHz, the transmission efficiency of reverberations of the A0 carrier mode increases when welding travel decreases (i.e. weld line thickness increases), while the reverberation behaviour of the S0 carrier mode remains approximately the same. This means the interference pattern caused by the superposition of the direct signal and the S0 reverberations does not change, but the one caused by the superposition of the direct signal and the A0 reverberations does. At 250 kHz, not only the A0 reverberation transmission becomes more efficient when travel is reduced, but also S0/A1 reverberation transmission becomes less efficient, thereby inducing a larger deviation from the baseline reverberation pattern than at 200 kHz.

In the normalised power spectral density (NPSD) curves from a specimen of each welding condition for 200 and 250 kHz excitation frequencies in Figure 4.17A and Figure 4.17B, respectively, it is possible to identify several local maxima caused by interference between the directly transmitted signal, reverberations [7] and edge reflections. As a result, the frequency of maximum NPSD does not correspond to the excitation frequency. The influence of welding travel on signal interference can be assessed by the changes in the pattern of ultrasonic spectrum local maxima with welding travel. To quantify those differences, the CC was computed between NPSD curves of every specimen of all welding conditions and that of a frequency-domain baseline. That frequency-domain baseline is defined as the average NPSD computed with the five spectra from the specimens of the 0.12 mm travel batch. The CC values compiled in Figure 4.18 are in agreement with the trends observed in Figure 4.16, and thereby seem to corroborate the hypothesis that, at the tested frequencies, difference in interference between the direct signal and reverberations is the main effect of variations of welding travel on Lamb wave response.

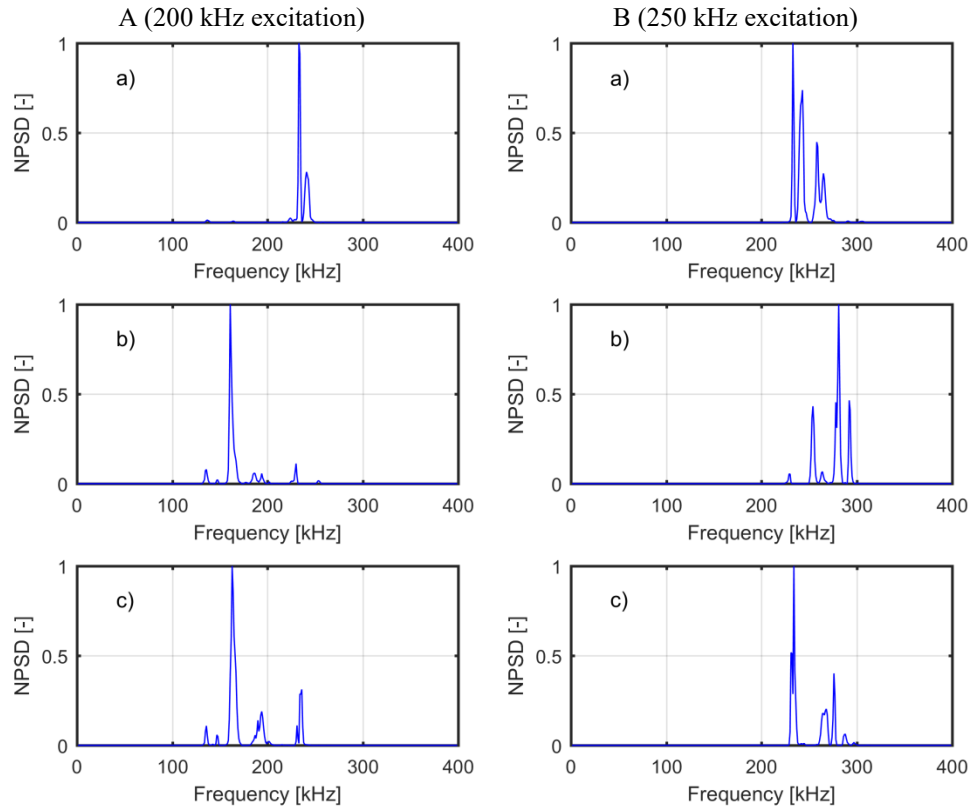


Figure 4.17. Normalised power spectral density at 200 kHz (column A) and 250 kHz (column B), for one specimen with welding travel of a) 0.12 mm, b) 0.08 mm, and c) 0.02 mm.

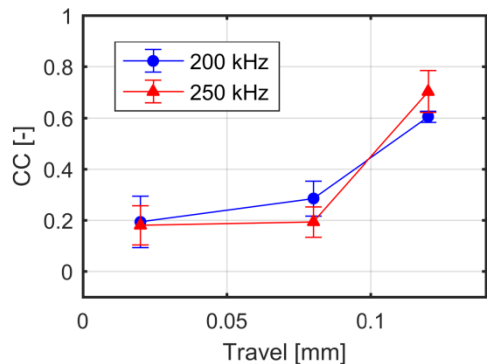


Figure 4.18. Variation of the correlation coefficient of the NPSD curves with welding travel at 200 and 250 kHz.

4.4.5. Non-destructive inspections

The results presented so far have been analysed assuming that specimens from the same welding travel batch have the same internal characteristics in the overlap region. However, if this were not true, the above developed reasoning could be invalid. Therefore, in order to ensure there were no significant changes in the effectiveness of molecular interdiffusion within each batch of welded joints which could compromise the previous results, it was decided to inspect all the samples with an Olympus OmniScan SX ultrasonic phased-array system at 5 MHz, using a 5L16-A10 probe mounted on a SA10-0L wedge. The coupling between the probe and the wedge was ensured by ultrasonic testing oil, and between the wedge and the sample by Sonotech Sonotrace ultrasonic couplant gel.

The results of these inspections are summarised in Figure 4.19, which shows A- and B-scans from specimens which were considered representative of each welding condition. The A-scan (on the left) shows the reflections of the ultrasonic beam from interfaces along the thickness under the centre point of the probe-wedge assembly. The B-scan (on the right) shows the reflections of the ultrasonic beam from interfaces occurring in the cross-sectional area under the probe-wedge assembly defined by the thickness of the inspected medium and the length of the probe. The reflection magnitude is indicated in percentage in the horizontal axis of the A-scan and is matched with the vertical colour scale in the B-scan.

The bi-dimensional view of the overlap cross-section is delimited by the first and third reflections, which indicate the top and bottom surfaces, respectively. The second, weaker, reflection corresponds to the weld interface. The magnitude of the reflection from the top surface is, approximately, always the same for all specimens, since it is the reflection that takes place when the ultrasonic beam enters the overlap. On the contrary, the magnitude of the third reflection (from the bottom surface) varies in an inverse way with the magnitude of the weld interface reflection, i.e. it becomes stronger when the latter becomes weaker. The small peaks after the third reflection correspond to reverberations of the beam inside the cross-section, and can be seen as “copies” of the first three.

In order to quantitatively correlate the results of the phased-array inspections with the welding conditions, the A-scan reflection magnitudes were read for all the specimens and translated into the graph of Figure 4.20 which illustrates the strength of the weld interface reflection peak as a function of welding travel. Small differences are found between 0.02 and 0.08 mm travel, with the weld interface reflecting 27% and 25% of the energy transmitted across the top surface, respectively. These are the cases where the weld interface reflection has a “blue” magnitude in the B-scan of Figure 4.19a) and Figure 4.19b). However, from 0.08 to 0.12 mm a significant drop to 17% is observed, revealing the existence of a turning point in the properties of the weld interface. This is visible in Figure 4.19c), where the weld interface reflection is mostly “light blue”.

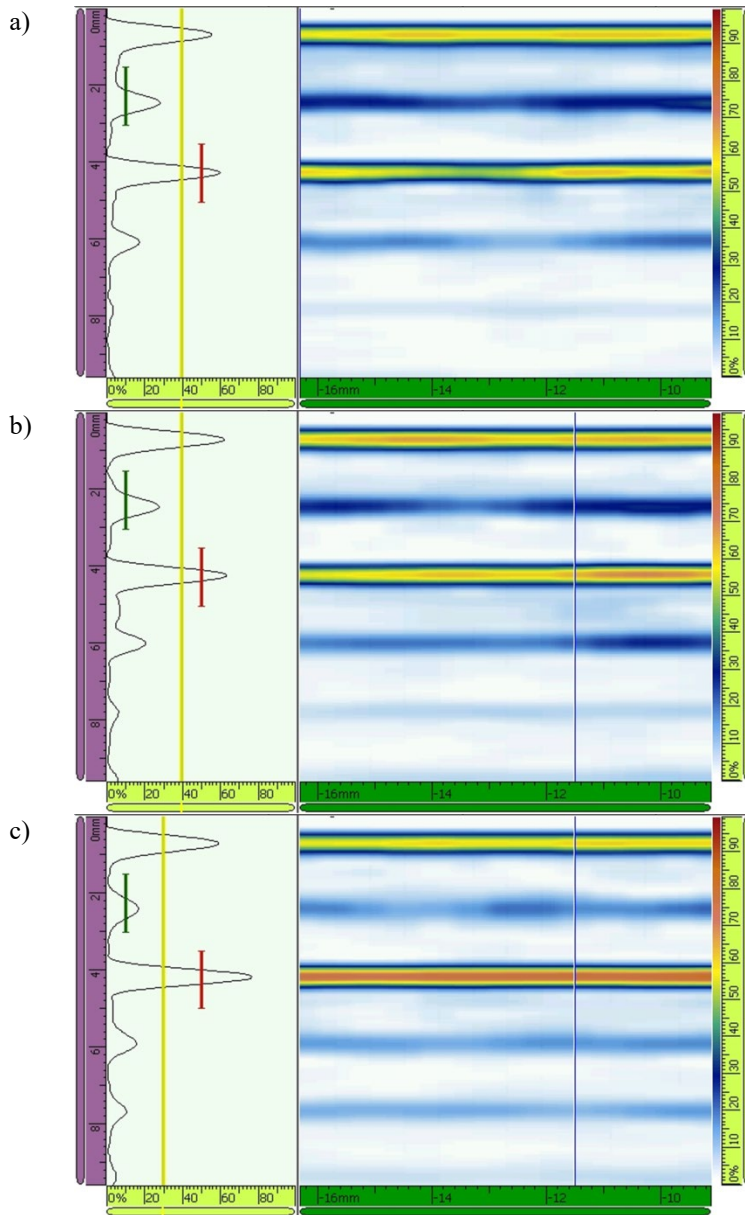


Figure 4.19. A- and B-scans from 5 MHz phased-array inspections of a representative specimen produced with a welding travel of a) 0.02 mm, b) 0.08 mm, and c) 0.12 mm. The A-scan percentage scale matches the B-scan colour scale (the closer to red, the stronger the reflection, the closer to white, the weaker the reflection).

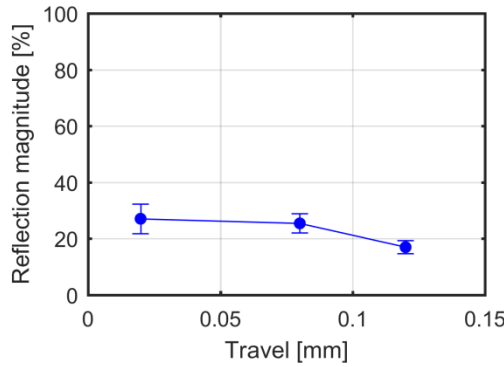


Figure 4.20. Variation of the maximum magnitude of the weld interface reflection with welding travel (extracted from A-scans of the phased-array results at 5 MHz).

It is interesting to note that the width of the weld interface reflection lobe at 10% magnitude barely changes with welding travel (from 0.6 mm for 0.02 and 0.08 mm, to 0.4 for 0.12 mm). That might be due to a combination of the type of filter used by the OmniScan to smoothen the A-scan curves, and the fact that the ultrasonic beam at 5 MHz does not have enough resolution to capture the actual differences in weld line thickness, since the longitudinal bulk wavelength at 5 MHz is between 0.6 and 1.2 mm, which is considerably larger than the weld line thicknesses encountered in the overlaps. Therefore, it is not possible to directly assess the actual differences in weld line thickness obtained by using different welding travel. In that sense, the direct verification of the squeezed-out status of the energy director cannot be made. However, it is still possible to perform an indirect evaluation.

Contrary to the laminate, where fibres and polymer are mixed, the weld line is a fibre-free region and, as such, it constitutes an interface from which ultrasounds are always reflected, independently of its thickness. In other words, even when very thin, the weld line is always a purely polymeric region, and thereby a discontinuity in the overlap. Moreover, welding travel seems to affect the effectiveness of molecular interdiffusion between the weld line and the adherends, as summarised in Section 4.1. Taking this reasoning into account, an evaluation of the second reflection peak shows that the larger the welding travel, the less discontinuous is the overlap cross-section. In other words, the larger the welding travel, the more similar to the adherend polymer-rich regions the weld line becomes. Therefore, it seems valid to say that the lower the second reflection peak, the stronger the molecular interdiffusion between the weld line and the adherends. The obtained reflection magnitude differences are in agreement with the observations of Villegas [2-4], as they confirm, on one hand, that the effectiveness of molecular interdiffusion at the weld interface increases with welding travel, and on the other hand that it is possible to produce TpC welds in a totally repeatable and controlled way by using the developed UW technique. More importantly, these non-destructive inspections show the consistency of the internal properties of specimens within each welding travel batch, thereby supporting the conclusions drawn from the Lamb wave tests. In particular, the low standard deviation observed in Figure 4.20 for the welds produced with a welding travel of 0.12 mm provides extra confidence on the baseline definition.

4.5. Conclusions

This chapter focused on studying the influence of one of the main parameters of the UW process, the welding travel, on the transmission of GWs across pristine TpC single-lap joints. Batches of five joints were manufactured with three different overlap thicknesses by varying the welding travel and keeping all the other process parameters constant. GW tests were performed by exciting only the two zero-order modes on one of the adherends and acquiring the response signal after the overlap.

The signal onset proved to be sensitive to small, local stiffness variations. This means it can potentially be used to detect changes in the stiffness of TpC ultrasonic welds, as long as the coupling conditions between the transducers and the specimens are constant. The absolute value of those changes, and hence the quality of the assessment, depends not only on the onset picking algorithm, but also, and mostly, on the sensors being unobtrusive so that the disturbance of the installation on the acquired signals is minimal.

Two things were observed in the sensed GW signals acquired from the joints welded with a welding travel different from the reference travel. On the one hand, the PTC revealed only a small amplitude variation with respect to the reference signals. On the other hand, the CC showed that, despite the small amplitude variations, there were large signal shape changes with respect to the reference signals. These observations were attributed to a variation in the phase velocity of the GW modes in the overlap, without a significant change of their displacement mode shapes. This affected the phase lag between the GW modes in the overlap and, consequently, the reverberation pattern inside the overlap. As a result, the modification of the interference between the reverberated wave packets and the directly transmitted wave packets was dominated by signal shape changes. These findings are valid for the range of thicknesses obtained with the UW setup and type of TpC material system described in Section 3.2.1, and for GW interrogation performed with a frequency at which only zero-order modes are excited in the adherend.

A correlation between welding travel and molecular interdiffusion across the weld interface was established by benchmarking the weld interface reflection magnitude obtained through ultrasonic phased-array inspections. The inspections showed that joints of the same welding travel batch have consistently similar internal structure. An evaluation of the weld interface reflection magnitude confirmed that the larger the welding travel, the more effective the molecular interdiffusion between the weld line and the adherends.

In short, this chapter addresses part of research question Q1), by analysing the interaction of GWs with pristine TpC ultrasonic welds. The knowledge gained is carried to Chapter 5 to complete the answer to that question, by studying GW interaction with defective welds.

References

1. Ochôa P, Villegas IF, Groves RM, Benedictus R. Experimental assessment of the influence of welding process parameters on Lamb wave transmission across ultrasonically welded thermoplastic composite joints. *Mech Syst Signal Pr* 2018; 99: 197-218.
2. Villegas IF. In situ monitoring of ultrasonic welding of thermoplastic composites through power and displacement data, *J Thermoplast Compos* 28(1) (2015) 66-85.

3. Villegas IF. Strength development versus process data in ultrasonic welding of thermoplastic composites with flat energy directors and its application to the definition of optimum processing parameters. *Composites Part A* 2014; 65: 27-37.
4. Villegas IF, Valle Grande B, Bersee HEN, Benedictus R. A comparative evaluation between flat and traditional energy directors for ultrasonic welding of CF/PPS thermoplastic composites. *Compos Interface* 2015; 22(8): 717-729.
5. Daggumati S, De Baere I, Van Paepegem W, Degrieck J, Xu J, Lomov SV, Verpoest I. Local damage in a 5-harness satin weave composite under static tension: part II - Meso-FE modelling. *Compos Sci Technol* 2010; 70: 1934-1941.
6. TenCate Cetex TC1100 PPS Resin System, TenCate Advanced Composites, Product Datasheet Revised 05/2014.
7. Lowe MJS, Challis RE, Chan CW. The transmission of Lamb waves across adhesively bonded lap joint. *J Acoust Soc Am* 2000; 107(3): 1333-1345.
8. Matt H, Bartoli I, Lanza di Scalea F. Ultrasonic guided wave monitoring of composite wing skin-to-spar bonded joints in aerospace structures. *J Acoust Soc Am* 2005; 118: 2240-2252.
9. Ochôa P. Supporting data for Guided wave testing of thermoplastic composite ultrasonic welds produced with different welding travel. 4TU.Centre for Research Data. Dataset, 2019. <https://doi.org/10.4121/uuid:a48f99de-f28e-4f5d-8d2d-f7bce3e87528>.
10. Tong C, Kennet BLN. Automatic seismic event recognition and later phase identification for broadband seismograms. *B Seismol Soc Am* 1996; 86(6): 1896-1909.
11. Gagar D, Martinez M, Yanishevsky M, Rocha B, McFeat J, Foote P, Irving P. Detecting and locating fatigue cracks in a complex wing-box structure using the acoustic emission technique: a verification study. Paper presented at: 9th International Workshop on SHM; September 10-12, 2013; Palo Alto (CA), USA.
12. Wilcox PD. *Lamb Wave Inspection of Large Structures Using Permanently Attached Transducers*. London, UK: Imperial College London; 1998.
13. Lanza di Scalea F, Rizzo P, Marzani A. Propagation of ultrasonic guided waves in lap-shear adhesive joints: case of incident a0 Lamb wave. *J Acoust Soc Am* 2004; 115(1): 146-156.

5

GWs in TpC ultrasonic welds: Diagnostic of manufacturing defects

The goal of this chapter is to give an understanding of GW transmission across TpC ultrasonic welds with manufacturing defects. Triangular EDs integrated into the lower composite adherends enabled the production of defective joints in a controlled manner. The produced defect types were unwelded areas and adherend fibre bundle distortion. The reference condition corresponded to the fully welded stage which showed the highest single-lap shear strength.

It was possible to detect adherend fibre bundle distortion through the increase in the negative shift of the signal characteristic frequency. Evidence of the presence of unwelded areas was found in the increase of TOF of the maximum amplitude Lamb wave group.

5.1. Introduction

The study presented in Chapter 4 shed some light on the mechanisms governing GW interaction with TpC ultrasonic welds, but only considering the pristine condition of the joints. A combined analysis of power transmission coefficient and correlation coefficient between GW signals was employed to show that slight variations of weld line thickness and supposedly associated molecular interdiffusion at the weld interface mainly affect the reverberation pattern inside the overlap. As a result, the modification of the interference between the reverberated wave packets and the directly transmitted wave packets was dominated by signal shape changes. To complete that analysis, and fully address the research question Q1), it is necessary to study GW transmission across welds with manufacturing defects.

Potentially useful approaches for this problem can be found in previous research on the use of ultrasonic GW to extract information about bond strength, as discussed in Section 2.4.3.2. However, it should not be forgotten that those studies were conducted only on adhesive bonds, which have a very different internal structure and are typically ten times thicker than ultrasonically welded TpC joints (see Section 2.2). Therefore, the research in this chapter took advantage of the utilisation of integrated triangular EDs for obtaining defective welds in a fully controlled way to study ultrasonic GW propagation through the resulting single-lap joints.

5

5.2. Test specimen manufacturing

The materials and process to manufacture the TpC plates are described in Section 3.2.1. However, for half of the plates, the lower mould had triangular grooves. As shown in Figure 5.1A), five 0.08 mm thick layers of neat PPS polymer were placed between the composite semipreg stack and the triangular grooves to produce consolidated plates with integrated triangular EDs [2]. It should be noted that the direction of the triangular grooves was perpendicular to the 0° direction of the composite laminate. The final height of the EDs was approximately 0.5 mm, as measured from Figure 5.1B).

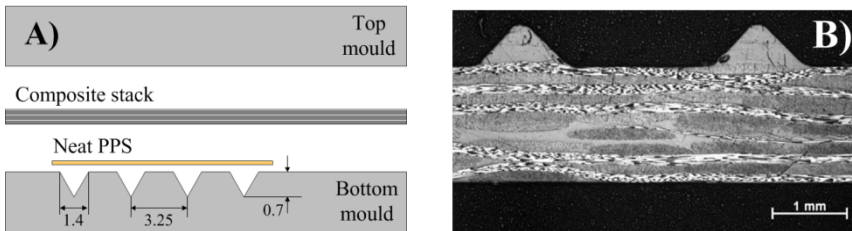


Figure 5.1. A) Diagram (not to scale) with the mould, neat PPS layers and composite stack; B) Cross-sectional micrograph of the laminate with integrated triangular EDs [2].

The adherends cut from the manufactured plates (see Section 3.2.1) still had to be manually sanded along the longitudinal edges in order to tightly fit the UW clamping tool (see Figure 3.4 in Section 3.2.1). As explained later in Section 5.4.3.1, it is important to highlight that the bottom mould had been originally produced for other research projects, with two sets of four triangular grooves. Because of that an additional sanding operation

had to be performed in order to have only one set of four ED rows and to allow the adherends to fit inside the clamping tool.

For the production of the specimens (see dimensions in Section 3.2.1) with well defined qualities we needed to consider the previous knowledge about the evolution of the welding process power and the sonotrode displacement (from here onwards called travel) with integrated triangular EDs, as studied by Villegas and Palardy [2] and reviewed in Section 2.2. In order to be consistent with the welding conditions employed by them, the same force, amplitude and solidification parameters were used: 500 N welding force, 86.2 μm peak-to-peak vibration amplitude, 1000 N solidification force, and 4 s solidification time. It was decided to produce three batches of specimens. An initial weld was produced with a travel of 0.5 mm in order to extract the power and travel curves covering all the process stages, shown in Figure 5.2.

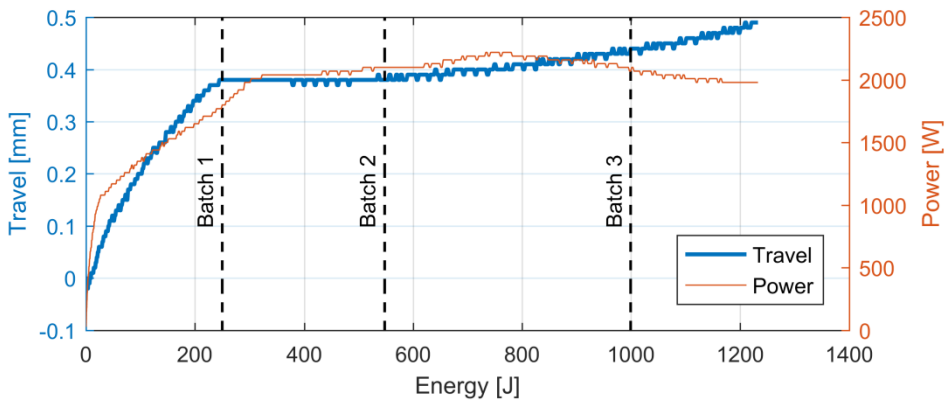


Figure 5.2. Power and travel curves as function of energy for the initial weld, produced with a travel of 0.5 mm. These curves were used to select the process parameters for the three batches. The welding points for the three batches are indicated by vertical dashed lines.

Based on those curves, the process parameters for the different weld stages were selected. The welding process parameters used for the three batches and the corresponding specimen names are summarised in Table 5.1. Specimens were named according to the convention B{batch#}-{specimen#}. Batch 1 was produced by stopping the travel-controlled process at the start of the travel plateau (see first vertical line in Figure 5.2), with a value of 0.36 mm. At that point the welds are expected to be incomplete, with interspersed welded and unwelded areas [2]. That state is reached after melting, collapse and partial flow of the EDs into the gaps between the adherends, where the melt-fronts are arrested by coming into contact with the adjacent colder adherends (see Figure 5.3A to C) [2]. Batch 2 was produced by stopping the process at the end of the travel plateau (see second vertical line in Figure 5.2). Since the transition from the first to the second welding point occurs at the same travel, it was decided to use energy-control welding, with a value of $E = 550$ J. At this point the joint is expected to be fully welded, after the previously arrested ED melt-fronts are remelted and start to flow out of the overlap (see Figure 5.3 D) [2]. Finally batch 3 was produced by taking the travel-controlled process beyond the power peak (see third vertical line in Figure 5.2). At this weld stage EDs are expected to be completely squeezed out from the welding interface, with melt and flow of the matrix

beyond the first layer of the adherends (see Figure 5.3 E) [2], which is expected to lead to adherend fibre bundle distortion [3].

Table 5.1. Welding process control parameters for the three batches and corresponding specimen names.

Specimen group	Control parameter	# Joints	Specimen names
Batch 1	Travel: 0.36 mm	5	B01-01 to B01-05
Batch 2	Energy: 550 J	5	B02-01 to B02-05
Batch 3	Travel: 0.42 mm ($\times 1$); 0.44 mm ($\times 3$)	4	B03-01 to B03-04

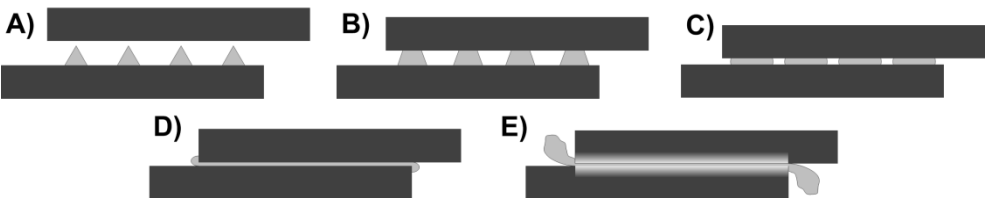


Figure 5.3. Different phases of the UW process with triangular EDs: A) intact EDs; B) collapse of the EDs due to melting; C) partial flow of the EDs and melt-front arrest; D) remelting of ED melt-fronts and subsequent flow out of the overlap; E) complete ED squeeze out from the welding interface, with melt and partial flow of the matrix beyond the first adherend ply.

5

5.3. Experiments

5.3.1. Ultrasonic GW testing

The full GW testing setup is shown in Figure 5.4. The ultrasonic excitation was produced by an Agilent 33500 B arbitrary waveform generator and transmitted to the specimen by a PZT transducer. The same type of PZT transducer was used to sense the ultrasonic response which was then acquired by a PicoScope 6402 A digital oscilloscope. The raw ultrasonic signals can be found in [4].

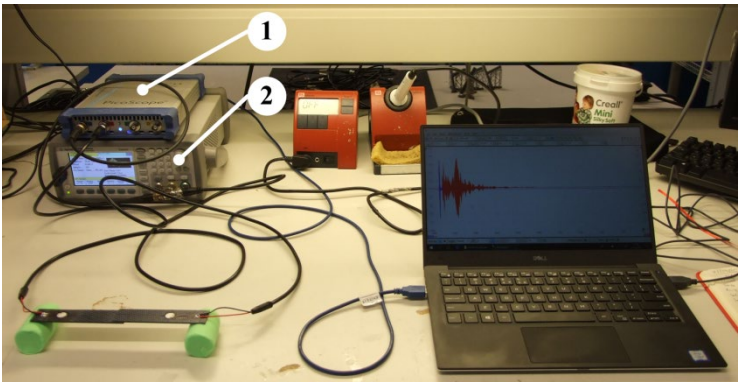


Figure 5.4. Setup used for GW testing: a) digital oscilloscope; 2) waveform generator.

The excitation signal shape and frequency, and the PZT transducers geometry were selected differently than in Chapter 4, by using the criteria proposed in Chapter 6, which are based on the optimisation of the sensor output, coupled electro-mechanical response of the transducer-structure assembly, energy transfer from the bonded PZT transducer to the structure, available area for transducer bonding, and measurement equipment capabilities. As a result, the PZT transducers consisted of bare APC 850 material (provided by American Piezo Ltd.) cut into discs of 10 mm diameter and 0.4 mm thickness, and poled in the out-of-plane direction. They were bonded to the composite adherends at the positions indicated in Figure 5.5. The excitation signal was a sinusoidal tone-burst with a 10-cycle Hanning window amplitude modulation generated with a maximum amplitude between 7 and 9 V at four frequencies: 204, 349, 486 and 619 kHz. At 204 and 349 kHz, the maximum input voltage was around 9 V, and the maximum output voltage was between 250 and 460 mV. At 486 and 619 kHz, the maximum input voltage was around 8 V, and the maximum output voltage was between 23 and 37 mV. According to the dispersion curves in Figure 5.6, at these frequencies the GW modes expected in the adherends are up to order one, while in the overlap the expected GW modes are up to order two. By testing at multiple frequencies it was possible to explore the sensitivity of both zero- and higher-order GW modes to the different welding defects (as investigated by Kundu et al. [5] and explained at the end of Section 2.4.3.2). In Section 5.6, the need for developing new, systematic criteria for designing the SHM system is put into context.

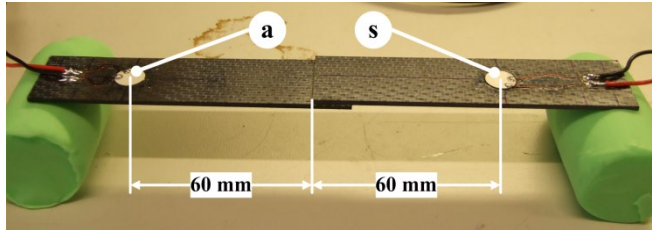


Figure 5.5. Single-lap joint instrumented with piezo-ceramic transducer discs, one functioning as actuator (a) and the other as sensor (s).

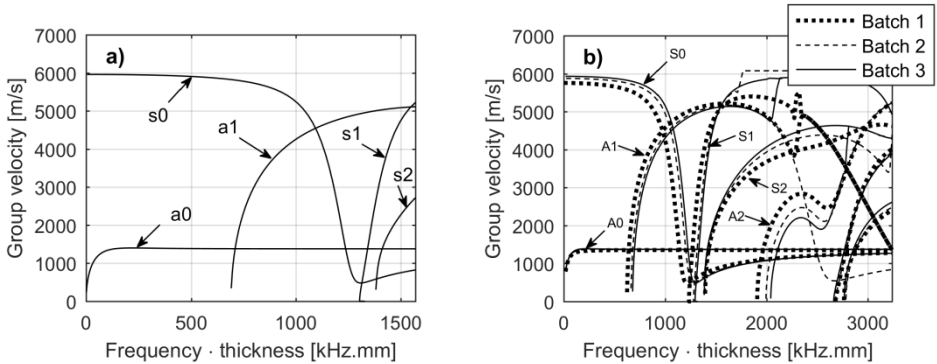


Figure 5.6. Simulated group velocity curves for a) the adherends and b) the overlaps of the three batches. The curves were computed with DISPERSE v2.0.20a using the approach explained in Section 4.3.1 and in [6]. The curves provide an approximation of the dispersive properties of the guided wave modes in the structures tested in this study.

5.3.2. Complementary testing and evaluation

The welded joints were mechanically tested according to the ASTM D1002 [7] standard in a Zwick/Roell 250 kN testing machine, in order to extract the SLSS (single-lap shear strength). The resulting fracture surfaces were photographed with a Zeiss SteREO Discovery.V8 microscope. The SLSS results and the fracture surface observations were used 1) to define the reference batch, and 2) to check if the joints had been welded with the manufacturing defects desired for this research.

Additionally, manual ultrasonic inspections of all the joints were conducted with an Olympus 10 MHz 10L32-A10 phased-array probe connected to an Olympus OmniScan SX. The probe was mounted on an Olympus SA10-0L wedge. The coupling between the probe-wedge assembly and the specimens was ensured by Sonotech ultrasonic coupling gel. These measurements had the purpose of verifying that it was possible to diagnose the manufacturing defects with a mature NDT technique.

5.4. Results and discussion

5.4.1. Selection of the reference state

The maximum load carried by the specimens during the single-lap shear tests was divided by the total overlap area to obtain the apparent SLSS. The results are plotted in Figure 5.7. The single-lap shear tests were useful to define the reference state for this study. Since, the maximum SLSS was achieved for batch 2 and the fracture surfaces of batch 2 specimens (see Figure 5.8) indicate a uniform welding quality without any unmolten EDs or fibre bundle distortion, it was decided to designate it as the reference one.

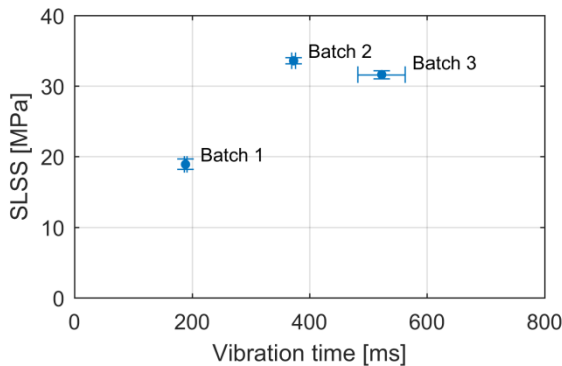


Figure 5.7. Single-lap shear strength as a function of welding vibration time.

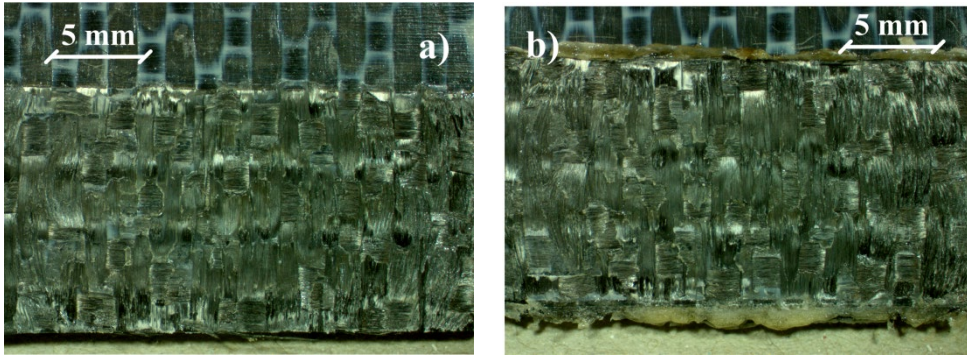


Figure 5.8. Fracture surfaces of the a) bottom and b) top adherends of specimen B02-02 (batch 2).

5.4.2. Evaluation of process consistency

The purpose of this section is to display proof that the desired manufacturing defects were effectively introduced in a fully controlled way during the ultrasonic welding process.

5.4.2.1. Batch 1

There were portions of the EDs that did not melt entirely and/or had resolidified before full molecular interdiffusion could be established across the areas through which they had flowed (see Figure 5.3 in Section 5.2). This was confirmed by the presence of remnant EDs on the bottom adherent after failure (Figure 5.9a) and by the welded areas interspersed with unwelded areas on the top adherent after failure (Figure 5.9b).

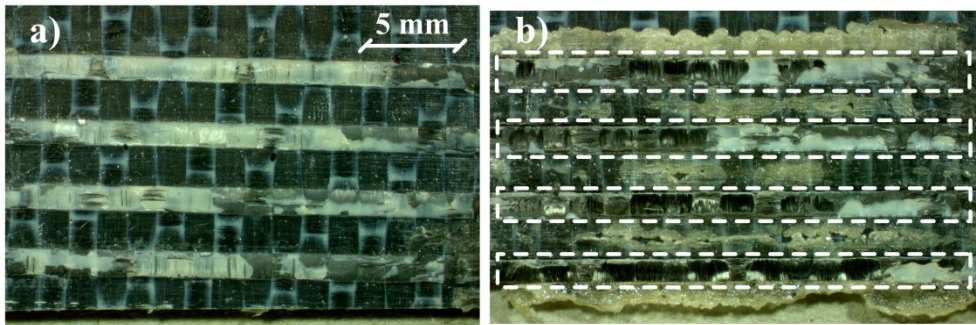


Figure 5.9. Fracture surfaces of the a) bottom and b) top adherends of specimen B01-04 (batch 1), welded with travel equal to 0.36 mm. In a) it is possible to see rows of whitish remnant EDs. In b) it is possible to see welded areas (highlighted by dashed-line rectangles) interspersed with unwelded areas (zones between the dashed-line rectangles). Also in b) irregular flow fronts in the unwelded areas indicate melt, incomplete squeeze-out and resolidification of the EDs.

The scans obtained by ultrasonic phased-array inspections also confirmed the existence of unwelded areas in batch 1, as depicted in the A- and B-scans of Figure 5.10. A reflection indicates a discontinuity in the structure. The higher the reflection magnitude, the higher the level of discontinuity. Based on this, it is possible to see that the zones of

higher ($\sim 55\%$) and lower ($\sim 30\%$) reflection magnitude (highlighted in dashed rectangles) within the weld interface correspond to zones of lower and higher continuity, respectively, which in turn correspond to unwelded and welded areas, respectively. Consequently, the reflection magnitude from the joint bottom surface is not homogeneous. Under the lower continuity zones the reflection magnitude is lower than under the higher continuity zones because there is less ultrasonic energy passing through the unwelded areas than through the welded areas.

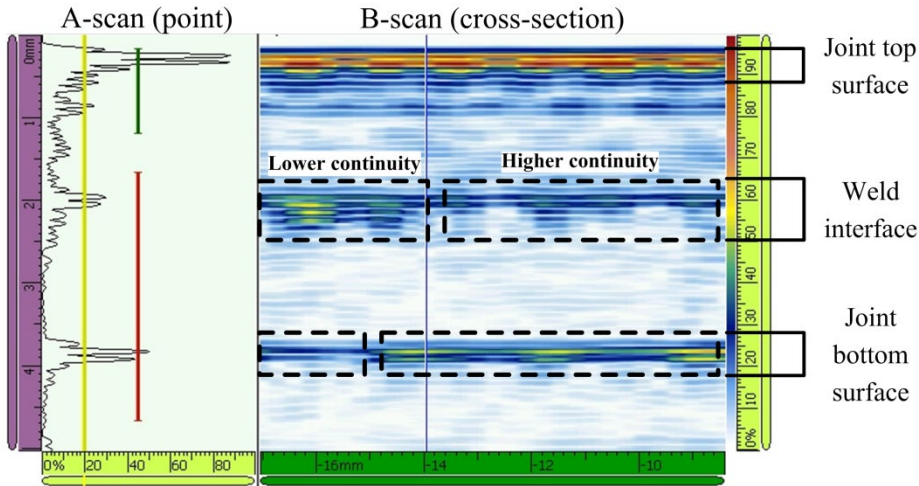


Figure 5.10. Ultrasonic A- and B-scans of the weld of specimen B01-04 (batch 1) at 10 MHz. Left vertical scale indicates thickness in mm; left horizontal scale indicates reflection magnitude in % for the A-scan; right horizontal scale indicates joint overlap length in mm; right vertical scale indicates reflection magnitude in % for the B-scan.

5.4.2.2. Batch 3

When comparing the fracture surfaces of batch 1 in Figure 5.8 with those of batch 3 in Figure 5.11 it is possible to confirm that the fibre bundles are no longer entirely perpendicular to each other, as they are deformed in directions which are slightly concentric with respect to the middle point of the fracture surface.

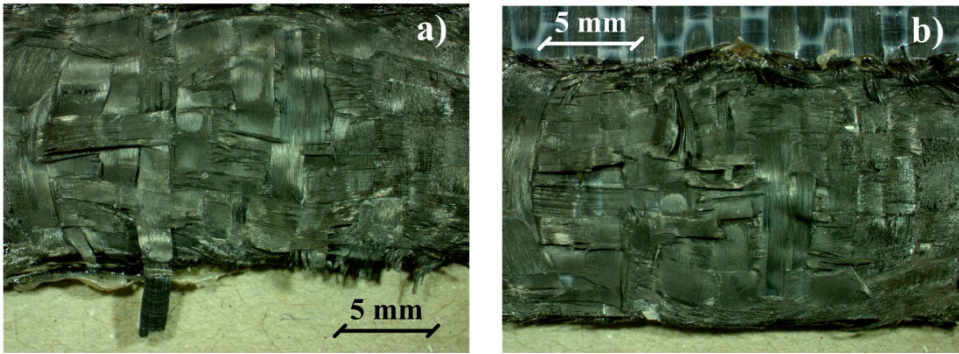


Figure 5.11. Fracture surfaces of the a) bottom and b) top adherends of specimen B03-02 (batch 3).

It is interesting to note that the comparison of the ultrasonic B-scans for batch 2 (Figure 5.12) and batch 3 (Figure 5.13) specimens did not allow the diagnostic of adherence fibre bundle distortion. In both cases there is high continuity along the entire weld interface and the weld interface reflection zone is narrower than for batch 1 (see Figure 5.10). The weld interface reflection magnitude for batch 2 is between 15% and 35% (Figure 5.12) while for batch 3 is between 15% and 25% (Figure 5.13). This means that there is higher material continuity across the overlap for batch 3 than for batch 2, which could potentially lead to the erroneous conclusion that there was no defect in batch 3 specimens. This is an example that illustrates that there are manufacturing defects that can go undetected in early inspections with ultrasonic NDT techniques, and that there is a real need for SHM to overcome this difficulty.

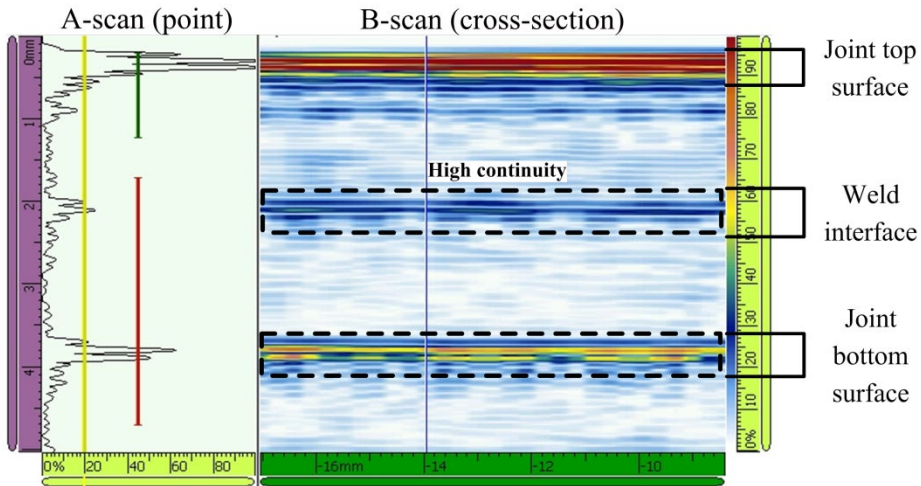


Figure 5.12. Ultrasonic A- and B-scans of the weld of specimen B02-03 (batch 2) at 10 MHz. Left vertical scale indicates thickness in mm; left horizontal scale indicates reflection magnitude in % for the A-scan; right horizontal scale indicates joint overlap length in mm; right vertical scale indicates reflection magnitude in % for the B-scan.

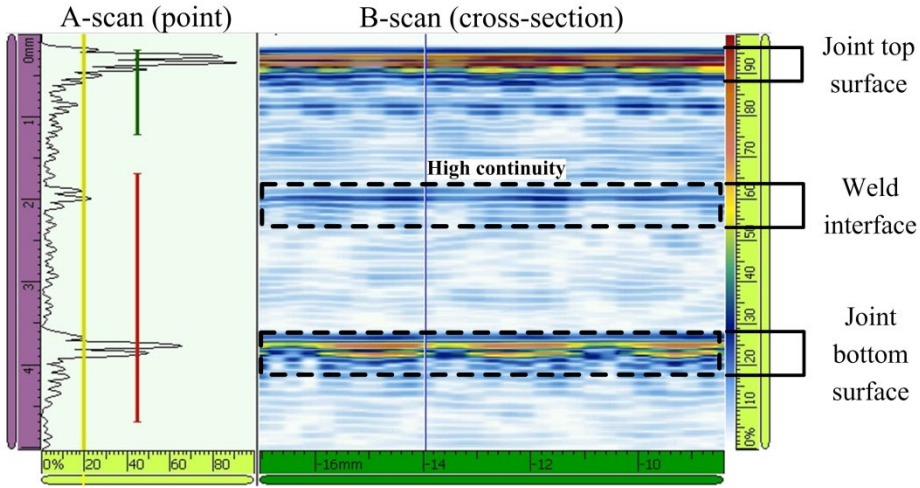


Figure 5.13. Ultrasonic A- and B-scans of the weld of specimen B03-04 (batch 3) at 10 MHz. Left vertical scale indicates thickness in mm; left horizontal scale indicates reflection magnitude in % for the A-scan; right horizontal scale indicates joint overlap length in mm; right vertical scale indicates reflection magnitude in % for the B-scan.

5

5.4.3. Ultrasonic GW detection

For a matter of consistency with the research presented in Chapter 4, the GW signals are analysed in the time and frequency domains by exploring the same parameters of signal energy, characteristic frequency, wave group TOF, and correlation coefficient.

5.4.3.1. Signal energy

For all the excitation frequencies and the three batches, the average time-domain GW signal energy, E_s , was computed according to Equation (2.9). The results are plotted in Figure 5.14.

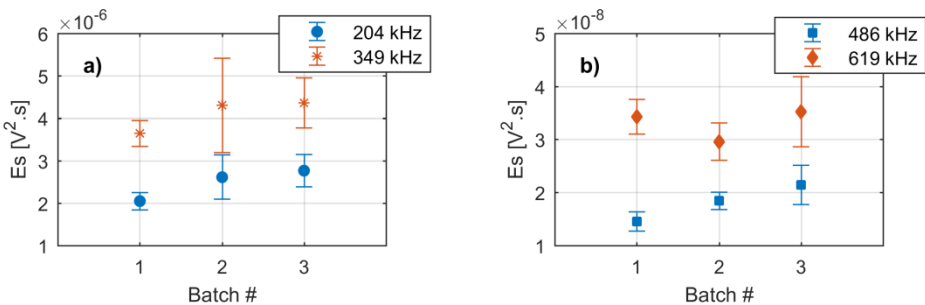


Figure 5.14. Time-domain signal energy for each batch at all excitation frequencies.

The high standard deviation of the mean values makes it very difficult to establish a clear logical trend. This large data scatter seems to be related to intra-batch variability. As explained in Section 5.2, during the preparation of the adherends it was necessary to sand

them twice. First to remove the extra set of ED rows. This created adherend thickness variability, as illustrated in Figure 5.15a). Second to trim the adherends width so that they would fit in the welding fixture. This added extra dimensional variability, as shown in Figure 5.15b). These two sanding operations created dimensional and mass variability among specimens of the same batch. As a result there was variability in final overlap thicknesses in each batch, as plotted in Figure 5.16.

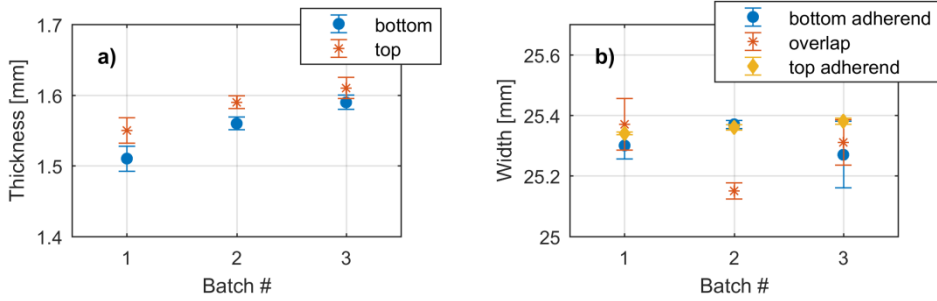


Figure 5.15. a) Variation of adherend thickness per batch; b) Variation of width in the three main zones of the single-lap joint specimens for each batch.

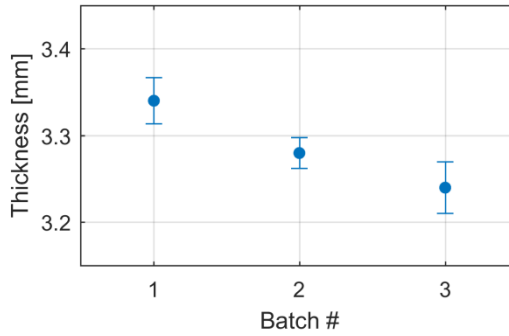


Figure 5.16. Overlap thickness for each batch.

As shown Chapter 4, small variations of weld line thickness (resulting in small variations of final overlap thickness) determine the possible overlap GW modes and influence their compatibility with the adherend GW modes, thereby determining the amount of ultrasonic energy transmitted across the welded joint. As we have seen above, intra-batch adherend dimensional variability led to joints with different final overlap thicknesses. This means each specimen was in fact tested at a different ‘frequency \times thickness’ point of the dispersion curves (see Figure 5.6), even though the excitation frequency was the same. Consequently, the possible adherend and overlap guided wave modes and their compatibility were different for each specimen, and so was the received signal energy. The effect of that variability is strongly felt in the GW signal energy results because the number of overlap modes is large and their characteristics vary sharply with frequency, as depicted in Figure 5.6b).

Nevertheless, Figure 5.14 clearly shows that at 486 kHz the energy for batch 1 is lower than for batch 2, which is in agreement with the expected results. The weld interface

of batch 1 is thicker and still has some unwelded regions, consisting of a larger acoustic impedance mismatch than in the case of batch 2, and thereby transmitting less energy than in the case of batch 2.

The lack of a clear trend in the energy results makes it impossible to use them for indicating the presence of the different manufacturing defects. However, they constitute strong evidence that tenuous intra-batch variability has a relevant impact on the GW test signals, despite the SLSS results showing adequate process consistency.

5.4.3.2. Characteristic frequency

According to Singher [8] and as explained in Section 2.4.3.2, the spectrum of the excited ultrasonic GW signal is always shifted towards the lower frequencies after passing through an adhesive bond. That negative shift increases when there is a delamination or a disbond. So it is possible to infer the bond strength by extracting the characteristic frequency shift (Δf_{ch}). For this study it was decided to assess the sensitivity of this signal feature to manufacturing defects in the ultrasonic weld, with a special focus on adherend fibre bundle distortion. To that end, the following hypothesis was formulated. As it is known from theory, the propagation of ultrasonic GW in composites follows the anisotropy of the material (see Section 2.4.4), i.e. they propagate preferentially along the directions with the highest stiffness, which in turn depend on the directions of the fibres. If the ultrasonic GW were scattered sideways by the distorted fibre bundles of the adherends, then the GW would be transmitted across the joint in more oblique directions which in turn would originate more reflections from the edges. These reflections would then be superimposed, thereby adding more side-frequencies to the signal. This would induce a more spread frequency spectrum and a larger negative Δf_{ch} .

As in [8], the characteristic frequency (f_{ch}) was computed according to Equation (2.31). The shift Δf_{ch} was then calculated as the characteristic frequency difference between the sensed signal and the excitation. The results for each batch, at each frequency are presented in Figure 5.17.

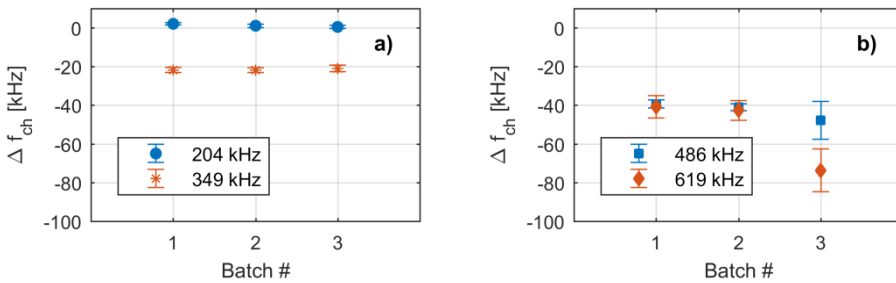


Figure 5.17. Characteristic frequency shift for the three batches at all excitation frequencies.

At 204 kHz there is almost no shift for any of the batches, with Δf_{ch} ranging between 2 kHz for batch 1 and 0.5 kHz for batch 3. At that frequency the only overlap GW mode shape which has a non-null in-plane component at the weld interface is the S0, as shown in Figure 5.18a). It has a wavelength of around 30 mm, which is larger than the overlap thickness and overlap length, and thus the weld line does not seem to have the negative shifting effect on f_{ch} [8]. At 349 kHz there is a negative Δf_{ch} of about -20 kHz, meaning

there is an in-plane interaction with the weld line. Since the S0 mode is still the only overlap GW mode shape with a non-null in-plane component at the weld interface, the Δf_{ch} value can be attributed to the wavelength of the S0 mode being approximately equal to the overlap length. However, this same fact prevents the detection of discontinuities within the overlap length by the S0 mode. In other words, the interaction is still not detailed enough to enable the differentiation between batches.

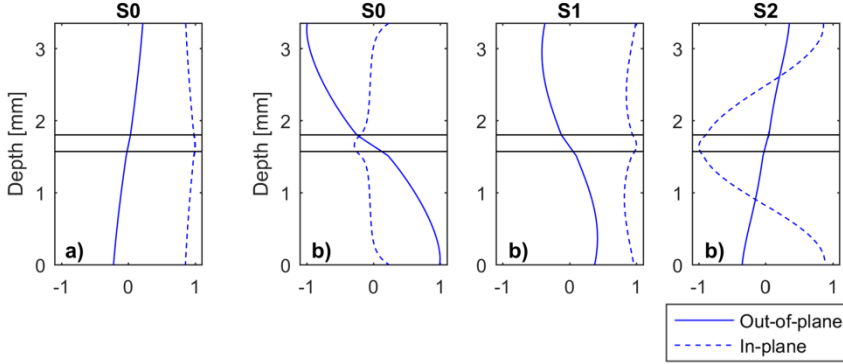


Figure 5.18. Guided wave displacement mode shapes with non-null in-plane component at the weld interface, for batch 3 overlaps, typically occurring at a) 204 and 349 kHz, and b) 486 and 619 kHz. The mode shapes were extracted by using the “Mode Shapes” tool of DISPERSE™ after tracing the dispersion curves in Figure 5.6. The dimensions are not exactly to scale and are only meant to highlight the boundaries within the overlap.

At 486 and 619 kHz, there is a more pronounced negative Δf_{ch} for all batches, together with an increase in standard error, meaning that the interaction with the weld interface is stronger than at 204 and 349 kHz. This is caused by an increase in the number of overlap GW mode shapes with non-null in-plane component at the weld interface from one to three: S0, S1 and A2 (see Figure 5.18b). Nevertheless, the scatter shown for batch 3 at 486 kHz prevents clear conclusions about the differences between batches 2 and 3. This scatter is probably due to the fact that only the S0 wavelength (around 4 mm) is smaller than the overlap length, while the S1 and A2 wavelengths are larger (around 13 and 28 mm, respectively), therefore still hindering a detailed interaction with the weld interface for all measurements of batch 3. But at 619 kHz, we observe that while Δf_{ch} is almost constant for batches 1 and 2, there is a clear increase in negative Δf_{ch} from batch 2 to batch 3, which can only indicate the presence of adherend fibre bundle distortion. It is possible to verify that the spatial resolution of the interaction with the weld interface was increased because both S0 and S1 wavelengths are both smaller than the overlap length (around 3 and 10 mm, respectively), and only the A2 wavelength remains larger than the overlap length. Therefore, the results for 619 kHz corroborate our hypothesis. Although it was not possible to detect the unwelded areas, the characteristic frequency shift appears to be a suitable parameter to indicate the presence of adherend fibre bundle distortion, as long as there are multiple overlap GW mode shapes with non-null in-plane component at the weld interface and with wavelengths smaller than the overlap length.

5.4.3.3. Time-of-flight

When considering ultrasonic GW propagation in composite materials, particle motion along one direction can induce motion in the perpendicular one, because the fibre direction changes across the thickness of the laminate. Consequently, all GW modes are coupled, some of them with very similar group velocities, as in the case of the S₀ mode and the SH₀ mode. This makes it almost impossible to identify the different GW modes, and to correlate their changes to interactions with different damage types [9]. Additionally, as introduced in Section 2.4.3.2, group velocity has been shown to be positively correlated to the bond strength of joints [8,10]. The group velocity is inversely proportional to the TOF (time-of-flight), i.e. the time a certain wave group takes to propagate along a certain known distance. Taking these two aspects into account, the definition of ToF was adapted in order to avoid incorrect conclusions. In our experiment, we define TOF as the time interval between the maximum amplitude point of the excitation pulse and the maximum amplitude point of the sensed signal. This definition allows a direct correspondence between ToF and group velocity to be established, without requiring a direct calculation of the group velocity of any specific GW mode. The point of maximum amplitude of the sensed signal may correspond to the maximum amplitude point of a directly arriving GW mode, but it may also be the result of constructive interference between a direct arrival and a reverberation, or between a direct arrival and a reflection, or both. Nevertheless, any difference in the time at which that maximum amplitude point occurs at a specific frequency can be attributed to a change in the group velocity of one or more GW modes. Therefore, by capturing differences in TOF defined in this way, it is possible to indirectly assess changes in group velocity. The results for the three batches at each excitation frequency are plotted in Figure 5.19.

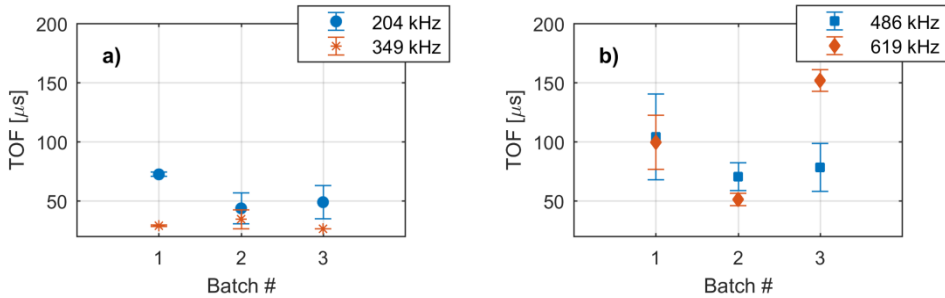


Figure 5.19. Time-of-flight for the three batches at all excitation frequencies.

As with the signal energy results, there is considerable variability within batches. However, in the cases of 204 and 619 kHz it is possible to identify a clear drop from batch 1 to batch 2 of about 29 and 48 μs, respectively. The fact that a clear TOF drop from batches 1 to 2 was consistently found at 204 and 619 kHz appears to correlate well with the magnitude of the changes occurring at the weld interface in the transition from batch 1 to batch 2 conditions. While the thickness variation from batch 1 to batch 2 was approximately the same as from batch 2 to batch 3 (see Figure 5.16), the joint had the most pronounced variation from batches 1 to 2, as it is in this transition that the joint becomes fully welded and the weld line continuous. This transformation had a marked effect on the single-lap shear strength, with batch 1 specimens consistently having a substantially lower

failure load than those of batch 2 specimens, as seen in Figure 5.20 (see the average SLSS values for each batch in Figure 5.7). Therefore, corroborating the proportionality of TOF to weld strength. It is important to note that the TOF drop at 204 kHz is three orders of magnitude higher than the values found in Chapter 4 for the maximum TOF difference caused only by differences in weld line thickness at the same excitation frequency.

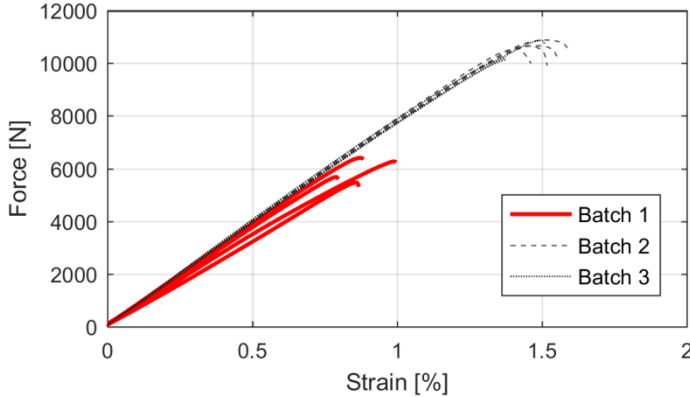


Figure 5.20. Force-displacement curves from the single-lap shear tests.

Also in Figure 5.19b), for batch 2 at 619 kHz, it is possible to clearly identify a global minimum at the frequency. From batch 2 to batch 3, the molecular interdiffusion and the crystallographic structure of the weld line are almost unaltered, and the main change is the distortion of adherend fibre bundles, (as visible from the comparison of Figure 5.8 in Section 5.4.1 and Figure 5.11 in Section 5.4.2.2) with no visible effect on the load-displacement curve slope (see Figure 5.20). As shown in subsubsection 5.4.3.2 the strongest and most detailed interaction of the GW with the weld interface occurs at 619 kHz, with the distorted fibre bundles of the adherends scattering the waves sideways and inducing extra reflections from the overlap edges. The occurrence of these extra reflections can clearly be identified by the larger number of narrow wave packets in the signals of batch 3 when compared to signals from batch 2, as shown in Figure 5.21. These reflections arrive at time instants very close to each other and interfere constructively, generating a wave packet with maximum amplitude at a later time than for batch 2. As a consequence, the ultrasonic energy arrives at the sensor at a slower rate for batch 3 than for batch 2, as illustrated by the corresponding average normalised cumulative energy curves in Figure 5.22.

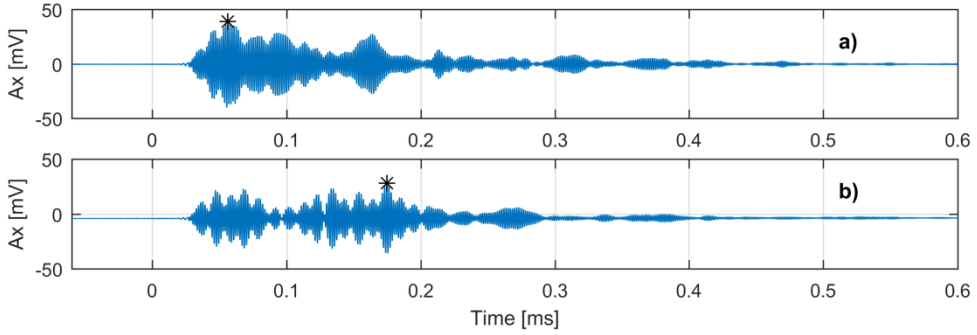


Figure 5.21. Ultrasonic GW signals from a) batch 2 (specimen B02-04) and b) batch 3 (specimen B03-04). The point of maximum amplitude is indicated with an asterisk.

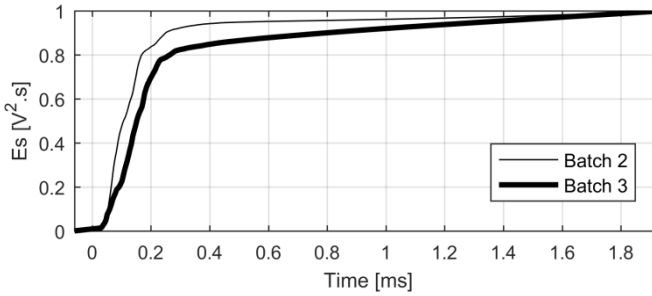


Figure 5.22. Average normalized cumulative energy curves for batch 2 and batch 3.

Given the results presented here, it seems that TOF is sensitive to both unwelded areas interspersed with welded zones and adherend fibre bundle distortion. Nevertheless, if Δf_{ch} and TOF are analysed together, it is possible to distinguish these two defective scenarios:

- a) Null Δf_{ch} and high $\Delta TOF \rightarrow$ Unwelded areas interspersed with welded zones;
- b) High Δf_{ch} and high $\Delta TOF \rightarrow$ Adherend fibre bundle distortion.

This detection criterion requires the definition of low-high thresholds for Δf_{ch} and ΔTOF . For Δf_{ch} the threshold is set at -20 kHz, based on the lowest non-null average values observed among all tested frequencies (see Figure 5.17a). For ΔTOF the threshold is set at 28 μs , based on the minimum average TOF difference that allows a distinction between batch 1 and 2 at 204 kHz (see Figure 5.19a). Using these thresholds, the obtained detection accuracy for unwelded areas is around 60% at 204 kHz, while the detection accuracy for adherend fibre bundle distortion is around 100%.

5.4.3.4. Correlation coefficient

As in Chapter 4, it was decided to resort to the CC (correlation coefficient) in order to quantify signal shape variations. The CC was computed between each batch 2 specimen and each specimen of the other batches for each frequency. The CC was first computed between full time-domain signals, i.e. without excluding any information about signal

amplitude or phase. It was decided to take the complement of the CC ($CC_{comp} = 1 - CC$) as in Equation (2.23) (Section 2.6.4.1) in order to make it a direct indicator of the differences between signals, i.e. the higher CC_{comp} , the larger the difference. The results are plotted in Figure 5.23.

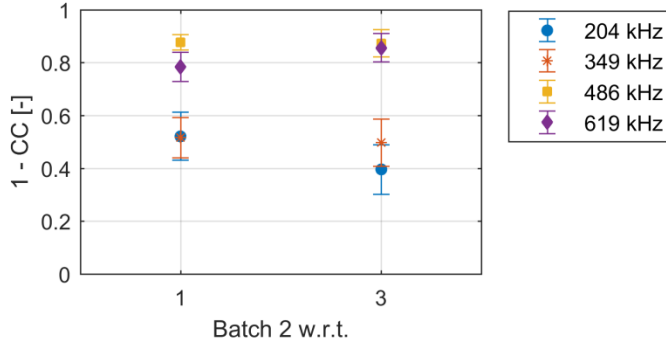


Figure 5.23. Complement of the CC between the full time-domain signals from batch 2 and the other batches for each excitation frequency.

It is possible to see that at 204 and 349 kHz the CC_{comp} values for both batches are grouped between 0.3 and 0.6, while at 486 and 619 kHz, they are grouped between 0.7 and 0.9, without a clear difference in level between batch 1 and batch 3. Despite the relatively large scatter, one could argue that at 486 and 619 kHz there were more GW signal changes than at 204 and 349 kHz. However, when phase information is excluded and the CC_{comp} is computed between the time-domain signal envelopes (see Figure 5.24a), all the obtained values seem to cluster between 0.1 and 0.3, with much lower standard error than in the case of the full time-domain signal. This shows that most of the GW signal shape changes are due to phase variations. In fact, the lower standard errors show that the consequences of intra-batch variability in ultrasonic GW metrics are mainly due to signal phase differences. This is in agreement with the conclusion from Chapter 4 that transformations at the weld interface affect ultrasonic GW propagation mainly by causing differences in reverberation pattern, and in the interference between reverberations and directly arriving groups.

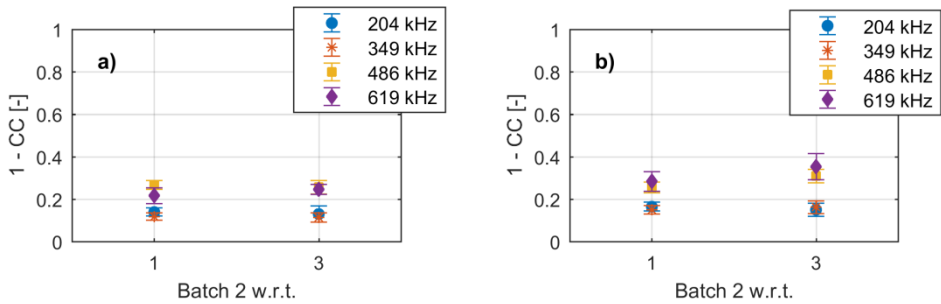


Figure 5.24. Complement of the CC between batch 2 and the other batches for each excitation frequency for a) the time-domain signal envelopes, and for b) the frequency-domain signals.

The CCcomp was also computed for the frequency-domain signals (see Figure 5.24b), in which phase information is also not taken into account. The results fall approximately in the same range as those in Figure 5.24a). However, there is a larger separation between 204/349 kHz and 486/619 kHz for batch 3, than in Figure 5.24a). This seems to be in agreement with our observations from Section 5.4.3.2 that the frequency spectrum of the signal is more affected by adherend fibre bundle distortion than by unwelded areas.

5.5. Conclusions

The study presented in this chapter builds upon the findings of Chapter 4, and had the goal of understanding the effect of ultrasonic weld manufacturing defects on GW transmission across TpC joints. Triangular EDs integrated into the lower composite adherends enabled the production of defective joints in a controlled manner. The produced defect types were unwelded areas interspersed with welded zones (batch 1), and adherend fibre bundle distortion due to overwelding (batch 3). The reference condition (batch 2) corresponded to the fully welded stage in between the other two, which showed the highest SLSS. Ultrasonic GW tests were performed at four frequencies (204, 349, 486 and 619 kHz). Excitation and sensing were accomplished by thin piezo-ceramic discs installed on the adherends at opposite sides of the overlap.

The negative Δf_{ch} showed a consistent increase with excitation frequency, revealing an increasing strength of the interaction of the ultrasonic GW with the weld interface. At 619 kHz, the interaction was strong and detailed enough to allow the distinction between batch 2 and batch 3. The significant increase in negative Δf_{ch} is attributed to the oblique scattering effect of the distorted fibre bundles on the GW. Thus, although it was not possible to detect the unwelded areas, Δf_{ch} appears to be a suitable parameter to indicate the presence of adherend fibre bundle distortion.

At 204 and 619 kHz, the lowest TOF was consistently found for the reference batch. The batch 1 joints had a significantly higher TOF than the reference specimens, meaning the wave group of maximum energy was slower for that defective case than for the reference one. Given the known sensitivity of TOF to joint stiffness changes, the results were considered to be well correlated with the lower failure load of the single-lap tests performed on batch 1 joints. Also at 619 kHz, batch 3 was found to have the highest TOF of all. This was due to the oblique scattering effect of the distorted fibre bundles on the GW, which caused the extra reflections from the overlap edges to interfere constructively and form the wave packet of maximum amplitude at a late time instant. Therefore it was concluded that TOF is sensitive to both unwelded areas interspersed welded zones and adherend fibre bundle distortion.

The analysis of the CC, computed between each batch 2 specimen and each specimen of the other batches for each frequency, added extra confidence to the conclusion that the frequency spectrum of the signal is more affected by adherend fibre bundle distortion than by unwelded areas.

In summary, by combining Δf_{ch} and TOF analysis it was possible to detect and distinguish the two defective scenarios. The case of null Δf_{ch} and high ΔTOF with respect to the reference corresponds to unwelded areas interspersed with welded zones, with a detection accuracy around 60%. The case of high Δf_{ch} and high ΔTOF with respect to the reference corresponds to adherend fibre bundle distortion, with a detection accuracy of 100%.

The research presented in Chapters 4 and 5 provided an understanding of GW interaction with the internal structure of the TpC ultrasonic welds, and thus an answer to the research question Q1). It showed that GWs are sensitive to manufacturing-related variations that can occur in both pristine and defective joints, and thereby established an initial approach for diagnosing manufacturing defects in ultrasonically welded TpC joints. The conclusions can potentially be used for a more adequate selection of the DI and corresponding diagnostic threshold, thereby being a valuable contribution for reducing the occurrence of false positives. In fact, since the fusion bonding in both ultrasonically welded joints and co-consolidated joints works through the mechanism of molecular interdiffusion, the physical principles behind the diagnostic approach in Chapters 4 and 5 were applied in Chapter 8 to detect damage in the component-scale torsion box panel. In turn this is an important step towards the development of SHM capabilities for modern TpC aircraft structures, where early detection of incipient defects is crucial to prevent unexpected failures.

5.6. Notes on the SHM system design

For the GW tests described in Chapter 4 there were limited resources for both the actuators and sensors. Not only was it impossible to choose the dimension and material of the PZT wafers, but also they were available in insufficient number for both actuation and sensing functions. Consequently, only the excitation signal was allowed to be defined, and the sensing capabilities were ensured by general purpose, wide band PZT transducers. In that case, the criteria listed in Section 4.3.2 were enough to accomplish the goal of the study, although they allow for some arbitrariness.

When proceeding to the research of Chapter 5, the situation was different. There was total freedom to define all the design variables, including transducer dimensions, PZT material and excitation signal, and it was possible to employ the same PZT wafer for both GW actuation and sensing. At that time, it was understood that, although the criteria in Section 4.3.2 could be used again, leaving the selection of the transducer dimensions and PZT material for a more or less informed decision, they were not suitable for designing the SHM system for the future tests on the component-scale torsion box panel (see Section 3.1). As discussed in Section 2.9, in GW testing of real-scale (1:1) composite structures the large propagation distances and the geometric-material complexity become preponderant factors that cannot be neglected if the SHM system is to achieve a certain minimum performance. Moreover, if certification of full-scale SHM systems is to be accomplished in the near future, the SHM system design process should be as consistent and repeatable as possible, and thus not be dependent on unfeasible, pure-GW-mode based approaches. In short, a systematic approach was lacking.

This was taken as the opportunity to address research question Q2) and develop a new SHM system design methodology which would take into account the multiple quantitative parameters governing the coupled physics of the transducer, structure, and equipment, without resorting to the simplistic approach of wavelength tuning (see Section 2.4.5), and could be consistently applicable to any level of the pyramid of Figure 3.1 from element scale to full scale. That new methodology is presented Chapter 6.

References

1. Ochôa P, Villegas IF, Groves RM, Benedictus R. Diagnostic of manufacturing defects in ultrasonically welded thermoplastic composite joints using ultrasonic guided waves. *NDT & E Int* 2019; 107: 102126.
2. Villegas IF, Palardy G. Ultrasonic welding of CF/PPS composites with integrated triangular energy directors: melting, flow and weld strength development. *Compos Interface* 2017; 24(5): 515-528.
3. Villegas IF. In situ monitoring of ultrasonic welding of thermoplastic composites through power and displacement data. *J Thermoplast Compos* 2015; 28(1): 66-85.
4. Ochôa P. Supporting data for Ultrasonic guided wave and single-lap shear tests in defective ultrasonically welded thermoplastic composite joints. 4TU.Centre for Research Data. Dataset, 2019. <https://doi.org/10.4121/uuid:190ac321-ad31-456c-919e-564f7e6333ef>.
5. Kundu T, Maji A, Ghosh T and Maslov K. Detection of kissing bonds by Lamb waves. *Ultrasonics* 1998; 35: 573-580.
6. Ochôa P, Villegas IF, Groves RM, Benedictus R. Experimental assessment of the influence of welding process parameters on Lamb wave transmission across ultrasonically welded thermoplastic composite joints. *Mech Syst Signal Pr* 2018; 99: 197-218.
7. ASTM D1002-10, Standard Test Method for Apparent Shear Strength of Single-Lap-Joint Adhesively Bonded Metal Specimens by Tension Loading (Metal-to-Metal), 2010.
8. Singher L. Bond strength measurement by ultrasonic guided waves. *Ultrasonics* 1997; 35: 305-315.
9. Putkis O, Dalton RP, Croxford AJ. The anisotropic propagation of ultrasonic guided waves in composite materials and implications for practical applications. *Ultrasonics* 2016; 65: 390-399.
10. Singher L, Segal Y and Segal E. Considerations in bond strength evaluation by ultrasonic guided waves. *J Acoust Soc Am* 1994; 96(4): 2497-2505.

6

SHM system design

When targeting the certification of GW-SHM systems for full-scale structures, the number of factors influencing GW propagation, and thus the performance of the SHM system, increases dramatically, and the lack of systematic quantitative criteria for selecting the SHM system parameters ends up hampering the reliability of damage diagnostic.

This chapter proposes a novel methodology to consistently define the GW excitation frequency, geometry and positioning of the piezoelectric transducers which is not tuned for a single damage size, does not resort to unrealistic usage of pure guided wave modes, and is applicable to a generic real-scale (1:1) composite aircraft primary structure.

6.1. Introduction

The transition to higher levels of the building-block pyramid implies that all SHM system parameters, become equally important, and not just the GW excitation signal ones. Even in the laboratory environment, GW testing of component-scale structures should take into account the possibility of multiple damage scenarios and a large diversity of ultrasonic scattering interactions. If the near-future need for certifying GW-SHM systems is considered, attention must be paid to the accomplishment of the SHM system mission. In this context, the design of the SHM system plays a determinant role, and it is a step where it is possible to prune some of the uncertainty that GW testing of real-scale composite structures entails.

However, as discussed in Section 2.9, it is not possible to achieve this if the design is based on criteria which are only applicable in overly simplistic cases (e.g. wavelength tuning effect), or if the criteria do not treat the transducer-structure-equipment as a whole set of coupled physical systems which affect each other. Therefore, this chapter addresses research question Q2) by proposing a novel multi-parameter methodology for systematically and quantitatively designing a GW-SHM system. The proposed design methodology is based on sensor output, coupled electro-mechanical (EM) response of the transducer-structure assembly, energy transfer from the bonded PZT transducer to the structure, wavefront coverage of the monitored area, and measurement equipment capabilities.

This chapter is structured in four sections. Section 6.2 explains the theoretical principles behind the development of the design methodology. Section 6.3 starts with a summary of the commonly adopted criteria for selecting the excitation signal and the transducer geometry. After justifying why it is not reliable to use those criteria for a real SHM application with real geometric complexity, the proposed novel SHM system design methodology is presented. Section 6.4 reports the implementation of the proposed design methodology for a component-scale composite aircraft primary structure. At the end (Section 6.5), the reader is directed to Chapter 8, where the experimental validation of the proposed design methodology is described and discussed in detail. The conclusions drawn from the development and validation of the novel design methodology can thus be found in Chapter 8.

6.2. Theoretical basis

6.2.1. Total sensor output

The performance of an SHM system is influenced by the signal-to-noise ratio of the sensor response. Therefore, one should look at the total GW response of a sensor as a function of frequency, as reported in previous studies [2-5]. For SHM transducer network design purposes, the wavelength solutions of the Rayleigh-Lamb wave equation for the structure should be taken into account, together with the shape of the PZT transducer, and the influence of the actuator on the sensor. Since it is desired to use circular transducers for wavefront omnidirectionality, the formulation presented by Sohn and Lee [3] for the sensor output voltage, V_o , is adopted here. Then the same logic as Raghavan and Cesnik [4] is followed, that $|V_o|$ is inversely proportional to the sensor radius, i.e. the smaller the sensor radius, the higher the sensor output voltage. On the other hand, $|V_o|$ also has a harmonic dependence on the actuator radius.

Therefore, if the effect of both the actuator radius and frequency are to be assessed, then $|V_o|$ can be written as being directly proportional to the harmonic function $f(\xi^S, \xi^A, r_a)$ on the right-hand side of

$$|V_o| \propto \left| r_a \left[\sum_{\xi^S} \xi^S J_1(\xi^S r_a) + \sum_{\xi^A} \xi^A J_1(\xi^A r_a) \right] \right| = f(\xi^S, \xi^A, r_a) \quad (6.1)$$

where J_1 is the Bessel function of the first kind of order 1, r_a is the actuator radius, and ξ^S and ξ^A are the wavenumbers of symmetric and antisymmetric Lamb wave modes, respectively (which in turn depend on their frequency). By evaluating the periodic behaviour of this function, it is possible to determine at which frequency the sensor output voltage reaches a maximum for a certain actuator size.

6.2.2. Electro-mechanical response of PZT transducer

The analysis of a piezoceramic transducer must include the study of its EM behaviour coupled with the mechanical response of the structure to which it is attached, because the dynamics of a bonded transducer differs considerably from the free condition [6]. During excitation, the piezoceramic may undergo two different types of extreme states, resonance and anti-resonance. The first is characterized by a sudden and pronounced increase in electrical current, accompanied by greatly amplified vibration, which may lead to rupture and/or disruption of the material. This occurs when the admittance tends to infinity and the impedance approaches zero. The second state corresponds to the opposite situation when the admittance drops to zero and the impedance tends to infinity, resulting in almost no electrical current being converted to mechanical response. There is a very narrow frequency window where it is possible to obtain very high amplitude GW signals at the resonance. Furthermore, the points of resonance and anti-resonance typically occur very close to each other, with an unstable transitory regime, which is detrimental for reliable SHM applications, where it is desired to have a steady generation of GW signals without any perturbations. Therefore, the unstable transitory regime of the resonance/anti-resonance should be avoided. The admittance, Y , of a PZT transducer can be calculated according to [6]

$$Y(\omega) = i\omega C \left\{ 1 - k_p^2 \left[1 - \frac{(1 + \nu_a) J_1(\gamma r_a)}{\gamma r_a J_0(\gamma r_a) - [(1 - \nu_a) - \beta(1 + \nu_a)] J_1(\gamma r_a)} \right] \right\} \quad (6.2)$$

where C is the electrical capacitance, k_p is the planar electromechanical coupling coefficient, ν_a is the Poisson's ratio of the piezoceramic material, J_0 is the Bessel function of the first kind of order 0, and $\gamma = \omega/c_{p,pzt}$ with ω being the angular frequency and $c_{p,pzt}$ the bulk pressure wave speed in the piezoceramic material. Because this equation is derived for the bonded transducer condition, it includes the effect of the structure through the ratio of the dynamic stiffness of the structure to that of the PZT, $\beta = k_{str}(\omega)/k_{pzt}$. The value of dynamic stiffness for the PZT transducer is considered to be independent of frequency and can be computed according to formulation given by Giurgiutiu [6]. In the case of the structure, the dynamic stiffness, k_{str} is calculated according to the formulation presented by Giurgiutiu and Zagari [7,8]. Because these equations take structural vibration modes into

account, values for the modal damping were taken from literature [9,10]. The impedance Z is equal to the multiplicative inverse of Y , i.e. $Z = 1/Y$.

The resonance points can be found by calculating the zeros of the denominator of Equation (6.2), while the anti-resonance points can be obtained by computing the zeros of the entire expression inside the curly brackets of Equation (6.2).

6.2.3. Energy transfer from the PZT transducer to the structure

The shear lag model of the bonding layer between the piezoceramic transducer and the structure derived by Giurgiutiu [2] can be used to perform an energy balance of the entire actuation system. For an SHM application it is important to maximize the energy transfer from the actuator to the structure. According to the shear lag model, and following the notation adopted by Giurgiutiu [11] the part of the energy generated by piezoelectric transduction that is transmitted to the host structure, W_{str} , can be approximately calculated by

$$W_{str} = \frac{\alpha_{mode}\psi}{(\alpha_{mode} + \psi)^2} \left(\frac{1}{2} E_a \varepsilon_{ISA}^2 t h_a 2r_a \right) \cdot I(\Gamma r_a) = \frac{\alpha_{mode}\psi}{(\alpha_{mode} + \psi)^2} \cdot W_{ISA} \cdot I(\Gamma r_a) \quad (6.3)$$

where E_a and $t h_a$ are the Young's modulus and thickness of the PZT transducer, respectively, $\varepsilon_{ISA} = -d_{31} \times (V/t h_a)$ is the strain induced by a voltage V on the PZT, $I(\Gamma r_a)$ is the bond efficiency factor, ψ is the two-dimensional relative stiffness coefficient between structure and PZT, and α_{mode} is a shear coefficient which “depends on the stress, strain and displacement distributions across the plate thickness” [11]. The bond efficiency factor in turn depends on the parameter Γ defined for the two-dimensional shear-lag model, as presented by Giurgiutiu [11].

If W_{str} is normalised by the total induced-strain energy generated through piezoelectric transduction, W_{ISA} , then the portion of that energy which is transmitted to the structure becomes a function of PZT thickness, for a certain PZT diameter. Therefore, the maximum of the normalised energy transmitted to the structure is a useful way to obtain a preliminary value for the theoretically optimal actuator thickness.

6.2.4. Measurement equipment capabilities

The selection of frequency and transducer size should also take into account the capabilities of the waveform generator. Although amplification of the excitation signal may be employed, if the waveform generator cannot be operated at its maximum allowable voltage, then it is not possible to maximize the voltage at the terminals of the actuator. Therefore, the waveform generator could be considered as the limiting element in the GW test setup, and the maximum allowable electrical current should be derived from maximum allowable voltage of the waveform generator.

The waveform generator can only generate up to a certain level of voltage, V , which has to be transmitted through a channel with a specific impedance, Z . This imposes a maximum limit on the electrical current, I , that can be supplied to the circuit, according to Ohm's law $V = I \times Z$. If the electrical current required by the circuit downstream of the waveform generator is above the maximum value that can be supplied, then the waveform generator will automatically adapt the generated voltage in order to reduce the current. This occurrence could prevent the waves from being generated with the highest possible

amplitude, which in turn affects the signal-to-noise ratio and the quality of the measurements. Therefore, the chosen frequency/actuator diameter combination should allow the corresponding electrical current to be below the maximum allowable current for the waveform generator. In other words, if the highest possible voltage amplitude can be transmitted with an electrical current below the maximum allowable value, then the frequency/actuator diameter combination can be used for the operation of the transducer.

In addition to that, it is also important to pay attention to two other constraints. Firstly, the maximum allowable electric field for the piezoceramic material should be respected. Secondly, the digital oscilloscope should be able to operate at a sampling frequency suitable for accurate acquisition of ultrasonic signals (e.g. ten times the centre frequency).

6.2.5. PZT transducer thickness effects

The sensor output response is directly proportional to its thickness [3]. Hence, a thicker PZT is in principle more beneficial, from a sensing point of view. From an actuation perspective, the actuation electrical current $I = YC$ depends on the transducer radius, r_a , and the transducer thickness th_a . This thickness influence is included through the capacitance of the transducer, as described by

$$C = \epsilon_{33}^T \frac{A_{PZT}}{th_a} = \epsilon_{33,r}^T \epsilon_0 \cdot \frac{\pi r_a^2}{th_a} \quad (6.4)$$

where A_{PZT} is the surface area of the PZT, and the product of the relative dielectric constant and the free-space permittivity, $\epsilon_{33,r}^T \epsilon_0$, defines the dielectric constant of the PZT material ϵ_{33}^T . In this case, the thinner the PZT, the higher the capacitance and the higher the actuation electrical current. So, although lower thicknesses promote the generation of a higher actuation voltage (through Ohm's law), the required electrical current might be above the capabilities of the waveform generator (as described in the previous subsection).

6

6.3. Design methodology

6.3.1. Previous approaches

According to the literature referenced in Section 2.4.5, the usually adopted approach for selecting the excitation frequency content and the PZT transducer geometry can be summarised as follows:

- a) GW mode of interest should be as non-dispersive as possible
- b) Higher-order GW modes should be avoided
- c) Frequency should allow mode interaction with damage to be detected
- d) In conjunction with a) and b), the minimum distance resolvable by the mode of interest should be close to the minimum damage size to be detected.

All these criteria are based on the ideal scenario of time-domain discrimination between specific GW modes for extracting signal features. However, that is not a realistic assumption in a real SHM application for composite structures, where the scatter from multiple geometric complexities material anisotropy prevent the recognition of individual

modes. Therefore, criterion a) should be dropped. Criterion b) should also be abandoned as one of the main guidelines if the residual time-trace is used, as only the difference between states matters. Moreover, although the interference of higher-order modes with the fundamental modes can potentially conceal wave features containing information about damage, it can still be argued that at some frequencies the presence of higher-order modes might be advantageous for damage diagnostic, depending on their mode shapes [12]. The concept behind criterion c) (i.e. the higher the frequency, the smaller the wavelength, and the stronger the wave-damage interaction) is important to keep in mind, although the relationship between wavelength and damage size is (partially) lost when frequencies around, or slightly beyond, the cut-off are excited. At those points the wavelength of higher-order modes is quite long which makes wave-damage interaction weak. So criterion c) does not seem useful as a design criterion. The reasoning behind criterion d) is again only valid for a pure mode, which, as mentioned before, does not hold true for a real SHM application. Additionally, none of the aforementioned criteria takes into account the working principles of GW piezoelectric transduction.

To supplement the design criteria, it is important to take into account mode-conversion and direction-dependent GW propagation caused by material anisotropy when designing a GW-SHM system for composite structures. There are interdigital configurations capable of generating ultrasonic GW directionally that take advantage of predominant excitation of one mode over another [13,14-16]. However, when propagating in composite structures with real geometric complexity, the predominantly generated GW mode would undergo mode-conversion at different structural features and become inevitably coupled with the other modes possible at the excited frequency band [17], preventing mode-selective sensing with piezoelectric transducers. More importantly, the use of mode-selective, directional actuators would only exacerbate the direction-dependent characteristics of GW propagation, and would not enable a complete coverage of the area to be monitored.

6.3.2. Proposed design methodology

In order to address this challenge, a novel methodology is proposed for designing the excitation frequency content and the transducer geometry more systematically. Instead of assuming single mode analysis, the aim is to optimize the response and operation of the transducer in conjugation with the measurement equipment, namely by focusing on the physical principles explained in Section 6.2. The selection criteria are formulated below.

- A. The PZT sensor output function should have at least one local maximum in a frequency bandwidth where only zero-order GW modes can be excited.
- B. The PZT sensor output function should have more than only one local maximum. More than one excitation frequency should be tested, in order to explore the detection capability of the network at higher frequencies.
- C. The chosen frequencies should not coincide with, or be in the close vicinity of, EM resonances or anti-resonances of the bonded PZT transducer.

- D. The electrical current required to drive the chosen PZT transducer at the chosen

frequency should be below the maximum allowable current for the waveform generator output channels. In other words, the required electrical current for the chosen PZT transducer, at the chosen frequency, should allow a waveform to be generated with the desired voltage amplitude.

- E. The selection of the PZT transducer thickness should take into account the maximization of energy transfer from the actuator to the structure.

6.3.2.1. Considerations about the transducer shape

One of the most important characteristics for the transducer network to have operational flexibility is to have interchangeable actuator/sensor functions. In other words, the coverage of the monitored area is maximized if all the GW propagation paths are explored, which in turn can be achieved by using each actuator as sensor, and vice-versa. Therefore, the PZT transducers should all have the same dimensions and properties, at least within each inspected area.

Furthermore, the wavefront coverage of the monitored area by each individual transducer should also be maximised, and those wavefronts should be (approximately) omnidirectional when generated in (quasi-) isotropic material, in an effort to increase the robustness against direction-dependent GW propagation. Additionally, as explained in Section 6.3.1, and as highlighted by criterion B, it is useful to have the possibility to excite different frequencies in order to explore different damage sensitivities of GWs. For all the above reasons, it was decided to develop the design methodology based on thin piezoceramic discs.

6.3.2.2. Considerations about transducer network configuration

The number and positions of the transducers in the network should be chosen so that there is enough virtual wavefront coverage of the region around each critical area. In other words, the monitored area would be covered most efficiently by the wavefronts emanating from all transducers if they would hypothetically generate ultrasounds omnidirectionally at the same time. By maximising the virtual wavefront coverage the cases of anisotropic wave propagation (e.g. wave propagation in composites) are not neglected. Although this is a criterion simply based on visual evaluation, it is well aligned with the concept of multi-path unit-cell network introduced in Section 2.6.4.3 through Equations (2.38) and (2.39).

6.3.2.3. Considerations about PZT material selection

If the only purpose of the PZT transducer was GW actuation, then the selection of the PZT material should predominantly focus on d_{31} , because it quantifies the induced strain in the in-plane direction (direction 1, in this case radially) per unit electric field applied in the out-of-plane direction (direction 3). On the other hand, if the only purpose of the PZT transducer was GW sensing, the selection of PZT material should predominantly focus on g_{31} , because it quantifies the induced electric field in direction 3 per unit stress applied in direction 1. Since it is desirable to maximize the amount of GW data acquired from the monitored area, it is crucial that the selected PZT material can be used for both sensing and actuation. Hence it is important that both d_{31} and g_{31} are high. From the materials with the

highest $d_{31} \times g_{31}$ product, the one with the highest g_{31} is chosen so that the sensing sensitivity is favoured.

6.3.2.4. Important design checks

After defining the PZT transducers positioning within the network, it is crucial to check if there is enough space available on the structure for the installation. Finally, the maximum allowable electric field for the PZT material should not be exceeded.

All the steps of the SHM system design implementation are reported in Section 6.4. First, the PZT transducer material is selected in Section 6.4.1. Then Section 6.4.2 describes the application of criteria A to E one by one to each structural area to be monitored. Finally, the result of the application of the guidelines for positioning the transducers within the network is shown in Section 6.4.3.

6.4. Design implementation

The design implementation presented in the following subsections was conducted for PZT disc diameters varying from 5 to 30 mm in steps of 5 mm, and for PZT thicknesses varying from 0.1 to 1 mm in steps of 0.1 mm.

6.4.1. PZT material selection

The values of the piezoelectric charge constant, d_{31} , and the piezoelectric voltage constant, g_{31} for the materials available from the selected PZT supplier (APC International, Ltd.) are presented in Table 6.1. As a result of the application of the guidelines for PZT material selection proposed in Section 6.3.2.3, the chosen material was APC 850.

Table 6.1. Piezoelectric charge and voltage constants in the 31-direction, for the different available piezoceramic materials.

Parameter	APC 840	APC 841	APC 850	APC 855	APC 880
$d_{31} \times 10^{-12}$ [m/V]	-125	-109	-175	-276	-95
$g_{31} \times 10^{-3}$ [Vm/N]	-11.0	-10.5	-12.4	-9.0	-10.0
$d_{31} \times g_{31} \times 10^{-15}$ [m ² /N]	1375	1144.5	2170	2484	950

6.4.2. Study of the critical areas

The application of design criteria A and B to structural areas to be monitored required the Rayleigh-Lamb wave solutions to be calculated in the form of dispersion curves. As shown later in Section 6.4.3, most of the transducers were placed on the skin of the stiffened panel. Thus the dispersion curves were calculated for the skin laminates. As explained in Section 3.2.2, three structural areas of a component-scale torsion box panel were selected for this study: areas 1 and 2 (which have approximately the same thickness and laminate stacking sequence) and area 3. The phase and group velocity dispersion curves for areas 1-2 and area 3 are depicted in Figure 6.1 and Figure 6.2, respectively. They were obtained

with DISPERSE v2.0.20a (Imperial College, London) by using the composite elastic properties in Table 3.2, and the symmetric and quasi-isotropic stacking sequences in Table 3.3 (see Section 3.2.2), all provided by the panel manufacturer.

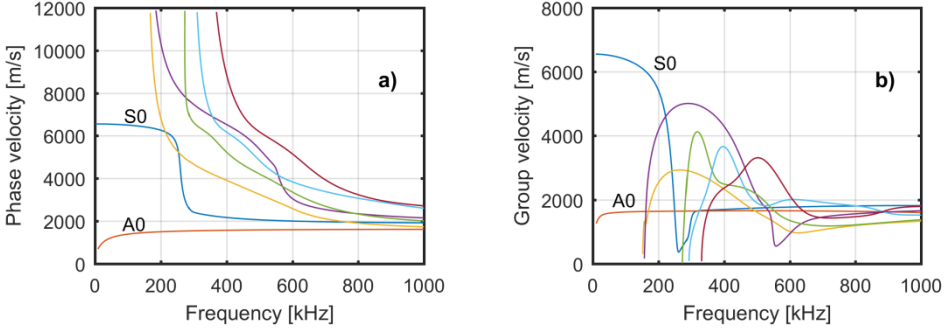


Figure 6.1. Dispersion curves for the skin of areas 1-2: a) phase velocity and b) group velocity. For clarity, higher-order modes with cut-off frequencies above 400 kHz (i.e. modes that were not excited in any of the tests) are not presented.

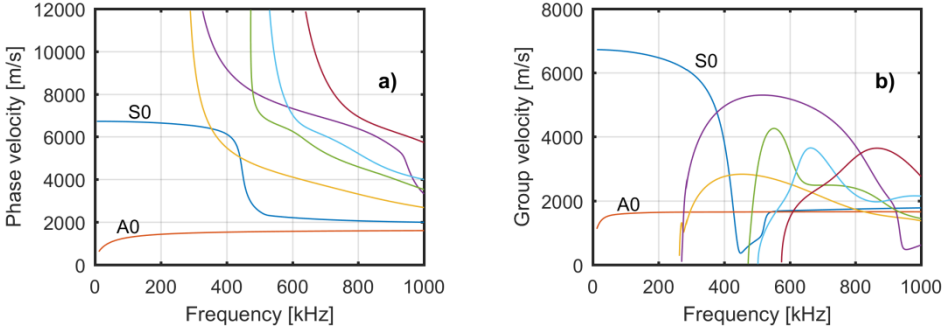


Figure 6.2. Dispersion curves for the skin of area 3: a) phase velocity and b) group velocity.

The phase velocity of the fundamental symmetric Lamb mode (S0) at approximately null frequency and the phase velocity of the fundamental anti-symmetric Lamb mode (A0) at the last calculated frequency were used as longitudinal and shear bulk wave velocities, c_L and c_s , respectively, for computing equivalent Poisson's ratio and equivalent Young's modulus, ν_{eq} and E_{eq} , i.e. elastic properties of the skin "perceived" by the wavefront, as if the material was isotropic. The relationship between the Lamé constants (λ_L and μ_L), density (ρ) for isotropic material and the bulk wave velocities in

$$\begin{cases} \mu_L = \rho c_s^2 \\ \lambda_L = c_L^2 - 2\mu \end{cases} \quad (6.5)$$

was used to solve

$$\begin{cases} \mu_L = \frac{E_{eq}}{2(1+\nu_{eq})} \\ \lambda_L = \frac{\nu_{eq} E_{eq}}{(1+\nu_{eq})(1-2\nu_{eq})} \end{cases} \Leftrightarrow \begin{cases} \nu_{eq} = \frac{\lambda_L/2\mu_L}{2(\lambda_L/2\mu_L)+1} \\ E_{eq} = 2\mu_L(1+\nu_{eq}) \end{cases} \quad (6.6)$$

In turn, E_{eq} was used in design criterion E.

Another important quantity for the application of design criterion A is the frequency bandwidth, as defined in

$$f_{up} = f_c \left(1 + \frac{k_{bw}}{N_{cyc}} \right) \Leftrightarrow f_c = \frac{f_{up}}{\left(1 + \frac{k_{bw}}{N_{cyc}} \right)} ; \quad f_{low} = f_c \left(1 - \frac{k_{bw}}{N_{cyc}} \right) \quad (6.7)$$

where f_{up} is the frequency bandwidth upper limit, f_c is the excitation centre frequency, f_{low} is the frequency bandwidth lower limit, k_{bw} is the so-called bandwidth parameter, and N_{cyc} is the number of cycles in the excitation pulse. According to Wilcox [13], the -40 dB bandwidth definition corresponds to a theoretical value of k_{bw} equal to 2.8. However, the computed -40 dB bandwidth experimental Hanning windowed excitation tone bursts with centre frequencies ranging from 200 to 750 kHz of (acquired from the extra GW tests described in Section 3.2.3) revealed actual values of k_{bw} approximately equal to 1.9. Taking $k_{bw} = 1.9$ and Equation (6.7), it is possible to inversely calculate the necessary f_c if only fundamental GW modes are to be generated, i.e. if f_{up} is to be at the first cut-off (read from the group velocity dispersion curves, because the group velocity is the one at which the pure mode propagates). The values for each area (see Table 6.2) were calculated for an excitation tone burst amplitude-modulated by a Hanning window with N_{cyc} cycles, which has a narrower frequency bandwidth than a simple sinusoid.

Table 6.2. Inversely calculated centre frequency corresponding to a bandwidth upper limit at the first cut-off, for all critical areas.

Critical area	f_{up} [kHz]	f_c [kHz]			
		$N_{cyc} = 5$	$N_{cyc} = 10$	$N_{cyc} = 15$	$N_{cyc} = 20$
Areas 1-2	152.52	109.84	127.70	135.03	139.01
Area 3	263.98	190.10	221.03	233.70	240.60

Finally, it is also important to keep in mind that the larger the number of pulse cycles, N_{cyc} , the longer will be the wave groups in the GW response and the more intense will be the interference between them, thereby increasing the probability of losing damage-related information. Hence, it was decided not to go beyond $N_{cyc} = 10$ to keep the duration of the excited wave groups below 0.1 ms.

6.4.2.1. Areas 1-2

Criterion A: Single sensor output local maximum

Although sensor output voltage V_o is directly proportional to transducer thickness (see Section 6.2.1), Equation (6.1) does not depend on thickness, so neither does the location of the maxima. Hence, it is possible to evaluate criterion A by looking at the graphs independently of the thickness value. As indicated in Table 6.2, if $N_{cyc} = 5$, then the sensor output function, $f(\xi^S, \xi^A, r_a)$, should have at least one local maximum around 110 kHz. By looking at Figure 6.3 it is possible to see that criterion A is satisfied for a PZT diameter, D , of 10 mm with a local maximum at 112 kHz. For PZT diameters of 20 and 30 mm, $f(\xi^S, \xi^A, r_a)$ at 110 kHz is not at a maximum, but it is in an ascending part of the curve and with a value comparable to the maximum for $D = 10$ mm. If $N_{cyc} = 10$, then $f(\xi^S, \xi^A, r_a)$ should have a local maximum around 128 kHz. In this case, criterion A is satisfied for $D = 10, 20$ and 30 mm, since that frequency falls on, or in the close vicinity of a maximum (for $D = 20$ mm there is a maximum at 123 kHz, and for $D = 30$ mm there is a maximum at 132 kHz). In summary, criterion A is satisfied in the following conditions:

- $D = 10, 20$ and 30 mm, with $N_{cyc} = 10$

Criterion B: Multiple sensor output local maxima

From the plots of Figure 6.3 it is also possible to see that criterion B is satisfied for transducer diameters above 10 mm. The frequencies of the relevant local maxima for the PZT diameters identified with criterion A are listed in Table 6.3. It worth mentioning that the peak at around 275 kHz for $D = 20$ mm was not selected as third local maximum because its amplitude and width are small with respect to the neighbouring peaks. In summary, criteria A and B are satisfied in the following conditions:

- $D = 20$ and 30 mm, with $N_{cyc} = 10$

Criterion C: EM response

For the evaluation of this criterion transducer thickness must be taken into account. Therefore, the previously identified candidate diameters are taken and the points of zero and infinite EM admittance for each thickness are calculated according to Equation (6.2). It is relevant to note that the EM resonance and anti-resonance points are always adjacent to each other (as seen in Figure 6.3, for example). Therefore, it is enough to find the EM resonance points. For $D = 20$ mm there are two EM resonances between 0 and 400 kHz, while for $D = 30$ mm there are four. The resonance frequency values vary with transducer thickness.

For $D = 20$ mm, all the three relevant sensor output local maxima (see Table 6.3) are away from any EM resonances. For $D = 30$ mm, the first two relevant sensor output local maxima are away from any EM resonances for all transducer thicknesses. The third local maximum only becomes distant from EM resonances for thicknesses above 0.5 mm. In summary, criteria A, B and C are satisfied in the following conditions:

- $D = 20$ mm, for all thicknesses, with $N_{cyc} = 10$
- $D = 30$ mm, for $th > 0.5$ mm, with $N_{cyc} = 10$

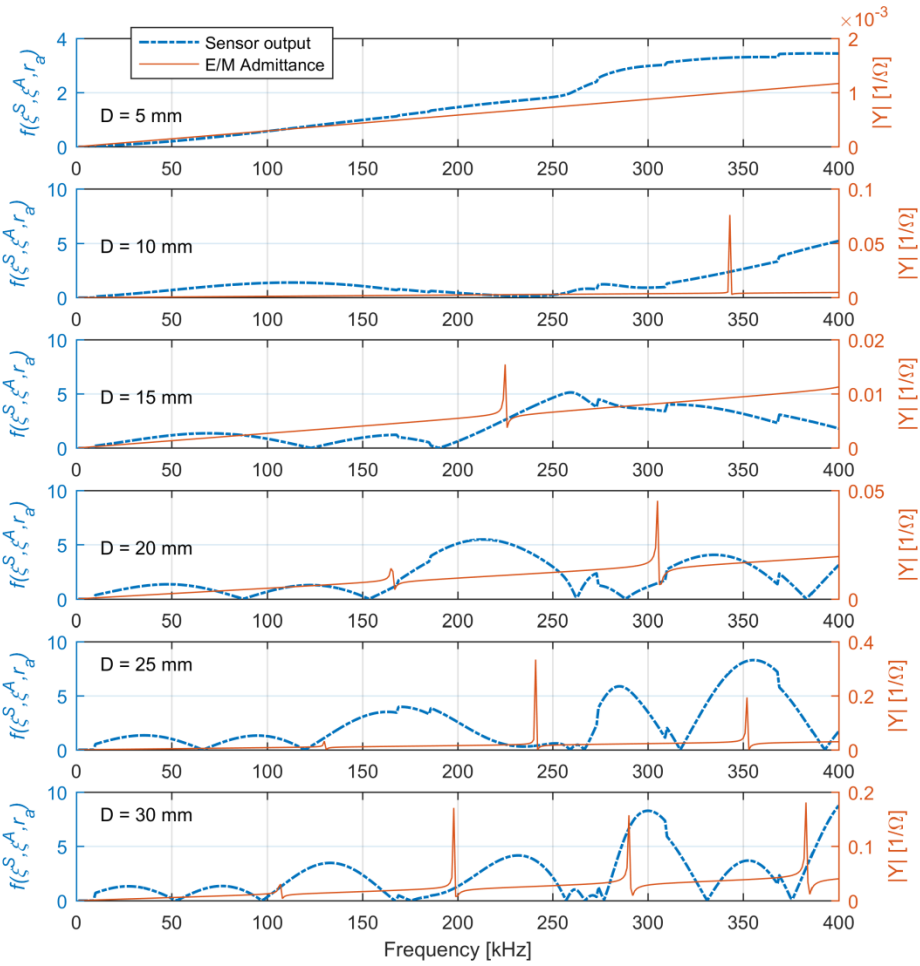


Figure 6.3. Sensor output function and electro-mechanical admittance response (according to Equations (6.1) and (6.2), respectively) of PZT transducer with 0.4 mm thickness and different diameters, for areas 1-2.

Table 6.3. Frequencies of the relevant local maxima of the sensor output in areas 1-2 for the PZT diameters identified with criterion A.

Diameter [mm]	f [kHz]		
	Max. 1	Max. 2	Max. 3
20	123	213	335
30	133	232	300

Criterion D: Electrical current limits

The Agilent 33500B waveform generator available in the laboratory has output channels with $50\ \Omega$ impedance, and the maximum signal amplitude it can produce is 10 Vpp. Hence, the maximum current that can be supplied by the equipment is 0.1 A. The evolution of electrical current as a function of frequency for $D = 20$ mm and different thicknesses (see Figure 6.4) was computed as the product of the inverse of Equation (6.2) (in which the capacitance is defined by Equation (6.4)) and the maximum allowable voltage. It can be seen that only for thicknesses above 0.3 mm is the electrical current at the three previously identified frequencies (see Table 6.3) below 0.1 A. From similar graphs for $D = 30$ mm it was observed that only for thicknesses above 0.6 mm is the electrical at the three previously identified frequencies (see Table 6.3) below 0.1 A. In summary, criteria A to D are satisfied in the following conditions:

- $D = 20$ mm, for $th > 0.3$ mm, with $N_{cyc} = 10$
- $D = 30$ mm, for $th > 0.6$ mm, with $N_{cyc} = 10$

Criterion E: PZT actuator energy transfer

The normalized energy transmitted to the structure by the PZT actuator calculated according to Equation (6.3) is plotted in Figure 6.5 as a function of actuator thickness, for actuator diameters ranging from 5 to 30 mm. For the calculations, the shear modulus and thickness of the bonding layer were assumed to be equal to 2 GPa and 10 μm [2], respectively. Although the curves deviate from each other, they all have an absolute maximum for a thickness equal to 0.3 mm. This means that, in ideal bonding conditions, transmission of ultrasonic energy to the structure is maximized if the transducer is 0.3 mm thick. However, this value falls outside of the design region identified by criteria A to D, which means the adopted PZT thickness does not match the ideal energy transmission conditions. Nevertheless, in the case of $D = 20$ mm, the normalized transmitted energy for $th = 0.4$ mm is only 2.4% lower than for $th = 0.3$ mm, which does not represent a detrimental deviation from the ideal conditions. On the other hand, in the case of $D = 30$ mm, the normalized W_{str} for $th = 0.7$ mm is approximately 16.6% lower than for $th = 0.3$ mm, which is low enough to justify the exclusion of this case from the design space. In summary, criteria A to E are satisfied in the following conditions:

- $D = 20$ mm, for $th = 0.4$ mm, with $N_{cyc} = 10$

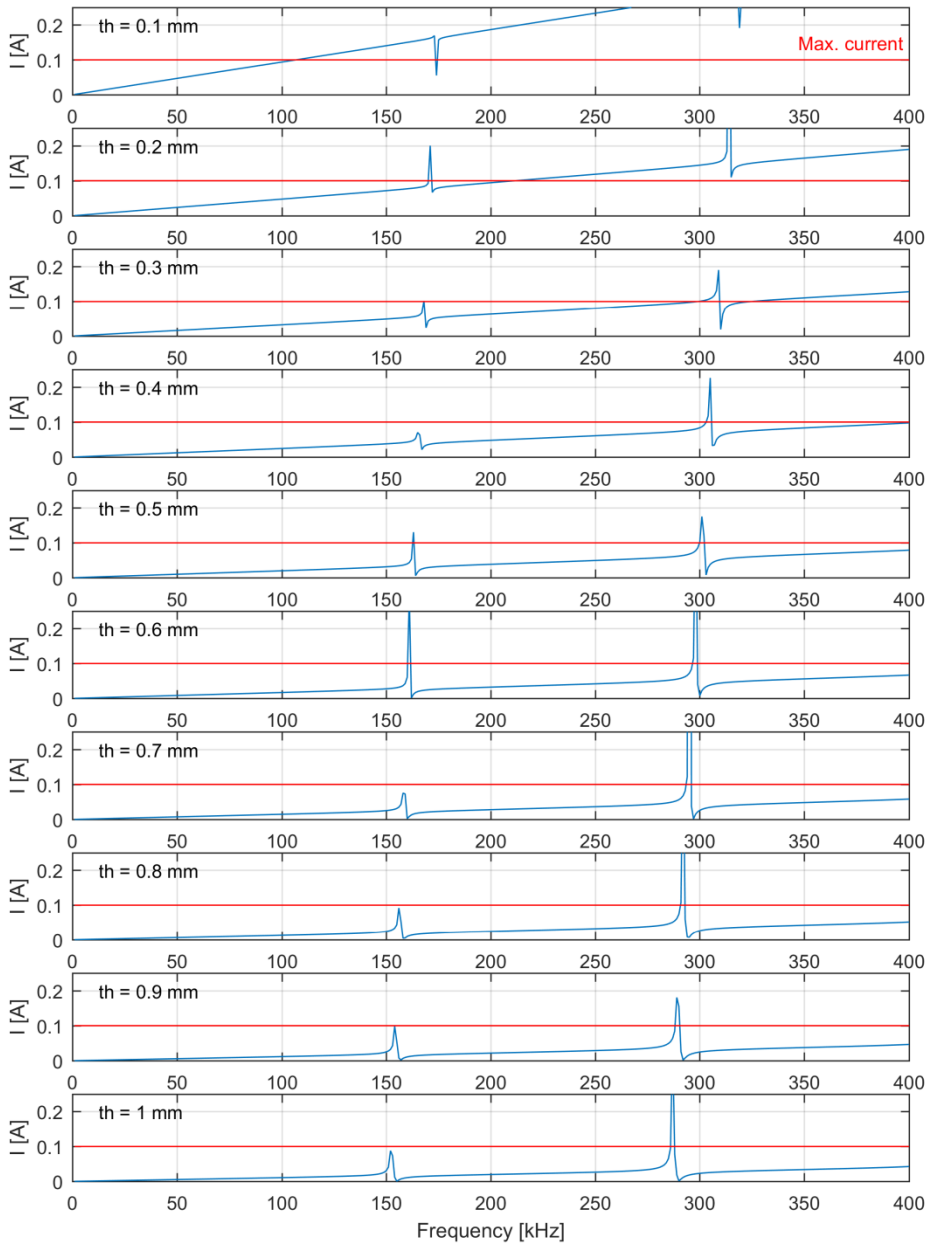


Figure 6.4. Electrical current (computed according to Ohm's law $I = V / Z$, with $Z = 1 / Y$ and Y defined in Equation (6.2)) as function of excitation frequency for $D = 20$ mm, and thickness varying from 0.1 to 1 mm on areas 1-2. The maximum possible current for the waveform is represented by a horizontal line in every graph.

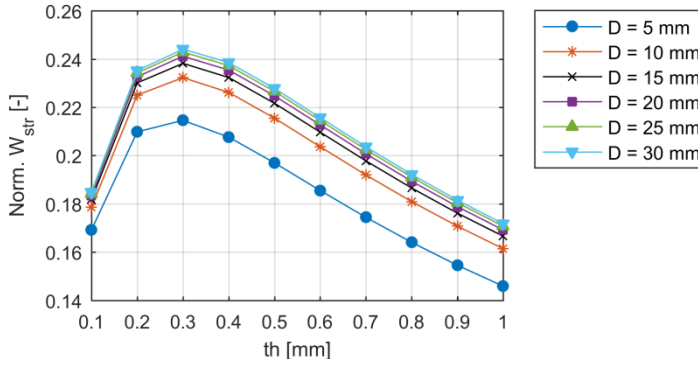


Figure 6.5. Normalized energy transferred by the PZT actuator to the structure (according to Equation (6.3)) as function of actuator thickness, for actuator diameters varying from 5 to 30 mm on areas 1-2.

Final transducer and excitation design

The selected PZT transducer geometry for areas 1 and 2 is a thin disc with a diameter of 20 mm and a thickness of 0.4 mm. The actuation of ultrasonic GW is to be performed at 123, 213 and 335 kHz, using a 10-cycle tone-burst with the amplitude modulated by a Hanning window.

6.4.2.2. Area 3

In this subsection the design implementation for area 3 is shown directly without further explanations, because the procedure for applying the design criteria is the same as that explained in Section 6.4.2.1 for areas 1-2. The frequencies that enable the application of criterion A can be found in Table 6.2. The diameters and the frequencies that satisfy criteria A and B for area 3 can be found in Table 6.4. Those values are taken as candidates for criteria C to E, until the final design of the transducer and excitation signal is obtained.

Table 6.4. Frequencies of the relevant local maxima of the sensor output in area 3 for the PZT diameters satisfying criteria A and B.

Diameter [mm]	f [kHz]		
	Max. 1	Max. 2	Max. 3
20	112	198	350
25	153	217	280
30	123	176	228

Criterion A: Single sensor output local maximum

In summary, criterion A is satisfied in the following conditions:

- $D = 20$ mm, with $N_{cyc} = 5$
- $D = 25$ and 30 mm, with $N_{cyc} = 10$
- $D = 5$ mm, with $N_{cyc} = 15$

Criterion B: Multiple sensor output local maxima

In summary, criteria A and B are satisfied in the following conditions:

- $D = 20$ mm, with $N_{cyc} = 5$
- $D = 25$ and 30 mm, with $N_{cyc} = 10$

Criterion C: EM response

In summary, criteria A, B and C are satisfied in the following conditions:

- $D = 20$ mm, for $0.1 \leq th \leq 1.0$ mm, with $N_{cyc} = 5$
- $D = 25$ and 30 mm, for $0.1 \leq th \leq 1.0$ mm, with $N_{cyc} = 10$

Criterion D: Electrical current limits

In summary, criteria A to D are satisfied in the following conditions:

- $D = 20$ mm, for $th > 0.3$ mm, with $N_{cyc} = 5$
- $D = 25$ mm, for $th > 0.4$ mm, with $N_{cyc} = 10$
- $D = 30$ mm, for $th > 0.5$ mm, with $N_{cyc} = 10$

Criterion E: PZT actuator energy transfer

In summary, criteria A to E are satisfied in the following conditions:

- $D = 20$ mm, for $th = 0.4$ mm, with $N_{cyc} = 5$

Final transducer and excitation design

The selected PZT transducer geometry for area 3 is a thin disc with a diameter of 20 mm and a thickness of 0.4 mm. The actuation of ultrasonic GW is to be performed at 112, 198 and 350 kHz, using a 5-cycle tone-burst with the amplitude modulated by a Hanning window.

6.4.3. Final transducer network configuration

The final transducer network configuration for each area is summarized in Table 6.5. The approximate transducer positions listed in Table 6.6 are relative to a coordinate system centred at PZT 01, with the x -axis coincident with the line connecting the centres of transducers 01 and 02. The origin (PZT 01) was positioned 200.9 mm to the left of the the stringer run-out edge and 30 mm above the upper stringer run-out edge. In Section 3.2.2, Figure 3.5 shows the component-scale horizontal stabilizer torsion box stiffened panel, where it is possible to have a general view of the entire transducer network. Figure 6.6 and Figure 6.7 show the detail of the network installation on critical areas 1-2 and 3, respectively.

Table 6.5. PZT transducer numbers and their configuration for each critical area.

Location	PZT No.	Configuration description
Area 1	1 - 5	On the skin, around stringer run-out
Area 2	6 - 10	On the skin, around stringer run-out
Area 3	11 - 14	On the skin, inboard of outboard rib, around stringer
	15, 16	On outboard rib, inboard side of the web, line
	17, 18	On the skin, outboard of outboard rib, line

Table 6.6. Approximate PZT transducers spatial coordinates relative to the origin at PZT 01, with the x -axis coincident the line PZT 01 – PZT 02. PZT 01 was in area 1, 200.9 mm to the left of the the stringer run-out edge and 30 mm above the upper stringer run-out edge. The transducer thickness is not taken into account.

PZT No.	x [mm]	y [mm]	z [mm]	PZT No.	x [mm]	y [mm]	z [mm]
01	0.0	0.0	0.0	10	470.9	183.5	0.0
02	140	0	0.0	11	-87.0	730.0	0.0
03	240.9	-64.5	0.0	12	134.6	730.0	0.0
04	140	-116.9	0.0	13	134.6	580.0	0.0
05	0.0	-116.9	0.0	14	-87.0	580.0	0.0
06	470.9	59.0	0.0	15	265.6	730.0	80.0
07	370.9	59.0	0.0	16	265.6	580.0	45.0
08	270.0	89.0	0.0	17	342.6	730.0	0.0
09	370.9	183.5	0.0	18	342.6	580.0	0.0

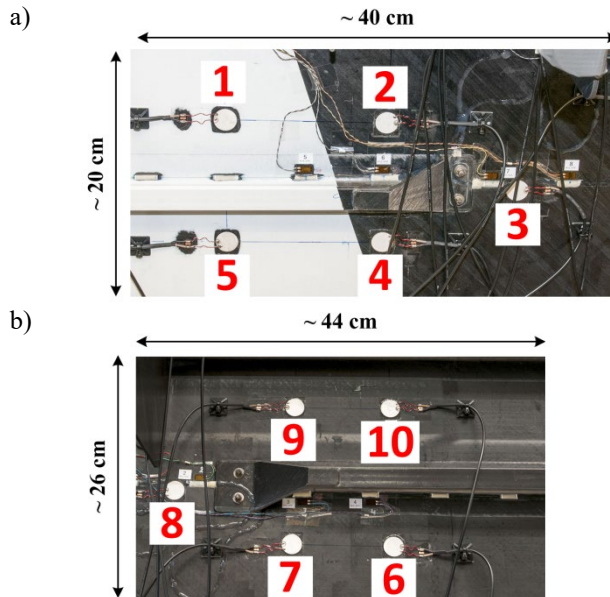


Figure 6.6. Transducer network on a) critical area 1 and b) critical area 2. Numbers 1 to 10 indicate the PZT transducer locations.

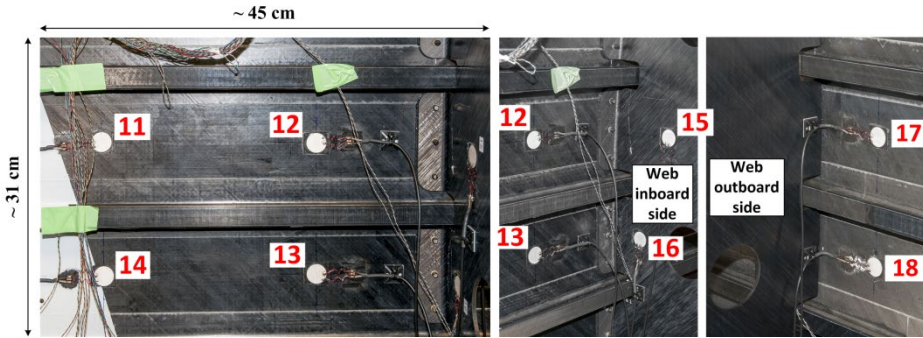


Figure 6.7. Transducer network on critical area 3. Numbers 11 to 18 indicate the PZT transducer locations.

6.4.4. Design checks

The maximum allowable electric field for APC 850 material is $5 \text{ V}_{AC}/\text{mil}$, i.e. $5000 \text{ V}_{AC}/\text{in} = 196.85 \text{ V}_{AC}/\text{mm}$. That means the maximum allowable (absolute) voltage for the transducers is 78.74 V . Since the maximum voltage that the waveform generator can supply is 10 Vpp , and the maximum amplification factor available was 1.6 , there is no risk of exceeding the allowable limits of the PZT.

6.5. Design methodology validation

The proposed design methodology was validated by testing the capabilities of the SHM system for diagnostic of BVID of different severities, applied in different locations of the TpC torsion box panel described in 3.2.2. Because this was a component-scale structure, and the chapters of this thesis follow the building-block pyramid of structural complexity, the experimental setup and the results of the validation are kept for Chapter 8, where the component-scale studies are presented.

References

1. Ochôa P, Groves RM, Benedictus R. Systematic multi-parameter design methodology for an ultrasonic health monitoring system for full-scale composite aircraft primary structures. *Struct Control Health Monit* 2019; 26(5): e2340.
2. Giurgiutiu V. *Structural health monitoring with piezoelectric wafer active sensors*. 2nd ed. Academic Press – Elsevier; 2014.
3. Sohn H, Lee SJ. Lamb wave tuning curve calibration for surface-bonded piezoelectric transducers. *Smart Mater Struct* 2010; 19(015007): 1-12.
4. Raghavan A, Cesnik CES. Modeling of piezoelectric-based Lamb-wave generation and sensing for structural health monitoring. *Proc SPIE* 2004; 5391: 419-430.
5. Pohl J, Willberg C, Gabbert U, Mook G. Experimental and theoretical analysis of Lamb wave generation by piezoceramic actuators for structural health monitoring. *Exp Mech* 2012; 52: 429-438.

6. Giurgiutiu V. PWAS resonators. In: Giurgiutiu V. *Structural health monitoring with piezoelectric wafer active sensors*. 2nd ed. Academic Press – Elsevier; 2014.
7. Giurgiutiu V, Zagari AN. Characterization of piezoelectric wafer active transducers. *J Intell Mater Syst Struct* 2000; 11: 959-975.
8. Giurgiutiu V, Zagari AN. Embedded self-sensing piezoelectric active sensors for on-line structural identification. *Trans ASME* 2002; 124: 116-125.
9. Kang YK, Park HC, Hwang W, Han KS. Prediction and measurement of modal damping of laminated composite beams with piezoceramic sensor/actuator. *J Intell Mater Syst Struct* 1996; 7: 25-32.
10. Chennamsetti R, Hood A, Guruprasad S, Roy S, Joshi M. Damping ratios of pristine composite beam and constrained layer damped composite beam of equal stiffness. *Int J Precis Eng Manuf* 2013; 14(9): 1655-1660.
11. Giurgiutiu V. Coupling of PWAS transducers to the monitored structure. In: Giurgiutiu V. *Structural health monitoring with piezoelectric wafer active sensors*. 2nd ed. Academic Press – Elsevier; 2014.
12. Kundu T, Maji A, Ghosh T, Maslov K. Detection of kissing bonds by Lamb waves. *Ultrasonics* 1998; 35: 573-580.
13. Wilcox PD. *Lamb wave inspection of large structures using permanently attached transducers*. London: Imperial College London; 1998.
14. Jin J, Quek ST, Wang Q. Design of interdigital transducers for crack detection in plates. *Ultrasonics* 2005; 43: 481-493.
15. Petculescu G, Krishnaswamy S, Achenbach JD. Group delay measurements using modally selective Lamb wave transducers for detection and sizing of delaminations in composites. *Smart Mater Struct* 2008; 17(015007): 1-9.
16. Schmidt D, Sinapius M, Wierach P. Design of mode selective actuators for Lamb wave excitation in composite plates. *CEAS Aeronaut J* 2013; 4: 105-112.
17. Putkis O, Dalton RP, Croxford AJ. The anisotropic propagation of ultrasonic guided waves in composite materials and implications for practical applications. *Ultrasonics* 2016; 65: 390-399.

7

Reliability analysis

The certification of an SHM system for a full-scale structure requires an analysis of its reliability, in which the damage diagnostic capabilities are evaluated under multiple operational-environmental scenarios. This is then translated into a statistical assessment of the SHM system performance, which is typically described by POD (probability-of-detection) curves.

The challenge, however, lies in acquiring the necessary amount of statistically relevant data to enable a complete quantitative reliability analysis. The large diversity of measurement variability factors makes it practically unfeasible to conduct such an analysis solely by experimental means. Therefore, this chapter presents a study of modelling approaches for including real-scale (1:1) structure complexity, material anisotropy and transducer network degradation in the reliability analysis of a GW-SHM system.

7.1. Introduction

How much trust can one have that a GW-SHM system will detect critical damage? And how many wrong detections are produced for each correct detection? In short, how reliable is a GW-SHM system? To answer these questions to the level required for real SHM applications it is necessary to acquire GW data from a large diversity of scenarios which the system is expected to encounter. Besides considering damages of different types and size, each scenario should include a combination of factors affecting GW measurements, for example structure properties, SHM system properties, or environmental conditions.

The particularity of SHM transducers having to be permanently installed on the structure removes the flexibility of testing multiple scenarios on a single specimen, and necessarily entails large and time-consuming test campaigns. Adding to the complexity of reproducing realistic operational-environmental conditions (e.g. loading, temperature), one can understand that it is hardly feasible (if not impossible) to acquire all the data necessary for the reliability assessment by means of experimental testing only. Alternatively, numerical models have been applied to assist the parametric GW data generation process, as discussed in Section 2.8.

However, as highlighted in Section 2.9, there are crucial GW measurement variability factors that have still not been simultaneously taken into account. In particular, geometric complexity, material anisotropy and transducer bonding degradation, are especially important in real-scale (1:1) composite structures. Hence, this chapter describes the development of numerical modelling and POD computation approaches for addressing research question Q3), and for studying the reliability of the GW-SHM system designed according to the criteria proposed in Chapter 6.

7.2. Reliability analysis protocol

The protocol developed for the reliability analysis consists of multiple steps which are depicted in the flowchart of Figure 7.1 and are explained in the following sections.

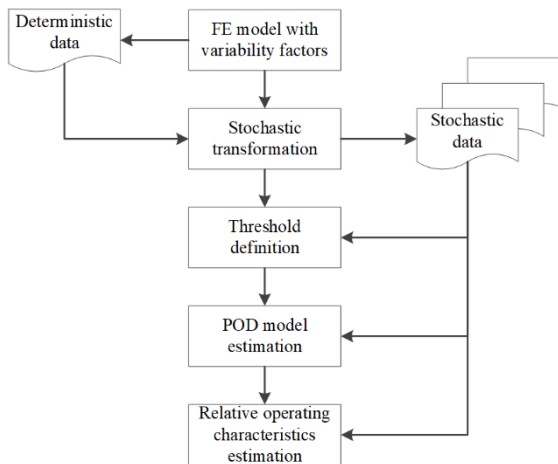


Figure 7.1. Flowchart of the reliability analysis protocol.

7.2.1. Variability factors

The first step in a reliability analysis of an ultrasonic GW-SHM system is the identification of its variability factors. Some of the most important can be found in Table 7.1. For the study presented in this chapter, it was decided to analyse the effect of factors that are directly related to characteristics of the transducer network (**g, h, i**), together with the effect of damage evolution (**m**).

Table 7.1. Main variability factors for an ultrasonic GW-SHM system.

Structure	a)	Dimensions of the structure
	b)	Material properties of the structure
Transducers	c)	Dimensions of the transducers
	d)	Material properties of the transducers
	e)	Material properties of the transducer adhesive
	f)	Thickness of the transducer adhesive layer
	g)	Integrity of the transducer adhesive layer
	h)	Position of the transducers within the network
	i)	Excitation frequency
Damage	j)	Type of damage
	k)	Location of damage
	l)	Orientation of damage
	m)	Size of damage
External	n)	Signal noise
	o)	Temperature
	p)	Pressure
	q)	Loading

Random variability factors **a-f** were considered to be covered by the study of Janapati et al. [2] (see Section 7.2.2). The combined effect of factors **o-q** on wave propagation is mostly felt in the amplitude and instantaneous phase of the sensed signals (see Section 2.4.6), which in turn changes the effectiveness of the selected threshold, thereby affecting the performance of the SHM system. Therefore, these factors, together with factor **n**, were partially assessed by computing the POD of the critical damage for several detection thresholds, which can also be referred to as relative operating characteristics (ROC) analysis. Factors **j-l** are associated with damage characteristics which are determinant for the change in ultrasound scattering in the structure. However, in this study, these parameters were not variable, as they were fixed by the manufacturer of the torsion box panel (see Section 3.2.2) in the definition of the *hot-spot* to be monitored.

The reliability analysis was conducted for the SHM system designed for area 3 of the component-scale torsion box panel (see Figure 6.7 in Section 6.4.3), as that area was expected to be subjected to a more detrimental damage scenario than the other two (the damage scenario is explained in Section 7.4). The chosen parameters were varied in a full factorial fashion, with the hierarchy of **i-h-g-m**, in order to cover the different regimes of operation and damage scenarios. The integrity of the PZT bonding layer (factor **g**) was taken as describing the fraction of the actuator patch area which was effectively bonded to the surface of the structure, and it ranged from 0.25 to 1, in steps of 0.25. Since the transducer distribution in area 3 is symmetric with respect to stringer 4, it was deemed sufficient to use locations 11, 12, and 17 (see Section 7.4 about the component-scale

model) for the position of the actuator within the network (factor **h**). The excitation frequency (factor **i**) took the values of 112 and 198 kHz. The length of the disbond (factor **m**) was varied from 0 to 10 mm in steps of 5 mm, and from 10 to 50 mm in steps of 10 mm. The summary of the parametric values is given in Table 7.2. The total number of modelled cases was 168, with 6 of them corresponding to the baseline states. For each excitation frequency and for each actuator position, the baseline for each actuator-sensor pair corresponded to the case of perfect actuator bonding and no disbond.

Table 7.2. Summary of the parametric values used.

Parameter	Values
Excitation frequency (i)	112; 198 [kHz]
Position of the actuator within the network (h)	11; 12; 17
Integrity of the actuator adhesive layer (g)	0.25; 0.5; 0.75; 1
Size of damage (m)	0; 5; 10; 20; 30; 40; 50 [mm]

7.2.2. Generation of stochastic database

The fundamental idea behind model-assisted approaches (see Section 2.8) is to use a properly validated model to simulate the monitoring environment, so that a measurement event database can be established numerically, and not experimentally. The simulation of all cases of interest requires some parameters to be varied deterministically, and others according to probability distributions which should also be validated. In this way it is possible to attribute a stochastic nature to the numerical database.

In the case of this research there were limited computational resources and a strictly time bounded framework. Thus it was decided to adopt a more efficient approach. Factors **g**, **h**, **i** and **m** were varied deterministically, and pseudo-randomness was directly added to the DI values obtained from the numerically generated signals to account for variability factors **a-f**, in line with the work of Kabban et al. [3]. The stochastic DI database was generated by using Monte Carlo sampling, according to which the stochastic DI value, DI_{stoch} , was defined as:

$$DI_{stoch} = DI_{num} \pm E_{DI} \quad (7.1)$$

where DI_{num} was the DI for the whole critical area computed according to the multi-path unit-cell concept (see Equation (2.38) in Section 2.6.4.3); the DI for each propagation path was calculated using Equation (2.27) (see Section 2.6.4.1); and E_{DI} was the random error which was assumed to have a normal distribution with null mean, $E_{DI} \sim N(0, std_{DI})$. So, in the end, the stochastic transformation generates a DI database equivalent to a database with random repeated measures.

It was decided to test two different definitions of the standard deviation of E_{DI} . Since the DI for each propagation path was the same as that used by Janapati et al. [2], the first definition was based on the relative standard deviation values (which correspond to percentages of the DI value) found by them, and the total relative standard deviation, $std\%$, was computed according to the theory of error propagation [4]:

$$Q = a + b + \dots + z \rightarrow \delta Q = \sqrt{(\delta a)^2 + (\delta b)^2 + \dots + (\delta z)^2} \Rightarrow$$

$$\Rightarrow std\% = \sqrt{0.58^2 + 0.55^2 + 0.12^2 + 10.84^2 + 1.18^2} \approx 10.92\% \quad (7.2)$$

The value of E_{DI} was then calculated as the product of $std\%$ with the maximum value of DI encountered by Janapati et al. [2] for the influence of sensor location, which was approximately 0.125:

$$Error\ 1: E_{DI} \sim N(0, 0.1092 \times 0.125) = N(0, 0.0014) \quad (7.3)$$

The second definition of E_{DI} was based on the average standard deviation found within each batch of specimens used for the study presented in Chapter 5 [5], when computing the DI between each possible permutation of two specimens. The value found was 0.0425, and the E_{DI} was defined as:

$$Error\ 2: E_{DI} \sim N(0, 0.0425) \quad (7.4)$$

The two error definitions include approximately the same variability factors. However, *Error 2* represents the variability of measurements on composite specimens, while *Error 1* is associated with measurements on metallic specimens.

7.2.3. Definition of the detection threshold

A detection can only be accomplished by establishing a criterion to evaluate the GW measurement events, which is typically denominated by a detection threshold. Following the same definition used by Cobb et al. [6], a linear regression was fitted to DI values corresponding to the damage sizes below the critical one for the reference condition of perfect actuator bonding, and the standard deviation of the errors between the linear regression estimates and the DI points was taken as the base threshold, thr_o . To enable the ROC analysis, the used threshold was equal to multiple of the base value, $thr = m_{thr} \times thr_o$, with integer multiples m_{thr} ranging from 1 to 6.

7.2.4. Estimation of the probability-of-detection

The method employed for POD estimation typically depends on the desired diagnostic of the SHM system user. If the interest is solely on detecting the presence of damage with a size above a certain critical value, then the POD model parameters can be determined by computing the most likely correct regression for the binary data “detected/not-detected”. This is the so-called *hit/miss* analysis. If the focus is on a more continuous assessment of damage growth, it is possible to perform a statistical analysis of the linear regression for the relationship DI vs damage, in what is called \hat{a} vs a analysis, for estimating the POD

model. The guidelines for SHM system implementation on fixed wing aircraft [7] refer to the Military Handbook (MIL-HDBK) 1823A [8] for reliability validation approaches, where the *hit/miss* analysis and \hat{a} vs a analysis are the two recommended methods. These methods are briefly described in the following sections, as they were both used in this study.

7.2.4.1. Hit/miss analysis

It is possible to treat DI responses in a binary way if the threshold crossings and non-crossings are transformed to Boolean values. Binary data can only have the values of 0 or 1, corresponding to non-detection or detection of an event, respectively. That is, the continuous variables describing damage (e.g. damage size) are connected to a discrete system response. However, by assuming the system response follows a Bernoulli distribution [9], it is possible to *link* the continuous variables to the probability of either discrete outcome, which varies continuously from 0 to 1. This transformation enables the POD to be modelled as a linear function of the damage variables, thereby constituting a generalised linear model (GLM).

In MIL-HDBK-1823A [8], four *link* functions are considered suitable for transforming the probability of detection: the *logistic* function, the inverse normal function, the complementary log-log function, and the log-log function. For this research only the *logistic* function is considered, as it is a common choice [9].

Let y be the system response, which, as previously mentioned, can only be 0 or 1, and is related to the damage variables (i.e. independent variables), x , by a linear function f , $y = f(x)$. The logistic link function applies a transformation such that:

$$f(x) = g(y) = \log[p/(1-p)] \quad (7.5)$$

where p can be interpreted as the probability of detecting damage with a certain size a_i , i.e. $p(y = 1 | x = a_i) = \text{POD}(a_i)$. By computing the inverse of function g , it is possible to write POD as a function of damage size:

$$\text{POD}(a) = \frac{\exp[f(x)]}{1 + \exp[f(x)]} \quad (7.6)$$

It is common practice to define $f(x) = b_0 + b_1 \ln(a)$ [8,9], in which case the POD model parameters to be estimated are b_0 and b_1 , or in an alternative terminology, $\mu = -b_0/b_1$ and $\sigma = \pi/(b_1\sqrt{3})$. This can be accomplished by maximizing the likelihood “*of obtaining the observed data as a function of the parameters*” [10].

Once the POD model is determined, it is possible to estimate the $1 - \alpha$ confidence bounds (usually with $1 - \alpha = 0.95$), which can be traced by finding the smallest and largest damage size, a , within the $1 - \alpha$ confidence interval for each percentile of probability p :

$$\ln(a) = \mu \pm z_p \sigma \quad (7.7)$$

where $z_p = \Phi^{-1}(p)$ and Φ is the standard cumulative normal distribution. It is thus necessary to determine the values of $\theta = (\mu, \sigma)$ that minimise and maximise a with a confidence of $1 - \alpha$. As explained above, the POD model parameters, θ , are approximated through maximum

likelihood estimates, $\hat{\theta}$, which means that if slightly different parameters are chosen, the associated likelihood decreases. Thus, a variable can be defined that describes the rate at which the likelihood varies with the model parameters [8,10], as in:

$$\mathbf{Q}(\boldsymbol{\theta}) = (\hat{\boldsymbol{\theta}} - \boldsymbol{\theta})^T \mathbf{I}(\boldsymbol{\theta}) (\hat{\boldsymbol{\theta}} - \boldsymbol{\theta}) \quad (7.8)$$

where $\mathbf{I}(\boldsymbol{\theta})$ is the Fisher information matrix defined by:

$$I_{ij}(\boldsymbol{\theta}) = -E \left[\frac{\partial^2 \ln(L)}{\partial \theta_i \partial \theta_j} \right] \quad (7.9)$$

with L as the likelihood function and $E(\dots)$ as the expected value.

A confidence region can then be defined by the probability \Pr that:

$$\Pr[\mathbf{Q}(\boldsymbol{\theta}) \leq \zeta] = 1 - \alpha \quad (7.10)$$

where, because $\mathbf{Q}(\boldsymbol{\theta})$ asymptotically follows a chi-squared distribution, ζ can be assumed to be described by the quantile of the chi-squared distribution with two degrees of freedom, χ_2^2 , i.e. $\zeta = \chi_2^2(\alpha)$. This means that the minimisation of a for (7.7) can be conducted under the constraint of:

$$\mathbf{Q}(\boldsymbol{\theta}) - \zeta = 0 \quad (7.11)$$

7.2.4.2. \hat{a} vs a analysis

The direct relationship between the DI response and damage sizes provides more information about the detection capabilities of the SHM system, and advantage can be taken to build a more detailed POD model. Additionally, as briefly discussed in Section 2.8, SHM data consists of repeated measurements made with the same transducers, in the same location on the same structure. This means that not all data points are independent observations, and it is important that the statistical methods incorporate this characteristic to allow a valid determination of the POD curves. Although the \hat{a} vs a analysis method recommended in MIL-HDBK-1823A requires that observations for different damage sizes are independent, it is possible to incorporate a structure of correlation between observation data points for the same damage size without disrespecting the mathematical conditions of validity of the method, as shown by Kabban et al. [3]. Thus, this section first describes the Delta method for POD model estimation based on \hat{a} vs a analysis for independent data (which is a valid approximation for NDT technique reliability analysis [8]), and then with the adaptations for incorporating data dependency [3].

Independent data

In this case all data points are treated as independent, and the analysis starts by fitting a linear regression to all of them:

$$\hat{a} = b_0 + b_1 a + \varepsilon \quad (7.12)$$

where $\hat{a} = [\hat{a}_1, \hat{a}_2, \dots, \hat{a}_m]^T$ are the DI responses for damage sizes $a = [a_1, a_2, \dots, a_m]^T$, and the linear model errors, $\varepsilon = [\varepsilon_1, \varepsilon_2, \dots, \varepsilon_m]^T$, are assumed to be independent and normally distributed with null mean and constant variance τ^2 , i.e. $\varepsilon \sim N(0, \tau^2)$. So, the variance of the model is $\text{Var}(\hat{a}) = \theta^2 = \tau^2$.

However, since the model parameters must be estimated, the variance of the employed \hat{a} vs a model must take into account the variance of the maximum likelihood estimates for all the model parameters, i.e. \hat{b}_0 , \hat{b}_1 and $\hat{\theta}^2$. Hence the covariance matrix of the regression can be written as:

$$\Sigma_{\text{reg}} = \begin{bmatrix} \text{Var}(\hat{b}_0) & \text{Cov}(\hat{b}_0, \hat{b}_1) & \text{Cov}(\hat{b}_0, \hat{\theta}^2) \\ \text{Cov}(\hat{b}_0, \hat{b}_1) & \text{Var}(\hat{b}_1) & \text{Cov}(\hat{b}_1, \hat{\theta}^2) \\ \text{Cov}(\hat{b}_0, \hat{\theta}^2) & \text{Cov}(\hat{b}_1, \hat{\theta}^2) & \text{Var}(\hat{\theta}^2) \end{bmatrix} \quad (7.13)$$

Since ε are independent, normally distributed errors:

$$\text{Cov}(\hat{b}_0, \hat{\theta}^2) = \text{Cov}(\hat{b}_1, \hat{\theta}^2) = 0 \quad (7.14)$$

Since it is valid to assume that the variance of random errors asymptotically follows a chi-squared distribution [3]:

$$\text{Var}(\hat{\theta}^2) = \frac{2(\hat{\theta}^2)^2}{m-2} \quad (7.15)$$

with $\hat{\theta}^2 = \tau^2$ calculated as the mean squared error, and m being the number of observations.

The connection between the DI response model and the POD model can then be established through the Delta method. The idea behind this method is the following. If $\hat{\eta}$ is a maximum likelihood estimator which is asymptotically distributed about the true value of a model parameter η , then the asymptotic normal distribution properties (mean and variance) of a function of $\hat{\eta}$, $f(\hat{\eta})$, which is in itself a parameter of another model, are related to those of the previous model by the rate of change of change of $f(\hat{\eta})$ when $\hat{\eta}$ is near η . In the limit, the asymptotic normal distribution of $\hat{\eta}$ becomes narrower and so does that of $f(\hat{\eta})$, and thus it is valid to define the standard deviation of $f(\hat{\eta})$ as the product of the standard deviation of $\hat{\eta}$ with the slope of the tangent at the mean value of $\hat{\eta}$, i.e.:

$$\text{std}_{f(\hat{\eta})} = \text{std}_{\hat{\eta}} \times \frac{\partial f(\hat{\eta})}{\partial \hat{\eta}} \quad (7.16)$$

Let the POD be approximately described by:

$$\text{POD}(a) = \Phi \left[\frac{a - \hat{\mu}}{\hat{\sigma}} \right] \quad (7.17)$$

where Φ represents the standard cumulative normal distribution, and $\hat{\mu}$ and $\hat{\sigma}$ are the POD model parameter estimates related to the linear \hat{a} vs a regression by:

$$\hat{\mu} = (thr - \hat{b}_0) / \hat{b}_1 ; \hat{\sigma} = \sqrt{\hat{\theta}^2} / \hat{b}_1 \quad (7.18)$$

with thr being the detection threshold for the DI. Then the covariance matrix for the POD model parameters can be computed as:

$$\Sigma_{pod} = \Phi^T \Sigma_{reg} \Phi \quad (7.19)$$

where Φ is the matrix of the first partial derivatives of the POD model parameters with respect to the linear regression model parameters defined by:

$$\Phi = \begin{bmatrix} \frac{\partial \hat{\mu}}{\partial \hat{b}_0} & \frac{\partial \hat{\sigma}}{\partial \hat{b}_0} \\ \frac{\partial \hat{\mu}}{\partial \hat{b}_1} & \frac{\partial \hat{\sigma}}{\partial \hat{b}_1} \\ \frac{\partial \hat{\mu}}{\partial \hat{\theta}^2} & \frac{\partial \hat{\sigma}}{\partial \hat{\theta}^2} \end{bmatrix} = \begin{bmatrix} \frac{-1}{\hat{b}_1} & 0 \\ \frac{-(thr - \hat{b}_0)}{\hat{b}_1^2} & \frac{-\sqrt{\hat{\theta}^2}}{\hat{b}_1^2} \\ 0 & \frac{\sqrt{\hat{\theta}^2}}{\hat{b}_1} \end{bmatrix} = \frac{-1}{\hat{b}_1} \begin{bmatrix} 1 & 0 \\ \hat{\mu} & \hat{\sigma} \\ 0 & -\sqrt{\hat{\theta}^2} \end{bmatrix} \quad (7.20)$$

Having fully defined the POD model, the Wald method [8] can be applied to define the confidence bounds as the damage size intervals centred at the sizes which are estimated to be detected with a probability p , a_p , and confidence of $1 - \alpha$:

$$a_{p|1-\alpha} = a_p \pm z_{1-\alpha} \sqrt{\mathbf{u}^T \Sigma_{pod} \mathbf{u}} \quad (7.21)$$

where a_p is:

$$a_p = \hat{\mu} + z_p \hat{\sigma} \quad (7.22)$$

the vector $\mathbf{u} = [1 \ z_p]^T$, and $z_q = \Phi^{-1}$ (Φ is again the standard cumulative normal distribution) where q can be p or $1 - \alpha$.

Dependent data

The need for incorporating data dependency stems from the fact that, during the monitoring process, multiple measurements of the same damage scenario/state are made (“repeated measures”), which are usually different from each other due to intra-measurement variability factors. As a result, it is more likely that a repeated measure comes from the same specimen than from a different one. Failure to incorporate this property results in overestimates of the POD. The approach proposed by Kabban et al. [3] does not fall outside the conditions of validity of the recommended Delta method for \hat{a} vs a

analysis [8]. Instead, it goes back to the linear regression phase and incorporates a structure of correlation between repeated measures into the variance of the POD model.

Repeated measures tend to result in DI values spread along the vertical axis. So it is possible to represent the multiple sets $i = 1, 2, \dots, n$ of repeated measures for all the $j = 1, 2, \dots, m$ encountered damage sizes by parallel linear regressions, each of them with its own (b_0, b_1) coefficients and errors. That can be formulated as follows:

$$\hat{a}_{ij} = b_0 + b_{0i} + b_1 a_{ij} + \varepsilon_{ij} \quad (7.23)$$

With this formulation the same model calculated under the assumption of independent data, characterised by parameters (b_0, b_1) , can be used, but the errors are no longer treated as independent or as having constant variance, because they are composed of b_{0i} (the random effect of the i^{th} repeated measure) and ε_{ij} (the previously described random errors) that are independent of b_{0i} . Each of these random error components can be described by normal distributions of null mean, with $b_{0i} \sim N(0, \omega^2)$ and $\varepsilon_{ij} \sim N(0, \tau^2)$. Consequently, $\text{Var}(\hat{a}_{ij}) = \theta^2 = \tau^2 + \omega^2$, and $\text{Cov}(\hat{a}_{ij}, \hat{a}_{ij'}) = \omega^2$.

The covariance matrix for the overall regression, Σ_{reg} , can thus be calculated by inserting the parameter estimates, (\hat{b}_0, \hat{b}_1) , and the total variance, $\hat{\theta}^2$, for all the repeated-measure linear regressions in Equations (7.13) to (7.15), thereby accounting for data dependency “*through the estimate of variance for the error terms.*” [3] The parameter estimators of the independent-data linear regression can then be used to determine the POD model, according to Equations (7.17) and (7.18). With those it is possible to determine the covariance matrix for the POD model parameter estimates through Equations (7.19) and (7.20), which in turn enables the computation of the desired confidence bounds for the POD curve through Equations (7.21) and (7.22).

7.2.4.3. Number of target points

According to MIL-HDBK-1823A [8], experience with reliability demonstration of NDT techniques suggests that at least 60 target points should be used for *hit/miss* analysis, and at least 40 target points for \hat{a} vs a analysis. Due to limited computational resources and available time it was decided to simulate only seven damage scenarios, including the one corresponding to no damage, while making sure that the stochastic transformation was applied a number of times sufficient to match the aforementioned suggested minimums for each damage size.

7.2.5. Estimation of the relative operating characteristics and levels

A high-level (although incomplete) assessment of the reliability of an SHM system can be conducted by defining the event of interest as the existence of damage with a size above a certain critical value, and building the contingency table of possible monitoring outcomes [8], as in Table 7.3.

Table 7.3. General contingency table of possible outcomes of a binary detection system.

Observations	Detection, De	No-detection, \overline{De}	Total
Event, Ev	h	ms	e
Non-event, \overline{Ev}	fal	cr	\overline{ev}
Total	de	\overline{de}	no

Among the total of no observations in Table 7.3, there are e events and \overline{ev} non-events. The total number of detections (i.e. threshold crossings) is de and the total of no-detections is \overline{de} . For all the detections, h occurred when there was an event, and are called hits (i.e. true positives), while fal occurred without any event and are called false alarms. The number of events that are undetected is quantified by the number of misses ms (i.e. false negatives), while the number of times there was no detection and no event is given by the number of correct rejections cr .

From the all these possible outcomes, the following conditional probabilities can be estimated [8,11]:

True positive detection (TPD) rate: Probability of a detection occurring if an event exists

$$TPD = P(De | Ev) = h/(h + ms) \quad (7.24)$$

False positive detection (FPD) rate: Probability of a detection occurring if an even does not exist

$$FPD = P(De | \overline{Ev}) = fal/(fal + cr) \quad (7.25)$$

False negative detection (FND) rate: Probability of a detection not occurring if an event exists

$$FND = P(\overline{De} | Ev) = ms/(h + ms) \quad (7.26)$$

True negative detection (TND) rate: Probability of a detection not occurring if an event does not exist

$$TND = P(\overline{De} | \overline{Ev}) = cr/(fal + cr) \quad (7.27)$$

Correct event prediction (CEP) rate: Probability of an event existing if a detection occurs

$$CEP = P(Ev | De) = h/(h + fal) \quad (7.28)$$

False event prediction (FEP) rate: Probability of an event not existing if a detection occurs

$$FEP = P(\overline{Ev} | De) = fal/(h + fal) \quad (7.29)$$

Missed event (ME) rate: Probability of an event existing if a detection does not occur

$$ME = P(Ev | \overline{De}) = ms/(ms + cr) \quad (7.30)$$

Correct rejection (CR) rate: Probability of an event not existing if a detection does not occur

$$CR = P(\overline{Ev} | \overline{De}) = cs / (cr + ms) \quad (7.31)$$

The evaluation of TPD against FPD is called a relative operating characteristic (ROC), although it is also possible to evaluate TPD against FND. Since the ROC relationship changes with threshold, typically, contingency tables are compiled for multiple threshold values in order to compute multiple ROC points. This in turn can be a useful tool to have a preliminary idea about a suitable threshold for detecting damage with a certain minimum size (i.e. the event of interest).

Ideally, one should aim at achieving high TPD at low FPD. However, the ROC is limited in the sense that it does not provide any information about the influence of damage characteristics (e.g. size) on the POD. Therefore it should be considered solely as a high-level, auxiliary tool for preliminary selection of threshold, and not for reliability demonstration of an SHM system [8].

The relationship between CEP and ME, or between CR and FEP, is called relative operating level (ROL), and it provides not only information about the detection capability of the system, but also some insight into the presence of damage in the structure being monitored. In other words, the ROL can be useful in providing a high-level indication of the presence of critical damage given an ensemble of data [11]. Therefore, in order to trace the ROL curve correctly, the detection threshold should be kept constant and the definition of event of interest should be different. In this sense, the ROL may give an indication of the damage size that can be best detected with a certain threshold definition. Equivalently to ROC, ideally one should aim for high CEP at low ME. By taking then the product of the area under the ROC curve by the area under the ROL curve it is possible to obtain a general index that summarises the “skill” of the detection system [11].

7.3. Development of the modelling approaches

7

Modelling GW propagation in a component-scale structure of the size of the torsion box panel of Figure 3.5 requires not only small elements and small time steps to ensure correct time-space representation of the ultrasounds, but also a great number of elements (in the order of millions, as shown in Section 7.4). Therefore, it is by far beneficial in terms of computational effort and time to employ an explicit solver, instead of an implicit one [12].

Since Abaqus was the FE programme used for creating the model, the aforementioned solver choice imposed restrictions in the available simulation tools, namely that it was not possible to employ elements with piezoelectric properties [13]. Hence, it was necessary to implement and validate an alternative approach for simulating the excitation of ultrasonic GWs in the structure.

Another key aspect was the composite material of the structure. The tools for defining composite laminates in Abaqus are developed for the use of shell elements [14]. However, it was necessary to be able to capture the three-dimensional shear components of GWs. Therefore, it was decided to employ three-dimensional solid elements, which forced the adoption and validation of an alternative approach for simulating the composite material. The implementation and validation of the two aforementioned modelling approaches (for simulating GW excitation and for simulating composite material) are explained in Sections 7.3.1 and 7.3.2.

7.3.1. Simulation of ultrasonic GW excitation

The experimental data used for this first validation phase came from the extra GW tests conducted on an aluminium plate, as described in Section 3.2.3 and depicted in Figure 7.2.

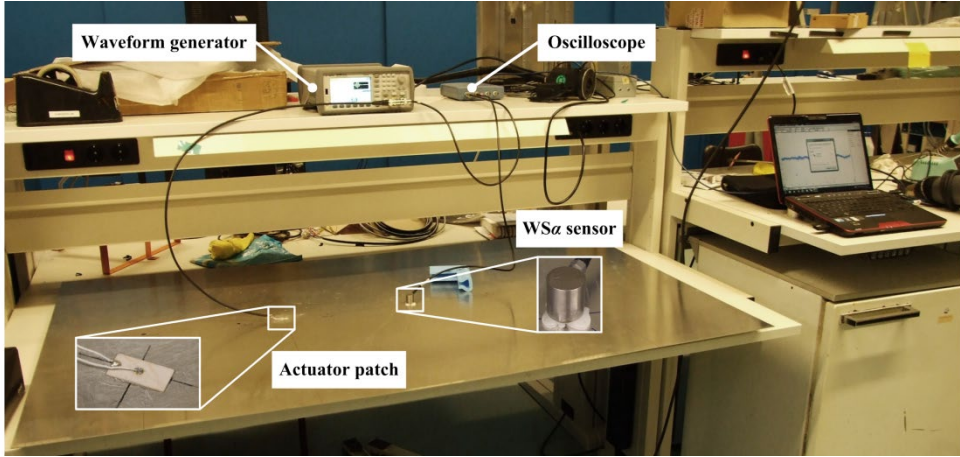


Figure 7.2. Setup of the extra GW tests performed on the aluminium plate.

In the extra GW tests the ultrasonic excitation was produced by an Agilent 33500 B arbitrary waveform generator and transmitted to the plate by a rectangular piezoceramic patch made of APC 850 material, supplied by American Piezo Ltd. The actuator was bonded with cyanoacrylate glue, 500 mm away from the left-hand edge of the plate. A Physical Acoustics WSA wideband PZT transducer, bonded with shear gel and adhesive tape 300 mm away from the actuator, was used to sense the ultrasonic response, which was then acquired by a PicoScope 4424 digital oscilloscope. The excitation signal was a sinusoidal tone-burst with a 5-cycle Hanning window amplitude modulation generated at 250 kHz.

The FE model was built to match the configuration of the GW tests described above. All the regions were defined as deformable three-dimensional volumes. The metallic plate material was modelled as isotropic homogeneous, with a Young's modulus of 70 GPa, a density of 2710 kg/m^3 and a Poisson's ratio of 0.33 [15]. The piezoceramic actuator material was modelled as an orthotropic homogeneous material, with elastic properties equal to those of APC 850 material [16,17], as listed in Table 7.4. The actuator patch was simulated with nominal dimensions of $16 \text{ mm} \times 8 \text{ mm} \times 0.4 \text{ mm}$. The actuator adhesive layer was assumed to be infinitesimally thin, and the connection between the plate region and the actuator patch region was ensured by a tie constraint.

7. Reliability analysis

Table 7.4. Properties of the APC 850 piezoelectric ceramic material [16,17]. The compliances (indicated with ‘*’) were obtained by inversion of the elastic stiffness matrix.

Property	Value ($\times 10^{10}$)	Property	Value ($\times 10^{-12}$)	Property	Value
c_{11}^E [N/m ²]	13.14	s_{11}^E [m ² /N]	15.70 ‘*’	ρ [kg/m ³]	7600
c_{12}^E [N/m ²]	8.23	s_{12}^E [m ² /N]	-4.67 ‘*’	ν [-]	0.35
c_{13}^E [N/m ²]	8.68	e_{31} [N/Vm]	6.91		
c_{33}^E [N/m ²]	12.25	e_{33} [N/Vm]	16.41		
c_{44}^E [N/m ²]	1.92	e_{15} [N/Vm]	13.65		

To explain the adopted approach for simulating the excitation load it is first necessary to revisit the constitutive equations for piezoelectric materials introduced earlier in Section 2.4.5 by Equations (2.4) to (2.8). The compressed matrix notation (also called Voigt notation), according to which “the stress and strain tensors are arranged as 6-component vectors, with the first three components representing direct stress and strain, and the last three components representing shear stress and strain” [16], allows the stress generated in a PZT element as the result of an applied electric field to be written as:

$$\begin{Bmatrix} T_1 \\ T_2 \\ T_3 \\ T_4 \\ T_5 \\ T_6 \end{Bmatrix} = \begin{bmatrix} c_{11}^E & c_{12}^E & c_{13}^E & 0 & 0 & 0 \\ c_{21}^E & c_{22}^E & c_{23}^E & 0 & 0 & 0 \\ c_{31}^E & c_{32}^E & c_{33}^E & 0 & 0 & 0 \\ 0 & 0 & 0 & c_{44}^E & 0 & 0 \\ 0 & 0 & 0 & 0 & c_{55}^E & 0 \\ 0 & 0 & 0 & 0 & 0 & c_{66}^E \end{bmatrix} \begin{Bmatrix} S_1 \\ S_2 \\ S_3 \\ S_4 \\ S_5 \\ S_6 \end{Bmatrix} + \begin{bmatrix} e_{11} & e_{21} & e_{31} \\ e_{12} & e_{22} & e_{32} \\ e_{13} & e_{23} & e_{33} \\ e_{14} & e_{24} & e_{34} \\ e_{15} & e_{25} & e_{35} \\ e_{16} & e_{26} & e_{36} \end{bmatrix} \begin{Bmatrix} E_1 \\ E_2 \\ E_3 \end{Bmatrix} \quad (7.32)$$

where $\{T_1, T_2, T_3, T_4, T_5, T_6\}^T = \{T_{11}, T_{22}, T_{33}, T_{23}, T_{31}, T_{12}\}^T$ and $\{S_1, S_2, S_3, S_4, S_5, S_6\}^T = \{S_{11}, S_{22}, S_{33}, S_{23}, S_{31}, S_{12}\}^T$, and where the thermal-induced component is not included for convenience. Common piezoceramic materials, such as the APC 850, are transversely isotropic, meaning $e_{32} = e_{31}$, $e_{24} = e_{15}$.

If, additionally, those materials are polarized in the 3-direction and the electric field is applied along the polarized direction, then (7.32) can be simplified to [16]:

$$\begin{Bmatrix} T_1 \\ T_2 \\ T_3 \\ T_4 \\ T_5 \\ T_6 \end{Bmatrix} = \begin{bmatrix} c_{11}^E & c_{12}^E & c_{13}^E & 0 & 0 & 0 \\ c_{12}^E & c_{11}^E & c_{13}^E & 0 & 0 & 0 \\ c_{13}^E & c_{13}^E & c_{33}^E & 0 & 0 & 0 \\ 0 & 0 & 0 & c_{44}^E & 0 & 0 \\ 0 & 0 & 0 & 0 & c_{44}^E & 0 \\ 0 & 0 & 0 & 0 & 0 & c_{66}^E \end{bmatrix} \begin{Bmatrix} S_1 \\ S_2 \\ S_3 \\ S_4 \\ S_5 \\ S_6 \end{Bmatrix} + \begin{bmatrix} 0 & 0 & e_{31} \\ 0 & 0 & e_{32} \\ 0 & 0 & e_{33} \\ 0 & e_{15} & e_{34} \\ e_{15} & 0 & 0 \\ 0 & 0 & 0 \end{bmatrix} \begin{Bmatrix} 0 \\ 0 \\ 0 \\ E_3 \end{Bmatrix} \quad (7.33)$$

where $c_{66}^E = 1/[2(s_{11}^E - s_{12}^E)]$ and $E_3 = V/th_a$, with V being the voltage applied along the actuator thickness, th_a .

If the PZT patch were in free space (i.e. not bonded to any structure), $\{T\} = 0$ and the strain generated in the material by an applied electric field would be equivalent to having external stresses acting on the patch with a value equal to $[e]\{E\}$. According to the PZT

force model by Nieuwenhuis et al. [18], the stress generated in the bonded PZT by an applied electric field can be approximated by those same external forces. Hence, the ultrasonic excitation was introduced by applying distributed perpendicular forces on the rectangular faces (i.e. pressure) of the actuator patch. The value of those stresses was computed based on Equation (7.33), for an excitation tone-burst amplitude of 8.2 V, modulated by a 5-cycle Hanning window.

The structured mesh was formed by solid, three-dimensional (3D), 8-node, reduced-integration elements (C3D8R) [19-23]. The first step in defining the mesh was to perform a convergence study to assess a suitable level of mesh refinement. To that end, different mesh sizes were created in order to have different number of elements per wavelength of S0 Lamb mode (λ_{S0}), and the in-plane displacement along the x -direction, U_1 , at the sensing node was extracted for each mesh size definition, as plotted in Figure 7.3.

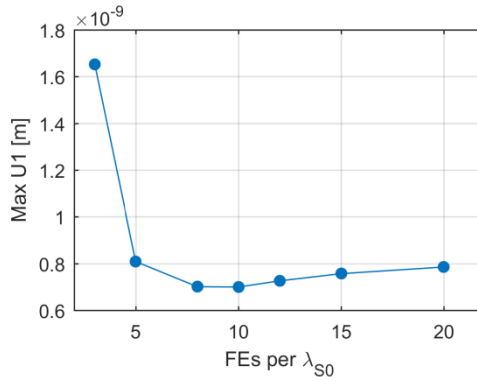


Figure 7.3. Convergence study results.

As U_1 seems to converge when the number of element per S0 wavelength is above 15, it was decided to employ 20 elements per wavelength of S0 Lamb mode along the in-plane propagation directions. Eight elements were defined along the thickness of the plate [20,22,24,25] and one element along the thickness of the PZT patch.

To ensure that the time-step was always shorter than the time required for the fastest wave component to propagate to an adjacent element (as stipulated by the Courant-Friedrichs-Lewy condition [26]), i.e. to always ensure convergence of the numerical solution, the simulation time-step was automatically defined by Abaqus by checking the stability condition element by element. The total simulated time interval was 0.1 ms so that the distance covered by the wavefront of the slowest mode at the centre frequency of excitation was at least 0.5 m.

Typically PZT sensors such as the Physical Acoustics WSA are primarily sensitive to out-of-plane particle motion. However, the coupling type influences the sensitivity to in-plane motion [27]. Since the coupling with the plate was ensured by high-viscosity shear gel, the sensitivity to shear stress, and thus the sensitivity to in-plane particle motion was expected to be higher than with “*conventionally considered to be high-performance ultrasonic couplant*” gels [27]. If the definition of dynamic viscosity, μ_{dyn} , is taken into account, one sees that the shear stress, τ , in the layer of couplant gel can be defined as $\tau = \mu_{dyn} \cdot \partial v / \partial y$, where $\partial v / \partial y$ is the velocity gradient in the couplant layer. Therefore, the total

ultrasonic GW response, V_{tot} , was taken as a combination of in-plane velocity, V_{rad} , and out-of-plane velocity, V_3 at the node associated with the sensing position, as in:

$$V_{tot} = p_{rad}V_{rad} + (1 - p_{rad})V_3 \quad (7.34)$$

where p_{rad} is the in-plane motion proportion.

The coefficient was varied between 0.05 and 0.9 and the root mean square deviation (RMSD, as in Equation (2.24)) between the numerical signal and the experimental signal was computed. In the time domain, the lowest value was $RMSD = 0.00755$ which corresponds to $p_{rad} = 0.3$. The numerical time-domain and frequency-domain signals are depicted in Figure 7.4 and Figure 7.5, respectively, together with their experimental counterparts.

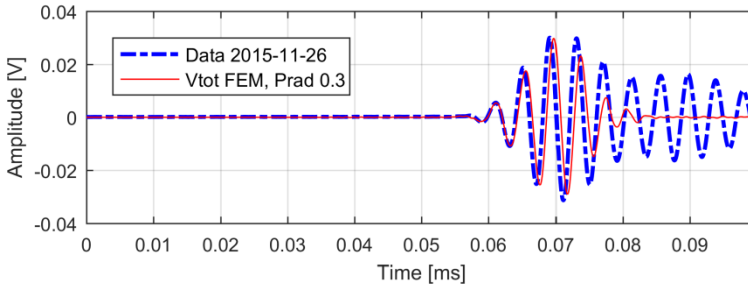


Figure 7.4. Time-domain comparison of the numerical and experimental signals.

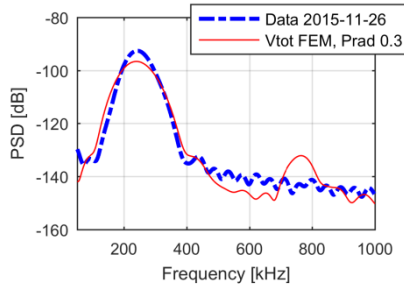


Figure 7.5. Frequency-domain comparison of the numerical and experimental signals.

For most of the propagation time (until 0.075 ms) the numerical signal approximated the experimental one to an acceptable level of accuracy. After 0.08 ms, the model was not capable to capture the last four GW cycles. The frequency spectra also showed an acceptable match for almost the entire frequency range, except for the 678-900 kHz interval. The differences observed in both time- and frequency domains were mainly attributed to three causes. First, the fact that the actual coupling between the sensor and the plate was not modelled might have had an influence on the signal phase and amplitude mismatch. Second, the absence of a model of the sensor dynamics itself, which, in the case of a relatively heavy transducer such as the Physical Acoustics WSA (stainless steel casing, with a mass of 32 grams), does influence the surface displacement of the plate under the

sensor. This could explain the high-frequency oscillations of almost negligible amplitude observed after 0.085 ms, which seem to correspond to the frequency spectra mismatch between 678 and 900 kHz, because “*linear reduced-integration elements tend to be too flexible*” [12]. Third, because the frequency response function of the sensor was not included in the simulation, it was not possible to simulate sensor resonance behaviour, which could explain the missing GW cycles in the numerical signal. Moreover, since the Physical Acoustics WSA is a wideband transducer, it has high sensitivity over a wide range of frequencies, but has low “*fidelity in terms of replicating the surface displacement of the structure on which they are mounted*” [28]. Taking all the above into account, it was deemed appropriate to use the PZT force model for simulating ultrasonic GW excitation.

7.3.2. Simulation of composite material

For this second validation phase, experimental data was taken from the GW tests conducted on TpC single-lap joints used for the study presented in Chapter 4. The test configuration and setup are described in Section 4.3.3 and shown in Figure 4.5 and Figure 4.6.

An FE model of the instrumented CF/PPS joints was built, with all the regions defined as deformable three-dimensional volumes. The dimensions of the adherends were set equal to their nominal values 101.6 mm \times 25.4 mm \times 1.62 mm, and the nominal value of 12.7 mm was used for the overlap distance. The CF/PPS woven composite material of the adherends was modelled as anisotropic homogenous, with the nine engineering constants (elastic moduli and Poisson’s ratios) and density taken from Daggumati et al. [29] and listed in Table 7.5. The composite layup was $[0^\circ/90^\circ]_{3s}$, as described in Section 3.2.1. The weld line was considered as isotropic homogenous, and its elastic properties equal to those of the PPS neat resin ($E = 3.80$ GPa, $G = 1.38$ GPa, $\nu = 0.37$, $\rho = 1350$ kg/m³ [30]). The chosen welding travel case was that of 0.12 mm, which was equivalent to having a weld line thickness of approximately 0.03 mm, as described in Section 4.3.1 and summarised in Table 4.2. The piezoceramic actuator patch was the same as the one used in the GW tests on the aluminium plate, and was modelled as described in Section 7.3.1.

Table 7.5. Properties of the CF/PPS woven composite material [29].

Property	Value	Property	Value	Property	Value
E_{11} [GPa]	56.49	G_{12} [GPa]	4.28	ν_{12} [-]	0.08
E_{22} [GPa]	56.41	G_{13} [GPa]	3.05	ν_{13} [-]	0.41
E_{33} [GPa]	10.53	G_{23} [GPa]	3.05	ν_{23} [-]	0.41
				ρ [kg/m ³]	1600

The mesh was formed by C3D8R elements, with all regions having twenty elements per λ_{SO} in the excitation bandwidth along the the xy -plane. Six elements were defined along the thickness of the adherends, and one element along the thickness of the weld line and PZT patch. The connection between all regions was ensured by tie constraints. The ultrasonic excitation was introduced by applying distributed forces on the faces of the PZT patch, according to the validated PZT force model described in Section 7.3.1. The value of those forces was computed for a voltage amplitude of 8 V and a 5-cycle sinusoidal tone-burst window with a Hanning amplitude modulation at 250 kHz.

The sensor clamp effect was simulated by applying clamping boundary conditions to surfaces on the top and bottom faces of the adherends, at a distance of 40 mm before and after the overlap. Those surfaces had an area equivalent to that of the Physical Acoustics WSA sensors (approximately 283.4 mm²). Just as with the first validation (see Section 7.3.1), the GW response was taken as a combination of V_{rad} and V_3 (see Equation (7.34)) at the sensing nodes (corresponding to the sensing positions R40 and T40 in Figure 4.5), but this time p_{rad} had to be redefined in order to account for the sensor clamping effect.

Again, to ensure that the time-step was always shorter than the time required for the fastest wave component to propagate to an adjacent element, the simulation time-step was automatically defined by Abaqus by checking the stability condition element by element. The total simulated time interval was 0.1 ms.

As expected, the sensor clamps allowed less friction between the sensors and the adherend surface, resulting in a smaller contribution of V_{rad} for the total GW signal. The best match between experimental and numerical signal was achieved for $p_{rad} = 0.05$, with an RMSD between time-domain signals of RMSD = 0.0538 for sensor 1, and RMSD = 0.0378 for sensor 2. The time- and frequency domain signals for both sensors are plotted in Figure 7.6 and Figure 7.7.

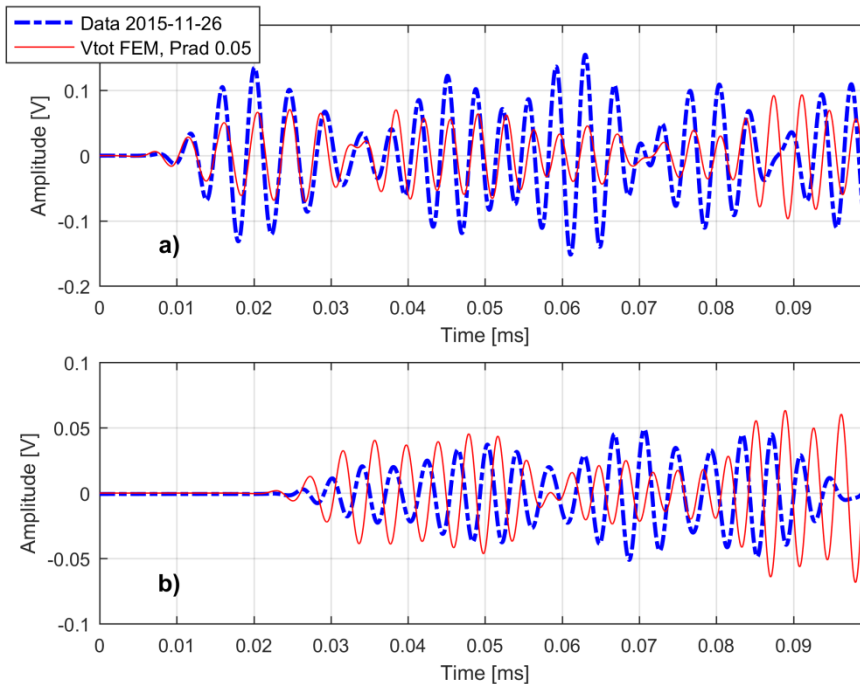


Figure 7.6. Time-domain comparison of the numerical and experimental signals from a) sensor at R40 (placed ahead of the lap joint) and b) sensor at T40 (placed after the lap joint). The R40 and T40 positions refer to Figure 4.5.

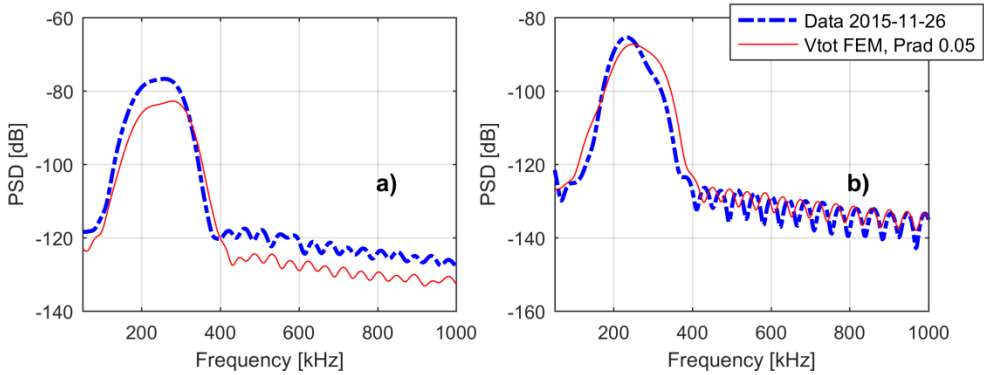


Figure 7.7. Frequency-domain comparison of the numerical and experimental signals from a) sensor 1 (before the overlap) and b) sensor 2 (after the overlap).

Two observations can be made about Figure 7.6. First, the signals from sensor 1 are in phase during almost all the propagation time (approximately until 0.085 ms), although there are some differences in amplitude. Second, the signals from sensor 2 are not in phase but are similar in amplitude. These two observations seem to indicate that the approach for modelling the composite material is appropriate, but the one used for modelling the weld interface is not (molecular interdiffusion is not included), even though the frequency-domain signals in Figure 7.7 from both sensors show good agreement. Focusing on the time-domain signal from sensor 1 (Figure 7.6a), one can argue that not modelling the woven characteristics of the composite adherends also played a role in the amplitude mismatch, as GWs are sensitive to small variations of stiffness in composite materials (as explained in Section 2.4.4). Additionally, there is also the combination of the three causes for mismatch in the first validation (see Section 7.3.1), exacerbated by potential inaccuracies in the simulation of the sensor clamping effect. Taking all this into account, it seems valid to consider the approach for modelling the composite material to be an appropriate approximation.

7.4. Component-scale model

The shape, dimensions and material properties of the component-scale structural model were inspired by area 3 of the torsion box panel described in Section 3.2.2 and depicted in Figure 3.5. The model was formed by six stringers and two ribs, as depicted in View A of Figure 7.8. The main dimensions of the assembly were 790 mm × 996 mm, with the thickness of the structural elements ranging between 3 and 3.5 mm. The simulated damage corresponded to the scenario considered as critical by the manufacturer and briefly introduced in Section 3.2.2: a disbond of the fourth stringer (see View B of Figure 7.8) due to peel forces caused by panel deformation after a low-energy impact (~ 50 J) at the stringer, on the outer side of the skin, near the support of rib 2 (see View C of Figure 7.8), with the disbond growing from the impact point towards the rib support. The transducer network had 8 PZT positions distributed as shown in Figure 7.9, according to the transducer network design for area 3 described in Section 6.4 and depicted in Figure 6.7.

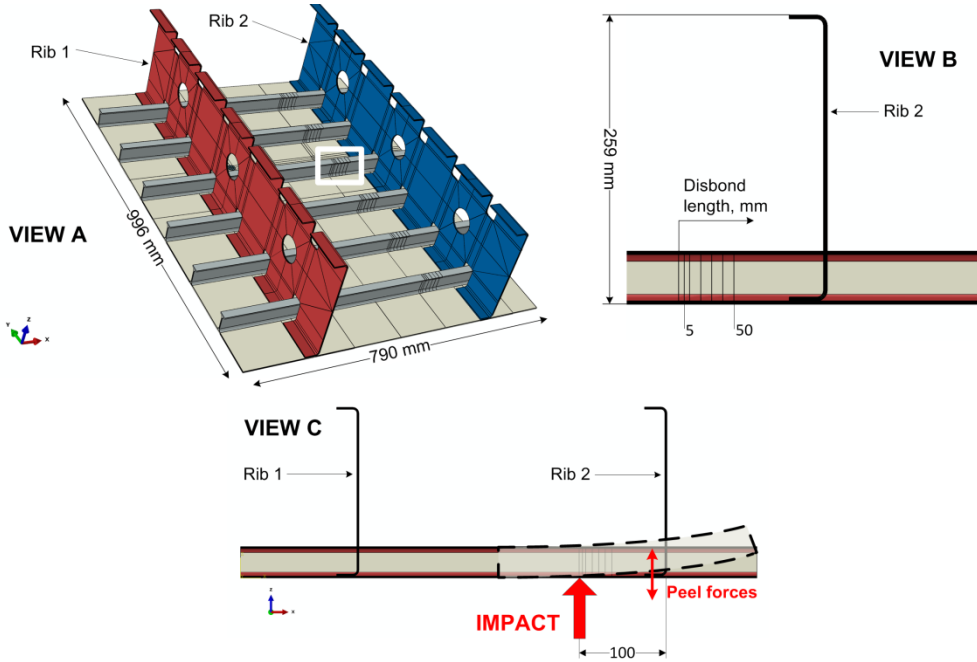


Figure 7.8. View A: Complete model with the panel, stringers (1 to 6 along the longest side), and ribs (1 and 2); damage (disbond) location indicated by a white rectangle. View B: Detail of the disbond area near the support of rib 2. View C: Diagram of the impact and resulting peel forces.

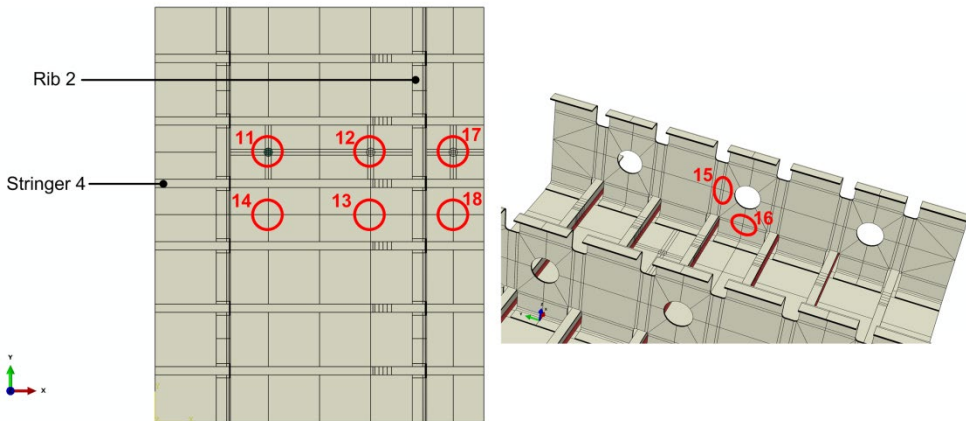


Figure 7.9. Positions of the PZT transducers on the model.

All the regions were defined as deformable three-dimensional volumes. The material for all the composite parts was modelled as anisotropic homogeneous, with the nine engineering constants and the density provided by Fokker Aerostructures BV and listed in Table 3.2. The symmetric stacking sequences adopted to model the composite parts were approximations of the real layups, and are presented in Table 7.6.

Table 7.6. Layup sequences used for all composite parts.

Part	Ply thickness [mm]	Ply fibre orientation [°]
Skin	[0.28/0.28/0.55/0.41] _s	[135/45/0/90] _s
Rib 1	[0.41/0.35/0.41/0.41] _s	[45/90/0/135] _s
Rib 2	[0.41/0.55/0.35/0.41] _s	[45/90/0/135] _s
Stringers	[0.32/0.32/0.48/0.39] _s	[135/45/0/90] _s

The PZT actuator patch was as an orthotropic homogeneous material, with elastic properties equal to those of APC 850 material presented in Table 7.4 with a nominal diameter of 20 mm and a thickness of 0.4 mm (according to the design of Section 6.4). The actuator bonding layer was assumed to be infinitesimally thin.

The mesh was formed by C3D8R elements, as employed in the validations of Sections 7.3.1 and 7.3.2. It was crucial to keep the number of FEs as low as possible in order to minimise the computational effort, and at the same time it was crucial to keep an acceptable level of accuracy. Therefore, it was decided to ensure that there were five elements per wavelength of A0 Lamb mode at the centre frequency of excitation [31,32]. This in turn allowed for approximately twenty elements per wavelength of S0 Lamb mode at the centre frequency of excitation, thus following the conclusions from the mesh convergence study presented in Section 7.3.1. Eight elements were defined along the thickness of the parts, with each composite ply being one layer element thick, according to the validated approach presented in Section 7.3.2. The PZT patch had one element along its thickness. The mesh controls for each part were defined to achieve the highest mesh quality while keeping the total number of elements as low as possible. As a result some parts were discretised with a sweep mesh pattern, while a structures mesh pattern was applied in the other parts.

The excitation load was introduced by applying distributed radial stress on the cylindrical face around the perimeter of the actuator patch and distributed perpendicular stress on the top and bottom faces of the actuator patch, according to the validated approach presented in Section 7.3.1. The value of those stresses was equal to $[e]\{E\}$ in Equation (7.33), for an excitation tone-burst amplitude of 50 V, modulated by a 5-cycle Hanning window. The ultrasonic GW response was taken from the out-of-plane displacement of the nodes associated with the sensing positions [33,34].

The undamaged connections between regions in the assembly were ensured by tie constraints. The disbond damage was modelled by a contact interaction between the fourth stringer and the panel [35-37]. The dynamics of the contacting surfaces was defined by the penalty formulation such that they were allowed to slide on each other while not interpenetrating each other. For the tangential behaviour, a friction coefficient of 0.2 [38] was adopted. For the normal behaviour, overclosure was dealt with by hard contact. The imperfect actuator bonding was modelled according to the same logic, by defining tie constraints for the bonded area portions, and contact interactions for the non-bonded ones, according to the circle divisions illustrated in Figure 7.10.

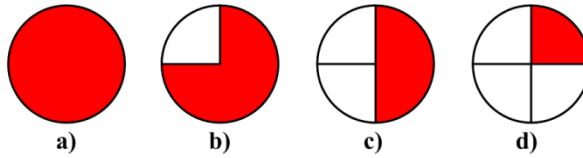


Figure 7.10. Portions of the actuator area corresponding to a) 100% bonding, b) 75% bonding, c) 50% bonding, and d) 25% bonding.

The simulation time-step was automatically defined by Abaqus by checking the stability condition element by element. The total simulated time interval was 0.8 ms such that the distance covered by the wavefront of the slowest mode at the centre frequency of excitation would be approximately 1 m. Given the scale of the model, it is relevant to provide an idea of the computational effort required to execute the simulations. The total number of elements was 2551940 for 112 kHz, and 6468004 for 198 kHz. The computation time was on average 3 hours and 14 minutes for 112 kHz, and 7 hours and 33 minutes for 198 kHz. For the sake of completeness and to give an a concrete idea of the propagation phenomena in the component-scale structure, Figure 7.11 shows the simulated ultrasonic wavefield at three consecutive instants. The numerical guided wave signals can be found in [39].

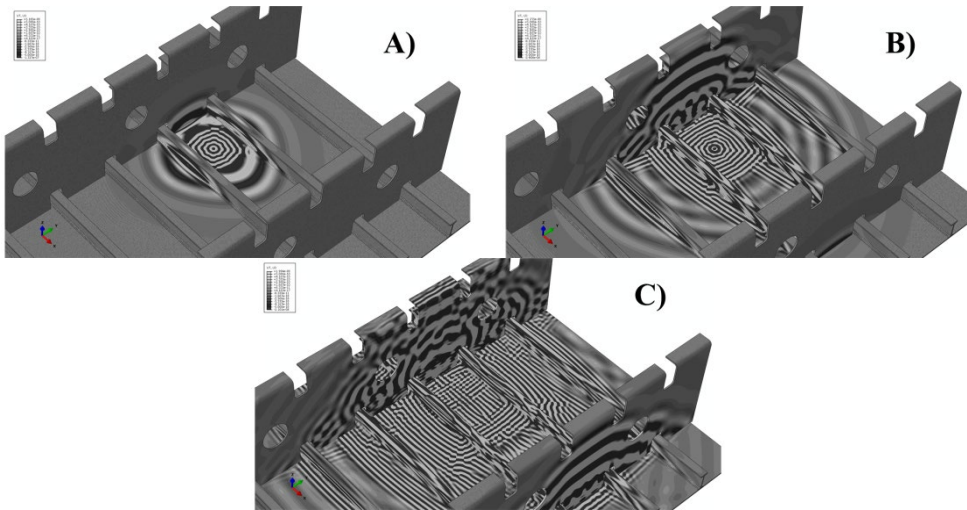


Figure 7.11. Simulated ultrasonic wavefield (z -displacement) after excitation by transducer 11, at time instants A) 16 μ s, b) 68 μ s, and C) 100 μ s.

7.5. Results and discussion

The reliability analysis protocol was applied to the scenarios of perfect actuator bonding and degraded actuator bonding. For the first scenario, the effects of error magnitude, number of repeated measures, excitation frequency and detection threshold were investigated. For the second scenario, the effect of actuator bonding degradation on the reliability of the GW-SHM was assessed, while taking into account the influence of

different excitation frequency and detection threshold on that effect. In all the aforementioned assessments the critical disbond size was equal to $a = 20$ mm, in agreement with the requirements from the manufacturer of the horizontal stabilizer torsion box panel specified in Section 3.2.2.

7.5.1. Perfect actuator bonding

7.5.1.1. Effect of error magnitude

Let the threshold, thr , be three times the base value, thr_0 , and let the number of repeated measures be 100. The DI databases generated through the stochastic transformation described in Section 7.2.2 with the error definitions 1 and 2 of Equations (7.3) and (7.4), respectively, for 112 and 198 kHz are depicted in Figure 7.12. For the sake of brevity, from here onwards the term “DI database” always refers to the stochastic DI database, unless mentioned otherwise.

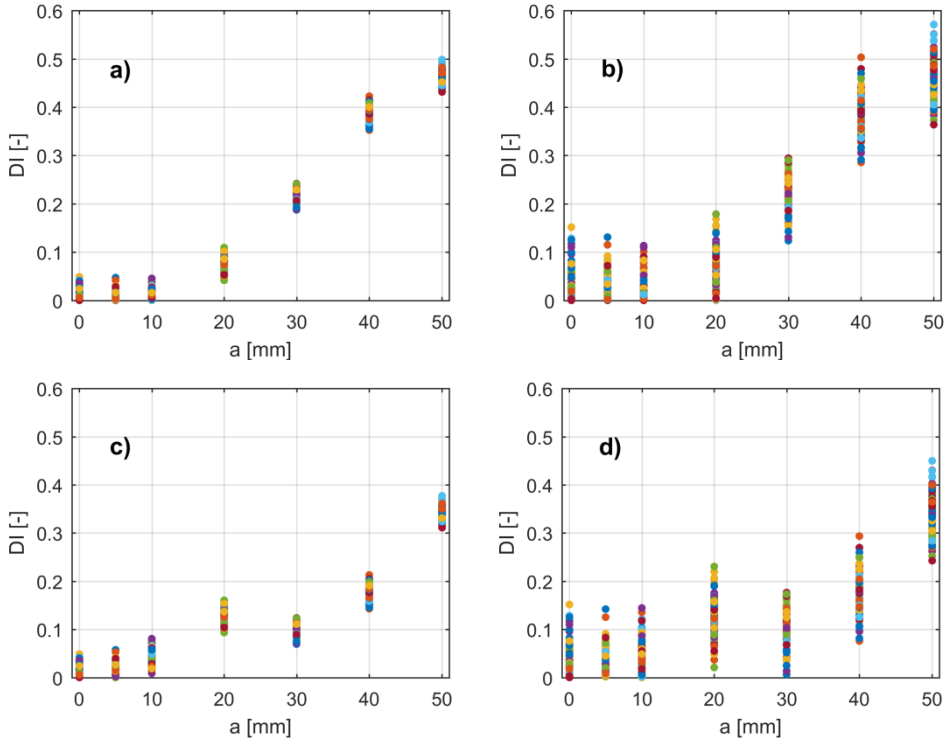


Figure 7.12. DI databases obtained with a) error 1 at 112 kHz, b) error 2 at 112 kHz, c) error 1 at 198 kHz, and d) error 2 at 198 kHz.

Naturally, graphs b) and d) have more dispersion per disbond size than graphs a) and c). So, at first glance, one would expect the non-critical damages (i.e. < 20 mm) to be detected more often with error 2 than with error 1. However, the POD curves obtained

with *hit/miss* analysis and \hat{a} vs a analysis for the 112 kHz databases show something different, as depicted in Figure 7.13.

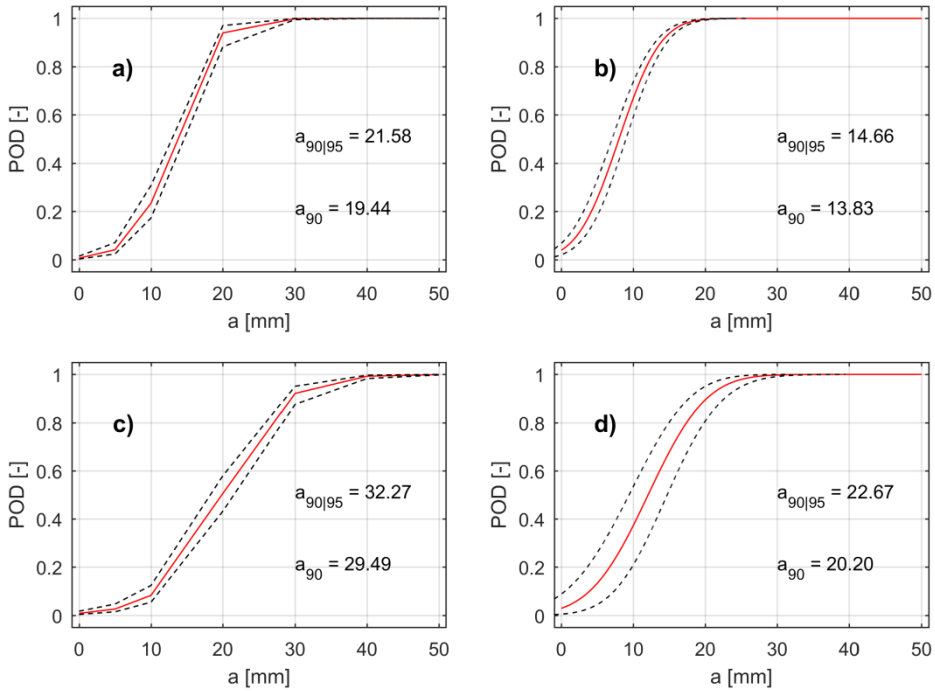


Figure 7.13. POD curves and 95% confidence bounds obtained at 112 kHz for $thr = 3thr_0$ with a) error 1 and *hit/miss* analysis, b) error 1 and \hat{a} vs a analysis, c) error 2 and *hit/miss* analysis, and d) error 2 and \hat{a} vs a analysis.

7

Curves obtained with the larger error (error 2, c) and d), are shifted to the right and have a slightly lower slope with respect to the ones obtained with smaller error (error 1, a) and b), thereby having a lower POD for damage sizes below 20 mm. Although this might seem counterintuitive, it has to do with the fact that the threshold base value, thr_0 , is defined as the standard deviation of the error between the DI points for non-critical damages and the points of the linear regression passing through those non-critical damage points (see Section 7.2.3). With the same threshold setting $thr = 3 thr_0$, the actual threshold value is higher for a larger error than for a smaller error. Because the adopted threshold definition is based on the trend for non-critical damages, it allows a change of response trend to be detected. Therefore, having a higher threshold value (due to a larger error) ends up being more robust against the detection of non-critical damages.

The higher magnitude of error 2 does result in wider 95% confidence bounds of the POD curves, in comparison with the curves for error 1. However, the performance of the GW-SHM with error 2 leads to less unnecessary diagnostic occurrences than with error 1, because non-critical disbonds are detected less times with the later than with the former. Nevertheless, it should be noted that if the error was of the same magnitude as the DI variation associated with the change from non-critical to critical damage size, then the above conclusions would no longer be true, as the the number of unnecessary detections would increase.

As explained in Section 7.2.2, error 2 was defined from experimental data acquired on composite specimens, while error 1 was defined based on data from metallic specimens. Hence, the variability in the DI database generated with error 2 is considered a more accurate representation of the influence of factors **a-f** (see Table 7.1) on the GW-SHM system than the variability in the database generated with error 1. Therefore, it was decided to adopt error definition 2 for the remaining analyses.

It is important to compare the results obtained with *hit/miss* analysis and with \hat{a} vs a analysis. The inverse link between the probability of the binary system response and the damage variable implies that the *hit/miss* regression parameters, and thus the POD model parameters, are only applicable for the damage points comprised in the dataset. On the contrary, the direct linear regression in the \hat{a} vs a analysis can be applied to damage sizes with no corresponding data points but still within the analysed range. For this reason, the POD curves from the *hit/miss* analysis are not as smooth as those from the \hat{a} vs a analysis. Also due the binary nature of the system response in the *hit/miss* analysis, the number of target damage points should be higher and more evenly distributed in the range of interest than in the \hat{a} vs a analysis [8]. Since the DI database was generated for only seven damage sizes, the *hit/miss* analysis underestimates POD, in comparison with the \hat{a} vs a analysis.

7.5.1.2. Effect of number of repeated measures

The number of times, n , the stochastic transformation was applied to each deterministic DI point was initially varied between 60 and 500 in order to assess the effect of the number of repeated measures on the POD. The resulting POD curves obtained at 112 kHz are plotted in Figure 7.14. For these calculations the threshold setting was kept at $thr = 3 \ thr_0$.

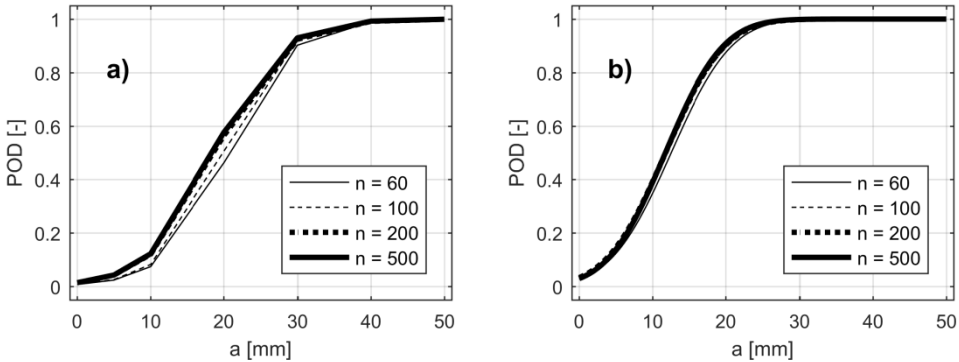


Figure 7.14. POD curves obtained at 112 kHz for different numbers of repeated measures, with a) *hit/miss* analysis, and b) \hat{a} vs a analysis.

Although they show little difference between them, the effect of increasing n from 60 to 100 is noticeable for both the *hit/miss* and the \hat{a} vs a analyses, and from 100 to 200 noticeable only for the *hit/miss* analysis. Within those two or three first increases of n , the POD curves shift towards the left, thus resulting in an increase of POD especially for the damage points in the middle of the curve. For $n > 200$ in Figure 7.14a) and for $n > 100$ in Figure 7.14b) the curves tend to coalesce to a common shape as the number of repeated

measure increases. The 95% confidence bounds (not included Figure 7.14 for the sake of clarity) also showed some variation in their width. To try to extract more information about the effect of varying n , it was decided to extend the range of n to 2000 and to focus on two specific aspects of the POD curves: 1) POD for the critical damage size, and 2) the width of the 95% confidence bounds. For that, the POD for $a = 20$ mm and the difference $a_{90/95} - a_{90}$ were plotted as functions of the number of repeated measures, both for *hit/miss* analysis and for \hat{a} vs a analysis, and for each excitation frequency (see Figure 7.15 and Figure 7.16).

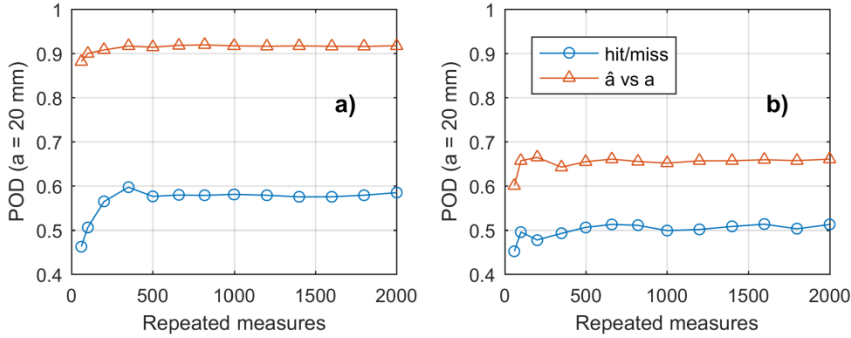


Figure 7.15. POD for critical damage size as a function of the number of repeated measures, for *hit/miss* and \hat{a} vs a analyses, for a) 112 kHz and b) 198 kHz.

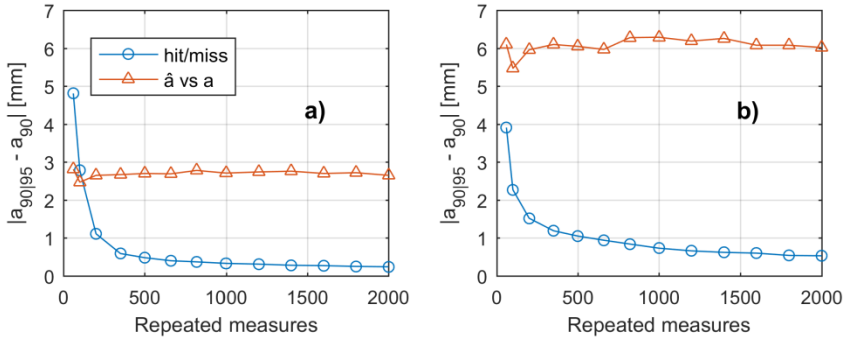


Figure 7.16. Semi-width of the 95% confidence bounds as a function of the number of repeated measures for *hit/miss* and \hat{a} vs a analyses, for a) 112 kHz and b) 198 kHz.

Generally, the POD for 20 mm increases in the first 2 or 3 increases of n and then stabilises around specific values for further increases of n . The slightly more irregular asymptotic behaviour with n at 198 kHz (Figure 7.15b) than at 112 kHz (Figure 7.15a) seems to be related to the DI points for 20 mm slightly deviating from the apparent linear trend of the rest of the DI points, as shown in Figure 7.12c) and d). When applying the stochastic transformation, the resulting random DI points also suffer from that deviation. Thus when n is varied, some DI databases have more DI points for 20 mm with a more downward deviation, other databases have more points with a more upwards deviation, thereby creating a certain fluctuation of the asymptotic behaviour of POD ($a = 20$ mm).

Looking now at Figure 7.16, the evolution of the semi-width of the 95% confidence bounds at both excitation frequencies is markedly different for \hat{a} vs a analysis and for *hit/miss* analysis. While for \hat{a} vs a analysis the confidence bounds remain practically unchanged, for *hit/miss* analysis they become considerably narrower within the first 2 or 3 first increases of n . This is another manifestation of the sensitivity of *hit/miss* analysis to the number of points used for the POD calculations, as discussed at the end of Section 7.5.1.1.

7.5.1.3. Effect of excitation frequency

The previous sections have already discussed some differences in diagnostic performance with different excitation frequencies. To further understand the effect of using a different excitation frequency, Figure 7.17 shows the POD curves obtained at 112 and 198 kHz with $thr = 3 thr_0$ and 200 repeated measures, for both analysis types.

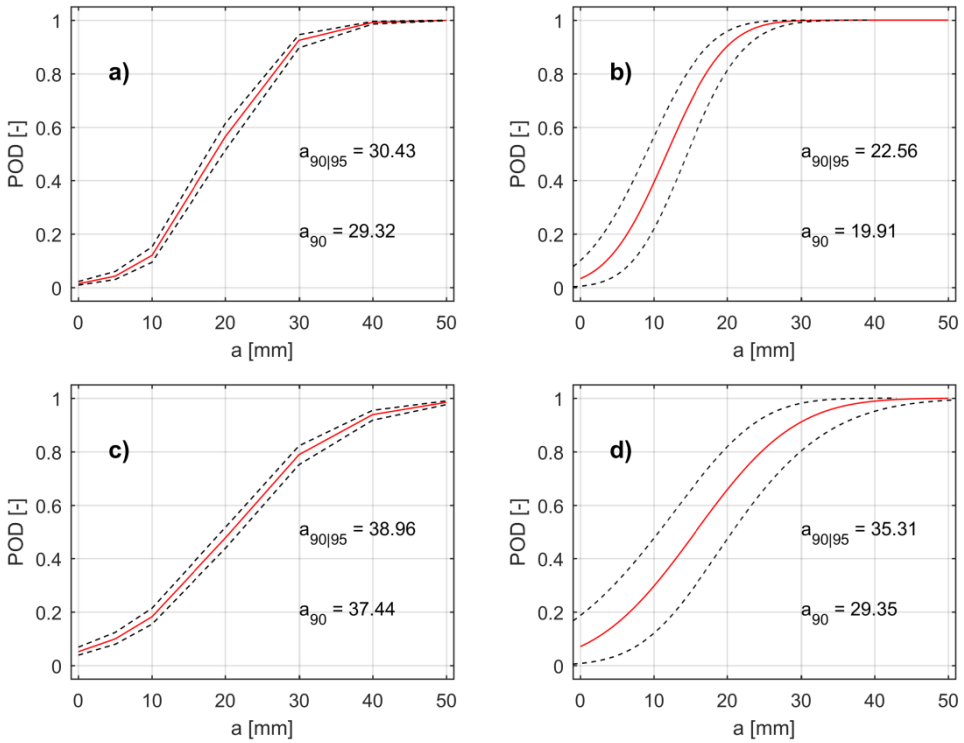


Figure 7.17. POD curves and 95% confidence bounds obtained for $thr = 3 thr_0$ at a) 112 kHz with *hit/miss* analysis, b) 112 kHz with \hat{a} vs a analysis, c) 198 kHz with *hit/miss* analysis, and d) 198 kHz with \hat{a} vs a analysis.

The POD curves for 198 kHz are shifted to the right and have a slightly lower slope than for 112 kHz, which results in lower POD values for the same disbond length. This was caused by lower DIs, and also by a less pronounced linear trend, for damage sizes above 20 mm at 198 kHz than at 112 kHz, as visible in Figure 7.12c) and d). But why is that? Table 7.7 shows the wavelength of the S0 and A0 Lamb modes at both excitation

frequencies, calculated from the phase velocity dispersion curves for area 3 plotted in Figure 6.2a).

Table 7.7. Approximate wavelength of the S0 and A0 Lamb modes at 112 and 198 kHz.

Mode	Frequency [kHz]	Wavelength, λ [mm]
S0	112	59.9
	198	33.6
A0	112	11.6
	198	7.2

The approximate wavelengths at 198 kHz are smaller than at 112 kHz, with the largest wavelength at 198 kHz being $\lambda_{S0} = 33.6$ mm. So, one possible explanation could be that at 198 kHz the wavelengths were not large enough to allow as strong a wave-disbond interaction as at 112 kHz for disbonds longer than 20 mm. Another possible explanation could be related to the fact that at 198 kHz the frequency bandwidth already allows the excitation of higher-order modes at frequencies just slightly above the cut-off. Those modes have a high phase velocities, which implies large wavelengths. In turn, this might result in some destructive interference between the higher-order and the zero-order modes when interacting with disbond longer disbonds (> 20 mm), thereby resulting in an apparently weaker DI response.

No change was observed in the 95% confidence bounds for *hit/miss* analysis, but for \hat{a} vs a analysis at 198 kHz they are wider than at 112 kHz, which is a sign of larger errors between the linear regression estimates and the data points. The deviation of the DI points for 20 mm from the apparent linear trend at 198 kHz (see Figure 7.12c and d) yields regressions which are less representative of all the points than at 112 kHz, thereby resulting in larger errors. The higher variances are then propagated through the computation to the POD model and the definition of the confidence intervals, as in Equation (7.21).

7

7.5.1.4. Effect of detection threshold

An important assessment to be made is that of the effect of varying the detection threshold on the reliability of the SHM system. Therefore integer multiples between 1 and 6 were employed to achieve different thresholds, as explained in Section 7.2.3. The POD curves obtained with \hat{a} vs a analysis for each threshold at 112 and 198 kHz are depicted in Figure 7.18 and Figure 7.19, respectively. The curves were generated by using 200 repeated measures.

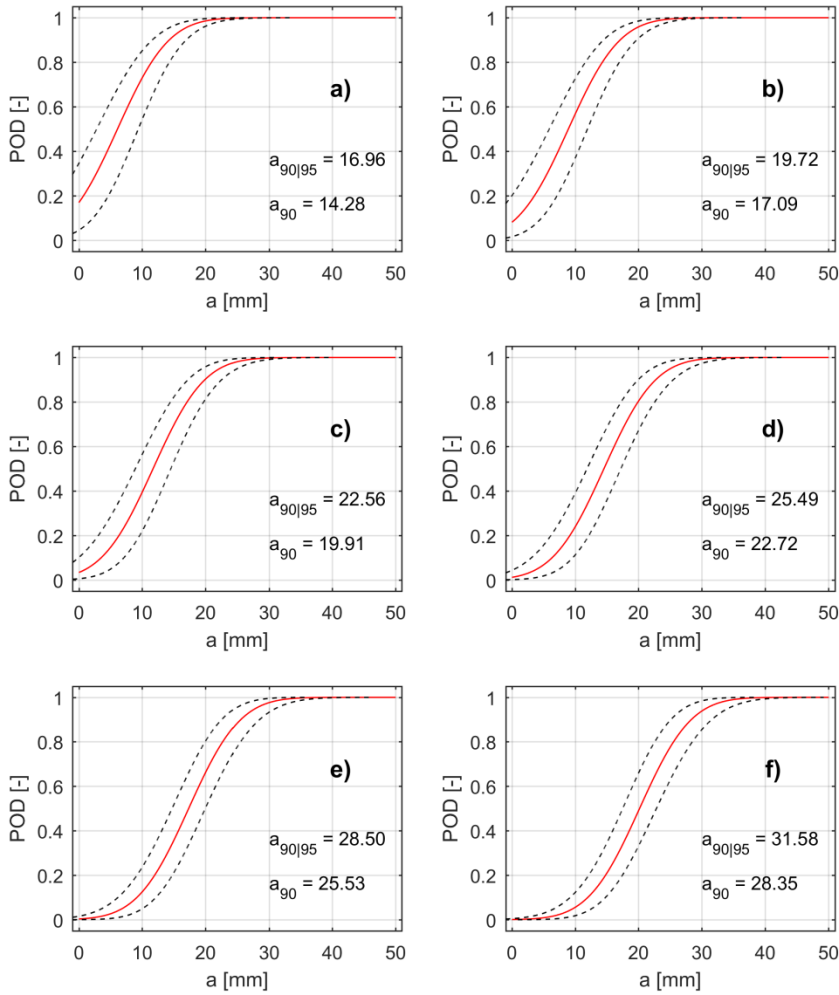


Figure 7.18. POD curves and 95% confidence bounds at 112 kHz obtained with \hat{a} vs a analysis for a) $thr = thr_0$, b) $thr = 2thr_0$, c) $thr = 3thr_0$, d) $thr = 4thr_0$, e) $thr = 5thr_0$, and f) $thr = 6thr_0$.

In both Figure 7.18 and Figure 7.19, from a) to f) the POD curve is shifted right without any visible change in its slope. Consequently, the POD for each damage size decreases for the points in between the asymptotes of the curve. On the one hand, an increase in threshold leads to less frequent detections of non-critical damages, which partially allows the avoidance of potential error-induced responses. On the other hand, high thresholds may prevent critical damages from being detected, which is clear from the increase of $a_{90|95}$ with increasing threshold. A useful way to visualise this trade-off is through the estimated ROC curves in Figure 7.20, where the TPD (true positive detection) and FPD (false positive detection) rates are plotted as a function of the threshold. It should be noted that the event of interest associated with the curves in Figure 7.20 is a disbond with a length equal to or greater than 20 mm.

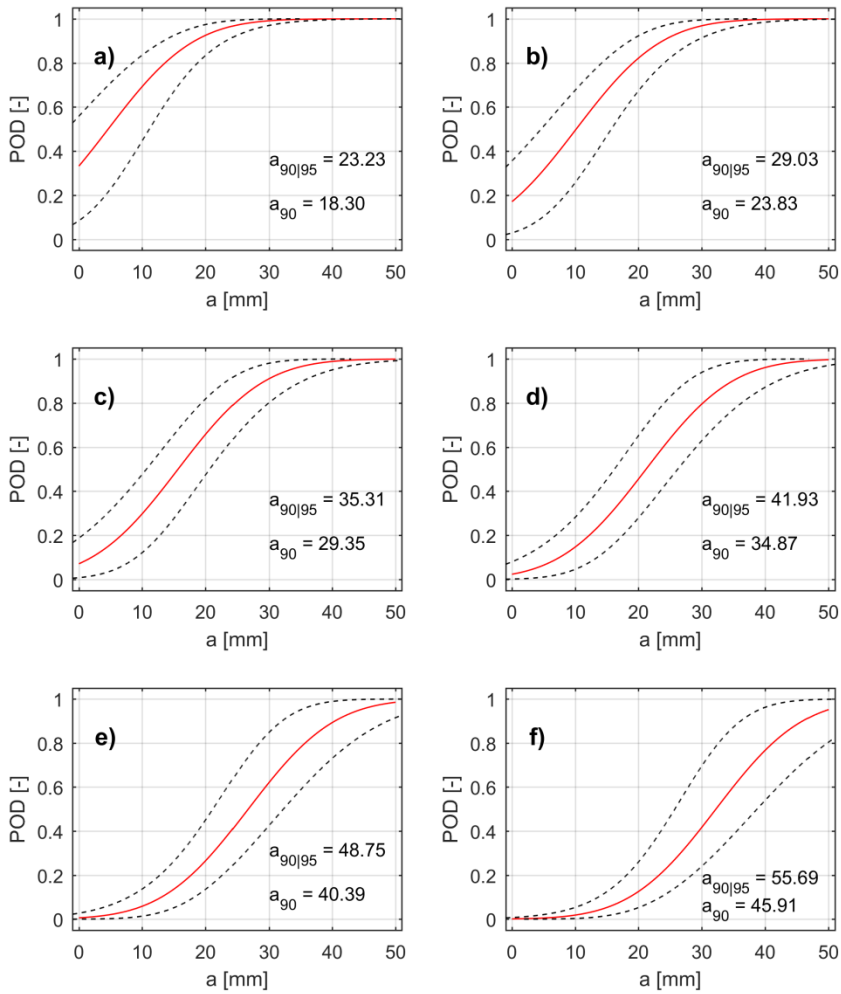


Figure 7.19. POD curves and 95% confidence bounds at 198 kHz obtained with \hat{a} vs a analysis for a) $thr = thr_0$, b) $thr = 2thr_0$, c) $thr = 3thr_0$, d) $thr = 4thr_0$, e) $thr = 5thr_0$, and f) $thr = 6thr_0$.

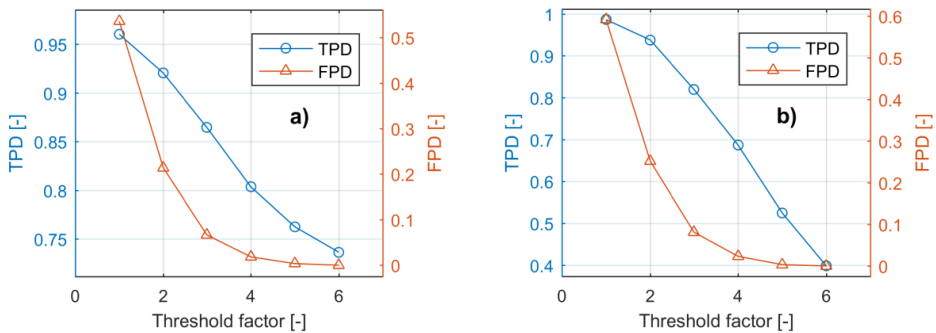


Figure 7.20. a) TPD and FPD rates for 112 kHz as functions of the threshold, and b) TPD and FPD rates for 198 kHz as functions of the threshold.

It is possible to see that if a FPD below 10% were desired, then the threshold should be at least $thr = 3thr_0$, which would allow a TPD of around 86% and 82 % at 112 and 198 kHz, respectively. For an FPD of no more than 1%, the threshold should be $thr > 4thr_0$, but the TPD would be reduced to less than 80% at 112 kHz and less than 67% at 198 kHz. In short, a decrease in FPD can only be achieved at the cost of a decrease in TPD.

It is interesting to note that, while for 112 kHz the width of the 95% confidence bounds remains practically unchanged, for 198 kHz there is a visible change, with wider confidence bounds at lower PODs for lower thresholds (Figure 7.19a and b), and wider at high PODs for higher thresholds (Figure 7.19e and f). As explained in Section 7.5.1.3, the confidence bounds are wider at 198 kHz than at 112 kHz because of the higher variance of the POD model, which in turn is the result of higher variance in the linear regressions for the DI points. However, the increase in confidence bound width is not uniform across the POD range because the confidence interval width, CIw , is dependent on a coupling between the linear regression variance and the threshold, as demonstrated by the expansion of the square root in the second term on the right-hand side of Equation (7.21) given below:

$$\sqrt{\mathbf{u}^T \boldsymbol{\Sigma}_{pod} \mathbf{u}} = CIw(\hat{\theta}^2, thr) = \sqrt{A_1 + B_1 + C_1 - D_1} \quad (7.35)$$

where A_1 , B_1 , C_1 and D_1 are defined as:

$$\begin{aligned} A_1 &= \frac{1}{\hat{b}_1} \left[\frac{Var(\hat{b}_0)}{\hat{b}_1} - \frac{Cov(\hat{b}_0, \hat{b}_1)(\hat{b}_0 - thr)}{\hat{b}_1^2} \right] \\ B_1 &= z_p \left\{ z_p \left[\frac{\hat{\theta}^2 Var(\hat{b}_1)}{\hat{b}_1^4} + \frac{\hat{\theta}^2 Var(\hat{\theta}^2)}{\hat{b}_1^2} \right] + \frac{\sqrt{\hat{\theta}^2}}{\hat{b}_1^2} \left[\frac{Cov(\hat{b}_0, \hat{b}_1)}{\hat{b}_1} - \frac{Var(\hat{b}_1)(\hat{b}_0 - thr)}{\hat{b}_1^2} \right] \right\} \\ C_1 &= z_p \left[\frac{Cov(\hat{b}_0, \hat{b}_1)\sqrt{\hat{\theta}^2}}{\hat{b}_1^3} - \frac{\sqrt{\hat{\theta}^2} Var(\hat{b}_1)(\hat{b}_0 - thr)}{\hat{b}_1^4} \right] \\ D_1 &= \frac{(\hat{b}_0 - thr)}{\hat{b}_1^2} \left[\frac{Cov(\hat{b}_0, \hat{b}_1)}{\hat{b}_1} - \frac{Var(\hat{b}_1)(\hat{b}_0 - thr)}{\hat{b}_1^2} \right] \end{aligned} \quad (7.36)$$

with all the variables defined in Section 7.2.4.2, in Equations (7.13) to (7.22).

When the threshold is low and thus close to \hat{b}_0 , the terms with the factor $(\hat{b}_0 - thr)$ almost vanish, and the confidence interval width becomes a function of $\hat{\theta}^2$ only:

$$CIw(\hat{\theta}^2) = \sqrt{A_2 + B_2 + C_2} \quad (7.37)$$

where A_2 , B_2 and C_2 are equal to:

$$\begin{aligned} A_2 &= \frac{Var(\hat{b}_0)}{\hat{b}_1^2} \\ B_2 &= z_p \left\{ z_p \left[\frac{\hat{\theta}^2 Var(\hat{b}_1)}{\hat{b}_1^4} + \frac{\hat{\theta}^2 Var(\hat{\theta}^2)}{\hat{b}_1^2} \right] + \frac{Cov(\hat{b}_0, \hat{b}_1) \sqrt{\hat{\theta}^2}}{\hat{b}_1^3} \right\} \\ C_2 &= z_p \frac{Cov(\hat{b}_0, \hat{b}_1) \sqrt{\hat{\theta}^2}}{\hat{b}_1^3} \end{aligned} \quad (7.38)$$

So, if the linear regression variance, $\hat{\theta}^2$, is high (as in the case of 198 kHz), the confidence interval width is amplified by z_p , which tends towards $-\infty$ when p tends to zero. When the threshold is high the factor $(\hat{b}_0 - thr)$ in Equation (7.35) is coupled with $\hat{\theta}^2$. If $\hat{\theta}^2$ is high (as in the case of 198 kHz) and the threshold is also high, then the coupling is magnified by the fact z_p , tends towards $+\infty$ when p tends to 1. Given that $z_p = 0$ at $p = 0.5$, the result is a non-uniform confidence interval width across the POD range for low and high thresholds at 198 kHz.

In the case of 112 kHz excitation, the linear regression variance is low (relatively close to zero), and the confidence interval width approaches the following expression:

$$CIw(thr) = \sqrt{A_3 - D_3} \quad (7.39)$$

with A_3 and D_3 defined as:

$$\begin{aligned} A_3 &= \frac{1}{\hat{b}_1} \left[\frac{Var(\hat{b}_0)}{\hat{b}_1} - \frac{Cov(\hat{b}_0, \hat{b}_1)(\hat{b}_0 - thr)}{\hat{b}_1^2} \right] \\ D_3 &= \frac{1}{\hat{b}_1^2} \left\{ (\hat{b}_0 - thr) \left[\frac{Cov(\hat{b}_0, \hat{b}_1)}{\hat{b}_1} - \frac{Var(\hat{b}_1)(\hat{b}_0 - thr)}{\hat{b}_1^2} \right] \right\} \end{aligned} \quad (7.40)$$

which is no longer dependent on z_p . That is why the confidence bounds at 112 kHz have an approximately uniform width across the POD range, for all threshold values.

At 198 kHz, for the thresholds of $thr = 3thr_0$ and $thr = 4thr_0$ (Figure 7.19c and d), the confidence bounds have an approximately uniform width, which means the A and D terms in Equation (7.36) attenuate the terms B and C , which contain the distorting element z_p . This seems to indicate that intermediate thresholds represent an optimum setting which should be implemented for a non-biased detection.

At this point of the discussion it is important to specify that at an excitation frequency of 112 kHz and for a threshold $thr = 2thr_0$ it is estimated to be possible to detect a disbond of 19.7 mm 90% of the times, with a confidence of 95%, and an estimated FPD rate of about 20%. If an FPD below 10% is preferred, it is still estimated to be possible to detect a 19.9 mm long disbond in 90% of the cases, although 95% confidence is only estimated to be ensured for a disbond with a length of 22.6 mm. These results provide some evidence

that the GW-SHM system designed according to the methodology proposed in Chapter 6 for area 3 of the real-scale (1:1) torsion box panel might be able to reliably accomplish its mission of detecting stringer disbonds.

7.5.1.5. Predictive capabilities of the system

It is also relevant to assess the capability of knowing about the existence of a critical damage given the (non-)occurrence of a detection. In the form of a question: what is the capability of knowing about the existence of a damage of interest for a certain set of system settings? It is then useful to consider the ROL curves in Figure 7.21, where the estimated CEP (correct event prediction), ME (missed event), CR (correct rejection) and FEP (false event prediction) rates are plotted. These curves were obtained with a threshold of $thr = 3thr_0$ and with 200 repeated measures.

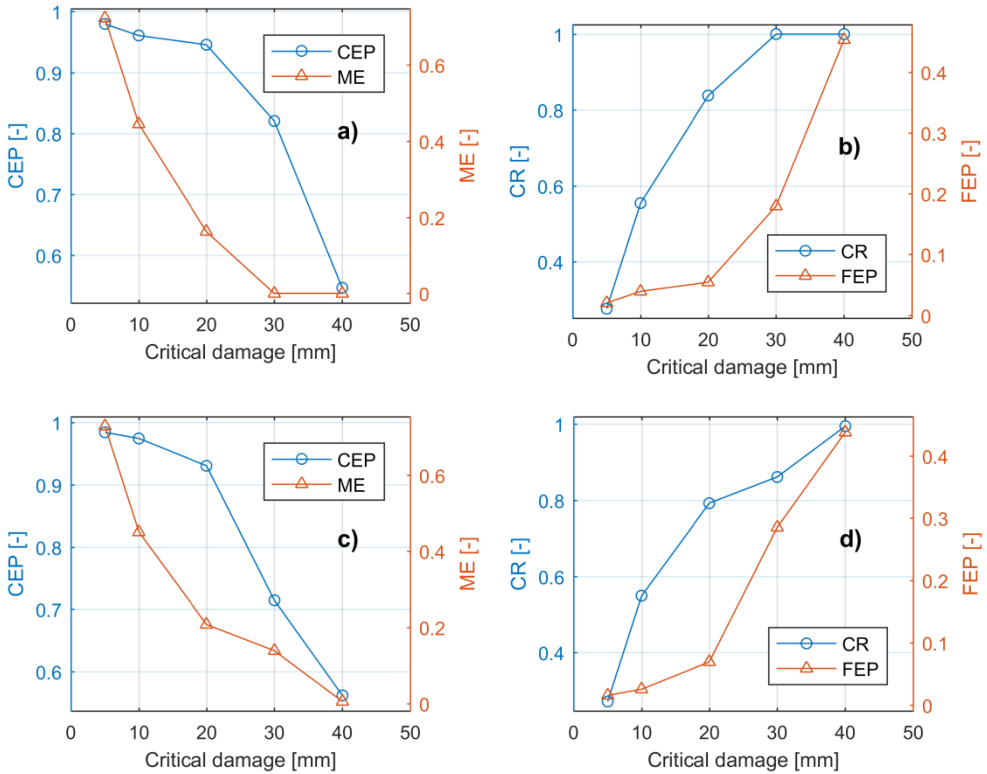


Figure 7.21. a) CEP and ME rates for 112 kHz as functions of critical damage of interest, b) CR and FEP rates for 112 kHz as functions of critical damage of interest c) CEP and ME rates for 198 kHz as functions of critical damage of interest, and d) CR and FEP rates for 198 kHz as functions of critical damage of interest.

At 112 kHz, the estimated probability of a 20 mm long disbond existing if a detection occurs is above 90%, with a corresponding estimated probability of missing it below 20%. At 198 kHz, the estimated probability of a 20 mm long disbond existing if a detection occurs is still above 90%, but the estimated probability of missing it slightly above 20%.

Nevertheless, at both excitation frequencies, the estimated probability of a 20 mm long disbond not existing if a detection does not occur is around 80%, with a corresponding estimated probability of falsely predicting below 7%. Therefore, the GW-SHM system is estimated to have reasonable predictive capabilities.

7.5.2. Degraded actuator bonding

The last step of this analysis is to include the cases with degraded actuator bonding, which were simulated by reducing the fraction of the actuator area which was effectively bonded to the surface of the structure, as explained in Section 7.2.1. The DI databases for 112 kHz with the cases of 75%, 50% and 25% bonded area are shown in Figure 7.22.

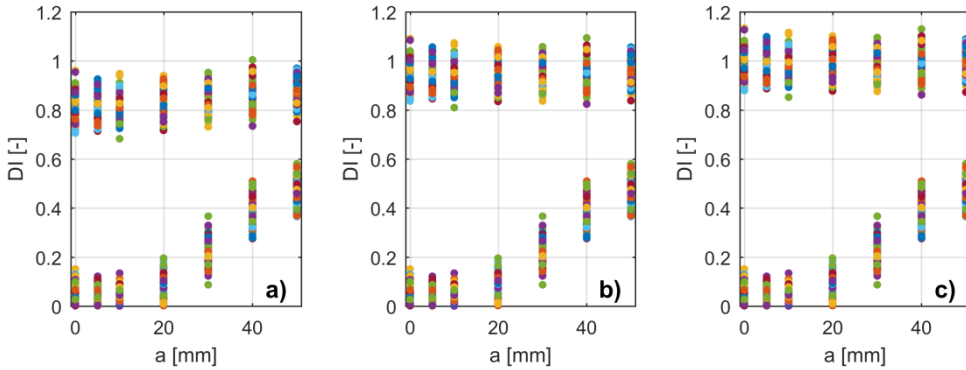


Figure 7.22. DI databases obtained for 112 kHz with an bonded actuator area of a) 75%, b) 50%, and c) 25%.

With just 25% less of bonded actuator area, the changes induced in the ultrasonic GW signals were enough to take the DI to values close to 1 (Figure 7.22a), due to the fact that GW scattering changes induced by the imperfect actuator bonding are comparable to those induced solely by damage. With even larger portions of degraded actuator bonding, the DI reaches or even exceeds the value of 1. Moreover, the trend of increasing DI with increasing disbond length was completely gone. The only remaining trend was that shown by the points for perfect actuator bonding.

The corresponding POD curves for 75% bonded actuator area at 112kHz, obtained with \hat{a} vs a analysis, six different thresholds and 200 repeated measures are shown in Figure 7.23.

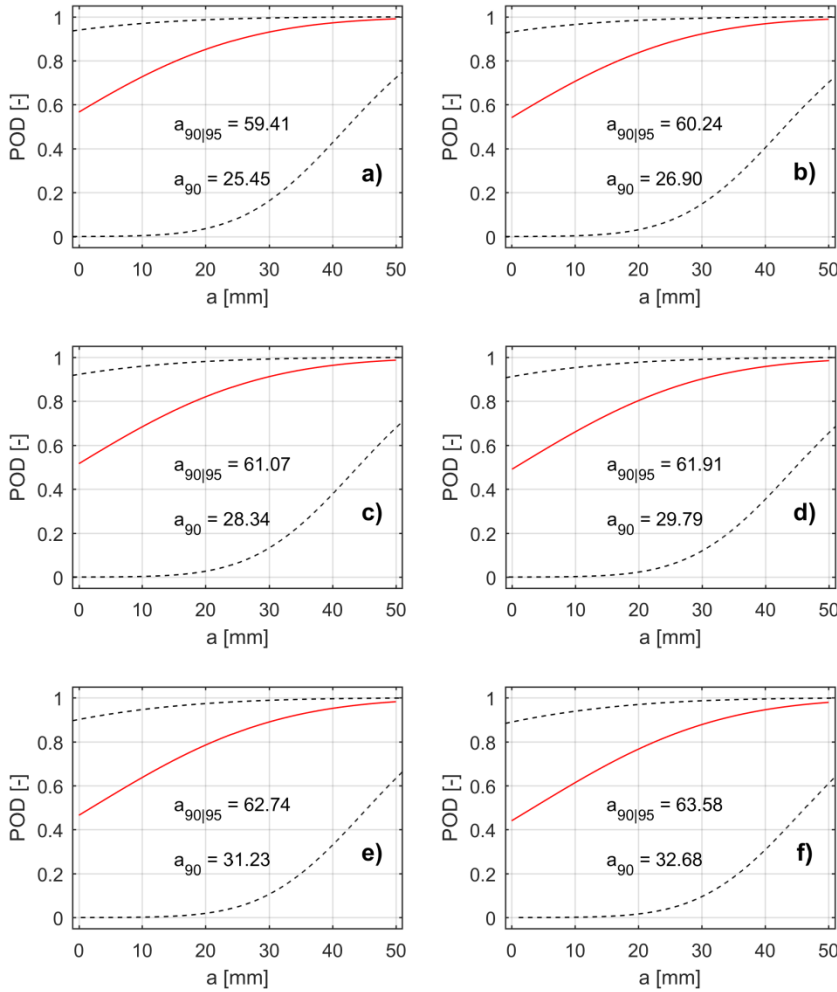


Figure 7.23. POD curves and 95% confidence bounds at 112 kHz, with 75% bonded actuator area, obtained with \hat{a} vs a analysis for a) $thr = thr_0$, b) $thr = 2thr_0$, c) $thr = 3thr_0$, d) $thr = 4thr_0$, e) $thr = 5thr_0$, and f) $thr = 6thr_0$.

The POD for $a = 0$ mm is estimated to be 50%, which means the lowest estimated FPD rate at 112 kHz is 50%. As illustrated by the succession from Figure 7.23a) to f), the variations of threshold have barely any influence on the POD in the case of 75% bonded actuator area, with $a_{90|95}$ remaining approximately equal to 60 mm for all thresholds. The confidence bounds are very wide because the linear regression errors are very high.

When considering the cases of an even more reduced bonded actuator area (50% and 25%) the POD curves (purposely omitted) are almost identical to the 75% case, also starting at around 50%, with little influence from threshold variation, and with $a_{90|95}$ remaining between 60 and 70 mm. At 198 kHz, the scenario is entirely similar.

Given these results, one question arises. In the case of some actuator bonding degradation, would the GW-SHM system still be capable of accomplishing the mission of reliably detecting stringer disbands in area 3 of the torsion box panel? The answer is

straightforward: No, the very high false positive detection rate renders practically impossible any reliable diagnostic.

It can be argued that the adopted model of actuator bonding degradation is not accurate, but it certainly is conservative and thereby lies on “the safe side”. Therefore, the analysis with actuator bonding degradation clearly shows how detrimental that variability factor is for the GW-SHM system performance, and how important it is to take it into account for the reliability assessment.

Nevertheless, the questions remains: how can GW-SHM systems be designed to cope with such scenarios of actuator bonding degradation? Besides the importance of having a system for monitoring the integrity of the transducer network itself, it might be advantageous for a GW-SHM system to employ two parallel lines of diagnostic. One for *absolute* diagnostic, in which the baseline signal represents the condition of the structure as it was right after manufacturing. And one for *relative* diagnostic, in which the baseline should be updated every x flight cycles (e.g. every flight, depending on the duration and/or loading spectrum of the flight). The relative baseline updating could even be an operation with dynamic settings within each flight. For example, if during a flight the transducer network integrity monitoring system would have an indication that some damage had been caused to one of the transducers, not only the actuation-sensing configuration of the network could be changed, but also the instruction for updating the relative baseline could be given.

7.5.3. Brief considerations about causality

It is reasonable to imagine a scenario in which a very small stringer disbond (e.g 2 mm) went undetected by NDT and the aircraft is back in the air. It can be expected that the probability of detecting the disbond growth will be affected by the measurement rate, i.e. the frequency of data acquisition. This relationship was not considered in the study presented in this chapter. Because loading cycles were not simulated, there was no damage growth, and thus no damage growth rate. In other words, the increase in damage size was not associated with the passage of time (there was no causality), and hence the scenario of failure was not assessed. Instead, the simulation of different damage sizes was intended to mimic different individual damage states that might occur due to fatigue loading.

7.6. Conclusions

The focus of this chapter was on improving the characterisation of ultrasonic GW-SHM systems for real-scale (1:1) composite structures. To that end, crucial GW measurement variability factors, such as geometric complexity, material anisotropy and transducer bonding degradation, were simultaneously taken into account in the development of numerical modelling and POD computation approaches for studying the reliability of the GW-SHM system designed for area 3 of the component-scale torsion box panel, according to the methodology proposed in Chapter 6, in detecting a stringer disbond. A protocol was implemented in order to incorporate the principles of model-assisted POD analysis. The reliability assessment was performed according to recommended statistical methods for *hit/miss* analysis and \hat{a} vs a analysis.

The study took into account the errors associated with material and dimensional variability of both the structure and the transducers, showing that a higher variability contributes to lower POD values and wider 95% confidence bounds. The increase of the

number of repeated measures was shown to contribute to a narrowing of the 95% confidence bounds, and to a convergence of the POD around its asymptotic value.

The excitation frequency affected the POD to the same extent as the DI, with higher values at 112 kHz than at 198 kHz. The lower DIs at 198 kHz were in turn correlated to a weaker GW-damage interaction at that frequency than at 112 kHz. The 95% confidence bounds were wider at 198 kHz than at 112 kHz as a result of higher variance of the regression used for the construction of the POD model.

The effect of varying detection threshold was also evaluated. At both excitation frequencies the expected trend was observed, with the false positives decreasing with increasing threshold, at the cost of decreasing true positives. There was an interesting finding regarding the width of the 95% confidence bounds. While at 112 kHz there was approximately no change in their width, at 198 kHz the width varied in a non-uniform way when the threshold was increased. For low thresholds, the confidence bounds were wider at low POD values than at high ones, while for high thresholds, they were wider at high POD values than at low ones. For intermediate thresholds, the confidence bounds had an approximately uniform width. It was demonstrated that the non-uniform width of the confidence bounds for the extreme thresholds was caused by a coupling between three regression variance and the threshold value, which was enhanced by the non-uniform value of the quantile of the standard normal distribution. Therefore, there seems to be an optimum threshold, at around 3 to 4 times the threshold base value, that enables detection with unbiased confidence levels.

The most important result obtained for the scenario of perfect actuator bonding was that, at 112 kHz, it was estimated to be possible to detect the critical disbond in 90% of the cases, with a confidence of 95%. This provided a complete answer to the research question Q3), along with some evidence that the GW-SHM system designed according to the methodology proposed in Chapter 6 for area 3 of the real-scale (1:1) torsion box panel might be able to reliably accomplish its mission of detecting stringer disbonds.

Finally the scenario of degraded actuator bonding was also studied. It was observed that a reduction of just 25% in the bonded actuator area results in a false positive detection rate of 50% for a disbond of null length, which renders any diagnostic impossible. This proved that it is crucial to include the integrity of the transducer adhesive layer in the reliability analysis of GW-SHM systems. By doing so, adaptive strategies can be devised to deal with data acquired in these type of scenarios, which is a vital step for the certification of GW-SHM systems.

References

1. Ochôa P, Groves RM, Benedictus R. Reliability analysis of an ultrasonic guided wave based structural health monitoring system for a carbon fibre reinforced thermoplastic torsion-box. Paper presented at: *11th IWSHM*, September 12-14, 2017; Palo Alto, CA (USA).
2. Janapati V, Kopsaftopulos F, Li F, Lee SJ, Chang FK. Damage detection sensitivity characterization of acousto-ultrasound-based SHM techniques. *Struct Health Monit* 2016; 15(2): 143-161.
3. Kabban CMS, Greenwell BM, DeSimio MP, Derriso MM. The probability of detection for structural health monitoring systems: Repeated measures data. *Struct Health Monit* 2015; 14(3): 252-264.

4. Ku HH. Notes on the use of propagation of error formulas. *J Res Nat Bur Stand* 1966; 70C(4): 263-273.
5. Ochôa P, Villegas IF, Groves RM, Benedictus R. Guided wave and mechanical testing of defective thermoplastic composite ultrasonic welds. 4TU.Centre for Research Data, 2018. DOI: 10.4121/uuid:190ac321-ad31-456c-919e-564f7e6333ef.
6. Cobb AC, Fisher J, Michaels JE. Model-assisted probability of detection for ultrasonic structural health monitoring. Paper presented at: *4th European-American Workshop on Reliability of NDE*; June 24-26, 2009; Berlin, Germany.
7. ARP6461:2013-09. Guidelines for implementation of structural health monitoring on fixed wing aircraft; 2013.
8. MIL-HDBK-1823A: 2009. Department of Defense Handbook: Nondestructive Evaluation System Reliability Assessment.
9. Knopp JS, Zeng L. Statistical analysis of hit/miss data. Wright-Patterson Air Force Base, OH: Materials State Awareness & Supportability Branch, Structural Materials Division, Air Force Research Laboratory; 2012. AFRL-RX-WP-TP-2012-0355.
10. Harding CA, Hugo GR. Statistical analysis of probability of detection hit/miss data for small data sets. *AIP Conf Proc* 2003; 657: 1838-1845.
11. Mason SJ, Graham NE. Conditional probabilities, relative operating characteristics, and relative operating levels. *Wea Forecasting* 1999; 14: 713-725.
12. Abaqus 6.14 Documentation. Abaus basics. In: *Getting started with Abaqus*. Dassault Systèmes, 2014.
13. Abaqus 6.14 Documentation. Part VI, 27.1.3. In: *Abaqus Analysis User's Guide*. Dassault Systèmes, 2014.
14. Abaqus 6.14 Documentation. Part III, 12. In: *Abaqus/CAE User's Guide*. Dassault Systèmes, 2014.
15. EN AW-6082 – EN AW-Al Si1MgMn, Almet Marine.
16. Giurgiutiu V. Electroactive and magnetoactive materials. In: Giurgiutiu V. *Structural health monitoring with piezoelectric wafer active sensors*. 2nd ed. Academic Press – Elsevier; 2014.
17. Pérez N, Buiocchi F, Andrade MAB, Adamowski JC. Numerical characterization of soft piezoelectric ceramics. *AIP Conf Proc* 2012; 1433: 648-651.
18. Nieuwenhuis JH, Neumann JJ, Greve DW, Oppenheim IJ. Generation and detection of guided waves using PZT wafer transducers. *IEEE Trans Ultrason, Ferroelect, Freq Control* 2005; 52(11): 2103-2111.
19. Abaqus 6.14 Documentation. Finite elements and rigid bodies. In: *Getting started with Abaqus*. Dassault Systèmes, 2014.
20. Ng CT, Veidt M, Rose LRF, Wang CH. Analytical and finite element prediction of Lamb wave scattering at delaminations in quasi-isotropic composite laminates. *J Sound Vib* 2012; 331: 4870-4883.

21. Murat BIS, Khalili P, Fromme P. Impact damage detection in composite panels using guided ultrasonic waves. *AIP Conf Proc* 2014; 1581: 286-293.
22. Manogharan P, Yu X, Fan Z, Rajagopal P. Interaction of shear horizontal bend (SH_B) guided mode with defects. *NDT&E Int* 2015; 75: 39-47.
23. Rajagopal P, Lowe MJS. Scattering of the fundamental shear horizontal guided wave by a part-thickness crack in an isotropic plate. *J Acoust Soc Am* 2008; 124(6): 2895-2904.
24. Demma A, Cawley P, Lowe M. Scattering of the fundamental shear horizontal mode from steps and notches in plates. *J Acoust Soc Am* 2003; 113(4): 1880-1891.
25. Guo N, Cawley P. The interaction of Lamb waves with delaminations in composite plates. *J Acoust Soc Am* 1993; 94(4): 2240-2246.
26. Courant R, Friedrichs K, Lewy H. On the partial difference equations of mathematical physics. *IBM J Res Dev* 1967; 11(2): 215-234.
27. Theobald P, Zeqiri B, Avison J. Couplants and their influence on AE sensor sensitivity. *J Acoustic Emission* 2008; 26: 91-97.
28. Wilcox PD, Lee CK, Scholey JJ, Friswell MI, Wisnom MR, Drinkwater BW. Quantitative structural health monitoring using acoustic emission. *Proc SPIE* 2006; 6173(6173K): 1-10.
29. Daggumati S, De Baere I, Van Paepegem W, Degrieck J, Xu J, Lomov SV, Verpoest I. Local damage in a 5-harness satin weave composite under static tension: part II - Meso-FE modelling. *Compos Sci Technol* 2010; 70: 1934-1941.
30. TenCate Cetex TC1100 PPS Resin System, TenCate Advanced Composites, Product Datasheet Revised 05/2014.
31. Drozd MB. *Efficient finite element modelling of ultrasound waves in elastic media*. London: Imperial College of Science Technology and Medicine, University of London; 2008.
32. Blake RJ, Bond LJ. Rayleigh wave scattering from surface features: wedges and down-steps. *Ultrasonics* 1990; 28: 214-228.
33. Luca A, Caputo F, Khodaei ZS, Aliabadi MH. Damage characterization of composite plates under low velocity impact using ultrasonic guided waves. *Composites Part B* 2018; 138: 168-180.
34. Leckey CAC, Wheeler KR, Hafiychuk VN, Hafiychuk H, Timuçin DA. Simulation of guided-wave ultrasound propagation in composite laminates: Benchmark comparisons of numerical codes and experiment. *Ultrasonics* 2018; 84: 187-200.
35. Kang KT, Chun HJ, Son JH, Byun JH, Um MK, Lee SK. Damage detection of composite plates using finite element analysis based on structural health monitoring. Paper presented at: 17th ICCM; July 27-31, 2009; Edinburgh, United Kingdom.
36. Zhang Z, Shankar K, Tahtali M, Morozov EV. Vibration modelling of composite laminates with delamination damage. Paper presented at: 20th ICA; August 23-27, 2010; Sydney, Australia.

37. Garcia D, Palazzetti R, Trendafilova I, Fiorini C, Zucchelli A. Vibration-based delamination diagnosis and modelling for composite plates. *Compos Struct* 2015; 130: 155-162.
38. Schön J. Coefficient of friction of composite delamination surfaces. *Wear* 2000; 237: 77-89.
39. Ochôa P. Supporting data for finite-element simulations of ultrasonic guided wave propagation on a full scale composite aircraft primary structure. 4TU.Centre for Research Data. Dataset, 2019. <https://doi.org/10.4121/uuid:680c2364-abe3-4645-89cc-1904c8d1e6fe>.

8

Component-scale testing

The culmination of the development cycle of an SHM system consists of a test campaign on a real-scale (1:1) structure, with different damage scenarios and external variability factors, and where all the equipment and tools are operated together, in an effort to achieve the most complete possible characterisation of the SHM system capabilities.

This chapter describes the test campaign conducted on the GW-SHM system developed for a component-scale stiffened panel of a thermoplastic composite horizontal stabilizer torsion box, and the two studies it enabled. One is on the validation of a novel methodology for systematically designing a GW-SHM system, and another is on the influence of audible structural vibrations on GW signals.

This chapter is adapted from two different articles published in:

- Proceedings of the 9th European Workshop on Structural Health Monitoring 2018 [1]
- Structural Control and Health Monitoring 26(5): e2340 (2019) [2]

and from an article submitted to the Journal of Sound and Vibration [3]

8.1. Introduction

Component-scale testing is a necessary step in the certification of an SHM system, as it allows the demonstration of the detection capabilities for different damage scenarios, under different operational and environmental conditions, and with setups that reproduce the equipment complexity to be instrumented on board the aircraft [4].

If in a non-certification phase, component-scale testing is an important part of the iterative process of developing an SHM system. The results of the detection capability assessment can not only be fed back to change the design of the system and thereby improve the diagnostic performance, but also can contribute with empirical parameters to perfect the model-assisted reliability analysis tools. Furthermore, component-scale testing is also a unique opportunity to study poorly understood interactions between system-extrinsic factors (e.g. temperature, loading, vibration) and system variables that can occur in real operation. The knowledge gained with such studies can then be employed to develop mechanisms to compensate for the effect of those extrinsic factors on the GW signals, and thus on the diagnostic metrics.

It is therefore in this context that this chapter describes all the steps in the test campaign of the GW-SHM system designed for the component-scale torsion box panel described in Section 3.2.2, according to the novel methodology proposed in Section 6.3.2. The objectives of the test campaign were 1) to validate the proposed GW-SHM system design methodology by evaluating the capability for detecting realistic BVID of different severities, and 2) to gain knowledge about the effects of high-amplitude, low-frequency structural vibrations (HA-LFV) and audible sound waves (SW) on ultrasonic GW signals.

8.2. Test campaign

8.2.1. Test specimen

The component-scale test specimen was the horizontal stabilizer torsion box panel described in Section 3.2.2, and depicted again in Figure 8.1 for convenience. The panel was entirely made of CF/PEKK and had real-scale (1:1) dimensions and complexity, as it consisted of a co-consolidated stiffened skin with multiple I-stringers in butt-joint configuration, and two riveted ribs. The panel had a maximum length and width of about 2.9 and 1.7 m, respectively, with skin thickness varying between 1.8 and 8.1 mm, and rib thickness between 3 and 3.5 mm.

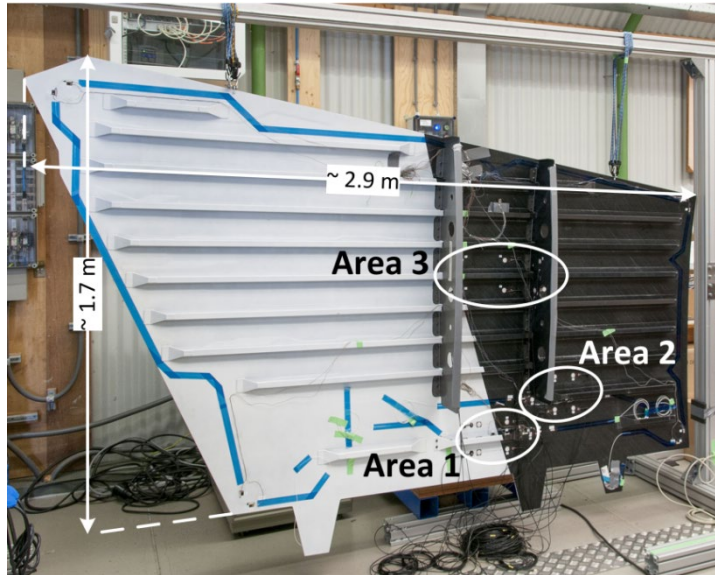


Figure 8.1. Horizontal stabilizer torsion box stiffened panel, with the three critical areas highlighted.

8.2.2. Test setup

8.2.2.1. Impact damage generation

The impacts were applied by a portable spring-mechanism impactor (see Figure 8.2) configured to generate the desired nominal impact energy. The projectile head diameter was 12.7 mm and its mass was around 2.7 kg.



Figure 8.2. Portable impact gun positioned on the outer side of the skin.

8.2.2.2. Guided wave measurements

The equipment used for GW measurements is depicted in Figure 8.3. The ultrasonic excitation was produced by an Agilent 33500B waveform generator, amplified by a TTI

WA301 wideband amplifier and transmitted to the structure by thin PZT actuator discs. The ultrasonic response was sensed by thin PZT sensor discs and acquired by two digital oscilloscopes, PicoScope 4424 and PicoScope 6402A, both connected to a computer. The raw ultrasonic GW signals can be found in [5,6].

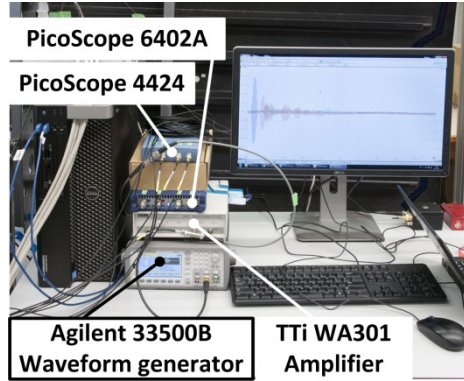


Figure 8.3. Guided wave measurement setup.

As explained in Section 3.2.2, critical areas 1 to 3 (highlighted in Figure 8.1) were selected to be monitored for the scenario of BVID. The novel methodology proposed in Section 6.3.2 was employed to design the GW-SHM system for the critical areas, resulting in the transducer network described in Section 6.4.3 and reproduced again in Figure 8.4 and Figure 8.5 for convenience.

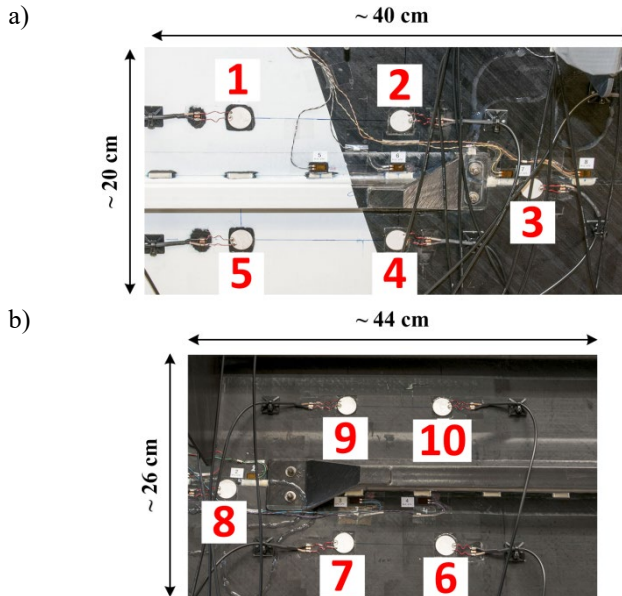


Figure 8.4. Transducer network on a) critical area 1 and b) critical area 2.

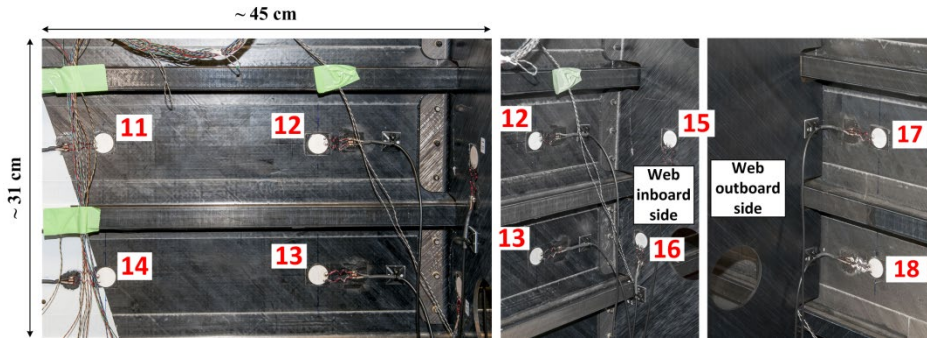


Figure 8.5. Transducer network on critical area 3.

8.2.2.3. Transducer integrity monitoring

The integrity of the transducer network was monitored during the entire test campaign, by measuring the EM susceptance (imaginary part of admittance) of the PZT transducers with a Hioki IM 3570 Impedance analyser connected to Hioki L-2000 4-terminal probe, as shown in Figure 8.6. The compared evolution of the EM susceptance spectra was used as an indicator of PZT transducer bonding condition and material cracks [7-9]. The EM reactance and admittance measurements are available in [5].

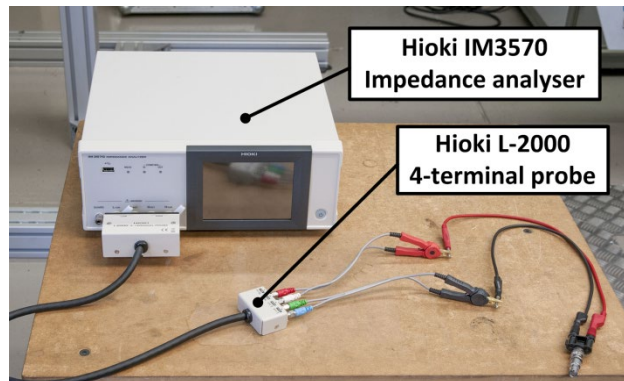


Figure 8.6. Electro-mechanical susceptance measurement setup.

8.2.2.4. Low-frequency vibration

A TIRAvib 50350 mechanical shaker was connected to the torsion box panel (see Figure 8.7) in order to apply a HA-LFV spectrum. The force signal of the applied LFV was measured by a PCB 208A03 force transducer mounted on the connecting spigot.

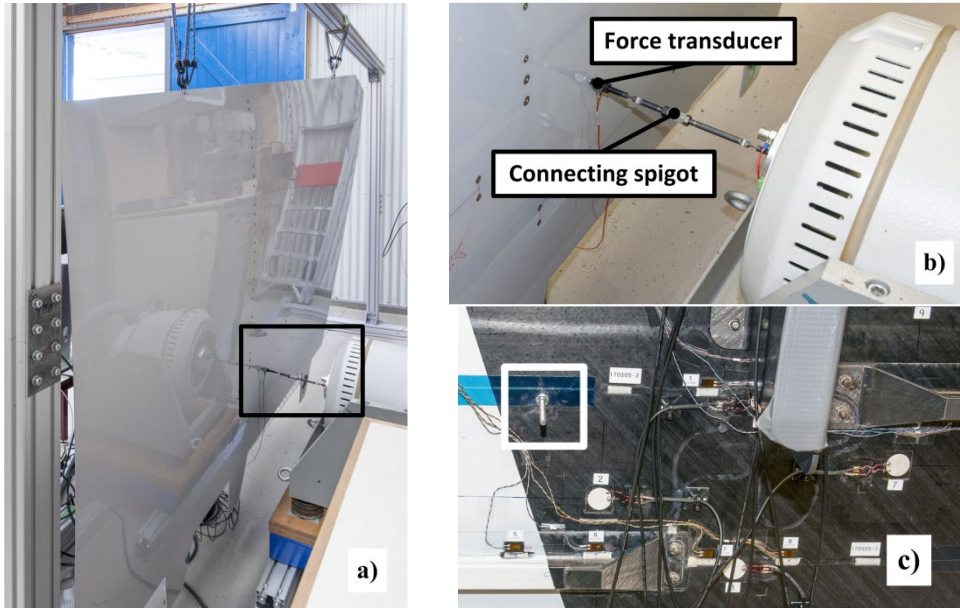


Figure 8.7. Connection of the mechanical shaker to the torsion box panel: a) general view, b) detailed view of connecting spigot, and c) detailed view of the bolted connection on the inner side of the panel.

8.2.3. Test procedure

The test campaign took place at the NLR - Netherlands Aerospace Centre during the months of May and June 2017. It consisted of the repetition of the following set of four operations for each structural state:

- 1) PZT check; 2) GW test; 3) GW test with LFV; and 4) PZT check.

In total, there were five object states measured: ND, D1, D2, D3 and D3+D3, corresponding to undamaged (or baseline), damage after impact on area 1, after impact on area 2, after first impact on area 3, and after second impact on area 3, respectively.

The PZT check was always performed for all the 18 PZT transducers. GW tests were conducted on the critical areas, for all possible actuator-sensor combinations, at all the selected excitation frequencies. The operation of GW testing with LFV was performed for only one actuator-sensor combination within a critical area. The goal of adding a step of GW testing with LFV was to study LFV effects on GW propagation and the subsequent damage diagnostic performance. Having a PZT check as the 1st and 4th operations had the purpose of assessing the effect of LFV on the transducer network integrity.

In addition to the standard *intra-area* GW tests, *inter-area* GW tests were performed with PZT01 as an actuator and PZT07, PZT10, PZT11 and PZT 18 as sensors, in order to evaluate the capability of detecting damage accumulation across all three critical areas.

8.2.3.1. PZT checks

The EM susceptance of the PZT transducers was always measured between 50 and 500 kHz, with steps of approximately 0.56 kHz.

8.2.3.2. GW tests

The novel methodology proposed in Section 6.3.2 was also employed to design the excitation signals for each critical area. According to the selection presented in Section 6.4.2, the ultrasonic GW tests were performed at three different nominal excitation frequencies: 123, 213 and 335 kHz for areas 1 and 2; 112, 198 and 350 kHz for area 3. The excitation pulse was a sinusoidal tone-burst with the amplitude modulated by a Hanning window. Ten sinusoidal cycles per pulse were used for areas 1 and 2, and five for area 3. The waveform generator was set to send an excitation pulse every 10 ms.

8.2.3.3. GW tests with LFV

In this case the procedure for the GW signal acquisition was exactly the same as the one described in Section 8.2.3.2. The difference was the simultaneous application of a single-axis, out-of-plane HA-LFV spectrum with frequency randomly varying between 20 Hz and 1000 Hz, amplitude randomly varying between 5 and 10 G_{RMS} , and duration of approximately 5 minutes. As shown in Figure 8.8, half of the vibrational energy was concentrated at frequencies up to 100 Hz, with the rest being transmitted at more isolated components beyond 170 Hz. The sound produced by the cooling system of the shaker when in stand-by state was used to test GW propagation in the presence of audible SW. During the GW tests with HA-LFV/SW the panel was suspended from a solid metallic frame (see Figure 8.1) in order to approximate free boundary conditions.

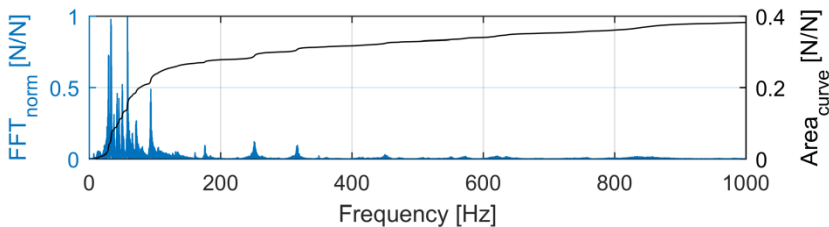


Figure 8.8. Frequency spectrum of the applied HA-LFV.

8.2.3.4. Impact application

The structure was impacted at the stringer locations on the outer side of the skin, at the locations listed in Table 8.1 and shown in Figure 8.9. The impact gun was configured to generate a nominal impact energy of 50 J. For the second impact on area 3 the nominal energy was 30 J.

Table 8.1. Impact locations along the stringers.

Abbreviation	Impact location
IL 1	100 mm from stringer run-out
IL 2	100 mm from stringer run-out
IL 3	100 mm away from outboard rib

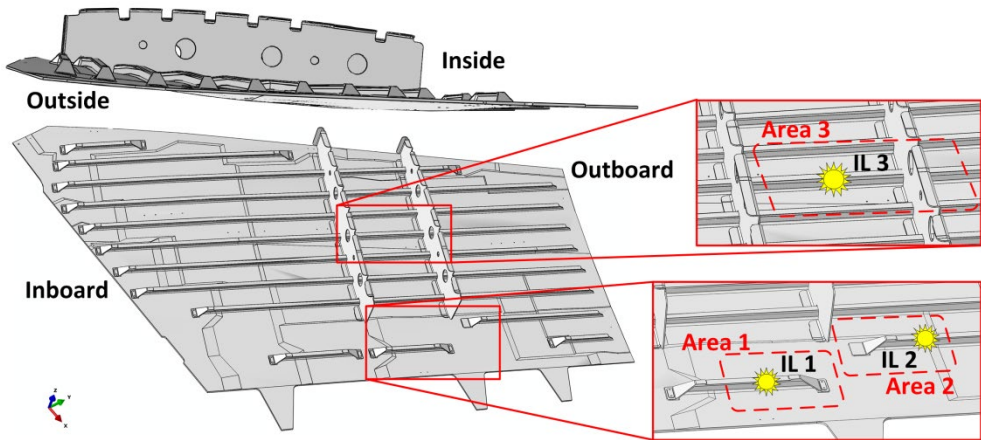


Figure 8.9. General views of the torsion box panel, with highlighted detailed views of the critical areas, with the corresponding impact locations (ILs). The impacts were performed on the outside of the skin.

8.2.3.5. Experimental limitations

The amplifier used for the excitation signal had a wide frequency band, which introduced non-linearity and parasitic frequencies in the signal if the amplification factor was higher than 1.6. Therefore, it was decided not to go beyond this value, thereby limiting the excitation signal amplitude to 16 Vpp.

The GW tests with HA-LFV could only be performed with the PicoScope 4424, because that was the only digital oscilloscope with an amplitude range high enough to capture the voltages induced by the HA-LFV. Consequently, there were only four channels available, which meant that only one actuator and three sensors could be connected.

The generation of ultrasounds was not synchronised with the applied HA-LFV. Therefore it was not possible to know what the LFV characteristics were at the moment of recording.

8.2.3.6. Setbacks during testing

During the test campaign there were some setup and time constraints which resulted in the setbacks below. Nevertheless, these did not compromise any of the objectives of the test campaign.

- a) GW tests with HA-LFV were not performed for area 3.
- b) GW tests with HA-LFV for area 1 were only performed at 123 kHz.

- c) Impact on area 1 had to be performed right after the second impact on area 3, preventing any testing in between the two occurrences.
- d) GW tests with a sparse transducer network were not performed for the baseline.
- e) GW tests with a sparse transducer network were only performed at one excitation frequency.

8.3. Validation of the SHM system design methodology

The component-scale test campaign enabled the evaluation of the capability for detecting realistic BVID of different severities, which in turn was crucial to complete the validation of the novel GW-SHM design methodology proposed in Section 6.3.2, and to arrive at an answer to research question Q2). The GW wave test results were backed up by visual inspections and ultrasonic NDT.

8.3.1. Visual inspection results

The real impact energies listed in Table 8.2 were in accordance with the nominal values introduced in the Section 8.2.3.4. It is important to explain that although impacts 1 to 3 had identical energies and were performed with exactly the same equipment and projectile, they occurred at different locations of the structure, where different arrangements of the panel stiffening elements impose different boundary conditions. This is a relatively realistic low-energy impact scenario, in which the size and severity of the produced barely-visible damages were not fully under control.

Table 8.2. Real energy of the impacts, skin indentation depth from visual inspection, and the code used to identify the damage created after each impact.

Impact No.	Area	Damage code	Indentation depth [mm]	Impact energy [J]
1	3	D3	0.18	49.6
2	1	D1	0.09	49.1
3	2	D2	0.07	47.5
4	3	D3 + D3	0.3	29.5

Visual inspections of the impacted areas revealed two types of BVID features. One was shallow indentations at the impact locations (see Table 8.1 in the Section 8.2.3.4), only perceptible from certain viewing angles and with depths ranging from 0.07 up to 0.3 mm (see Table 8.2). The other one was a small, irregular crack in the stringer filler across the impact location, which only occurred for impact no. 1 (on area 3) and was difficult to visually measure. Both occurrences are depicted in Figure 8.10.

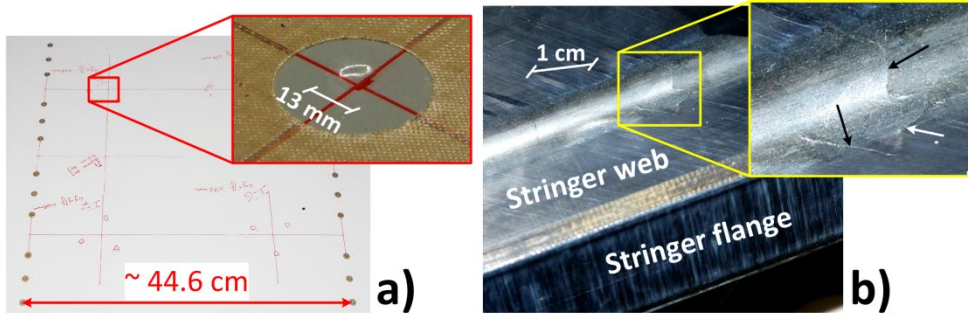


Figure 8.10. Barely-visible damages after first impact on area 3: a) indentation, and b) stringer filler crack, with irregular shape indicated by arrows.

8.3.2. NDT results

Ultrasonic NDT performed at a frequency of 5 MHz with an Olympus OmniScan MX unit connected to a phased-array roller probe revealed internal damages at the stringer-skin interface of different severities and sizes. The C-scans obtained for areas 1-2 and area 3 are depicted in Figure 8.11 and Figure 8.12, respectively.

The comparison of the C-scans in Figure 8.11a) and Figure 8.11b) shows damage after impact on area 1 (D1) as a few spots of low reflectivity (about 20%). In Figure 8.11c) the damage after impact on area 2 (D2) is more clearly visible than in the aforementioned case with a reflectivity around 70-80%, but covering only an area of approximately 350 mm² along the centre-front of the stringer, and extending for about 10 mm along the stringer run-out bond edge. It is interesting to note that, although the energy of the impact at area 2 was lower than that of the impact at area 1, the internal features of damage D2 appeared to be larger and more severe than those of D1. By combining this observation with the differences in indentation depth read from Table 8.2, it is possible to grasp the effect of different boundary conditions on the damage generated by impacts with identical energy.

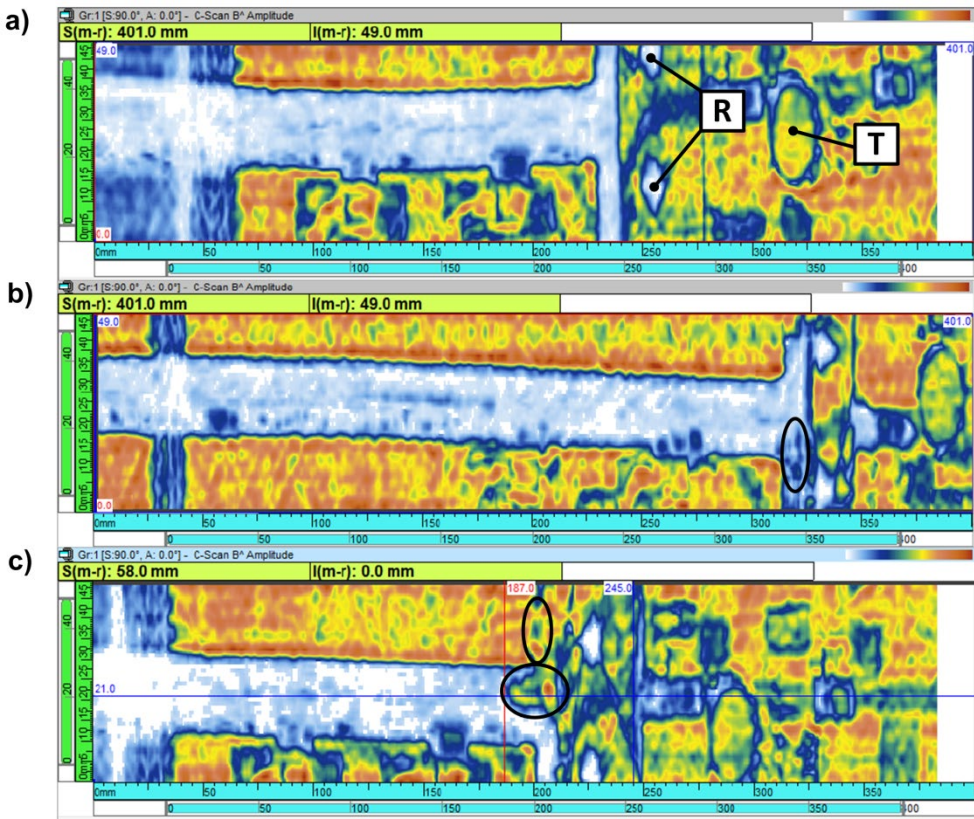


Figure 8.11. Ultrasonic C-scans of stringer run-outs: a) reference, b) after impact at area 1, and c) after impact at area 2. The reflectivity changes attributed to damage are highlighted by ellipses. The elements with legend in the reference C-scan (a) are: R – rivets, T – PZT transducer (see Figure 8.4 for a clearer geometry identification).

The damage after the first impact on area 3 (D3) can be unambiguously identified when Figure 8.12a) and Figure 8.12b) are compared, as there is a clear delamination running along the stringer-skin interface, with a length and an area of approximately 164 mm and 2952 mm², respectively. Additionally, there are other damage features on the sides of the stringer, which could be related to the irregular filler crack depicted in Figure 8.10. When comparing C-scans obtained after the first and second impacts on area 3, Figure 8.12b) and Figure 8.12c), respectively, it is not possible to observe any relevant difference, even though it was possible to identify a slight increase in indentation depth, as registered in Table 8.2.

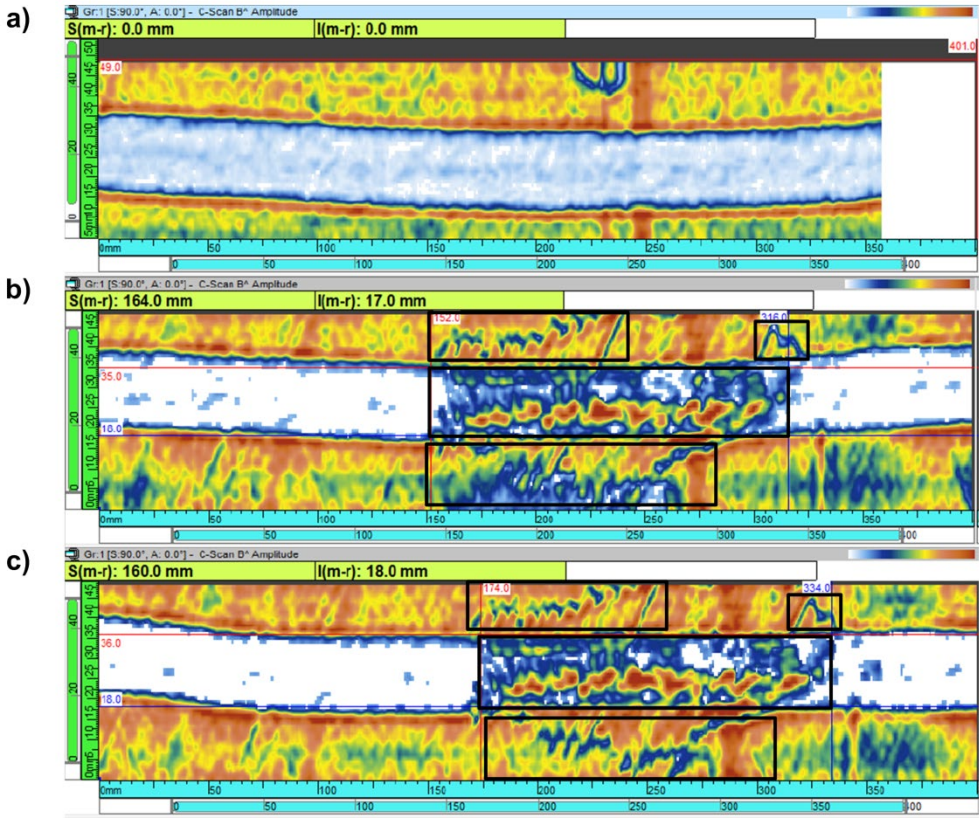


Figure 8.12. Ultrasonic C-scans of stringer at area 3: a) reference, b) after first impact, and c) after second impact. The reflectivity changes attributed to damage are highlighted by rectangles.

8.3.3. GW-SHM results

The GW signals were processed with the continuous wavelet transform using the Morlet wavelet in order to filter out the frequencies outside the 20-1000 kHz band. The filtered baseline and new-state signals for each propagation path p were then Fourier-transformed to the frequency-domain and inserted in Equation (2.24) to compute the root-mean-square deviation (RMSD_f). This index corresponds to the standard deviation of the differences between the frequency-domain signals, thereby being a measure of the signal shape change. Hence it resorts to the same approach employed in Chapters 4 and 5 for studying the effects of weld line thickness variations and manufacturing defects, respectively, on GW transmission across ultrasonically welded TpC joints. The multi-path unit-cell network concept (introduced earlier in Section 2.6.4.3) was applied and the final DI value for a monitored area was computed as the weighted-average of all N_{as} paths in that area, as defined by Equation (2.38). The final DI values for each state and frequency are plotted in Figure 8.13. In the figure, excitation frequencies 1, 2, 3 were 123, 213, 335 kHz for areas 1-2, and 112, 198, 350 kHz for area 3, and states 0, 1, 2, 3, 4 correspond to the previously introduced codes ND, D1, D2, D3, D3+D3, respectively.

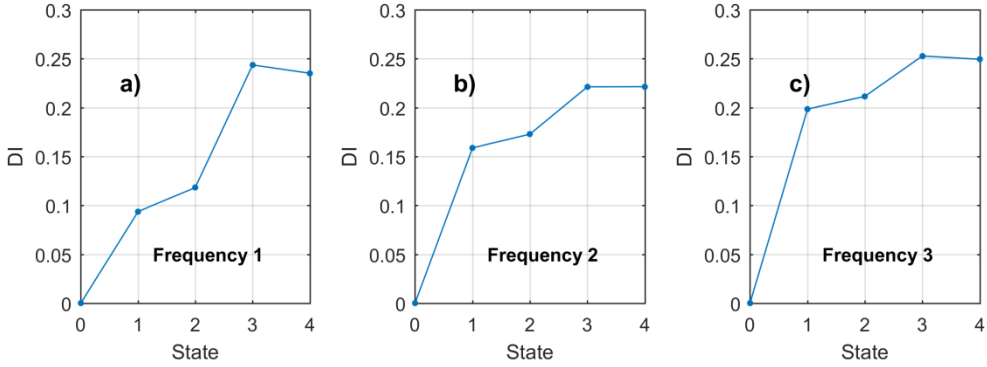


Figure 8.13. Weighted-average DI values for each state at frequency a) 1, b) 2, and c) 3. Frequencies 1, 2, 3 were 123, 213, 335 kHz for areas 1-2, and 112, 198, 350 kHz for area 3. States 0, 1, 2, 3 and 4 correspond to codes ND, D1, D2, D3 and D3+D3, respectively.

All frequencies have the same trend with a consistent monotonic increase from non-damaged (ND) to damage D3, and an almost constant value from D3 to D3+D3. The DI values for damage states D1 and D2 increase with frequency, while those for states D3 and D3+D3 remain approximately the same at the three frequencies. Thus, damage states D1, D2 and D3 were unambiguously detected and quantified by the transducer network. In fact, the detection of D1 is clearer than by observing the ultrasonic C-scan presented in Figure 8.11b). The DI values for damages D3 and D3+D3 are comparable to the values obtained by Monnier [10] for similar BVID in similar real-scale (1:1) composite component monitored at similar frequencies, thereby confirming the accuracy of quantification. However, contrary to previous research [11], the transducer network showed equal sensitivity to BVIDs with considerably different areas.

It is interesting to observe that there is a slight reduction in DI from D3 to D3+D3 for frequency 1, and an even slighter one for frequency 3. As previously explained, the adopted DI measures changes in the frequency spectrum, whether due to the appearance/disappearance of frequency components, or due to the increase/decrease of magnitude at existing frequency components. These changes are the consequence of interference between new reverberations created by the presence of damage. However, if those reverberations are partially attenuated within damage features, then the difference of the sensed signals with respect to the baseline condition becomes less pronounced. Even though the ultrasonic C-scan performed after the second impact on area 3 (see Figure 8.12c)) did not reveal any noticeable difference with respect to the first impact, there might be some increase in delamination opening without increase in length [12] causing the aforementioned partial attenuation. This could explain the slight DI reductions observed. In order to test this hypothesis the energy ratio defined in Equation (2.22) was computed for each path of area 3 for states D3 and D3+D3, and termed ΔE_r . The difference between the two damage states was taken for 112 and 350 kHz and is presented in Table 8.3 and Table 8.4, respectively.

8. Component-scale testing

Table 8.3. Variation of energy ratio between damage states D3 and D3+D3 for all propagation paths within area 3 at 112 kHz.

PZT #	11	12	13	14	15	16	17	18
11	0	-0.0099	0.0230	-0.0008	0.0104	-0.0397	0.0314	-0.1166
12	-0.0135	0	-0.0059	0.0116	0.0307	-0.0652	0.0307	-0.2859
13	0.0283	-0.0239	0	0.0113	0.0834	0.0033	-0.1772	-0.0084
14	0.0024	0.0098	0.0067	0	0.0337	-0.0203	-0.0114	0.0394
15	0.0014	0.0246	0.0642	0.0349	0	0.0191	0.0352	0.2006
16	-0.0278	-0.0527	-0.0062	-0.0174	0.0185	0	0.0810	0.0534
17	0.0572	0.0133	-0.1252	-0.0193	0.0645	0.0743	0	-0.0343
18	-0.0628	-0.2186	-0.0334	0.0307	0.1751	0.0506	-0.0355	0

Table 8.4. Variation of energy ratio between damage states D3 and D3+D3 for all propagation paths within area 3 at 350 kHz.

PZT #	11	12	13	14	15	16	17	18
11	0	0.0344	-0.0783	0.0148	0.1630	0.0363	0.0037	-0.0678
12	0.0393	0	-0.0996	0.0168	-0.0464	0.1490	-0.0078	-0.2443
13	-0.0980	-0.0781	0	0.0287	-0.3240	0.0848	-0.0353	0.0194
14	0.0212	0.0224	0.0211	0	-0.0257	-0.0900	-0.0108	0.0172
15	0.2545	-0.0776	-0.0833	0.0344	0	0.0233	-0.1487	0.0775
16	0.2377	0.1342	0.0595	-0.0742	0.0278	0	0.0134	0.0746
17	-0.0254	-0.0241	-0.0417	-0.0145	-0.1519	0.0049	0	-0.0164
18	0.0580	-0.2789	0.0174	0.0075	0.1073	0.0837	-0.0201	0

In order to identify the relevance of the propagation paths, their weighting factors based on the energy ratio for damage D3 at 112 and 350 kHz are presented in Table 8.5 and Table 8.6, respectively.

Table 8.5. Weighting factors for all propagation paths within area 3, based on the energy ratio for damage state D3 at 112 kHz. Path relevance is proportional to filled area in circle icon.





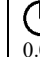
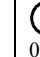
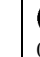
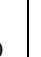



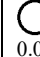
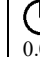
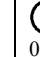
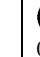
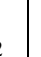



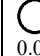
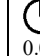
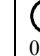
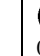
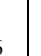



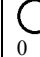
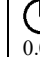
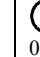
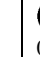
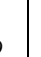




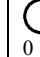
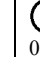
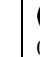
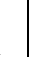





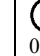
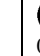
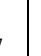




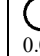
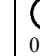
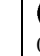
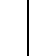

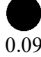

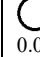
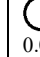
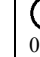
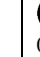
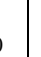



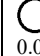
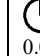
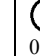
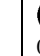
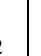




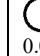

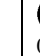
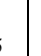




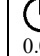
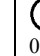
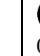
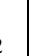



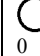
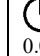
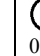
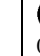





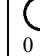
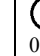
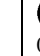
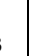
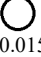



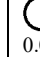
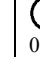
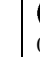
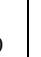


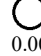

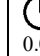
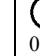
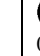
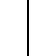
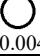



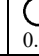
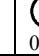
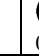
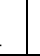
PZT #	11	12	13	14	15	16	17	18
11	 0	 0.0076	 0.0045	 0.0020	 0.0287	 0.0207	 0.0030	 0.0155
12	 0.0067	 0	 0.0014	 0.0043	 0.0356	 0.0059	 0.0062	 0.0958
13	 0.0029	 0.0023	 0	 0.0005	 0.0280	 0.0182	 0.0576	 0.0200
14	 0.0020	 0.0050	 0.0019	 0	 0.0315	 0.0126	 0.0419	 0.0059
15	 0.0293	 0.0361	 0.0299	 0.0323	 0	 0.0052	 0.0021	 0.0024
16	 0.0202	 0.0046	 0.0192	 0.0125	 0.0051	 0	 0.0037	 0.0068
17	 0.0024	 0.0081	 0.0534	 0.0441	 0.0012	 0.0063	 0	 0.0316
18	 0.0137	 0.0910	 0.0221	 0.0062	 0.0043	 0.0067	 0.0310	 0

Table 8.6. Weighting factors for all propagation paths within area 3, based on the energy ratio for damage state D3 at 350 kHz. Path relevance is proportional to filled area in circle icon.

PZT #	11	12	13	14	15	16	17	18
11	 0	 0.0019	 0.0061	 0.0003	 0.0237	 0.0064	 0.0182	 0.0061
12	 0.0024	 0	 0.0077	 0.0045	 0.0047	 0.0921	 0.0195	 0.0525
13	 0.0082	 0.0070	 0	 0.0072	 0.0297	 0.0095	 0.0032	 0.0208
14	 0.0003	 0.0038	 0.0094	 0	 0.0234	 0.0260	 0.0434	 0.0192
15	 0.0261	 0.0062	 0.0133	 0.0128	 0	 0.0077	 0.0263	 0.0162
16	 0.0150	 0.0707	 0.0111	 0.0223	 0.0076	 0	 0.0250	 0.0047
17	 0.0212	 0.0199	 0.0060	 0.0509	 0.0239	 0.0257	 0	 0.0040
18	 0.0046	 0.0548	 0.0231	 0.0205	 0.0137	 0.0052	 0.0044	 0

The combined analysis of Table 8.3 and Table 8.5 indicates noticeable ΔE_r reductions at 112 kHz for the three most relevant paths, 12-18, 13-17 and 18-12. At 350 kHz, Table 8.4 and Table 8.6 indicate relevant reductions for paths 12-18, 14-17, 17-14 and 18-12, as well as for other less relevant paths. However, because there is an increase for the most relevant paths, 16-12 and 12-16, the drop in final DI is not as marked as at 112kHz.

Therefore, although the hypothesis cannot be entirely proven, it seems valid to say that a fraction of the energy scattered by the damage D3+D3 does not arrive at the sensors. Nevertheless, the SHM system was able to detect the presence of damage D3+D3 through DI increases for individual propagation paths.

A sparser transducer network configuration was also tested in order to evaluate the robustness of the placement approach. The sparser configuration consisted of an actuator at PZT 01 and sensors at PZTs 07, 10, 11 and 18, thereby covering the three critical areas. The tested frequency was 123 kHz. In this case, the selected baseline condition, ST0, was the state after the first impact on area 3, D3. The $RMSD_f$ for each propagation path is depicted on Figure 8.14.

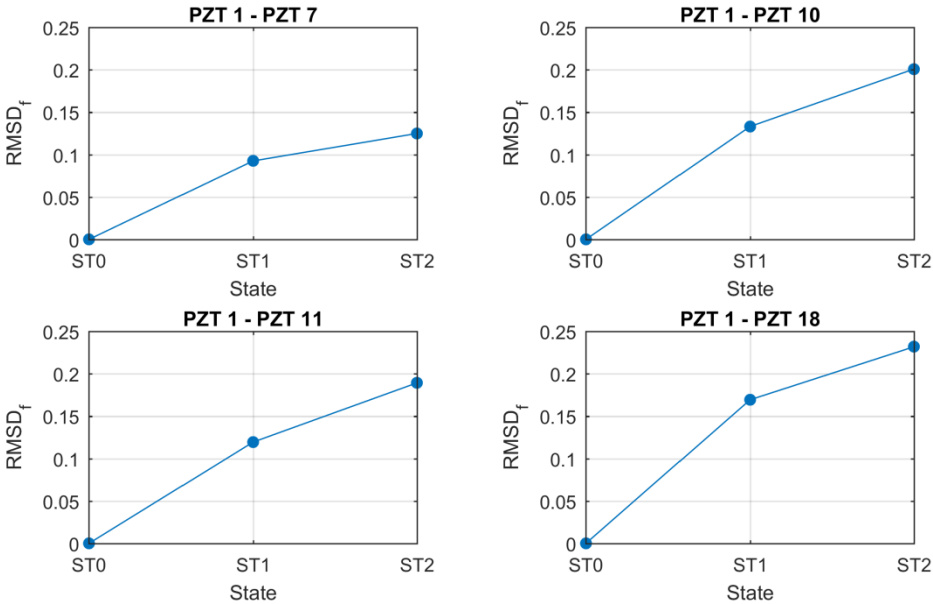


Figure 8.14. $RMSD_f$ for sparse transducer network at 123 kHz. ST0 = D3 (reference for inter-area tests); ST1 = D3+D3+D1; ST2 = D3+D3+D1+D2.

The main contribution for the $RMSD_f$ value for state D3+D3+D1 (ST1 in Figure 8.14) for path 1-7 is due to the presence of damage D1 (apart from the influence of the reflections coming from area 3), because area 1 is the only region crossed by that propagation path (recall the relative PZT positions within the transducer network shown in Figure 8.4 and Figure 8.5). The same can be said for the path 1-10, for which the detected value is just slightly higher than for path 1-7 because PZT 10 is closer to area 3 than PZT 07. For the path 1-18, the propagating wavefront crosses areas 1 and 3. So, the $RMSD_f$ value reflects the presence of both D3+D3 and D1, almost reaching the double of the value acquired for path 1-7. Finally, although path 1-11 crosses areas 1 and 3, the wavefront arriving at the sensor captures the presence of both D3+D3 and D1 only through reflections. As a result, the $RMSD_f$ value lies in between those acquired for paths 1-7 and 1-18. After the impact on area 2 (state ST2 in Figure 8.14), the accumulation of damage D2 is detected by all the paths of the sparse network, with a sensitivity which is in agreement with the explanation given for the cumulative state D3+D3+D1. When Figure

8.14 is compared to the ultrasonic C-scans in Figure 8.11b) and in Figure 8.12c), it is possible to see that the diagnostic of the cumulative state D3+D3+D1 by the ultrasonic GW-SHM system is more unambiguous.

Therefore, the SHM system was able to detect the cumulative BVID without needing an optimization of the transducer network configuration for each damage size, while using an excitation frequency which was not an optimum for the entire covered region.

For the sake of result transparency, Figure 8.15 shows the evolution of the degradation of all PZT transducers as a function of time (i.e. data set number within the sequence of tests). In this case, the transducer network degradation is quantified by the complement of the coefficient of correlation, $DI_{PZT} = 1 - CC$, (according to Equation (2.23)) between each EM susceptance curve (recorded at each PZT check of the test campaign) and the one at the start [7-9]. The EM susceptance was measured between 50 and 500 kHz. As it is visible from the graph, the PZT transducer damage indicator remains very low and with almost no relevant variation, which confirms that the DI variations for GW signals acquired by the SHM system from the critical areas were not caused by degradation of the transducer network.

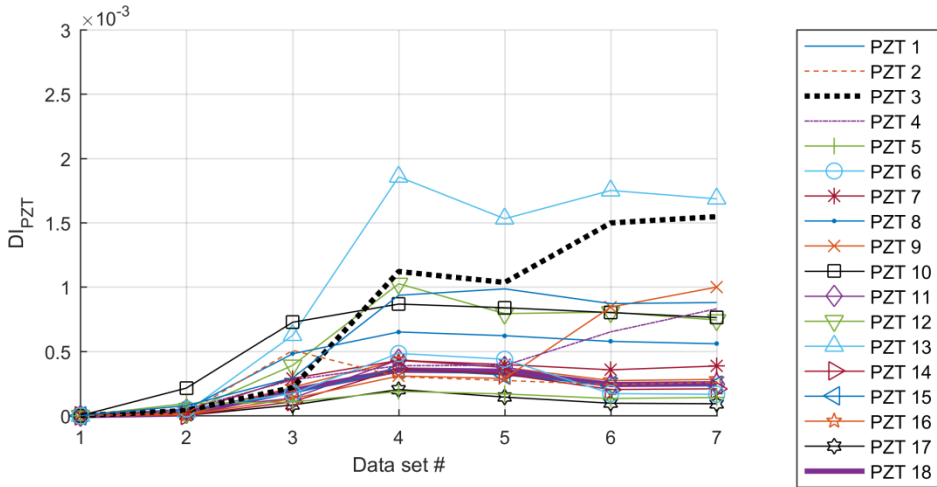


Figure 8.15. Evolution of the transducer network degradation during the test campaign. The damage indicator for the transducer network, DI_{PZT} , is calculated as the complement of the coefficient of correlation CC ($DI_{PZT} = 1 - CC$).

As this discussion reaches an end, it is relevant to mention that the design methodology proposed in Section 6.3.2 can be useful both for researchers developing their own GW-SHM systems, and for users of commercially available system solutions who want to have a well-informed decision on their purchase.

8.4. Effects of audible structural vibration on GW propagation

The component-scale test campaign also enabled the study of the interaction between HALFV and ultrasonic GWs and between SW and GWs, which was crucial to start bridging

the knowledge gap identified by research question Q4). The investigation resorted to both experimental and numerical GW signals to test a working hypothesis and draw useful conclusions.

For this study, it is important to highlight that the test specimen was suspended from a solid metallic frame (as shown in Figure 8.1) in order to approximate free boundary conditions. The shaker was used to realistically induce high-amplitude out-of-plane displacement of the test specimen at low-frequency. Therefore, the focus was on correlating the changes in the GW signals with the vibration parameters.

Signal plots are available in Appendix A in order to complete the analysis in this section. They show the raw signal, the filtered signal, and the normalized frequency spectrum in the tested cases for selected actuator-sensor pairs of areas 1 and 2. The signals for the pristine condition are also included so that the reader can compare them with the signals for the corresponding damage condition. The raw ultrasonic GW signals can also be found in [6]

8.4.1. Working hypothesis

The frequency of random loads to which aircraft primary structures are typically subjected varies between 1 and 1000 Hz [13], which are frequencies 10^2 to 10^5 times lower than the typical ultrasonic GW excitation frequencies. Thus, a GW excitation pulse lasts only a short fraction of one SW/HA-LFV cycle. As a result, the SW/HA-LFV induced stress is almost constant during the entire recorded GW time-window. Therefore, taking into account the knowledge reviewed in Section 2.4.6, it was established as a working hypothesis that a short time window of GW propagation under audible SW or HA-LFV can be described by GW propagation in a structure with a permanently corrugated shape. If this hypothesis is true, then the effects of audible SW and HA-LFV on GW propagation should be detectable through changes in GW arrival time and in some frequency components [15].

8.4.2. High-amplitude low-frequency vibration (HA-LFV) effects

8.4.2.1. Experimental results

As seen from Figure 8.16a) the GW signal was overshadowed by HA-LFV. Therefore, continuous Morlet wavelet transform (CWT) filtering was applied to all signals in order to eliminate all the frequency components outside the -3dB band centred at the main GW excitation frequency. It is important to note that this CWT filtering was also applied to the signals acquired without the influence of HA-LFV. Thus, all signals are equally affected by the same filter-induced attenuation.

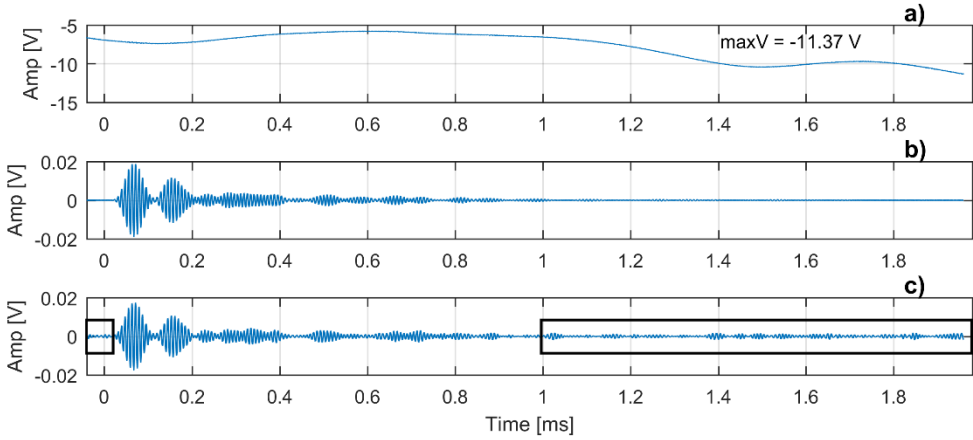


Figure 8.16. Signals from actuator-sensor pair 6-9 (Area 2) at 123 kHz, after 50 J impact on stringer run-out: a) raw signal with HA-LFV, b) filtered signal without HA-LFV, and c) filtered signal with HA-LFV. The background wave groups are highlighted by rectangles.

When comparing filtered signals for the cases of GW propagation without (Figure 8.16b) and with (Figure 8.16c) HA-LFV, background wave groups (BWGs) can be seen in the latter. If BWG appear in the filtered signal, it means they occupy the same frequency band as the main GW signal, which indicates that they correspond to ultrasonic GWs propagating in the structure. Thus, the BWGs cannot be attributed to electrical noise from the shaker circuitry occurring at the power-line frequency or at lower integer multiples. They also cannot be attributed to fretting between the connecting spigot and the panel occurring at the HA-LFV frequency.

The observed BWGs constitute a case of coherent noise, which can be demonstrated by computing the average signal over successive acquisitions. Figure 8.17 shows the band-pass filtered signals acquired by transducers 7, 8 and 9 after excitation by transducer 6 at 123 kHz in the D2 damage scenario, averaged over eight successive acquisitions. As it can be seen, the BWGs do not average out over successive acquisitions, thereby demonstrating that they correspond to coherent noise.

To provide a more tangible demonstration, It is possible to quantify the coherent noise by calculating a signal-to-background ratio (SBR) as defined in [16]

$$SBR = \left(Ax_{signal} / Ax_{back} \right)^2 = \left(Ax_{max} / RMS_{last-third} \right)^2 \quad (8.1)$$

where Ax_{signal} is taken as the maximum amplitude of the signal, and Ax_{back} is taken as the root mean square value of the last third portion of the signal. The last third portion of the signal is used for the estimate of Ax_{back} , because it is an interval in which there is most certainly only BWG. In Figure 8.18 the SBR is plotted as a function of the number of acquisitions used for the averaging of the signals in Figure 8.17, showing that the BWG intensity remains approximately the same.

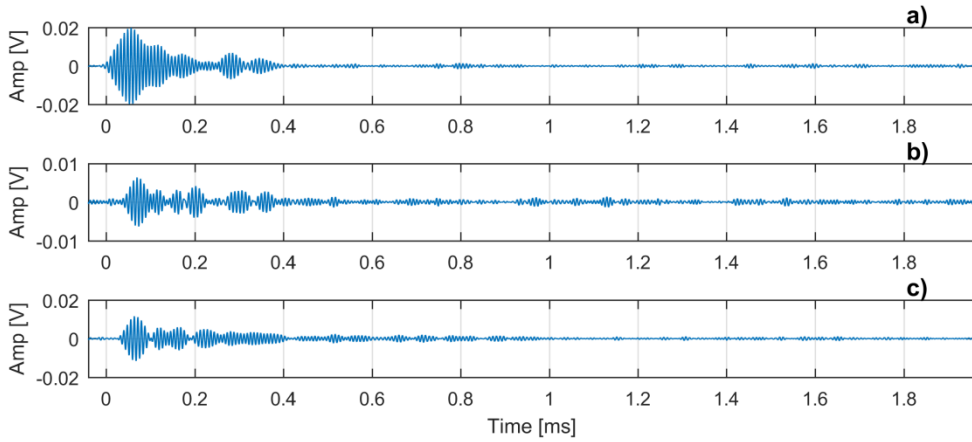


Figure 8.17. Average filtered signal from actuator-sensor pair 6-7 (a), 6-8 (b) and 6-9 (c) at 123 kHz, after the 50 J impact on the stringer run-out, averaged over eight successive acquisitions.

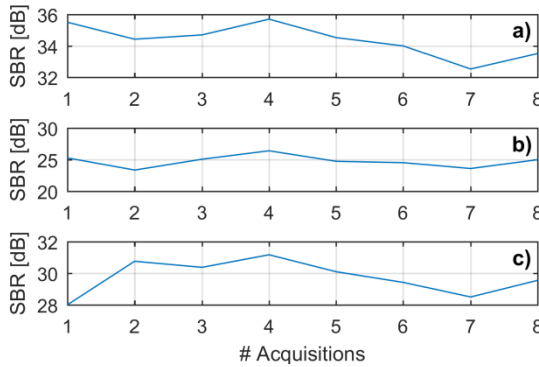


Figure 8.18. Evolution of the signal-to-background ratio (SBR) with the number of acquisitions used for averaging the filtered signal from actuator-sensor pair 6-7 (a), 6-8 (b) and 6-9 (c) at 123 kHz, after the 50 J impact on the stringer run-out.

The appearance of coherent noise is interpreted as a consequence of panel corrugated shape induced by vibration. When GWs propagate in the corrugated state of the panel the guiding mechanism takes place with more reflections at the plate surfaces per unit distance than in the non-corrugated state. Each of those reflections is accompanied by mode conversion, resulting in the generation of a higher number of dispersive wave groups per unit distance than in the non-corrugated state. The additional dispersive wave groups spread in space and time when propagating, and hence decay in amplitude, thereby overlapping and promoting the generation of coherent noise. This explanation is in line with mechanism described by Banerjee and Kundu [15]. It is also in agreement with the observations of Pedram et al [16] who investigated the scenario of long-range ultrasonic testing, where propagation distances of 5 m or more induce a guiding mechanism with a higher number of reflections (and thus of mode conversions), thereby generating extra dispersive wave groups which overlap and result in coherent noise.

As it can be seen from Figure 8.16b), in the case without HA-LFV, the employed excitation pulse period (10 ms) allowed the acquisition of GW signals without wave groups before the main arrival. However, in the case with HA-LFV, using the same excitation pulse period, there was coherent noise before the main arrival, as shown in Figure 8.16c). According to our explanation for the coherent noise, this corresponds to the lingering BWGs from the trailing edge of the previous GW signal window. This observation gives extra support to the explanation for the appearance of BWGs in the case of HA-LFV.

While in Figure 8.16 and other cases the coherent noise level is relatively low, there are others where the signal of interest is partially (see Figure 8.19b and c) or completely (see Figure 8.20b and c) overshadowed by it.

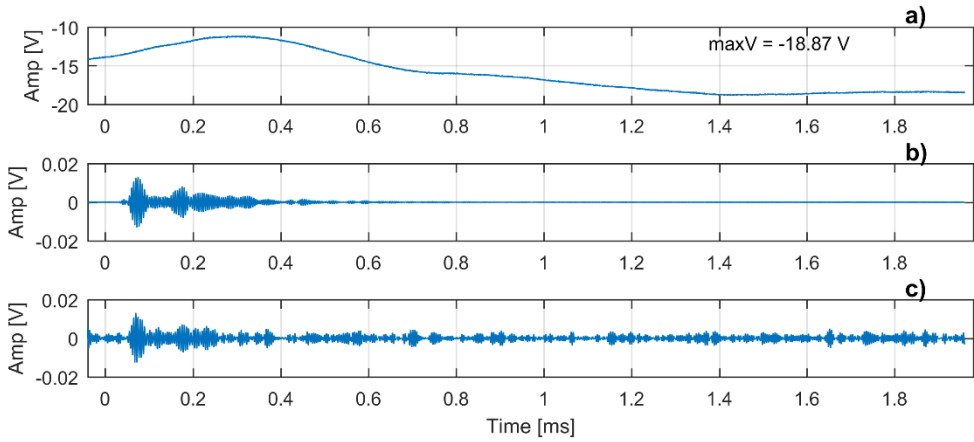


Figure 8.19. Signals from actuator-sensor pair 6-9 (Area 2) at 213 kHz, after 50 J impact on stringer run-out: a) raw signal, b) filtered signal without HA-LFV, and c) filtered signal with HA-LFV.

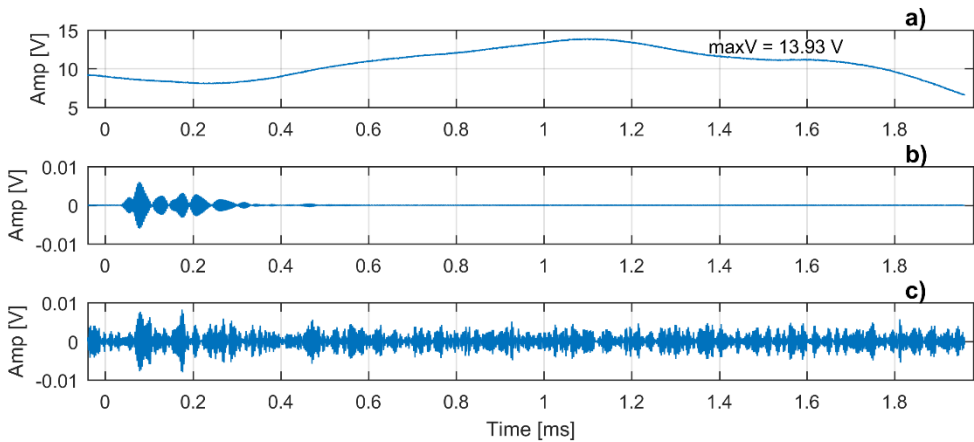


Figure 8.20. Signals from actuator-sensor pair 6-9 (Area 2) at 335 kHz, after 50 J impact on stringer run-out: a) raw signal, b) filtered signal without HA-LFV, and c) filtered signal with HA-LFV.

The SBR estimates were computed for all cases (including those without HA-LFV), and the values for all tested actuator-sensor pairs in each area are plotted in Figure 8.21. The SBR decreased for all cases tested under HA-LFV, meaning that coherent noise was always induced by the HA-LFV. It is interesting to note that all actuator-sensor pairs for the cases D1+LFV at 123 kHz and D2+LFV at 123 kHz were less strongly affected, with SBR reductions between -9 and -16.5 dB with respect to the non-HA-LFV counterparts.

It seems thus that the intensity of the coherent noise depends not only on the amplitude of the HA-LFV (which controls the height of the plate corrugation), but also on the ratio between the ultrasonic excitation frequency (which determines the dispersive properties of the propagating GW modes) and the HA-LFV frequency (which determines the corrugation wavenumber and hence the number of reflections per unit distance). For example, in Figure 8.16 and Figure 8.20 the raw signals have similar LFV amplitudes (between 11 and 14 V) but in the second one the GW signal is completely overshadowed by the coherent noise, which seems to be related to the aforementioned frequency ratio.

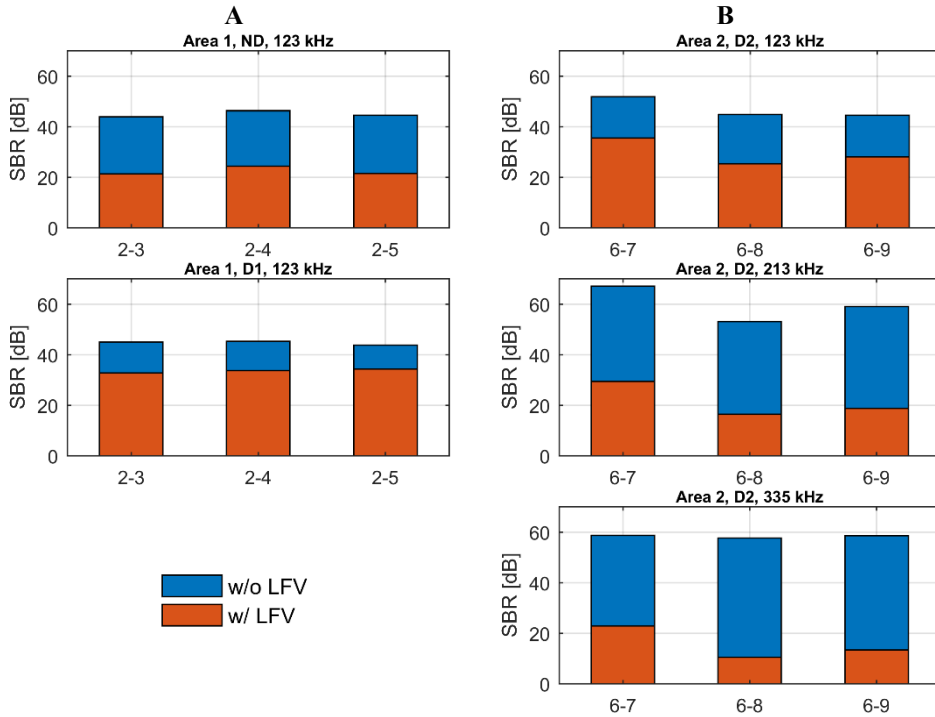


Figure 8.21. Signal-to-background ratio (SBR) in the cases without and with HA-LFV for all tested actuator-sensor pairs of area 1 (column A) and area 2 (column B). Actuator-sensor pairs are indicated in the horizontal axis.

To analyse the cases at 335 kHz it is helpful to look at the theoretical group velocity dispersion curves depicted in Figure 6.1b), and reproduced in Figure 8.22 for convenience. At 335 kHz there are six ultrasonic GW modes propagating in a highly dispersive regime, dividing the energy among them, and thereby attenuating much faster with propagation distance than at 123 or 213 kHz. As a result, for the cases without HA-LFV, the GW signals acquired at 335 kHz have lower amplitude than at 123 or 213 kHz, as shown in

Figure 8.23. In the presence of HA-LFV, the extra BWG end up having the same amplitude as the signal of interest, preventing an unambiguous assessment. The influence of ultrasonic excitation frequency on the SBR is clear in the trend observed for area 2 (column B of Figure 8.21).

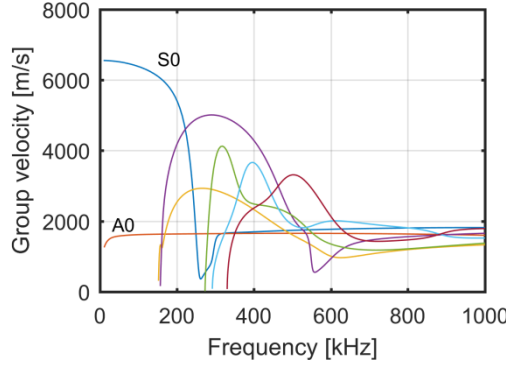


Figure 8.22. Group velocity dispersion curves for the skin of areas 1-2. For clarity, higher-order modes with cut-off frequencies above 400 kHz (i.e. modes that were not excited in any of the tests) are not presented.

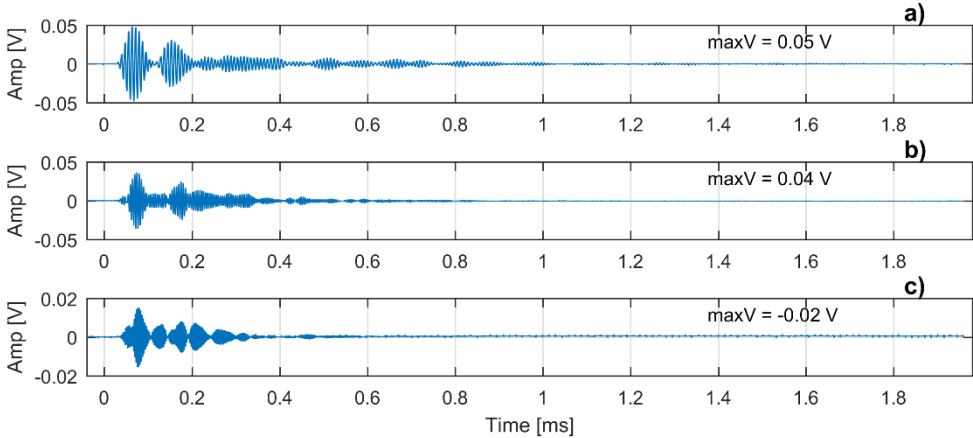


Figure 8.23. Raw signals from actuator-sensor pair 6-9 (Area 2), without HA-LFV, after 50 J impact on stringer run-out: at a) 123 kHz, b) 213 kHz, and c) 335 kHz.

The effect of HA-LFV on GW signals can be further quantified by time- and frequency-domain metrics, which can provide extra information about the physical interaction between the two phenomena and thereby help in testing the working hypothesis. Two quantities were selected for analysis. One was the 10%-duration time, $t_{10\%}$, as introduced in Section 2.6.4.1 in Equation (2.20). The other one was the characteristic frequency, f_{ch} , as defined in Section 2.6.4.2 through Equation (2.31). Considering first the changes induced by the small BVID of D1 and D2 plotted in Figure 8.24, $t_{10\%}$ shows no variation for some propagation paths, while for other propagation paths it varies approximately between 3% and 7%. The Δf_{ch} remains always between 0% and

0.7%. Hence, $\Delta t_{10\%}$ reveals the changes in the GW scattered field induced by the presence of the BVID. As a result of GWs scattering at the BVID, a higher number of wave groups are generated along the propagation path than in the ND condition. In turn, these extra wave groups interfere with the directly arriving ones, thereby inducing phase changes with respect to the baseline.

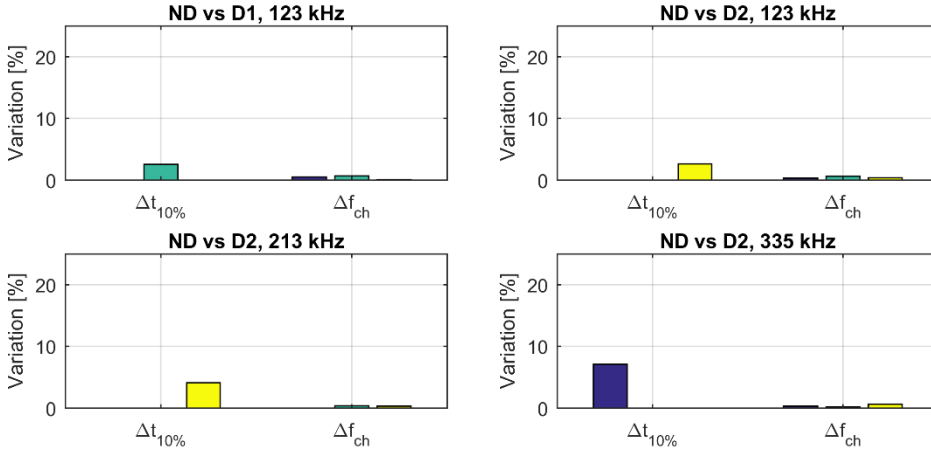


Figure 8.24. Variation of 10%-duration time ($t_{10\%}$) and characteristic frequency (f_{ch}) due to differences in GW scattering at the damage, for the tested actuator-sensor pairs in areas 1 and 2. The three bars (purple, green, yellow) for each quantity correspond to the three actuator-sensor pair analysed in each area: 2-3, 2-4 and 2-5 in area 1; 6-7, 6-8 and 6-9 in area 2.

Looking now at the cases with HA-LFV in Figure 8.25, $t_{10\%}$ varies mostly between 2.6% and 7.1%, with some propagation paths not revealing any change. So, $\Delta t_{10\%}$ has values similar to those caused by the occurrence of D1 and D2. Thus, the phase changes caused by the BWGs seem to be equivalent to the phase changes caused by the extra wave groups generated after scattering at the BVID. It is relevant to note that the case of D2+LFV at 335 kHz had the highest $\Delta t_{10\%}$ and the highest ΔSBR in Figure 8.21.

For the majority of the cases, f_{ch} shows variations between 5% and 20%. The effects on the characteristic frequency can be clearly visualized through the comparison of FFT spectra in Figure 8.26. In comparison to the cases without HA-LFV (e.g. Figure 8.26a), the filtered signals acquired under HA-LFV (e.g. Figure 8.26b) have multiple, small frequency components spread along the useful bandwidth, which are the result of the interference between BWG.

For the case of D2+LFV at 335 kHz (bottom graph in column B of Figure 8.25), Δf_{ch} remains between 0.4% and 1.1%, which seems to be an exception to the trend observed at the other frequencies. However, this has to do with the low amplitude of the wave packets of interest at this frequency. At 335 kHz, the BWG amplitude is comparable or equal to the amplitude of the wave packets of interest (as shown in Figure 8.20), resulting in an FFT spectrum where the magnitude of the frequency components corresponding to the wave packets of interest is not prominent (see Figure 8.27). In other words, the FFT spectrum is much flatter than at 123 or 213 kHz. Therefore, the weighting of the average of the FFT coefficients is balanced out, preventing the f_{ch} shift from being clearly revealed. Hence, if

the maximum amplitude of the GW signal acquired without HA-LFV was higher than 0.01 V, Δf_{ch} would be expected to follow the trend observed at the other frequencies.

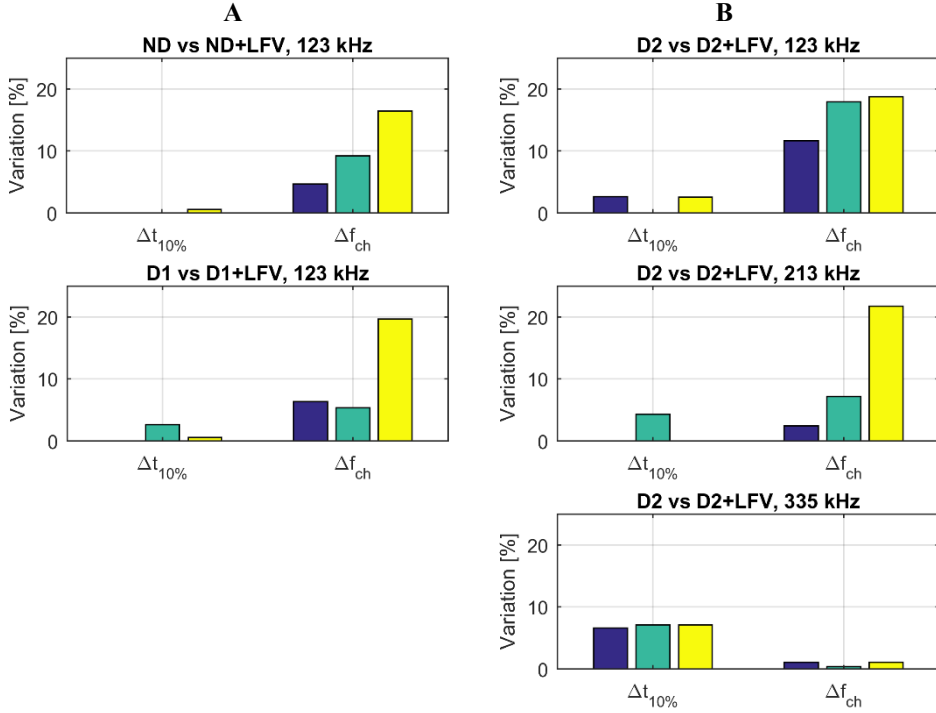


Figure 8.25. Variation of 10%-duration time ($t_{10\%}$) and characteristic frequency (f_{ch}) due to the HA-LFV for all tested actuator-sensor pairs of area 1 (column A) and area 2 (column B). The three bars (purple, green, yellow) for each quantity correspond to the three actuator-sensor pair analysed in each area: 2-3, 2-4 and 2-5 in area 1; 6-7, 6-8 and 6-9 in area 2.

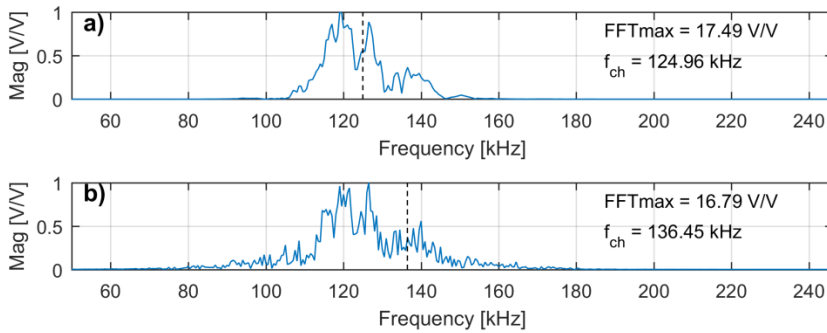


Figure 8.26. Normalised FFT spectra of the signals from actuator-sensor pair 2-4 (area 1) at 123 kHz, for the ND scenario a) without HA-LFV, and b) with HA-LFV.

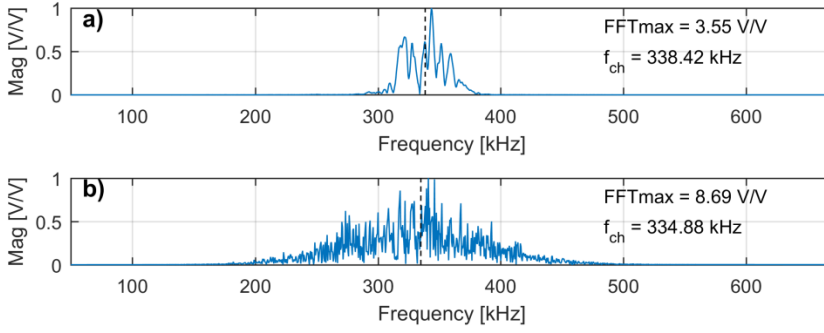


Figure 8.27. Normalised FFT spectra of the signals from actuator-sensor pair 6-9 (area 2) at 335 kHz, for the D2 scenario a) without HA-LFV, and b) with HA-LFV.

8.4.2.2. Numerical results

In an effort to further investigate the dependency of the coherent noise on the HA-LFV amplitude and on the LFV-GW frequency ratio, and to further test the working hypothesis, the modelling approaches described in Sections 7.3.1 and 7.3.2 were employed to build an FE model of a square aluminium plate with a permanently corrugated shape, with two thin PZT discs for GW actuation and sensing, as represented in Figure 8.28. Boundary conditions (BC) were applied to the two top vertices of the upper surface by blocking the displacements in all directions. The aluminium and the piezoceramic materials were the same as in Section 7.3.1. The dimensions of the plate were $1 \text{ m} \times 1 \text{ m} \times 2 \text{ mm}$, and the PZT discs had a diameter of 20 mm and a thickness of 0.4 mm. The actuator was positioned at $(x, y) = (0.1, 0.1) \text{ m}$, while the sensor was at $(x, y) = (0.9, 0.9) \text{ m}$. The permanently corrugated shape of the region between the two transducers was defined by a periodic geometry based on the corrugation height, h_c , and the corrugation wavelength, $w_c = 760/\text{\#Lobes}$, as illustrated in Figure 8.28.

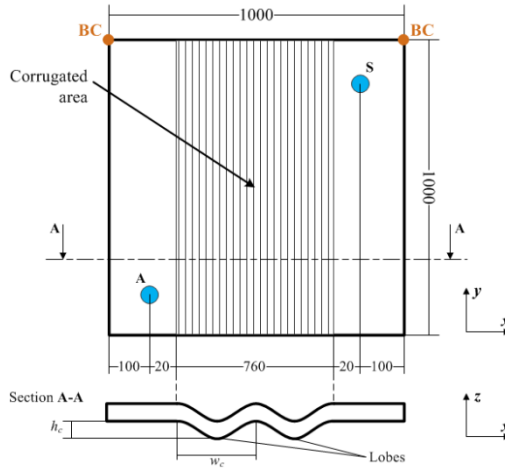


Figure 8.28. Geometric definitions of the plate model with permanent corrugated shape. The GW actuator and sensor are “A” and “S”, respectively. The $U_x = U_y = U_z = 0$ boundary conditions are applied on the two top vertices of the upper surface indicated by the BC circles. All dimensions are in millimetres.

To ensure the plate corrugated shape was modelled in a realistic way, Abaqus/Standard was used to perform a modal analysis to obtain the first hundred free vibration mode shapes. In this case, the structured mesh was formed by solid, 3D, 20-node, quadratic, reduced-integration elements (C3D20R) to allow enough spatial resolution with fifty elements along the plate side. Following the frequency components observed in the HA-LFV spectrum in Figure 8.8, mode 23 (at around 100 Hz) and mode 74 (at around 353 Hz) were selected, as depicted in Figure 8.29. These were then the basis for defining the number of corrugation lobes and parameter w_c : 2 lobes for 100 Hz, 5 lobes for 353 Hz. The parameter h_c was defined based on the vibration amplitude estimates made during the tests of the torsion-box panel.

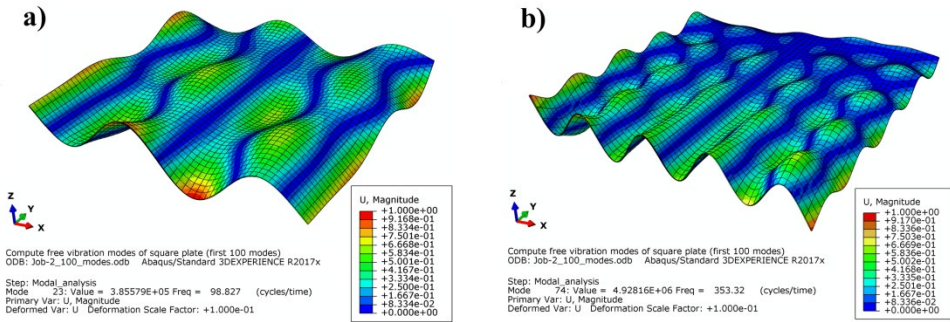


Figure 8.29. Free vibration mode shape 23 at around 100 Hz (a) and 74 at around 353 Hz (b) for the modelled aluminium plate.

A parametric study was conducted by varying the GW excitation frequency, the number of corrugation lobes and the corrugation height. The executed runs are summarised in Table 8.7, and the numerical signals are available in [17].

Table 8.7. Runs of the FE parametric study.

Run	GW freq [kHz]	# Lobes	w_c [mm]	h_c [mm]
1	100	0	0	0
2		2	380	15
3				30
4		5	152	15
5				30
6	300	0	0	0
7		2	380	15
8				30
9		5	152	15
10				30

Since it was decided not to implement any absorption layer, the numerical signals contain the reflections from the plate edges. Therefore, the analysis was focused on the directly arriving wave groups. For that reason, Figure 8.30 shows the time-domain

numerical signals for runs 1 to 5 up to 0.6 ms. The signals are dominated by the GW modes with a predominance of out-of-plane particle motion.

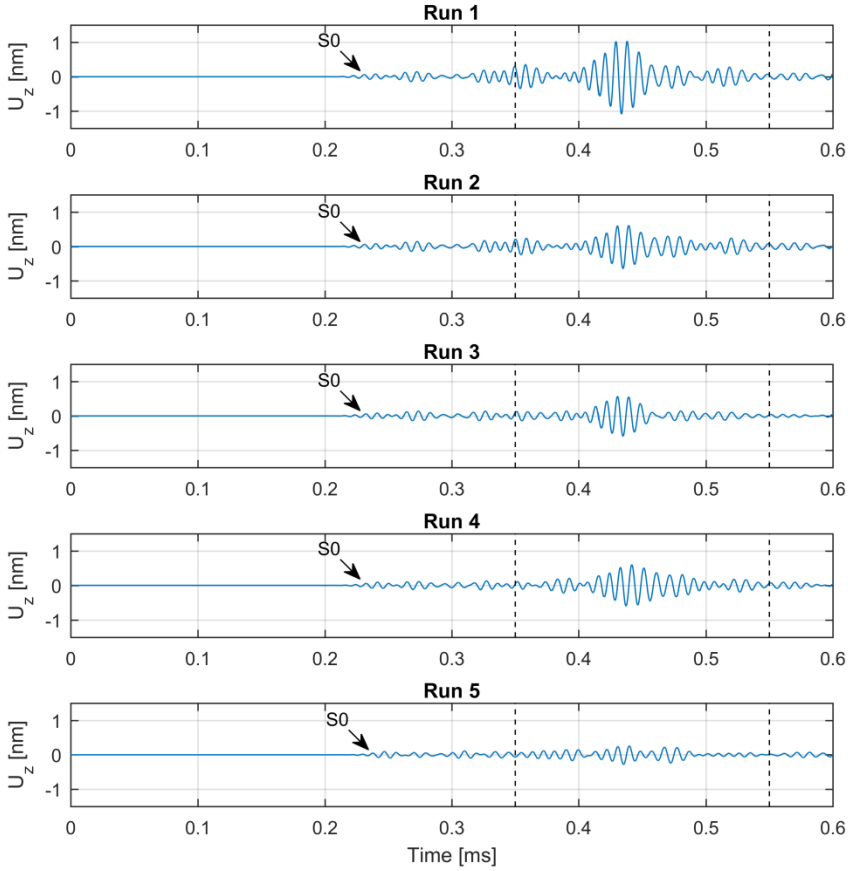


Figure 8.30. Numerical time-domain signals for runs 1 to 5. The dashed lines delimit the window used for the analysis.

Taking the theoretical group velocity dispersion curves for the 2 mm aluminium plate (see Figure 8.31), at 100 kHz, the first S0 mode arrives slightly after 0.2 ms and the first A0 mode slightly after 0.4 ms. Hence, the following analysis focuses on the signal window between 0.35 and 0.55 ms, delimited by the dashed lines in Figure 8.30.

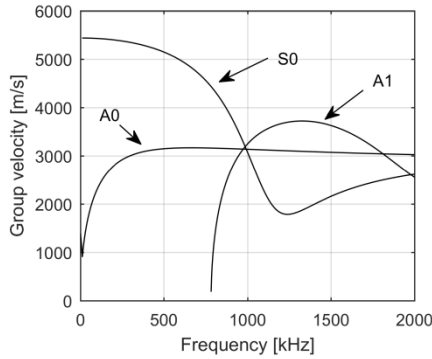


Figure 8.31. Group velocity dispersion curves for the aluminium plate with 2 mm thickness (computed with DISPERSE®).

While the directly arriving S0 mode remains the same from run 1 to 5, the directly arriving A0 mode loses amplitude and spreads when the panel surface is corrugated. Both the amplitude loss and the spreading increase with increasing corrugation height and with increasing number of corrugation lobes, with the most severe case being run 5. The changes observed in the numerical signals can be explained by following the rationale put forward in Section 8.4.2.1 to explain the coherent noise in the experimental signals. The corrugated shape of the plate induces more reflections and mode conversions along the propagation path, and hence the generation of a larger number of dispersive wave groups which destructively interfere with the directly arriving A0 mode. The exact same tendency can be observed in Figure 8.32 for runs 6 to 10 by looking at the window between 0.37 and 0.43 ms (at 300 kHz, the first S0 mode also arrives slightly after 0.2 ms and the first A0 mode slightly before 0.4 ms).

Using Equation (8.1) with A_{back} equal to the RMS value of the analysed signal window, it is possible to have a measure of the prominence of the A0 mode with respect to the wave groups in the immediate vicinity. By taking the free plate vibration frequencies associated to the corrugation lobes (100 Hz for 2 lobes, 353 Hz for 5 lobes), it is possible to plot the percent variation of SBR as a function of LFV-GW frequency ratio (F_{LFV}/F_{GW}), for different corrugation heights, as in Figure 8.33. The destructive interference trend which was qualitatively explained for Figure 8.30 and Figure 8.32 can thus be evaluated quantitatively. It seems valid to state that corrugation height has a slightly stronger influence on the intensity of BWGs generation than F_{LFV}/F_{GW} .

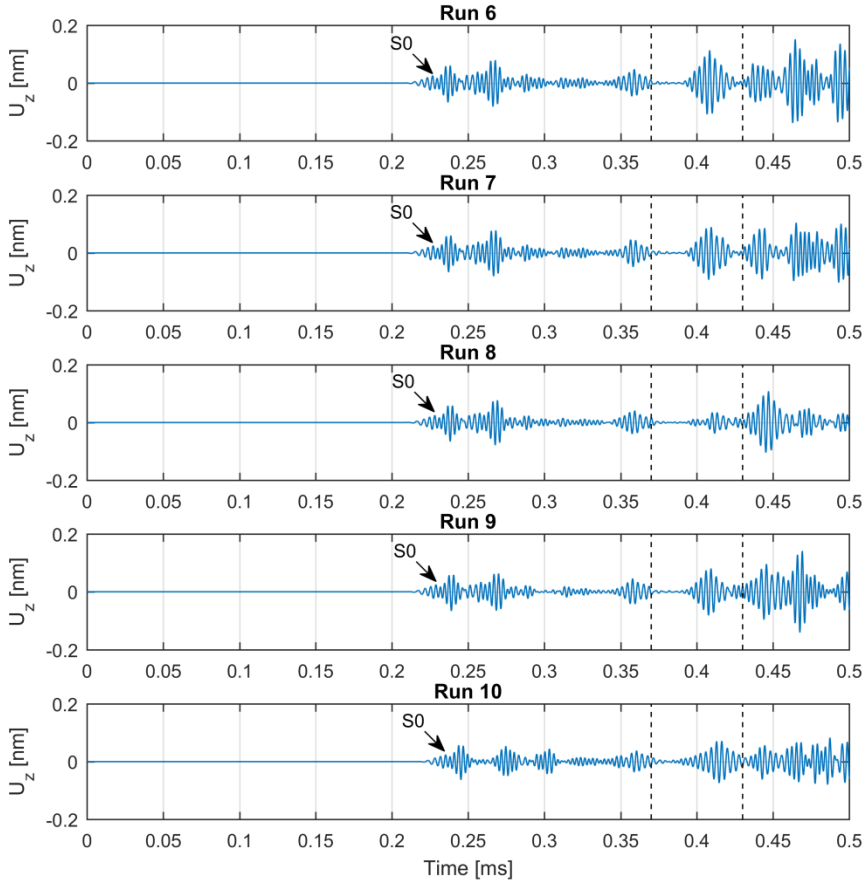


Figure 8.32. Numerical time-domain signals for runs 6 to 10. The dashed lines delimit the window used for the analysis.

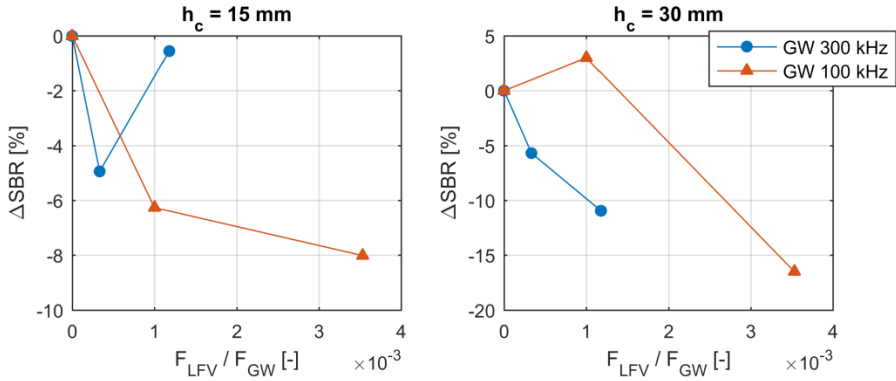


Figure 8.33. Variation of signal-to-background ratio (SBR) in the numerical signals as a function of LFV-GW frequency ratio for a corrugation height of a) 15 mm and b) 30 mm.

Figure 8.34 presents the variation of $t_{10\%}$ and f_{ch} computed for the analysed signal windows ([0.35;0.55] ms for 100 kHz and [0.37;0.43] ms for 300 kHz) as function of F_{LFV}/F_{GW} , for different corrugation heights. It is important to highlight that the ranges of $\Delta t_{10\%}$ and Δf_{ch} are similar to those obtained experimentally and presented in Figure 8.25. The increase in $t_{10\%}$ with increasing F_{LFV}/F_{GW} is higher for a corrugation height of 30 mm than for 15 mm, which connects back to the stronger influence of corrugation height on the BWGs and their interference with directly arriving wave groups.

At this point, it seems valid to state that the conjugation of moderate changes in $t_{10\%}$ and in f_{ch} is strongly correlated with the presence of HA-LFV effects on ultrasonic GW propagation. Most importantly, there seems to be enough evidence to confirm the working hypothesis that a short time window of GW propagation under HA-LFV can be described by GW propagation in a structure with a permanently corrugated shape.

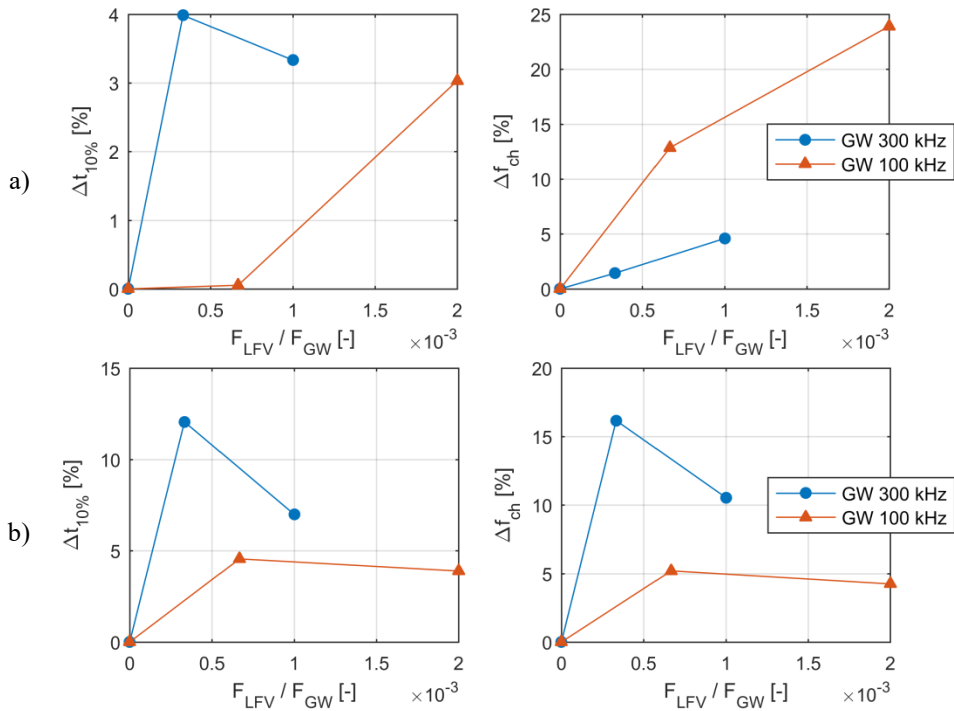


Figure 8.34. Variation of 10%-duration time ($t_{10\%}$) and characteristic frequency (f_{ch}) in the numerical signals as a function of LFV-GW frequency ratio for a corrugation height of a) 15 mm and b) 30 mm.

8.4.3. Audible sound wave (SW) effects

The visual comparison of Figure 8.35a) and c) shows there was no coherent noise in the filtered signals for the cases under the effect of audible SW cases, which was reflected in SBR values (Figure 8.36) identical to those obtained at rest (see bar graphs for area 1, D1, 123 kHz without LFV in column A of Figure 8.21). In fact, both the time-domain and the frequency-domain representations of the filtered signals look identical for all of them. As a result, the $t_{10\%}$ and f_{ch} variations (purposely omitted) were practically null. This shows that

audible SW did not induce corrugation of the panel, even though it still interacts with the PZT sensor and hence with the acquired signal, as seen in Figure 8.35b).

In short, when the audible SW and the GW signal have amplitudes of the same order of magnitude, there is no detectable effect in the CWT filtered signal, which is turn is in agreement with previous research [18]. However, this might not be the case if the amplitude of the SW would reach the range of 1-10 V in the raw signal.

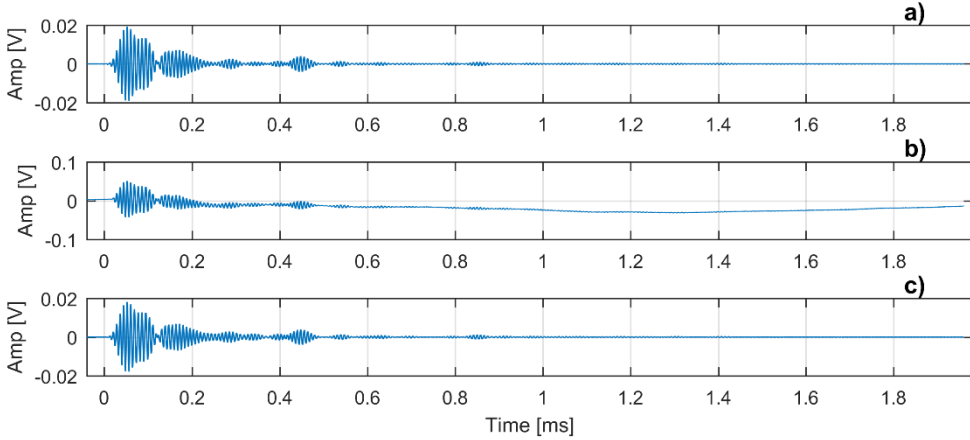


Figure 8.35. Signals from actuator-sensor pair 2-4 (area 1) at 123 kHz, after 50 J impact on stringer run-out: a) filtered signal without SW, b) raw signal with SW, and c) filtered signal with SW.

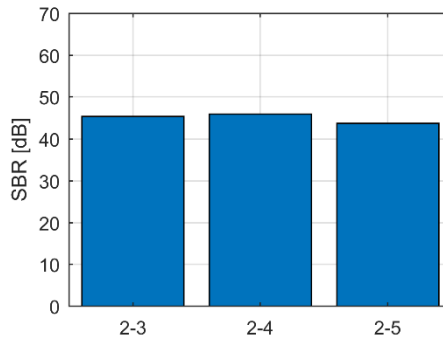


Figure 8.36. Signal-to-background ratio (SBR) for all actuator-sensor pairs of area 1, after 50 J impact on stringer run-out, with audible SW.

8.4.4. Diagnostic capabilities under HA-LFV or SW

The relevant question at this point seems to be: *Can damage diagnostic be reliably performed in the presence of HA-LFV or audible SW?* The first thing to do before providing an answer is to look at the DI values for the tested HA-LFV and SW cases and compare them with the cases at rest. The DIs based on the CC (correlation coefficient) and the RMSD (root mean square deviation), as defined in Equations (2.23) and (2.24), were

applied to quantify the differences in the time- and frequency-domain representations of the signals. From all of them, the frequency-domain CC-based DI (DI_{CC}) had the weakest influence of LFV/SW effects, and was thus the selected DI. The CC was computed between each normalized frequency spectrum and the corresponding baseline at rest. The obtained DI_{CC} values for the HA-LFV and audible SW cases (along with corresponding cases at rest) are plotted in Figure 8.37 and Figure 8.38, respectively.

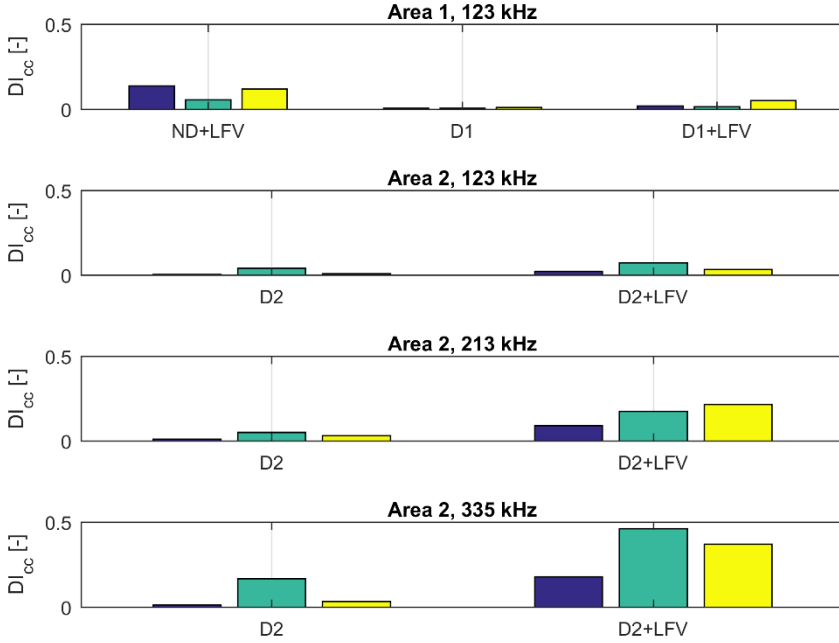


Figure 8.37. Frequency-domain CC-based DI for all tested HA-LFV cases, together with corresponding reference states. The three bars (purple, green, yellow) for each condition correspond to the three actuator-sensor pair analysed in each area: 2-3, 2-4 and 2-5 in area 1; 6-7, 6-8 and 6-9 in area 2.

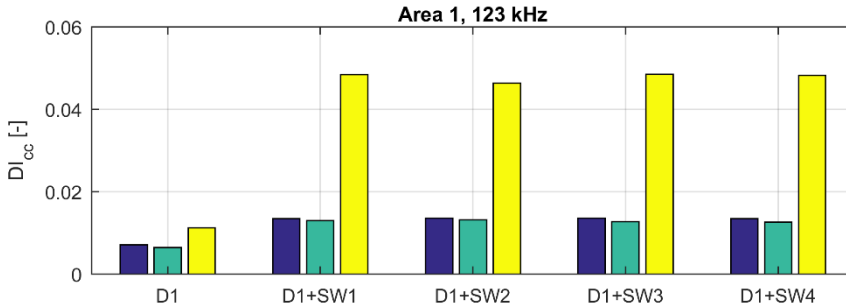


Figure 8.38. Frequency-domain CC-based DI for all tested audible SW cases. The three bars (purple, green, yellow) for each condition correspond to the three actuator-sensor pairs, 2-3, 2-4 and 2-5, in area 1.

From an operational point of view, the DI_{CC} obtained in area 1 at 123 kHz in the ND+LFV case would lead to an erroneous diagnostic, as there was no damage present in the structure and still the DI_{CC} was around 0.1 (see first graph of Figure 8.37). An

erroneous diagnostic would also be obtained for area 2 in the D2+LFV cases at 213 and 335 kHz (see third and fourth graphs of Figure 8.37), as no extra damage was present in the structure with respect to the D2 state and yet the DI_{CC} was increased by about 0.1 and 0.2, respectively. However, the diagnostic for area 1 at 123 kHz in the D1+LFV case (see first graph of Figure 8.37), and for area 2 at 123 kHz in the D2+LFV case (see second graph of Figure 8.37) would be practically the same as for the corresponding cases at rest D1 and D2, respectively.

For the audible SW cases (see Figure 8.38), the DI_{CC} seems to be weakly affected for only one of the actuator-sensor pairs, which means that the diagnostic would be reliable. It is important to remember that the amplitude of the audible SW in the raw signals was of the same order of magnitude as the GW groups.

Thus, the question posed in the beginning of this section can be answered in two parts. For a system with no LFV compensation mechanism, it is possible to reliably perform diagnostic 1) only in some of the cases where HA-LFV is present; and 2) in cases where audible SW is present and has an amplitude of the same order of magnitude as the GW groups.

It is clear that a compensation mechanism would be required if damage diagnostic was to be reliably accomplished at all times. The automated identification of LFV/SW cases is not expected to be problematic, as experience shows that raw GW signals without LFV/SW effects have amplitudes below 200 mV. Therefore, HA-LFV or audible SW cases could potentially be identified if the absolute value of the raw signal amplitude would go beyond 200-500 mV. Once this identification was done, an algorithm could use information about the relationship between amplitude and frequency of the LFV/SW and the effects on the frequency-domain representation of the filtered signal in order to define the necessary DI compensation. In this study, however, both the amplitude and frequency of the LFV were varying randomly during the tests, which prevented a relationship being established between those quantities and the observed variations of DI , $t_{10\%}$ and f_{ch} . Additionally, the auxiliary FE model described in Section 8.4.2 did not include the simulation of damage, and hence did not allow the assessment of the evolution of the DI with the LFV frequency and amplitude. A potential alternative to DI compensation could be, for example, the utilization of split-spectrum signal processing [16] instead of CWT filtering in order to try to reduce the coherent noise in the GW signals.

8.5. Conclusions

8

This last technical chapter describes two studies performed during the test campaign conducted on the GW-SHM system developed for a real-scale (1:1) stiffened panel of a thermoplastic composite horizontal stabilizer torsion box.

The first study was on the evaluation of the capability for detecting real BVID of different severities and in different critical locations of the structure, which, together with the results from the model-assisted reliability assessment of Chapter 7, aimed to complete the validation of the GW-SHM system design methodology proposed in Section 6.3.2 and provide an answer to research question Q2).

According to the ultrasonic C-scans of the critical areas, the length of the BVID-related stringer-skin delamination ranged from a couple of millimetres up to 164 mm. All the different BVID were detected by the SHM system. By following the physical principles of the detection approach from Chapters 4 and 5, the frequency-domain representation of the GW signals was used to compute the DI. The obtained DI values for

the largest BVID were comparable to the values for similar damage size obtained by other researchers, thereby confirming the accuracy of damage quantification. However, contrary to those other researchers, the SHM system designed according to the novel methodology was equally sensitive to both large and small BVID. In fact, the DI values for area 1 allowed a less ambiguous detection than the ultrasonic C-scan, where the damage showed up only as a few spots with low reflectivity of about 20%.

Additionally, it was also possible to detect and quantify the accumulation of successive BVID, both in normal and sparse transducer network configurations, thereby showing that it is not necessary to perform a transducer network optimization for each different damage scenario. The performance of the SHM system in the detection of accumulated BVID at area 3 even surpassed that of the ultrasonic C-scan, where the second impact did not produce any noticeable reflectivity difference with respect to the first impact.

Therefore, given the results of the POD study of Chapter 7, it was concluded that the proposed methodology for consistently designing the transducer network has the potential for maximizing the diagnostic effectiveness of a GW-SHM system, as it enabled the mission accomplishment for a variety of damage sizes in different critical areas of the structure.

It is important to state that the physics used for each design criterion in Section 6.3.2 was not novel. However, it was the first time such physical criteria have been used in a fully integrated way in order to develop a procedure for systematically designing a PZT transducer network for GW-SHM without depending on damage size tuning or relying on single guided mode analysis.

The second study enabled by the component-scale test campaign had the objective of gaining knowledge about the effects of audible SW and HA-LFV on ultrasonic GW propagation. The research was based on the hypothesis that a short time window of GW propagation under audible SW or HA-LFV can be described by GW propagation in a structure with a permanently corrugated shape.

The visible effect of HA-LFV on ultrasonic GW propagation was the presence of coherent noise in the filtered signals. This coherent noise was interpreted as the result of superposition of multiple dispersive wave groups produced by mode conversion at the moment of reflection on the corrugated panel surface. Strong evidence of this was found in the frequency-domain through the appearance of multiple components within the useful bandwidth, which resulted in a consistent increase of the characteristic frequency (f_{ch}). Increases in the 10%-duration time ($t_{10\%}$) of GW signals appeared to indicate propagation through paths affected by phase changes, which in turn were caused by the altered scattered field in the corrugated structure. It was also possible to observe that the coherent noise amplitude depends on the amplitude of the LFV, and on the ratio between the LFV frequency and the ultrasonic excitation frequency.

The audible SW generated by the cooling system of the mechanical shaker had a maximum amplitude of the same order of magnitude as the maximum GW amplitude. As a result, no coherent noise was observed in the filtered signals and, hence, it barely affected the diagnostic capabilities.

After applying the FE modelling approaches developed in Chapter 7 to simulate GW propagation in an aluminium plate with a permanent corrugated shape, there was strong evidence supporting the hypothesis that ultrasonic GW propagation with HA-LFV effects can be analysed under the assumption of a structure with a permanent corrugated shape.

From an SHM operation point of view, reliable diagnostic was still possible in the HA-LFV cases with weaker coherent noise. The other cases would require an algorithm to

be developed in order to either apply more effective filtering, or to compensate for the influence of the coherent noise on the DI.

References

1. Ochôa P, Groves RM, Benedictus R. Full-scale testing of an ultrasonic guided wave based structural health monitoring system for a thermoplastic composite aircraft primary structure. Paper presented at: 9th EWSHM, July 10-13, 2018; Manchester, United Kingdom.
2. Ochôa P, Groves RM, Benedictus R. Systematic multi-parameter design methodology for an ultrasonic health monitoring system for full-scale composite aircraft primary structures. *Struct Control Health Monit* 2019; 26(5): e2340.
3. Ochôa P, Groves RM, Benedictus R. Effects of high-amplitude low-frequency structural vibrations and machinery sound waves on ultrasonic guided wave propagation for health monitoring of composite aircraft primary structures. *J Sound Vib* 2019, under review.
4. ARP6461:2013-09. Guidelines for implementation of structural health monitoring on fixed wing aircraft; 2013.
5. Ochôa P. Supporting data for ultrasonic guided wave and electro-mechanical reactance tests on a full scale composite torsion box panel. 4TU.Centre for Research Data. Dataset, 2019. <https://doi.org/10.4121/uuid:8c743b60-69f3-4f59-b738-8f58b784bb9f>.
6. Ochôa P. Supporting data for guided wave tests with structural vibrations. 4TU.Centre for Research Data. Dataset, 2019. <https://doi.org/10.4121/uuid:5deaf8cf-ec57-4e33-86c4-8253a00dfd4>.
7. Buethe I, Moix-Bonet M, Wierach P, Fritzen CP. Check of piezoelectric transducers using the electro-mechanical impedance. Paper presented at: 7th EWSHM; July 8-11, 2014; Nantes, France.
8. Park G, Farrar CR, Di Scalea FL, Coccia S. Performance assessment and validation of piezoelectric active-sensors in structural health monitoring. *Smart Mater Struct* 2006; 15: 1673-1683.
9. Blackshire JL, Cooney AT. Characterization of bonded piezoelectric sensor performance and durability in simulated aircraft environments. *AIP Conf Proc* 2006; 820: 1694-1701.
10. Monnier T. Lamb waves-based impact damage monitoring of a stiffened aircraft panel using piezoelectric transducers. *J Intell Mater Syst Struct* 2006; 17: 411-421.
11. Eckstein B, Moix-Bonet M, Bach M, Fritzen CP. Lamb wave interaction at debondings due to impact damage in complex stiffened CFRP structures. *Proc SPIE* 2017; 10170(101701Q): 1-14.
12. Richardson MOW, Wisheart MJ. Review of low-velocity impact properties of composite materials. *Composites Part A* 1996; 27(12): 1123-1131.
13. Schijve J. *Fatigue of Structures and Materials*. 2nd ed, Springer, 2010.

14. Gandhi N, Michaels JE, Lee SJ. Acoustoelastic Lamb wave propagation in biaxially stressed plates. *J Acoust Soc Am* 2012; 132(3): 1284-1293.
15. Banerjee S, Kundu T. Symmetric and anti-symmetric Rayleigh-Lamb modes in sinusoidally corrugated waveguides: An analytical approach. *Int J Solids Struct* 2006; 43(21): 6551-6567.
16. Pedram SK, Fateri S, Gan L, Haig A, Thornicroft K. Split-spectrum processing for SNR enhancement of ultrasonic guided wave. *Ultrasonics* 2018; 83: 48-59.
17. Ochôa P. Supporting data for finite-element simulations of ultrasonic guided wave propagation on a plate with a permanently corrugated shape. 4TU.Centre for Research Data, 2019. <http://doi.org/10.4121/uuid:faa62d35-1444-4e40-a970-404c2b0c83cd>.
18. Radzienski M, Cao M, Wei X, Kudela P, Ostachowicz W. Combined vibration and guided wave-based approach for composite panels health assessment. *Proc SPIE* 2017; 10170(101702D): 1-8.

9

Conclusions and recommendations

We mortals are but shadows and dust...

(Gladiator)

This last chapter summarises the main conclusions and contributions from each of the interconnected topics studied in this thesis. At the end, it provides some recommendations for further research on reliability improvement of GW-SHM of composite aircraft.

9.1. Main conclusions and contributions

The goal of this thesis was to improve the reliability of GW-SHM for thermoplastic composite aircraft, as a step towards the future implementation of CBM programmes. It was decided to guide the research such that the problems associated with full geometric and material complexity were addressed without losing sight of the physics governing the sensing capabilities and the GW interactions with critical structural details. Therefore, the focus was on 1) GW propagation in ultrasonically welded TpC structures, 2) systematization of the GW-SHM system design, 3) reliability analysis of the GW-SHM system, and 4) effects of HA-LFV on GW signals.

9.1.1. GWs in ultrasonically welded TpC structures

TpCs have developed into cost-effective alternatives to thermoset composites among aircraft manufacturers, due to research not only in new materials but also in improvements of joining technologies. In particular, the promising developments of the technology for UW of TpC parts have opened new possibilities for composite aircraft primary structure assembly. At the same time, it has become increasingly important to conduct research on SHM of TpC structures in order to enable reliable damage diagnostic. Therefore, Chapters 4 and 5 were dedicated to understanding GW propagation in TpC ultrasonic welds.

First (Chapter 4), the focus was on studying the influence of the welding travel on the transmission of zero-order GW modes across pristine TpC single-lap joints. Two things were observed. On the one hand, the power transmission coefficient revealed only a small amplitude variation with respect to the reference signals. On the other hand, the correlation coefficient showed that, despite the small amplitude variations, there were large signal shape changes with respect to the reference signals. These observations were attributed to a variation in the phase velocity of the GW modes in the overlap without a significant change of their displacement mode shapes. This affected the phase lag between the GW modes in the overlap and, consequently, the reverberation pattern inside the overlap. As a result, the modification of the interference between the reverberated wave packets and the directly transmitted wave packets was dominated by signal shape changes.

Building upon these findings (Chapter 5), the effect of ultrasonic weld manufacturing defects on GW transmission across TpC ultrasonic welds was investigated. Triangular EDs integrated into the lower composite adherends enabled the production of defective joints in a controlled manner. The produced defect types were unwelded areas interspersed with welded zones, and adherend fibre bundle distortion due to overwelding. The oblique scattering effect of the distorted fibre bundles on the GWs induced a negative shift of characteristic frequency (Δf_{ch}) of the GW signal. It also caused the extra reflections from the overlap edges to interfere constructively and form the wave packet of maximum amplitude at a late time instant, thereby increasing the time-of-flight (TOF). The higher thickness and lower average cross-sectional stiffness of the joints with unwelded areas resulted in a consistent increase of TOF. In the end, it was possible to detect and distinguish the two defective scenarios by combining characteristic frequency and TOF analysis. The case of null Δf_{ch} and high ΔTOF with respect to the reference corresponds to unwelded areas interspersed with welded zones. The case of high Δf_{ch} and high ΔTOF with respect to the reference corresponds to adherend fibre bundle distortion.

In short, the research presented in Chapters 4 and 5 showed that GWs are sensitive to manufacturing-related variations that can occur in both pristine and defective joints, and

thereby established an initial approach for diagnosing manufacturing defects in ultrasonically welded TpC joints. Since the fusion bonding in both ultrasonically welded joints and co-consolidated joints occurs through the mechanism of molecular interdiffusion, the physics behind that diagnostic approach was then important in defining the DI for the tests on component-scale torsion box panel presented in Chapter 8. Overall, the knowledge acquired in Chapters 4 and 5 represents an important step towards the development of SHM capabilities for modern TpC aircraft structures, where early detection of incipient defects is crucial to prevent unexpected failures.

9.1.2. Systematization of GW-SHM system design

The development of reliable GW-SHM capabilities for real structures implies systematisation and standardisation of practices, but also realistic outputs to make those practices feasible. This is especially true when it comes to designing the SHM system, and it becomes necessary to go beyond the limited structural complexity level of Chapters 4 and 5. For that reason, Chapter 6 presented a novel methodology to systematically design an ultrasonic GW-SHM system which is not limited to a single damage size, does not resort to unrealistic usage of GWs (e.g. Lamb mode selection), and is applicable to a generic real-scale (1:1) composite aircraft primary structure. The proposed set of criteria for defining the excitation frequency content, geometry and positioning of PZT transducers was based on the optimization of the sensor output, coupled electro-mechanical (EM) response of the transducer-structure assembly, energy transfer from the bonded PZT transducer to the structure, wavefront coverage of the monitored area, and measurement equipment capabilities. Moreover, the choice of PZT material reflected the need for having transducers with interchangeable function between actuator and sensor.

The proposed design methodology was validated in two phases. Firstly, a quantitative analysis of the SHM system reliability (Chapter 7) estimated it to be 90% probable that the GW-SHM system would allow the detection of critical BVID in the torsion box panel with a confidence level of 95%. Secondly, the capabilities of the SHM system for diagnosing BVID of different severities were experimentally demonstrated. The different cases of BVID were introduced in different locations of a component-scale horizontal stabilizer torsion box panel entirely made of TpC material (Chapter 8). Since the fusion bonding in the co-consolidated joints of the torsion box panel works through the same mechanism of molecular interdiffusion as in ultrasonically welded joints, the understanding acquired at element-scale in Chapters 4 and 5 was employed in the definition of the detection approach at component-scale. Not only did the SHM system detect all the different BVID, but it was also possible to detect and quantify the accumulation of successive BVID, both in normal and sparse transducer network configurations, thereby showing that it is not necessary to perform a transducer network optimization for each different damage scenario.

As a result of the reduction of the variability associated with SHM system design parameters, the uncertainty in damage diagnostic was also reduced. Furthermore, it was concluded that the proposed methodology for systematically designing the transducer network has the potential for maximizing the diagnostic effectiveness of a GW-SHM system, as it enabled the mission accomplishment for a variety of damage sizes in different critical areas of the structure.

9.1.3. Reliability analysis of GW-SHM systems

The complete validation of an SHM system implies a statistical characterisation based on scenarios that are expected to be encountered in real operation. Therefore, crucial GW measurement variability factors, such as geometric complexity, material anisotropy and transducer bonding degradation, were simultaneously taken into account in the development of real-scale (1:1) numerical models, which in turn enabled the implementation of an improved protocol for studying the reliability of GW-SHM systems. Model-assisted POD studies were conducted for the GW-SHM system designed for area 3 of the component-scale torsion box panel, according to the methodology proposed in Chapter 6.

Not only did the reliability analysis contribute to the validation of the GW-SHM system, but it also enabled the evaluation of varying threshold on the POD. While at 112 kHz there was approximately no change in the width of the 95% confidence bounds, at 198 kHz the width varied in a non-uniform way when the threshold was increased. For low thresholds, the confidence bounds were wider at low POD values than at high ones, while for high thresholds, they were wider at high POD values than at low ones. For intermediate thresholds, the confidence bounds had an approximately uniform width. It was demonstrated that the non-uniform width of the confidence bounds for the extreme thresholds was caused by a coupling between the regression variance and the threshold value, which was enhanced by the non-uniform value of the quantile of the standard normal distribution. Therefore, there seems to be an optimum threshold, at around 3 to 4 times the threshold base value (defined in Section 7.2.3), that enables detection with non-biased confidence levels.

The implemented protocol allowed the study of the scenario of degraded actuator bonding. It was observed that a reduction of just 25% in the bonded actuator area results in a false positive detection rate of 50% for a disbond of null length, which renders any diagnostic impossible. This proved that it is crucial to include the integrity of the transducer adhesive layer in the reliability analysis of GW-SHM systems. By doing so, adaptive strategies can be devised to deal with data acquired in these type of scenarios, which is a vital step for the certification of GW-SHM systems.

9.1.4. Effects of HA-LFV on GW signals

Future certification of a GW-SHM system requires demonstration of damage diagnostic capabilities in real operation-environmental conditions, such as large temperature changes and high-amplitude, low-frequency structural vibrations (HA-LFV). To that end, mechanisms must be put in place to compensate for the effect of those variations on GW signals, which in turn requires an understanding of the physics behind those effects. This thesis took a first step in bridging the gap of knowledge about the effect of HA-LFV on GW propagation.

The visible effect of HA-LFV on ultrasonic GW propagation was the presence of coherent noise in the filtered signals. This coherent noise was interpreted as the result of superposition of multiple dispersive wave groups produced by mode conversion at the moment of reflection on the corrugated panel surface. Strong evidence of this was found in the frequency-domain through the appearance of multiple components within the useful bandwidth, which resulted in a consistent increase of characteristic frequency (f_{ch}). Increases in the 10%-duration time ($t_{10\%}$) of GW signals appeared to indicate propagation through paths affected by changes of phase velocity, which in turn were caused by the

altered stress state along the corrugated structure. By resorting to the modelling capabilities developed in Chapter 7, it was also possible to observe that the coherent noise amplitude depends on the amplitude of the LFV, and on the ratio between the LFV frequency and the ultrasonic excitation frequency. Therefore, there was strong evidence supporting the hypothesis that ultrasonic GW propagation with HA-LFV effects can be analysed under the assumption of a permanently corrugated structure subjected to static stress.

9.1.5. Considerations about signal processing

It is worth emphasising that all the conclusions summarised in Sections 9.1.1 to 9.1.4 were achieved by using *minimalist* signal processing (see Section 3.4). The algorithm complexity level was kept at a minimum so that the diagnostic capabilities were deployable in the largest possible diversity of cases, and contributions to SHM system reliability were attainable. It is envisioned that this approach allows the generation of *accurate-enough* quantitative measures of damage that indicate its presence within the monitored area and show a monotonic evolution with damage severity. In turn, this fits within the vision that SHM should not be seen as a means to replace detailed NDT inspections, but as a tool to enable a more cost-effective allocation of those resources and the subsequent optimisation of maintenance programmes.

9.1.6. SHM as a catalyst for composite aircraft design optimisation

The findings of this thesis can also be regarded as contributions for enabling a reduction in the conservatism of composite aircraft design [1]. It was demonstrated that GW-SHM systems can detect real BVID of different severities in real-scale (1:1) primary structures, with high estimated reliability. This means that future designs can be allowed to be less conservative than in the case of current composite aircraft, because it will not be necessary to endure until the next scheduled inspection. As a result, material utilisation can be optimised, structures can be made thinner and considerable weight savings can be achieved [2].

In the medium-long term, the large amounts of data collected by GW-SHM systems can potentially bring a better understanding of damage progression in composite structures and of its effects on the load bearing capabilities. In turn, this knowledge can be employed in further optimising the design (principles) of composite aircraft and lowering knock-down factors, without compromising airworthiness and safety [3].

9.2. Recommendations

9.2.1. Damage progression diagnostic in TpC structures

A deeper understanding about damage progression in TpC welded structures is required. Furthermore, it is also necessary to study the interaction of progressive damage in those structures with ultrasonic GWs. Therefore, large TpC joints produced either by continuous ultrasonic welding or by induction welding could be tested with GWs under fatigue, with different loading spectra, including variable amplitude tension, compression and bending.

The progression of damage externally introduced after a predefined number of fatigue cycles could also be studied. Although realistic, the features of BVID are difficult to

control. An interesting alternative to BVID could be laser-induced delaminations, which have been proven to be reliably controllable [4].

As demonstrated in Section 7.5.1.4, the detection threshold strongly affects the GW-SHM system reliability and must be defined according to the scale and history of the structure. In other words, it must take into account the physics of damage progression in the structure under consideration. Therefore, the GW studies recommended above for TpC welded subcomponents under fatigue would allow the development of a method to define the detection threshold in a systematic way.

9.2.2. Guided wave transducers

The research line proposed in Section 9.2.1 would also contribute to characterise the degradation of PZT transducer bonding under fatigue loading of composite structures. The quantifier of the transducer adhesive layer integrity could be the EM susceptance at the transducer terminals, measured at a predefined fatigue cycle interval. The internal structure of the adhesive layer could be assessed through B-scans obtained by ultrasonic phased-array testing. This knowledge could then be incorporated in the reliability analysis of GW-SHM, thereby leading to more accurate estimates.

In an effort to reduce the GW measurement errors, research could also be conducted on improving the repeatability of the transducer installation. New piezo-composite transducers with a thermoplastic substrate layer could be developed such that their installation would be achieved by welding them to the TpC structure. This would eliminate many manual (error-prone) steps from the traditional bonding procedure, thereby contributing to a more systematic installation of GW transducers.

9.2.3. Towards three level diagnostic

This thesis shares the vision that an SHM system should at least have the capabilities of reliably detecting the presence of damage, estimating the severity of the damage, and approximately locating the damage. While GW testing can be employed to fully accomplish the first two missions, it is limited when it comes to the third one.

The exact same PZT transducer network for GW-SHM can also be used in passive mode for capturing elastic waves emitted from the initiation or progression of damage in the structure (the so-called acoustic emission, AE) [5]. Since, in this case, damage is the source of the elastic waves, it is possible to directly correlate the passively acquired signals to the damaging event and its location. The typically higher frequencies of ultrasonic GWs and their controlled excitation allow a detailed interaction with the damage, thereby enabling the determination of the damage severity.

Although it is a logical combination of measurement approaches, no systematic study has been attempted yet. Hence, the recommendation would be to acquire AE and GW data with the same transducers, from the TpC subcomponents proposed in Section 9.2.1. This would give the opportunity to develop signal processing algorithms for acousto-ultrasonic signals in order to enable the aforementioned three levels of damage diagnostic.

9.2.4. New damage indicator

A very interesting quantity to study is the Shannon entropy of the wavelet coefficients of ultrasonic GW signals (EWC), as defined by Equation (3.1) in Section 3.4. As stated by Li

et al. [6], the EWC curve is immune to signal noise, and is just slightly affected by a small delamination in a composite plate. Therefore, a legitimate hypothesis to test could be that if the load bearing capabilities of a composite structure are truly affected by damage, then there should be a clear change in the EWC curve. Should this hypothesis be confirmed, the valley depth and width of the EWC curve could then be used for a new damage indicator which would potentially be a real measure of the residual strength.

9.2.5. Improvement of the SHM environment model

There is plenty of room for improvement of the numerical model used for simulating the real-scale (1:1) GW-SHM environment. Starting with the composite material, the laminate can be more accurately modelled by using the existing Abaqus tools for composite layup definition. However, those tools can only be used for shell elements. Thus, it should be verified whether the use of shell elements (as employed by Luca et al. [7]) allow the same accuracy in ultrasonic GW simulation as the solid three-dimensional elements. The use of shell elements would in turn enable the simulation of double curved panels, just like the ones used in the component-scale torsion box panel (Section 3.2.2). Another improvement could be achieved by modelling the degradation of transducer bonding in a more realistic way. The disbonded area contour could be changed, and the potential findings of the study proposed in Section 9.2.2 could be incorporated in order to model the adhesive layer itself.

It is crucial to have accurate real-scale (1:1) FE simulations, while keeping the computational cost as low as possible, which implies using the explicit solver for solving the transient dynamic equations. As explained in Section 7.3, it is not possible to use FEs with piezoelectric properties when solving the problem with Abaqus/Explicit. Therefore, an alternative to using externally applied stresses for mimicking the piezoelectric excitation could be to employ *co-simulation*, which allows the implicit solver (Abaqus/Standard) to be used for a part of the problem/domain. In that sense, the excitation could be more accurately modelled by implicitly solving the piezoelectric equations for the actuator only, the GW propagation problem could then be solved explicitly for the entire domain, and finally the piezoelectric equations could be solved again for the sensors only. Consequently, this implementation would also enable a more accurate representation of the sensed GWs, because the numerical signals would be extracted from the voltage outputs of FEs with piezoelectric properties, and not from isolated nodal displacements.

It would also be interesting to simulate different damage types in order to cover more diagnostic scenarios. Finally temperature and structural loading should also be included to mimic realistic environmental-operational conditions of the GW-SHM system. Ultimately, all the improvements proposed above would allow more accurate reliability analyses of GW-SHM systems.

It is an undeniable truth that conventional FE models employed in ultrasonic GW-SHM studies require very small time steps and extremely refined meshes, thus being computationally very demanding, even when solved explicitly. Therefore, new modelling approaches should be sought in order to enable faster simulations, and, consequently, larger and more accurate parametric studies. A very promising alternative could be the utilization of hybrid-Trefftz FEs, which “*satisfy exactly the differential equations governing*” of the wave problem [8,9]. This characteristic makes them ideal for modelling ultrasonic GW propagation without a fine spatial and temporal discretisation.

9.2.6. Effects of HA-LFV on GW propagation

It is crucial to continue the research about the effects of HA-LFV on GW propagation in order to make GW-SHM possible during aircraft operation. Following the rationale of Section 8.4.2, GW tests could be performed at multiple ultrasonic frequencies in large structural details or subcomponents (e.g. the same type of joints proposed in Section 9.2.1) subjected to vibration at a well-defined frequency. The LFV frequency and amplitude should be varied in different groups in order to assess the effect of their variation separately. Those tests should be conducted first without any damage, and then with damage applied in a controlled fashion (e.g. laser-induced delamination). The GW data acquisition could be synchronized with strain data acquisition (e.g. through digital image correlation), so that the stress state could be evaluated.

To further test the research hypothesis of Section 8.4.1, FE modelling could be employed to simulate GW propagation in a permanently corrugated panel, with a corrugation equivalent to that induced by the studied HA-LFV. The results of the numerical and experimental tests just proposed would allow a relationship to be established between LFV amplitude and frequency, and the selected GW signal feature, which in turn could potentially enable the implementation of a HA-LFV compensation algorithm. At the same time, split-spectrum processing [10] could be explored for filtering out the HA-LFV effect from the GW signals.

9.2.7. Flying research

One of the most difficult obstacles to overcome in SHM research is to reproduce truly realistic environmental-operational conditions during testing. The ideal solution would be to conduct research on flying aircraft. It can be argued that the readiness level of GW-SHM technology might not be high enough to conduct extensive test campaigns on fully operational aircraft in normal service routes with the approval of the authorities. However, it would be less of a problem to conduct a research programme in which regular missions would be flown by unmanned aerial vehicles (UAVs) instrumented with GW-SHM systems. The valuable conclusions could then be almost directly upscaled to commercial aircraft.

References

1. Achenbach JD. Structural health monitoring – What is the prescription? *Mech Res Commun* 2009; 36: 137-142.
2. Dienel CP, Meyer H, Werner M, Willberg C. Estimation of airframe weight reduction by integration of piezoelectric and guided wave-based structural health monitoring. *Struct Health Monit* 2018; 1-11.
3. Giurgiutiu V. *Structural health monitoring with piezoelectric wafer active sensors*. 2nd ed. Academic Press – Elsevier; 2014.
4. Ghrib M, Berthe L, Mechbal N, Rébillat M, Guskov M, Ecault R, Bedreddine N. Generation of controlled delaminations in composites using symmetrical laser shock configuration. *Compos Struct* 2017; 171: 286-297.

5. Groman MR. Chapter 4: Acoustic Emission. In: *Encyclopedia of Structural Health Monitoring*. Eds. Christian Bller, Fu-Kuo Chang and Yozo Fujino. John Wiley & Sons, Ltd; 2009.
6. Li F, Meng G, Kageyama K, Su Z, Ye L. Optimal mother wavelet selection for Lamb wave analyses. *J Intel Mat Sys Str* 2009; 20: 1147-1161.
7. Luca A, Caputo F, Khodaei ZS, Aliabadi MH. Damage characterization of composite plates under low velocity impact using ultrasonic guided waves. *Composites Part B* 2018; 138: 168-180.
8. Moldovan, DI, Correia AG, Pereira C. Bender-based G_0 measurements: A coupled numerical-experimental approach. *Comput Geotech* 2016; 73: 24-36.
9. Moldovan, DI, Correia AG. Fixed point automatic interpretation of bender-based G_0 measurements. *Comput Geotech* 2017; 89: 128-142.
10. Pedram SK, Fateri S, Gan L, Haig A, Thornicroft K. Split-spectrum processing for SNR enhancement of ultrasonic guided wave. *Ultrasonics* 2018; 83: 48-59.



Supplementary data

Experimental signals for the study of low-frequency structural vibrations on guided waves.

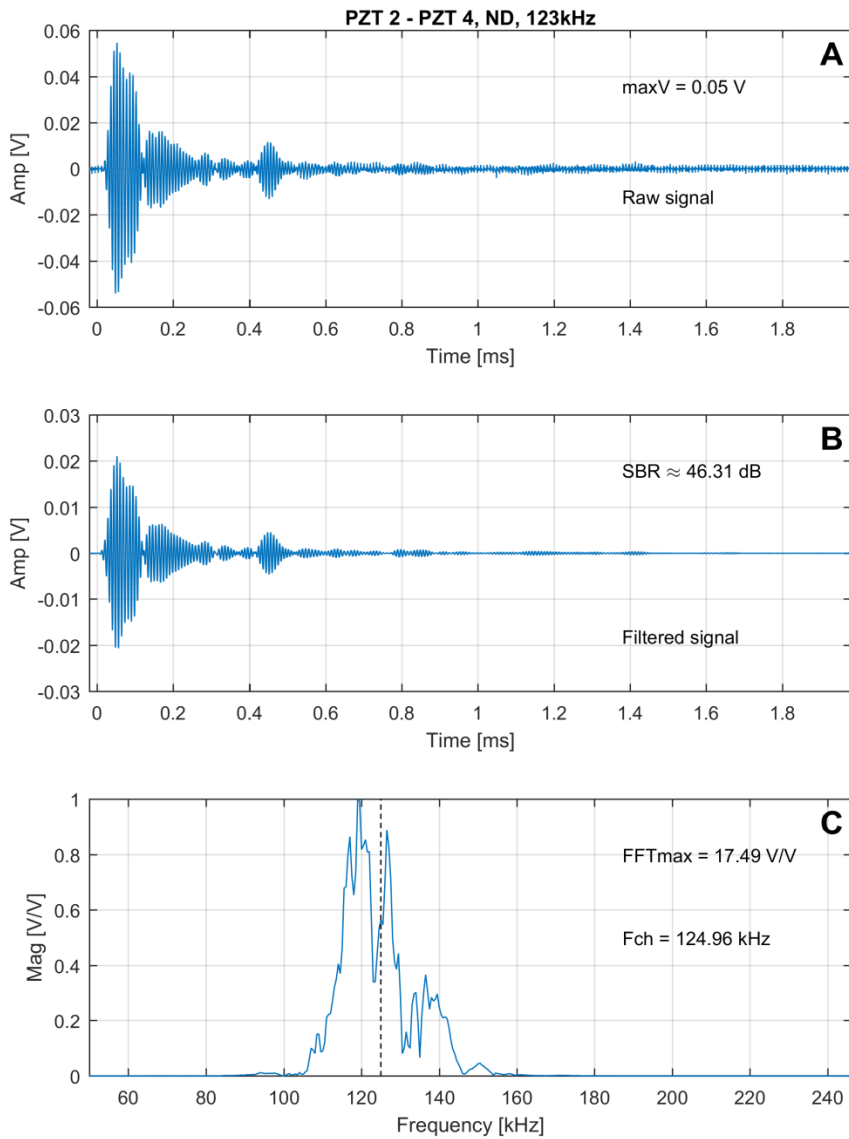


Figure A.1. Plots for actuator-sensor pair 2-4 (Area 1) at 123 kHz, for pristine condition, without structural vibration. From top to bottom: A) raw signal, B) filtered signal, and C) normalized frequency spectrum (characteristic frequency indicated by the dashed line).

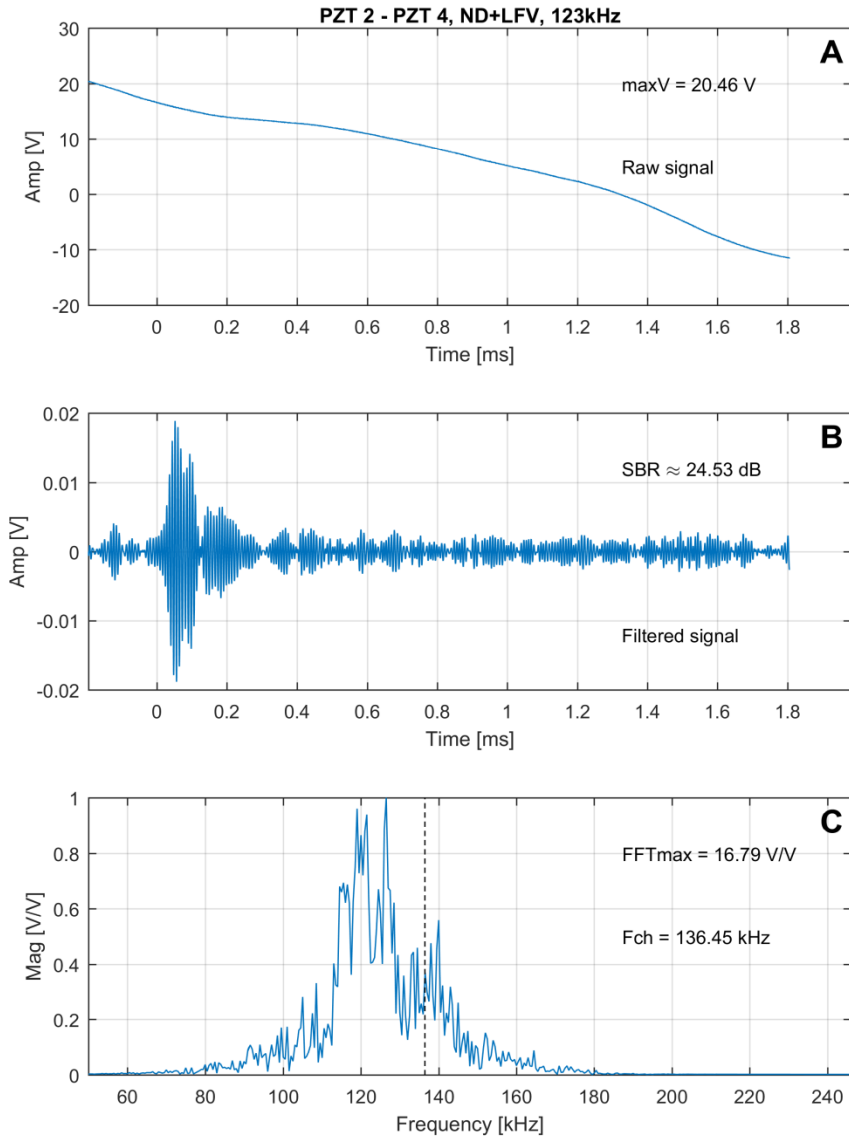


Figure A.2. Plots for actuator-sensor pair 2-4 (Area 1) at 123 kHz, for pristine condition, with low-frequency structural vibration. From top to bottom: A) raw signal, B) filtered signal, and C) normalised frequency spectrum (characteristic frequency indicated by the dashed line).

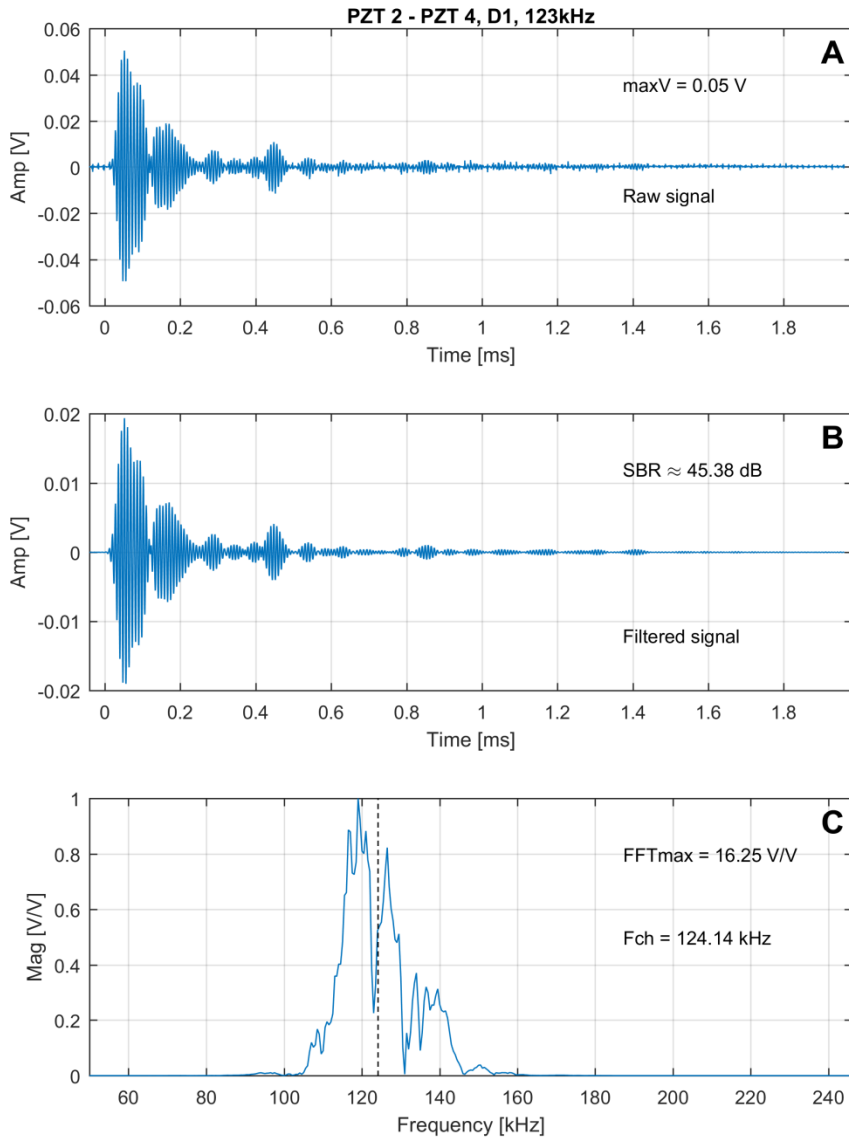


Figure A.3. Plots for actuator-sensor pair 2-4 (Area 1) at 123 kHz, after 50 J impact on stringer run-out, without structural vibration. From top to bottom: A) raw signal, B) filtered signal, and C) normalised frequency spectrum (characteristic frequency indicated by the dashed line).

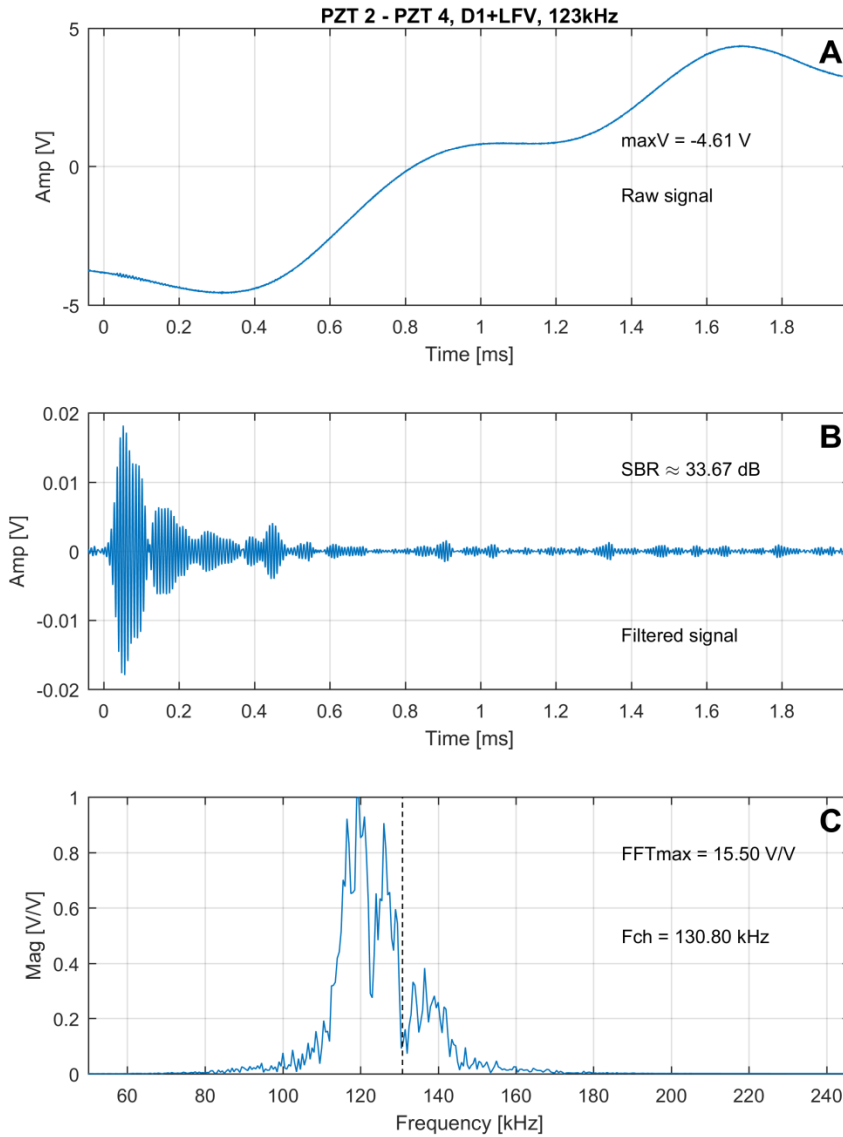


Figure A.4. Plots for actuator-sensor pair 2-4 (Area 1) at 123 kHz, after 50 J impact on stringer run-out, with low-frequency structural vibration. From top to bottom: A) raw signal, B) filtered signal, and C) normalised frequency spectrum (characteristic frequency indicated by the dashed line).

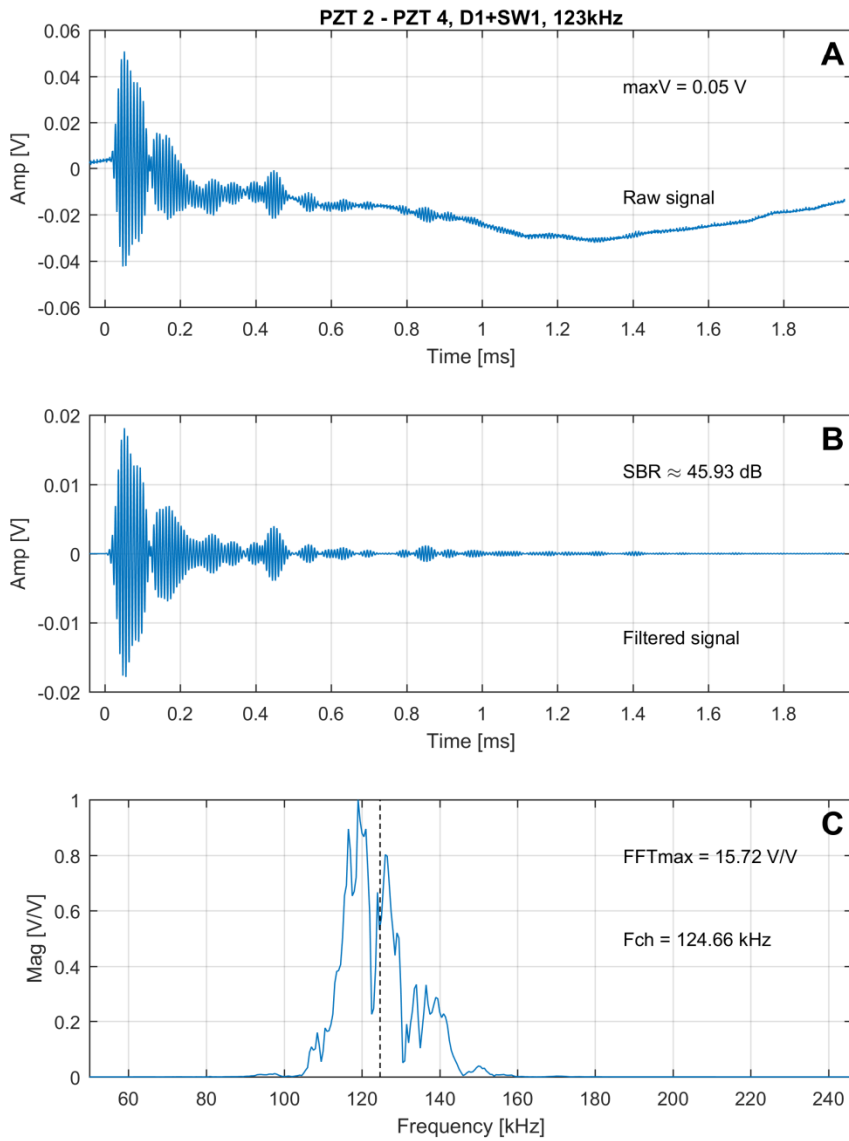


Figure A.5. Plots for actuator-sensor pair 2-4 (Area 1) at 123 kHz, after 50 J impact on stringer run-out, with audible sound waves (test 1) from the cooling system of the mechanical shaker. From top to bottom: A) raw signal, B) filtered signal, and C) normalised frequency spectrum (characteristic frequency indicated by the dashed line).

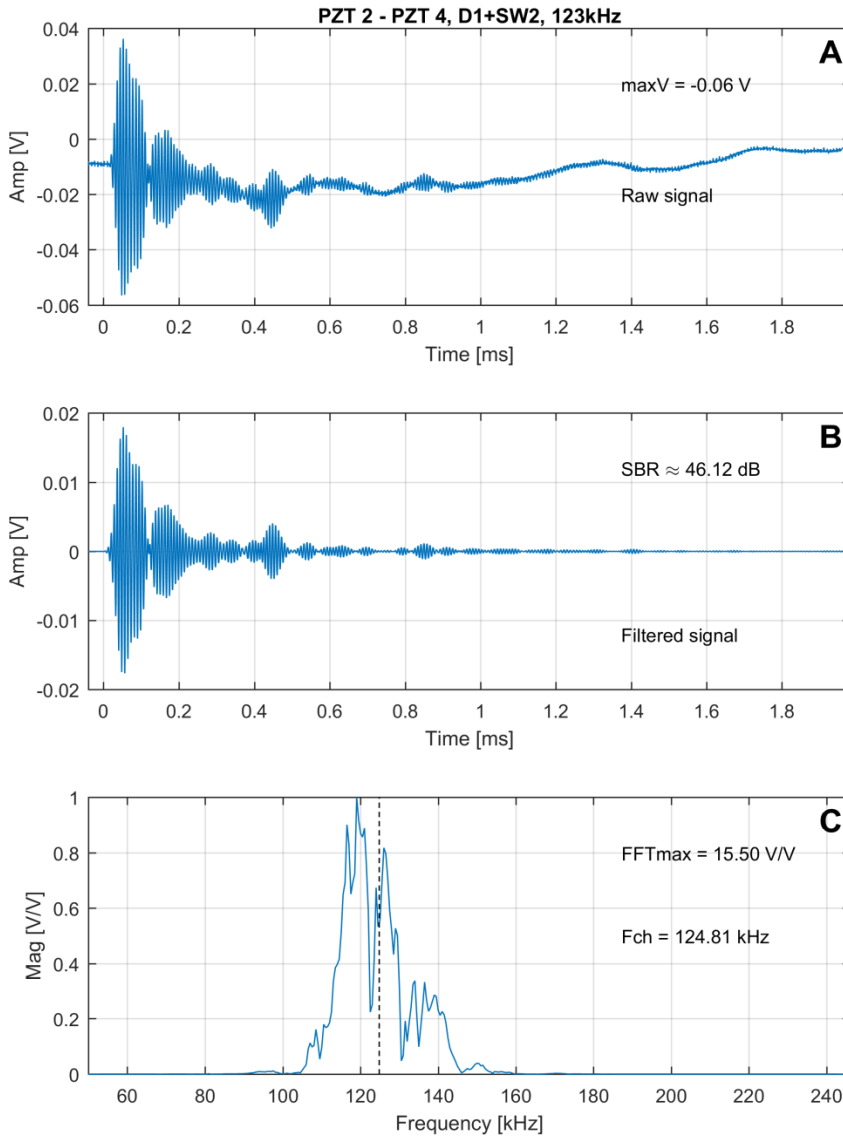


Figure A.6. Plots for actuator-sensor pair 2-4 (Area 1) at 123 kHz, after 50 J impact on stringer run-out, with audible sound waves (test 2) from the cooling system of the mechanical shaker. From top to bottom: A) raw signal, B) filtered signal, and C) normalised frequency spectrum (characteristic frequency indicated by the dashed line).

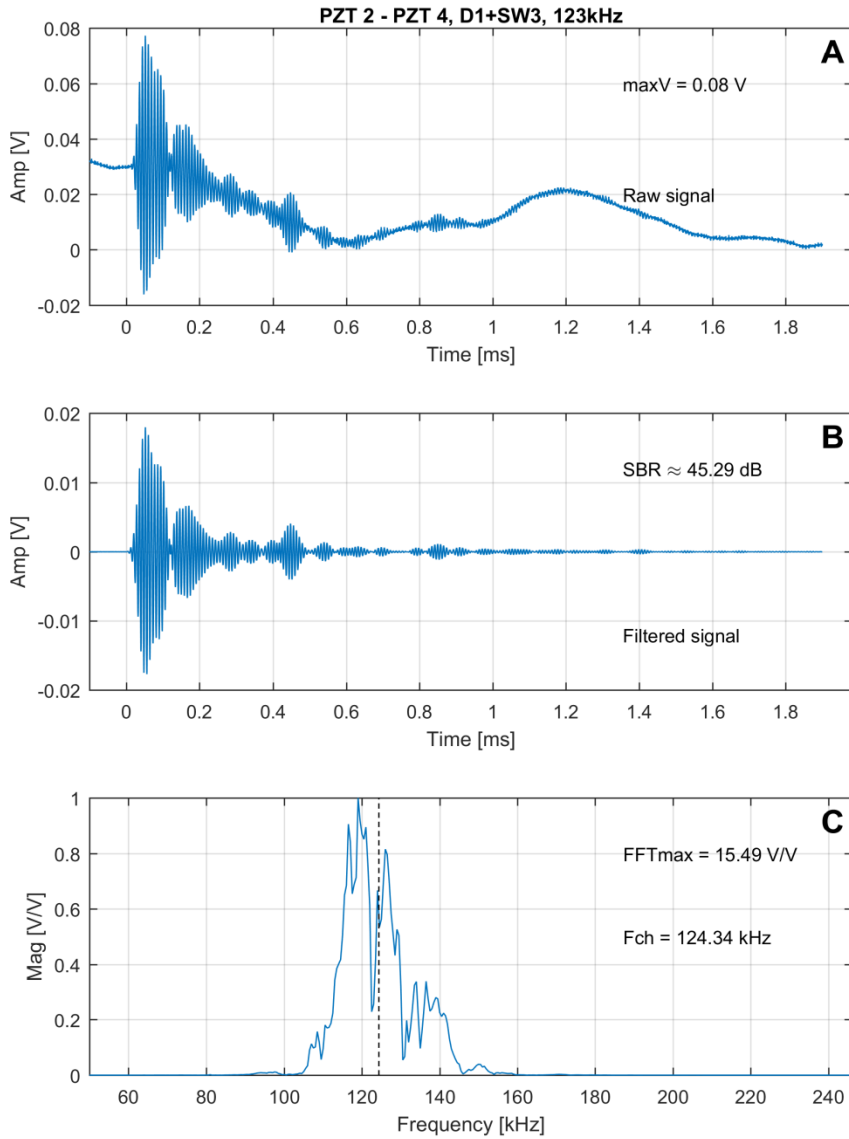


Figure A.7. Plots for actuator-sensor pair 2-4 (Area 1) at 123 kHz, after 50 J impact on stringer run-out, with audible sound waves (test 3) from the cooling system of the mechanical shaker. From top to bottom: A) raw signal, B) filtered signal, and C) normalised frequency spectrum (characteristic frequency indicated by the dashed line).

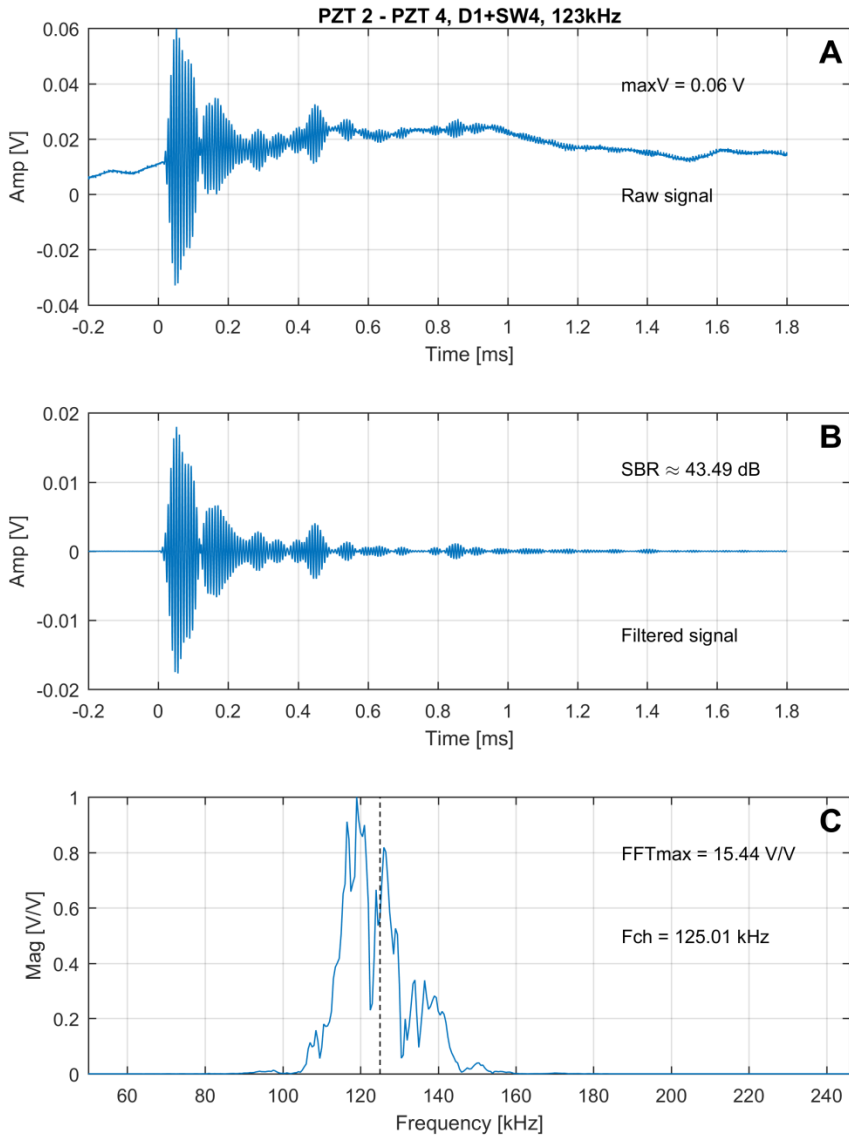


Figure A.8. Plots for actuator-sensor pair 2-4 (Area 1) at 123 kHz, after 50 J impact on stringer run-out, with audible sound waves (test 4) from the cooling system of the mechanical shaker. From top to bottom: A) raw signal, B) filtered signal, and C) normalised frequency spectrum (characteristic frequency indicated by the dashed line).

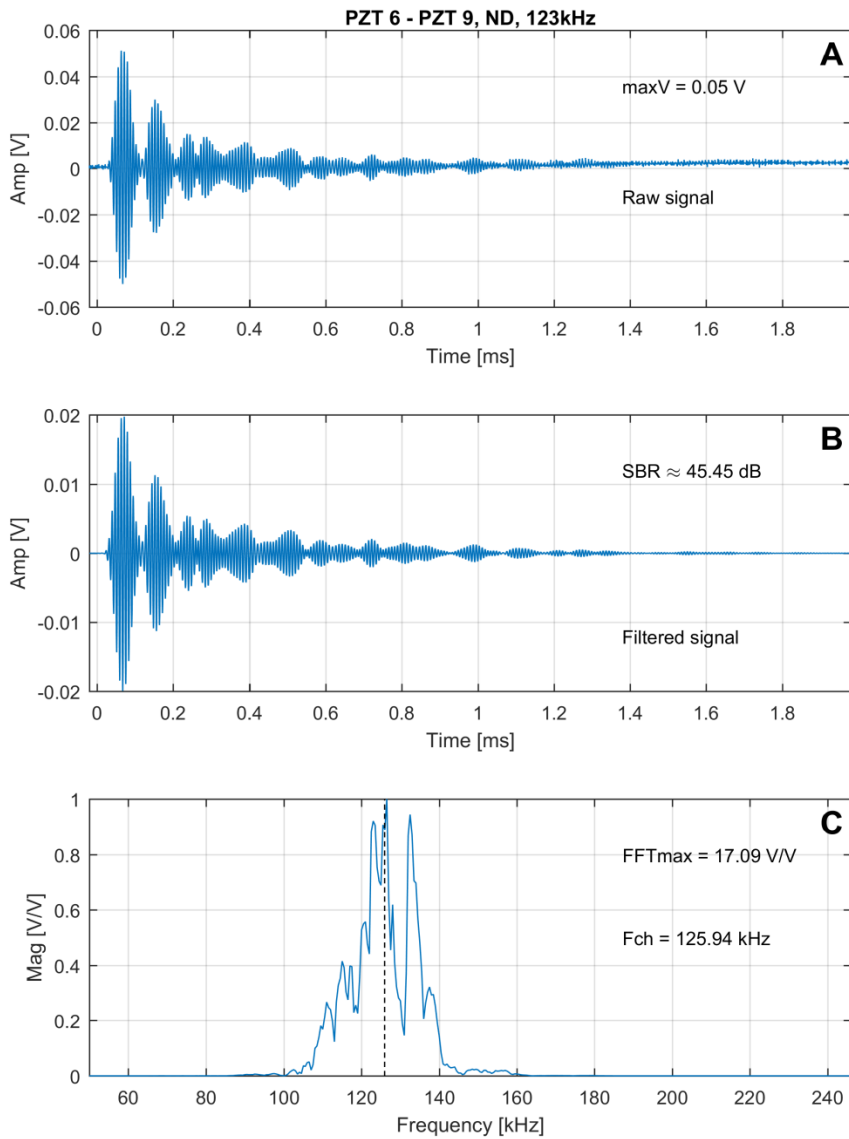


Figure A.9. Plots for actuator-sensor pair 6-9 (Area 2) at 123 kHz, for pristine condition, without structural vibration. From top to bottom: A) raw signal, B) filtered signal, and C) normalized frequency spectrum (characteristic frequency indicated by the dashed line).

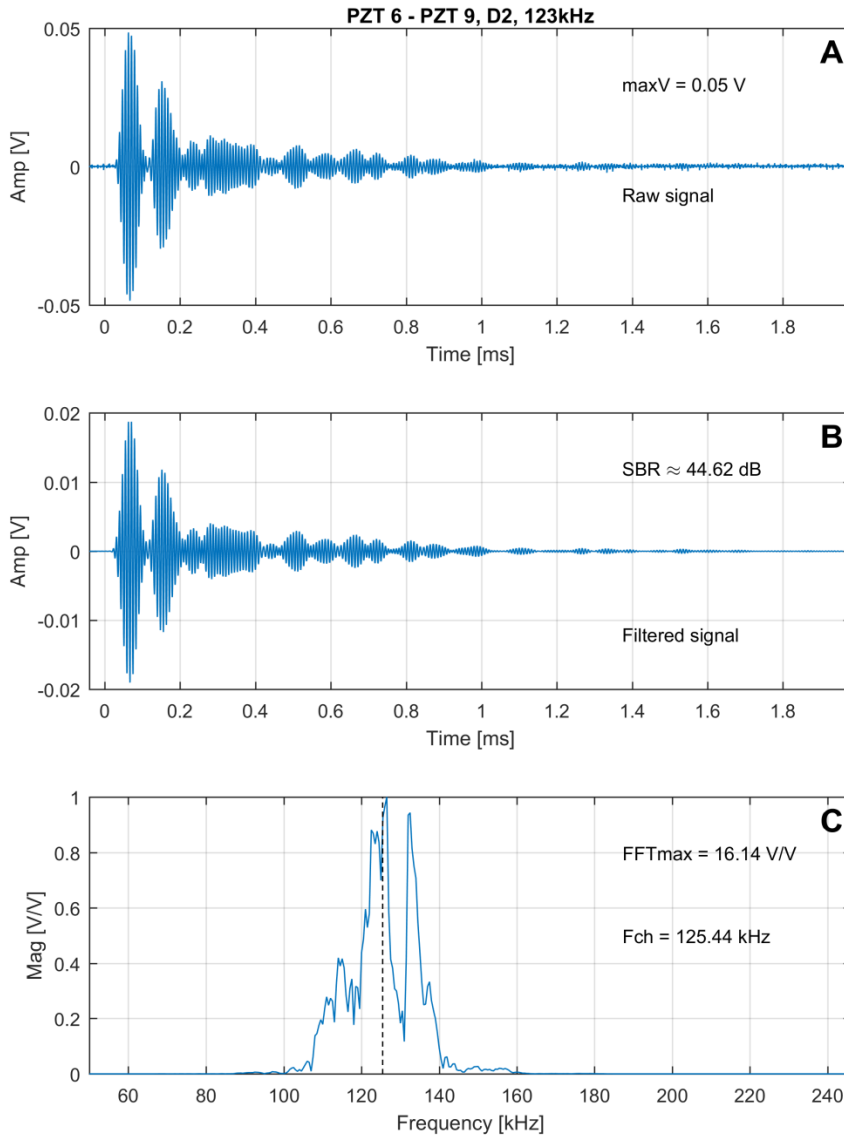


Figure A.10. Plots for actuator-sensor pair 6-9 (Area 2) at 123 kHz, after 50 J impact on stringer run-out, without structural vibration. From top to bottom: A) raw signal, B) filtered signal, and C) normalised frequency spectrum (characteristic frequency indicated by the dashed line).

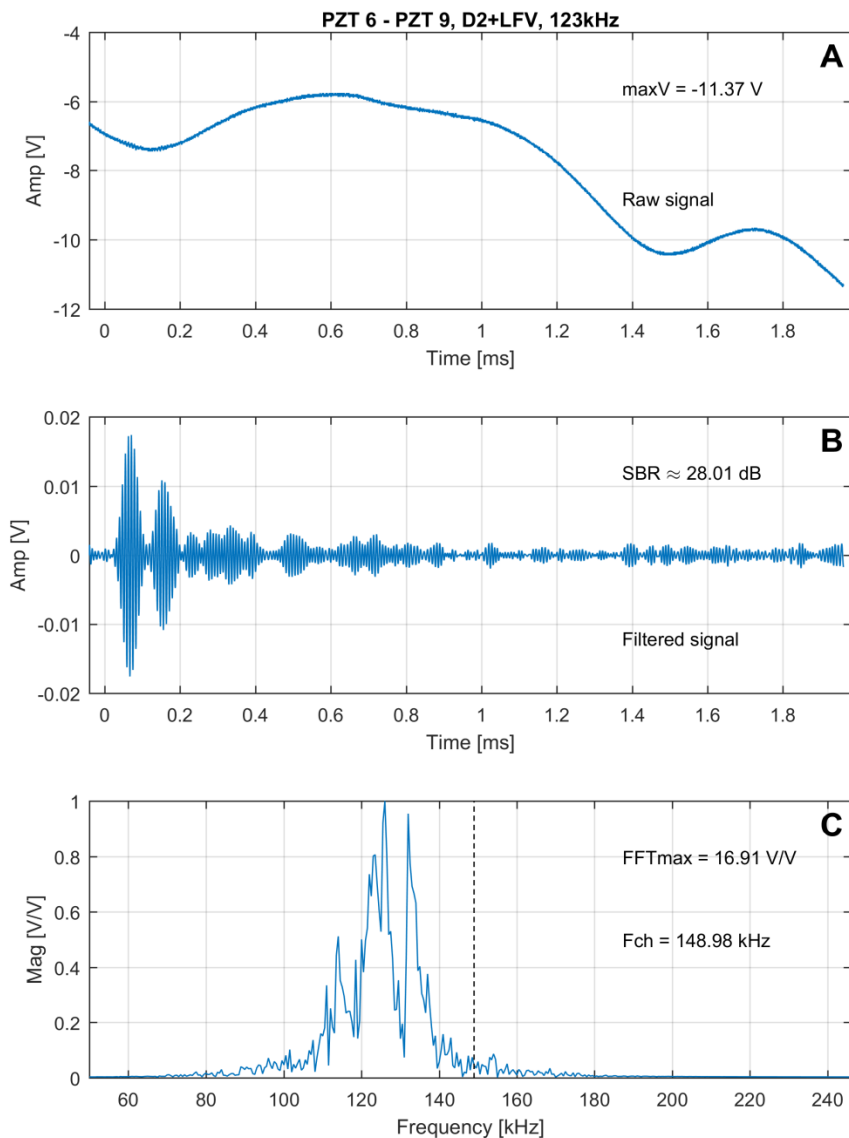


Figure A.11. Plots for actuator-sensor pair 6-9 (Area 2) at 123 kHz, after 50 J impact on stringer run-out, with low-frequency structural vibration. From top to bottom: A) raw signal, B) filtered signal, and C) normalised frequency spectrum (characteristic frequency indicated by the dashed line).

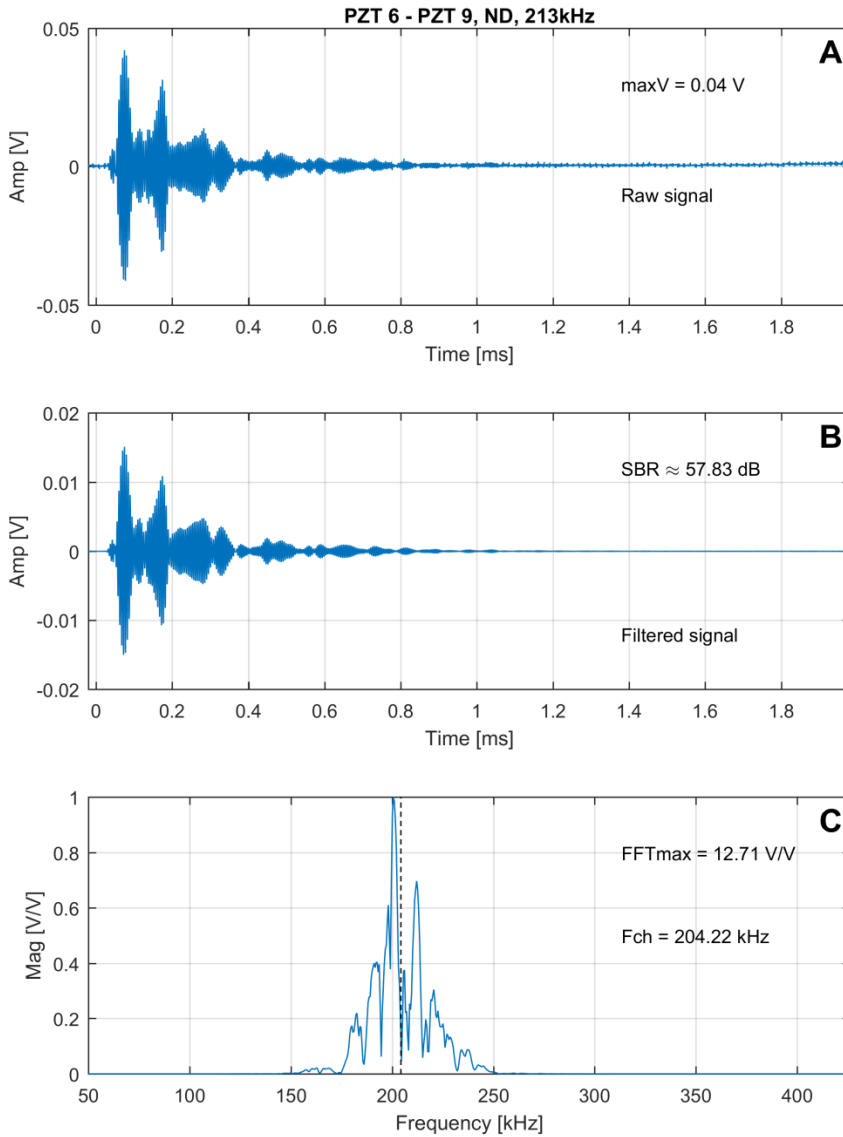


Figure A.12. Plots for actuator-sensor pair 6-9 (Area 2) at 213 kHz, for pristine condition, without structural vibration. From top to bottom: A) raw signal, B) filtered signal, and C) normalized frequency spectrum (characteristic frequency indicated by the dashed line).

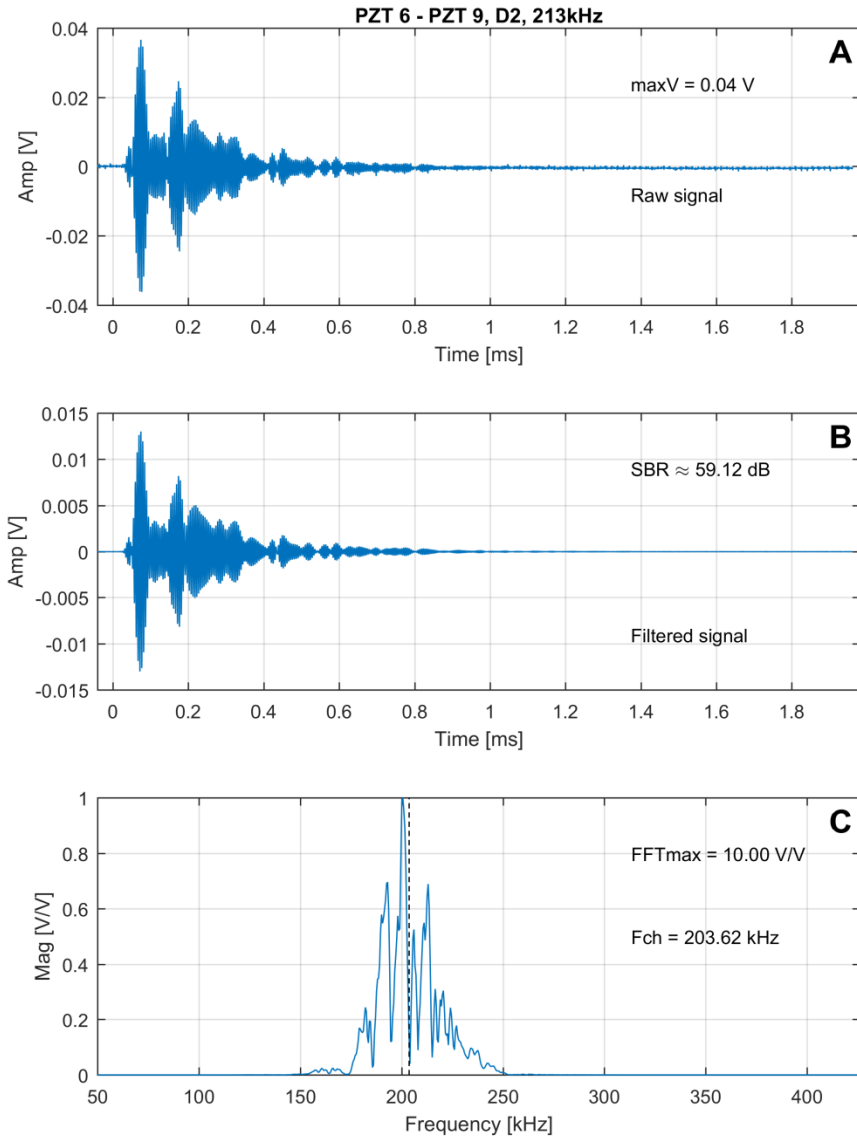


Figure A.13. Plots for actuator-sensor pair 6-9 (Area 2) at 213 kHz, after 50 J impact on stringer run-out, without structural vibration. From top to bottom: A) raw signal, B) filtered signal, and C) normalised frequency spectrum (characteristic frequency indicated by the dashed line).

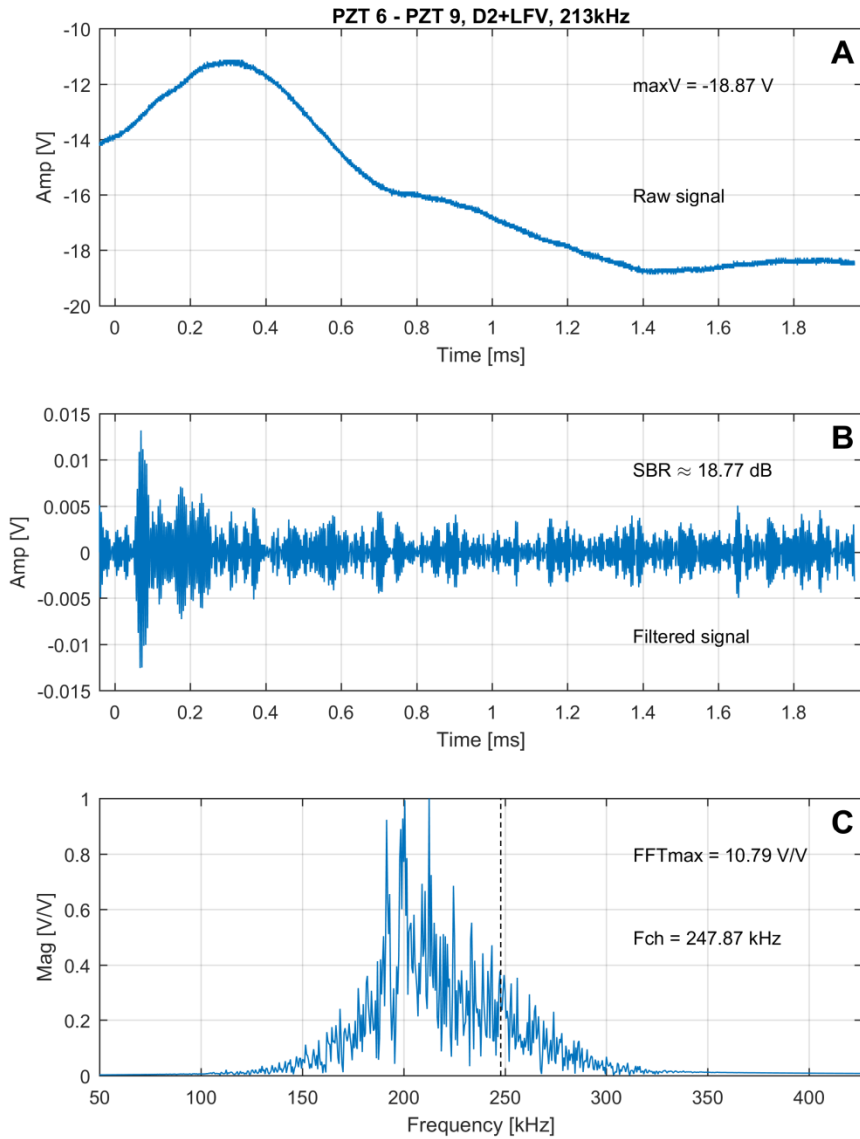


Figure A.14. Plots for actuator-sensor pair 6-9 (Area 2) at 213 kHz, after 50 J impact on stringer run-out, with low-frequency structural vibration. From top to bottom: A) raw signal, B) filtered signal, and C) normalised frequency spectrum (characteristic frequency indicated by the dashed line).

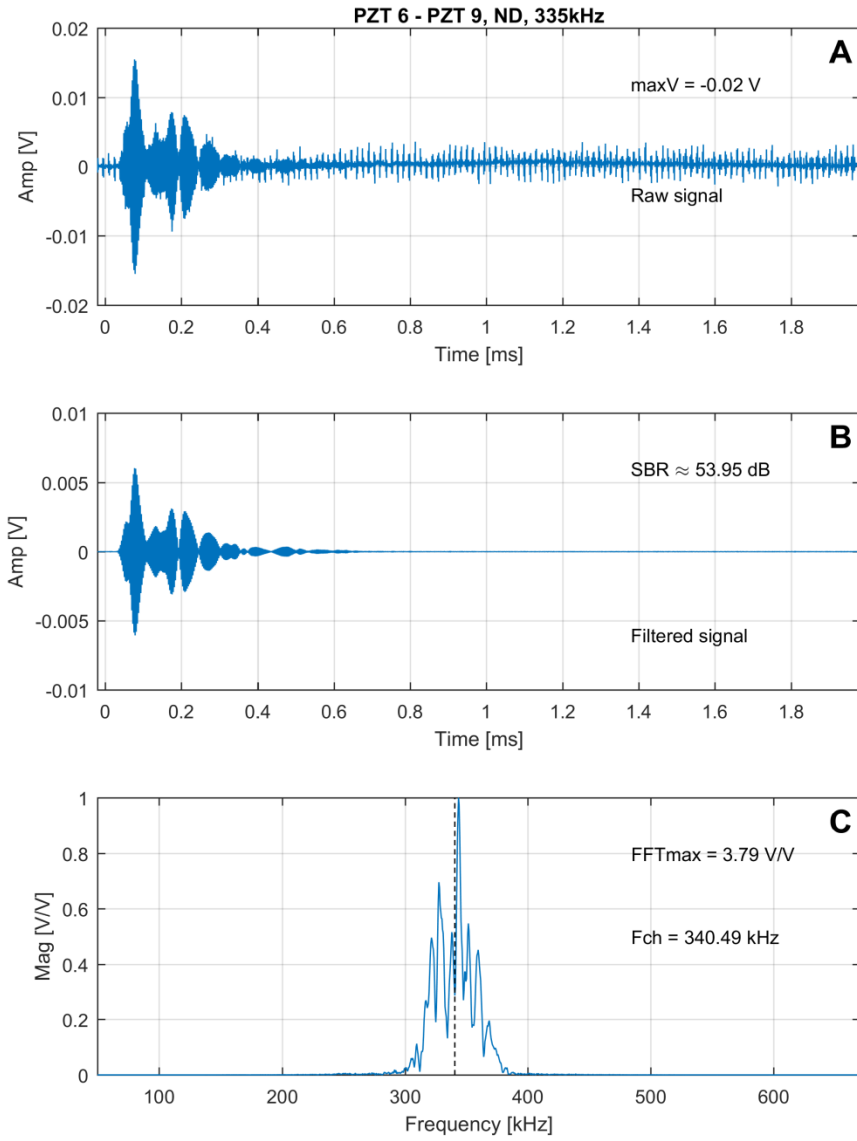


Figure A.15. Plots for actuator-sensor pair 6-9 (Area 2) at 335 kHz, for pristine condition, without structural vibration. From top to bottom: A) raw signal, B) filtered signal, and C) normalized frequency spectrum (characteristic frequency indicated by the dashed line).

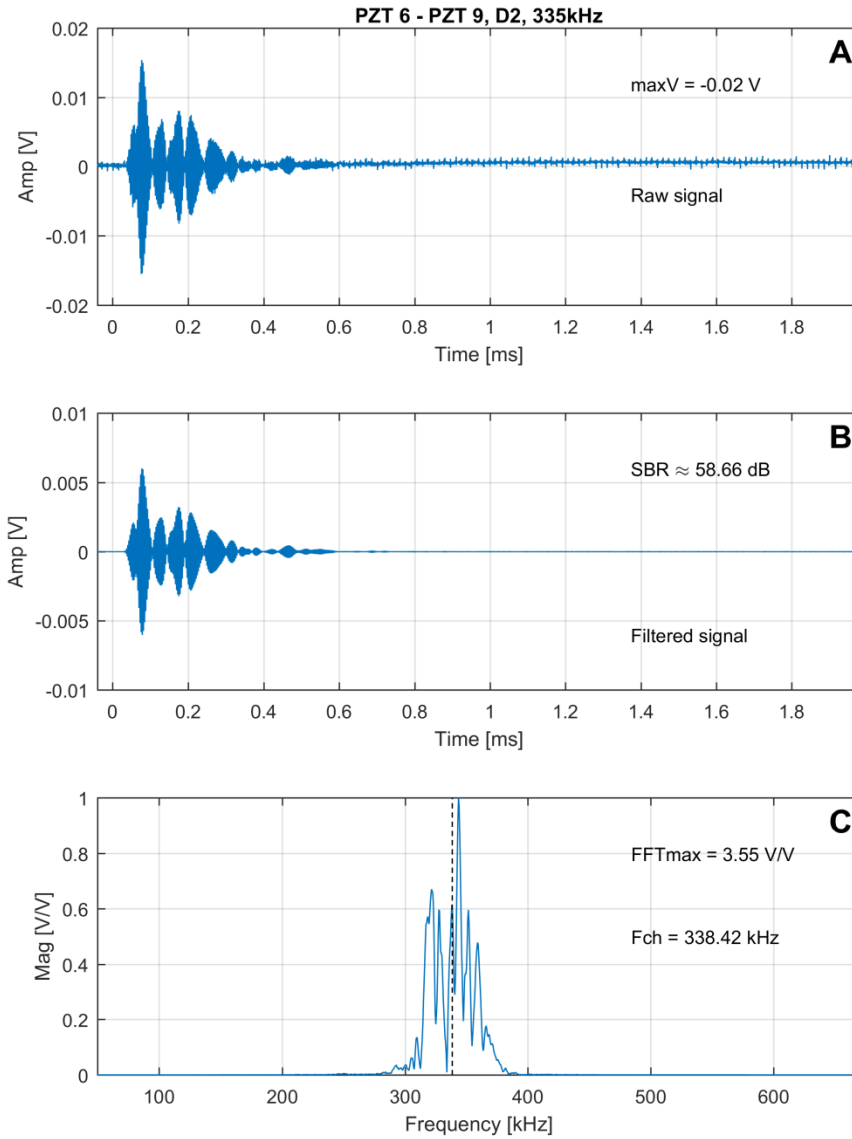


Figure A.16. Plots for actuator-sensor pair 6-9 (Area 2) at 335 kHz, after 50 J impact on stringer run-out, without structural vibration. From top to bottom: A) raw signal, B) filtered signal, and C) normalised frequency spectrum (characteristic frequency indicated by the dashed line).

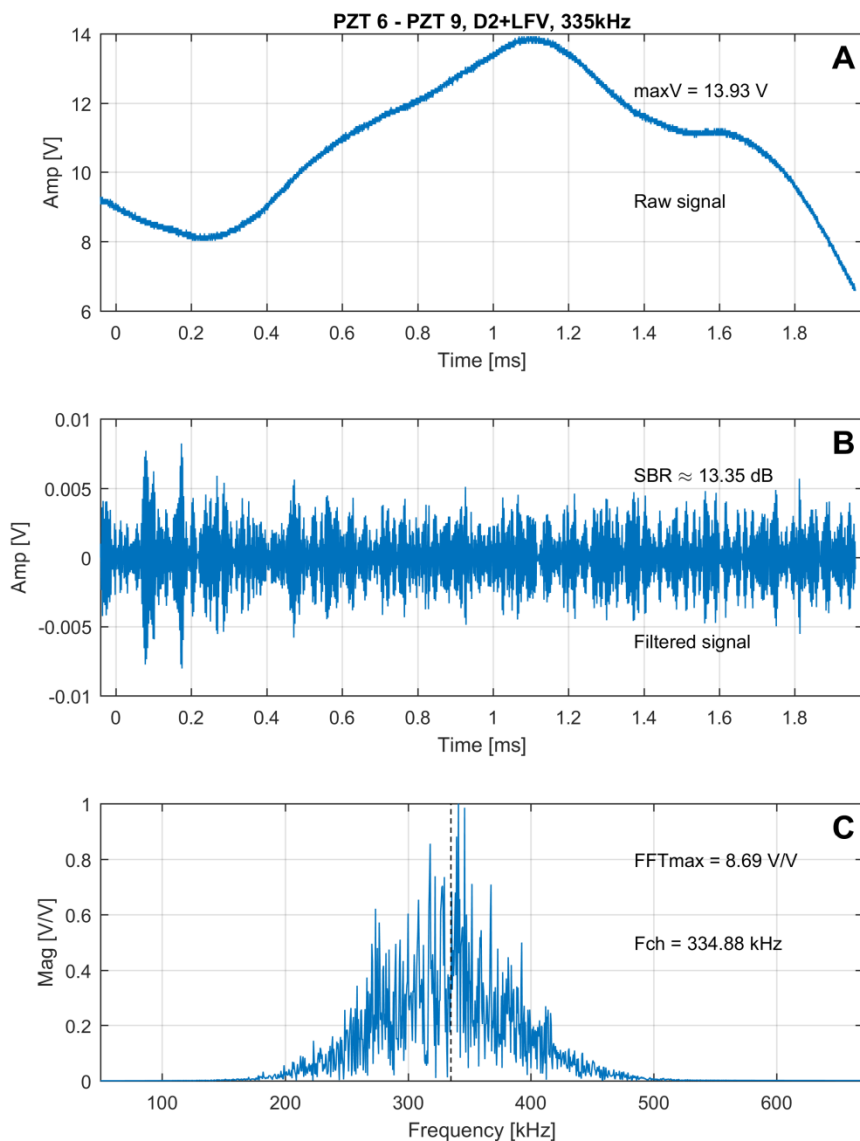


Figure A.17. Plots for actuator-sensor pair 6-9 (Area 2) at 335 kHz, after 50 J impact on stringer run-out, with low-frequency structural vibration. From top to bottom: A) raw signal, B) filtered signal, and C) normalised frequency spectrum (characteristic frequency indicated by the dashed line).

Acknowledgments

Some years ago a friend of mine said that “the PhD is a mission”. I would say it is a pilgrimage, and as such, it is something you do on your own. But along the way you meet other pilgrims, who have their own paths to walk, and with whom you end up sharing part of the journey. It is these interactions that bring new intellectual and emotional growth, making the pilgrimages complete. Here I pay tribute to all those who helped me complete my PhD.

First of all, I would like to thank my daily supervisor, Dr. Roger Groves, who always trusted me and gave me the freedom to take my own decisions during the entire research process. He allowed me to take responsibility for meeting, preparing and executing test activities with the project partners, which was very constructive and enriching for me, despite all the challenges and uncertainties in the process.

Secondly, an important thank you goes to my co-supervisor, Dr. Irene Villegas, who never lost the enthusiasm for my project, and always had very constructive ideas. She promoted my involvement with the research activities on welding of thermoplastic composites, from which I keep learning a lot. She always kept a sharp eye for the details, being a positive-critical influence on my research.

There is one person to whom every single person working in the Structural Integrity and Composites (SI&C) Group should be thankful to, and that is Gemma van der Windt. Thanks to her competence and efficiency, different type of necessary bureaucratic procedures can be executed smoothly, from ordering equipment, organizing important meetings and events, to making the link to the human resources and finance departments.

In a PhD project with experimental work, such as mine, laboratory and workshop personnel play a crucial role in the success of the research. Therefore, I want to thank all the technicians and the secretary of the Delft Aerospace Structures and Materials Laboratory for all their help. I also want to show my gratitude to technicians Lourens Prikken and Dion Baptista, from the NLR – Netherlands Aerospace Centre, for all their help and support during the largest test campaign of my PhD, in May and June of 2017.

I would also like to acknowledge my promotor, Prof. Dr. Rinze Benedictus, who gave me the chance to work as a researcher in the SI&C Group.

During the last four years I had the privilege of working in a very diverse international environment, with colleagues from almost all the continents. Each of them with stories to tell (especially at lunch time). Thank you all for those stories that sometimes helped relaxing and going through frustrating moments in the research. Due to the constant daily contact, a more special bond was formed with my office mates, Nikos Koutras, Wandong Wang, Freek Sluis, Hongwei Quan, Nakash Nazeer, Tiago Filipe, Ilias Tapeinos, Michiel Hagenbeek and Giacomo Struzziero, whom I thank for the far-reaching conversations, the silly jokes, and for supporting each other.

Thank you Fabricio Ribeiro, Romina Fernandes, Leila Sauvage and Nikos Eleftheroglou for all the wonderful moments of friendship, for sharing (a bit) of your lives with me and for being a source of inspiration. Thank you Niels for always being genuinely interested in enjoying a constructive discussion about difficult political, economic, social, and historical topics with me.

There is a couple of colleagues who deserve a special tribute. Thank you Maria Barroso for the discussions about guided waves and signal processing, and for the help with preparing coaxial cables. Thank you Nikos Koutras for the precious help with manufacturing composite panels, polishing overlap cross-sections and for explaining how to work with the optical stereo microscope. Thank you Geneviève Palardy for teaching me how to use the old ultrasonic welding machine. Thank you Bram Jongbloed for teaching me how to use one of the new ultrasonic welding machines, and for helping me out with the translation of this thesis summary.

In my mind, the start of my PhD will forever be connected to the happening of meeting my girlfriend, Jildou Brander. The circumstances of our lives at the end of September 2014 made our mind-sets, somehow, receptive to one another. Sometimes I find myself thinking, “What did she see in me?” (I guess it’s that tiny bit of immigrant-inferiority complex speaking...). For all your love and affection, for all your honesty and respect, for all your understanding about me and my culture, thank you Jildou. By the way, thank you for helping me with the translation of this thesis summary too.

A special thanks to my Portuguese friends, some in Portugal, some scattered throughout Europe, for helping keep the flame burning for all these years.

Finally, because they do not belong to any of the above categories of people and because they are more important than anybody else, I want to pay the most sincere tribute to my parents, Graça e Pedro, to my sister, Inês, and to my grand-parents, Júlia, Francisco, Emília e Fernando. I wish I am able to reciprocate all the love and support they have always given me.

Pedro André

Curriculum Vitae

Pedro André Viegas OCHÔA de Carvalho

The author was born in Lisbon, Portugal, on the 10th of May of 1988. In June 2006 he graduated from José Gomers Ferreira High School in Lisbon. In September that year, he enrolled in Instituto Superior Técnico (IST), University of Lisbon, where he obtained a Bachelor of Science (BSc) degree in Aerospace Engineering in 2009.

The author proceeded his studies in Aerospace Engineering, following a specialisation in Aircraft. In the academic year 2010/2011, he went on an Erasmus exchange programme to Delft University of Technology (TU Delft), the Netherlands. There he took one semester of courses and worked on the experimental activities of his master's thesis, entitled: "Detection of Multiples Low-Energy Impact Damage in Composite Plates Using Lamb Wave Techniques". This work was performed under the supervision of Dr. Virgínia Infante, Dr. José Miguel Silva and Dr. Roger Groves. The author obtained the degree of Master of Science (MSc) in Aerospace Engineering from IST in October 2011.

One month later, the author started as a Research Scientist at Knowledge Centre WMC, the Netherlands. There, and during one year, he studied extreme temperature effects on static and fatigue behaviours of composites for wind turbine rotor blades. In November 2012, he joined Atkins BV, the Netherlands, as a Stress Engineer, where he was responsible for fatigue and damage tolerance analysis of the structures of high-lift devices for Airbus aircraft.

Almost after two years, in October 2014, the author started the research project that resulted in this PhD thesis, integrated in the Thermoplastic Affordable Primary Aircraft Structures 2 project, which was funded by Netherlands Enterprise Agency of the Ministry of Economic Affairs. The work was conducted under the supervision of Prof. Dr. Ir. Rinze Bendictus as promotor, Dr. Roger Groves as co-promotor and daily supervisor, and Dr. Irene Villegas as second supervisor.

List of publications

Journal papers

5. **Ochôa P**, Groves RM, Benedictus R. Effects of high-amplitude low-frequency structural vibrations and machinery sound waves on ultrasonic guided wave propagation for health monitoring of composite aircraft primary structures. Under review at the *Journal of Sound and Vibration*.
4. **Ochôa P**, Villegas IF, Groves RM, Benedictus R. Diagnostic of manufacturing defects in ultrasonically welded thermoplastic composite joints using ultrasonic guided waves. *NDT & E International* 2019; 107: 102126
3. **Ochôa P**, Groves RM, Benedictus R. Systematic multi-parameter design methodology for an ultrasonic health monitoring system for full-scale composite aircraft primary structures. *Structural Control and Health Monitoring* 2019; 26(5): e2340.
2. **Ochôa P**, Villegas IF, Groves RM, Benedictus R. Experimental assessment of the influence of welding process parameters on Lamb wave transmission across ultrasonically welded thermoplastic composite joints. *Mechanical Systems and Signal Processing* 2018; 99: 197-218.
1. **Ochôa P**, Infante V, Silva JM, Groves RM. Detection of multiple low-energy impact damage in composite plates using Lamb wave techniques. *Composites Part B* 2015; 80: 291-298.

Conference papers

4. **Ochôa P**, Groves RM, Benedictus R. Full-scale testing of an ultrasonic guided wave based structural health monitoring system for a thermoplastic composite aircraft primary structure. Paper presented at: *9th European Workshop on Structural Health Monitoring*, July 10-13, 2018; Manchester, United Kingdom.
3. **Ochôa P**, Groves RM, Benedictus R. Reliability analysis of an ultrasonic guided wave based structural health monitoring system for a carbon fibre reinforced thermoplastic torsion-box. Paper presented at: *11th International Workshop on Structural Health Monitoring*, September 12-14, 2017; Palo Alto, CA (USA).
2. **Ochôa P**, Villegas IF, Groves RM, Benedictus R. Experimental characterisation of Lamb wave propagation through thermoplastic composite ultrasonic welds. Paper presented at: *15th Anglo-French Physical Acoustics Conference*, January 13-15, 2016; South Croydon, United Kingdom.
1. **Ochôa P**, Groves RM, Benedictus R. Lamb wave dispersion time-domain study using a combined signal processing approach. Paper presented at: *6th International Conference on Emerging Technologies in Nondestructive Testing*, May 27-29, 2015; Brussels, Belgium.

